

Ferroelectric Tunnel Junctions

I n a u g u r a l – D i s s e r t a t i o n

zur

Erlangung des Doktorgrades

der Mathematisch-Naturwissenschaftlichen Fakultät

der Universität zu Köln

vorgelegt von

Julio Rodríguez Contreras

aus Hürth

Eigenverlag Forschungszentrum Jülich, Jülich, 2004

Berichterstatter:

Prof. Dr. Ch. Buchal
Prof. Dr. M. Braden

Tag der mündlichn Prüfung:

10. November 2003

Kurzzusammenfassung

Ferroelektrizität und quantenmechanisches Elektronentunneln sind gut bekannte physikalische Phänomene, die seit einem Jahrhundert untersucht werden. Während dieser langen Zeit beschäftigte sich die wissenschaftliche Forschung entweder mit Ferroelektrizität *oder* mit dem Elektronentunneln. Niemals zuvor hat eine Verbindung dieser beiden Phänomene stattgefunden und niemals ist ein neues Phänomen beobachtet worden, das auf ihrer Wechselwirkung beruht.

In dieser Arbeit stelle ich das Konzept eines ferroelektrischen Tunnelkontakts vor. Der Begriff *ferroelektrisch* bezieht sich hierbei auf eine Eigenschaft des Barrierenmaterials. Ein solcher Tunnelkontakt besteht aus einer ferroelektrischen Schicht, die sich zwischen zwei Metallelektroden befindet. Die ferroelektrische Schicht ist dabei dünn genug, um Elektronentunneln durch sie hindurch zu ermöglichen.

Zum ersten Mal wird die Wechselwirkung von makroskopischen Größen, wie z. B. der spontanen Polarisation und der Gitterverzerrung, mit quantenmechanischem Elektronentunneln experimentell untersucht.

Begleitet wird die experimentelle Arbeit durch theoretische Ideen und Vorhersagen über den Einfluß der Piezo- und Ferroelektrizität auf das direkte Elektronentunneln.

Abstract

Ferroelectricity and quantum-mechanical electron tunneling are well-known physical phenomena that have been studied for as long as a century. During this long period, scientific research has been restricted either to ferroelectricity *or* to electron tunneling. Never before have these subjects been combined into a new phenomenon based on their interaction.

Within this work, I present the novel concept of a ferroelectric tunnel junction, where the term *ferroelectric* refers to a property of the barrier material. This device consists of a ferroelectric layer sandwiched between metal electrodes. The thickness of the ferroelectric layer is thin enough to allow for electron tunneling.

For the first time, the influence of macroscopic parameters, such as the spontaneous polarization and strain on quantum-mechanical electron tunneling through a ferroelectric tunnel barrier is studied experimentally.

In addition, the experimental work is accompanied by theoretical ideas and predictions concerning the manifestation of piezoelectricity or ferroelectricity in direct electron tunneling.

Contents

Introduction	vii
I Theory	1
1 The ferroelectric thickness limit	3
1.1 Piezoelectricity	3
1.2 Ferroelectricity	5
1.3 Electrical boundary conditions	16
1.4 Mechanical boundary conditions	20
2 Quantum-mechanical tunneling	27
2.1 Tunneling effect	27
2.2 Elastic and inelastic electron tunneling	30
3 Concept of a Ferroelectric Tunnel Junction	35
3.1 Piezoelectricity and tunneling	36
3.2 Ferroelectricity and tunneling	42
4 Heteroepitaxy of oxide perovskites	49
4.1 Material systems	49
4.2 Deposition techniques	55
5 Characterization techniques	61
5.1 Structural characterization	61
5.2 Electrical characterization	68
II Experimental results	71
6 Structural properties	73
6.1 Pulsed-laser-deposited $(Ba, Sr)TiO_3$ thin films	73
6.2 Molecular beam epitaxy of $SrRuO_3$ and $BaTiO_3$ thin films . .	76

6.3	High-pressure sputtered $SrRuO_3$ and $Pb(Zr,Ti)O_3$ thin films	89
7	Ferroelectric properties	97
7.1	Influence of different patterning methods	98
7.2	Influence of boundary conditions	101
7.3	Thickness dependence of ferroelectric properties	107
8	Current transport through ultrathin films	119
8.1	Resistive switching effects in I - V curves	120
8.2	Current transport mechanisms	124
8.3	Similar switching effects reported by other groups	131
8.4	Final remarks on resistive switching and current transport mechanisms	134
	Summary	139
	Literaturverzeichnis	145

Acknowledgements

Many people have provided me with assistance, guidance and support while I was working on my PhD.

First, I am greatly indebted to Prof. Dr. Christoph Buchal for supervising this thesis, for his support during the last three years and for our fruitful discussions.

Thanks are also due to Prof. Dr. Markus Braden for accepting the task of co-examiner. The interest he showed in my thesis is uncommon and is greatly appreciated.

I wish to express my deepest gratitude to Dr. Hermann Kohlstedt for his unwavering enthusiasm and his relentless pursuit of excellence. Hermann's caring and support during my thesis are truly above and beyond the call of duty. He deserves more than the traditional "thanks".

I would like to thank Prof. Dr.-Ing. Rainer Waser for giving me the opportunity to work on this thesis and for giving me the freedom and resources from which I greatly benefitted.

I am immensely grateful and deeply indebted to Prof. Dr. Darrell Schlom for giving me the opportunity to spend nine *awesome* months at PennState. I am particularly grateful for Darrell's generosity, his exceptional enthusiasm and for many inspiring and fascinating discussions.

Special mention deserves to be made of the continuous assistance provided by Dr. Nicholas Pertsev. He contributed in a large manner to the work in this thesis. In addition, his critical comments on my draft are acknowledged with gratitude.

I also owe thanks to Dr. Jürgen Schubert for many inspiring discussions, for his support and for providing PLD-grown films.

I am obliged to Dr. Ulrich Poppe for his support with the high-pressure sputtering system and many stimulating discussions.

Special credit is also due to Bernd Hermanns for his contribution to this work during his diploma.

My special appreciation goes to Dr. Kristof Szot and Dr. Chunlin Jia for providing AFM and HRTEM measurements, respectively. I am also grateful to Dr. Theo Schneller, Daliborka Vukelic and Hans Haselier for providing *Pt* top electrodes.

I wish to express my sincere gratitude to Dr. James Lettieri, who recently passed away. My stay at PennState would not have been as exceptional as it was without James' support and encouragement during this time. Our discussions about science, sports and life are among my happiest memories.

Other members of the Schlom group who provided a relaxed atmosphere and continuous entertainment (inside and outside the lab) were Dr. Jeff Haeni, Goh Asayama, Mike Biegalski, Dr. Venu Vaithyanathan, Lisa Friedman Edge, and Sven Clemens.

I would also like to thank all colleagues at Research Center Jülich and RWTH Aachen, including my office-mates Simon Stein, Andreas Gerber, Martin Weides, and Dr. Vladimir G. Kukhar.

I owe special acknowledgements to the many extremely talented collaborators who I have had the pleasure working with including Prof. Dr. Philippe Ghosez, Dr. Javier Junquera, Prof. Dr. Chang-Beom Eom, Prof. Dr. Ramamoorthy Ramesh, Dr. V. Nagarajan, Dr. Wei Tian, Prof. Dr. Xiaoqing Pan, Dr. Christian Loppacher, Dr. Frank Schlaphof, Prof. Dr. Lukas Eng, Dr. Klaus Michael Indlekofer, Dr. Stephan Tiedke and aixACCT Systems.

Thanks are also due to Carol and Martin Stoffel, Janet Carter-Sigglow, Dr. Bernd Holländer, and Dr. Peter Ehrhart for their careful reading of several Chapters of this thesis.

I acknowledge the valuable role played by my high-school teacher, Bruno Tuchscherer, who introduced me to the world of physics. His enthusiastic and fascinating teaching made a lasting impact on me.

I am indebted to the German Academic Exchange Service (DAAD), who supported my stay at PennState University.

On a personal note, I would like to express my deepest gratitude to my girl-friend, Katrin Felusch, for her emotional support. My grandmother, Fidela Herrero Jiménez, took care of me when I wrote a good part of this thesis at her place in Salamanca, Spain. My family has been my biggest gift in life. I have enjoyed love and constant support from my sister Susana, my mother Maria del Carmen, and my father Tomás.

Introduction

In the last few years, tremendous progress has been made in the investigation of the ferroelectric limit in thickness. This is partly due to the accelerating interest in ferroelectric materials for technological applications, and it is partly due to the natural scientific interest in understanding and studying the limits of physical phenomena.

Ferroelectricity is a collective phenomenon discovered at the beginning of the last century [1]. Thirty years ago Batra and Silverman [2] predicted the ferroelectric minimum thickness to be around 400 nm. Since then the predicted minimum thickness has been reduced continuously. This development is based on a better understanding of the electrical and mechanical boundary conditions in ferroelectric thin films. Some of the most important contributions came from Batra and coworkers [3], Kretschmer and Binder [4], and Pertsev *et al.* [5]. Based on recently published theoretical studies by Zembilgotov and coworkers using a thermodynamic theory [6], as well as on ab-initio calculations performed by Ghosez and Junquera [7], ferroelectricity in thin films under favorable boundary conditions is believed to survive in epitaxial films as thin as a few nm.

The experimental progress in studying finite size effects (i.e. the dependence of ferroelectric properties on the sample size) has been quite remarkable as well, especially in the last five years. This progress mainly arises from constructing experiments based on a better theoretical understanding of ferroelectricity and from improvements in the deposition techniques and analytical methods. In 1999, Yanase and coworkers showed ferroelectricity in 12 nm thick $BaTiO_3$ films [8]. In the same year, Tybell and coworkers presented scanning probe microscopy measurements claiming the demonstration of ferroelectricity in 4 nm thick $PbTiO_3$ thin films [9]. Recently, Streiffer and coworkers found 180° stripe domains in 3 monolayers of $PbTiO_3$ by *in situ* grazing-incidence x-ray scattering and predicted the existence of ferroelectricity in this only 1.2 nm thick film [11, 10].

The pursuit of the ferroelectric minimum thickness has reached a thickness range where tunneling through these films may be expected. Quantum-mechanical electron tunneling through an insulating barrier is one of the most amazing phenomena in physics. The so-called tunneling effect has been studied for 80 years. In this long period, the combination of ferroelectricity and tunneling has never been experimentally investigated. Unlike ferroelectricity, the combination of magnetism and tunneling, as well as superconductivity and tunneling, are the origin of well-known effects known as tunneling magnetoresistance (Juillère 1975 [12]) and the Josephson effect (Josephson 1962 [13]), respectively.

Magnetic tunnel junctions and superconducting tunnel junctions, as well as their combination, have been studied in the past. The aim of this work is the study of a possible interaction of ferroelectricity and electron tunneling. It should be stressed that unlike the term *magnetic* and the term *superconducting* in magnetic tunnel junction and superconducting tunnel junction, respectively, which both refer to a property of the electrode material, in a ferroelectric tunnel junction the collective phenomenon is situated in the barrier itself.

This thesis is organized as follows. In Chapter 1 piezoelectricity and ferroelectricity are introduced and various origins of size effects in ferroelectric thin films are discussed. Chapter 2 deals with the relevant theories on electron tunneling through a thin barrier. In Chapter 3 the concept of a ferroelectric tunnel junction is presented. In this Chapter some ideas and predictions are given about how the ferroelectric polarization reversal and the converse piezoelectric effect may interact with direct electron tunneling through an ultrathin ferroelectric barrier. In Chapter 4 the studied material systems and the different deposition techniques used in this work are reported. Chapter 5 is about the characterization techniques that were employed to study both the structural and electrical properties of the thin films. The results of the former are shown in Chapter 6. In Chapter 7 and 8 a detailed report on the studies of the electrical properties and current transport mechanisms is given. It also contains the fabrication procedures of ferroelectric capacitors and tunnel junctions. Finally, the results obtained in Chapter 8 are evaluated and compared with the theoretical ideas and calculations presented in Chapter 3.

Part I
Theory

Chapter 1

The ferroelectric thickness limit

The question of whether or not there is a ferroelectric minimum in lateral dimensions and in thickness is a subject of ongoing discussion for more than 30 years. The pursuit for miniaturization in micro- and nanotechnology is a challenge that requires the knowledge and understanding of how reduced dimensions affect the physical properties of a particular material.

This Chapter will start with an introduction of piezoelectricity and ferroelectricity. Afterwards various origins of size effects in ferroelectric thin films will be discussed.

1.1 Piezoelectricity

A dielectric material can be polarized by application of an electric field \vec{E} . The total surface charge density induced in the material by the applied field is given by the dielectric displacement vector:

$$D_i = \varepsilon_0 E_i + P_i, \quad (1.1)$$

where $\varepsilon_0 = 8.854 \times 10^{-12} \text{ Fm}^{-1}$ is the dielectric permittivity of vacuum, and \vec{P} is the polarization.

A dielectric material is referred to as a piezoelectric material, if it can be polarized, in addition to an electric field, by application of mechanical stress.

The *direct piezoelectric effect* describes the linear relationship between the applied stress X_{ik} and the resulting charge density D_i :

$$D_i = d_{ijk} X_{jk}, \quad (1.2)$$

where d_{ijk} represents a third-rank tensor of the piezoelectric coefficients.

For this work, the *converse piezoelectric effect* is more important. This effect describes the field-induced strain S_{ij} in a piezoelectric material:

$$S_{ij} = d_{ijk}E_k. \quad (1.3)$$

It can be shown that the piezoelectric coefficients for the direct and converse piezoelectric effect are identical [14]. For symmetry reasons the only non-zero piezoelectric coefficients are d_{333} , $d_{311} = d_{322}$ and $d_{131} = d_{113} = d_{223} = d_{232}$ [15]. This tensor notation can, therefore, be simplified by introducing the matrix notation [16]. Here, the above mentioned non zero piezoelectric coefficients are referred to as **longitudinal component** d_{33} , **transverse component** $d_{31} = d_{32}$ and **shear component** $d_{15} = d_{24}$, respectively (see Fig. 1.1).

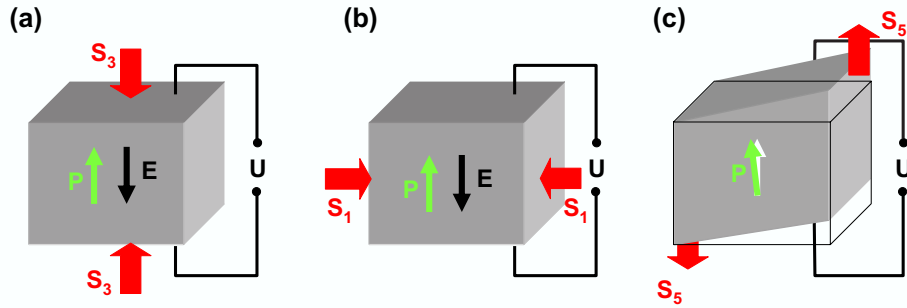


Figure 1.1: Illustration of the three different non-zero piezoelectric coefficients for a material with symmetry $8m$: a) d_{33} for a dielectric displacement, if a stress is applied in the same direction or, for a strain, if the electric field is acting in the same direction. b) d_{31} for a dielectric displacement, if a stress is applied in the perpendicular direction or, for a strain, if the electric field is acting in the perpendicular direction. c) d_{15} for a dielectric displacement, if a shear stress is applied or, for a shear strain, if the electric field is acting. [17]

The converse piezoelectric effect is different from *electrostriction*, observed in all dielectric materials, since the converse piezoelectric effect is linear in the applied electric field. The electrostrictive effect is based on a non-linear coupling between elastic and electric fields. The application of an electric field produces strain, which will not change on reversal of the electric field, i.e. the effect is quadratic. With the exception of so-called relaxor-ferroelectrics¹, the electrostrictive effect is relatively small.

¹Relaxors (e.g. $(Pb,La)(Zr,Ti)O_3$) display a diffuse phase transition with a broad maximum in the dielectric permittivity. Relaxors do not obey the Curie-Weiss behavior.

1.2 Ferroelectricity

Figure 1.2 (a) schematically shows the displacement of the ions in an ABO_3 perovskite structure due to an applied electric field. Ferroelectric materials exhibit an electric dipole moment, even in the absence of an external electric field. The polarization associated with the spontaneously formed dipole moment is called spontaneous polarization \vec{P}_S . Ferroelectrics possess at least two equilibrium orientations of the spontaneous polarization vector, \vec{P}_S . The spontaneous polarization vector may be switched between those orientations by application of an oppositely oriented electric field (see Fig. 1.2 (b)) [18].

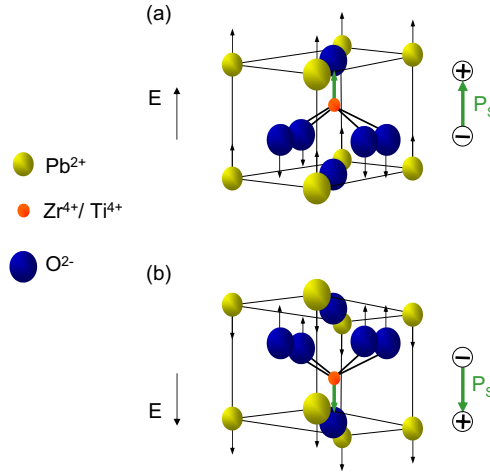


Figure 1.2: ABO_3 perovskite structure, here $Pb(Zr,Ti)O_3$, under an external electric field E applied along the polar axis (a) and in the opposite direction (b).

The hysteresis of the polarization P , as a function of the field E , is shown in Fig. 1.3 (a) for single-domain single crystals and in Fig. 1.3 (b) for polydomain samples. The polarization at zero field is called remanent polarization P_r . It is identical to the spontaneous polarization for single domain samples. In order to reverse the polarization, a coercive field E_c is necessary. In polydomain samples the field necessary to reduce the polarization to zero is referred to as coercive field E_c .

I would like to point out that the polarization P , as well as the coercive field E_c , are both macroscopic parameters.

Ferroelectric materials undergo a phase transition from a higher symmetry paraelectric phase to a lower symmetry ferroelectric phase. The paraelec-

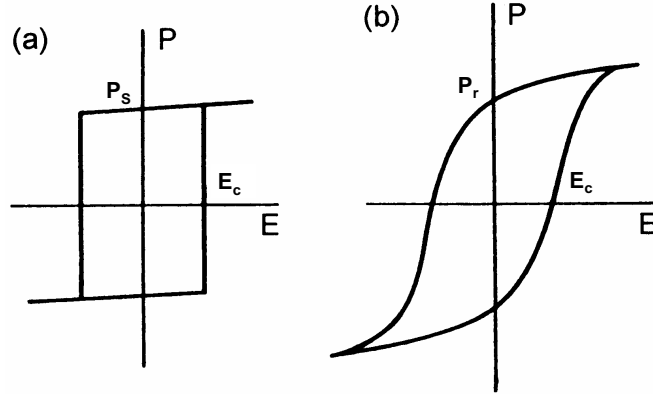


Figure 1.3: Ferroelectric P - E curve for (a) single-domain and (b) polydomain samples.

tric phase is not ferroelectric, but may be piezoelectric [18]. The temperature, where this phase transition occurs, is termed T_C .

Mean-field theory

In order to calculate the phase transition, Landau [19] and Ginzburg [20] expanded the thermodynamical potential near the phase transition temperature in a power series and introduced the spontaneous polarization as an order parameter. Devonshire used this formalism, which assumes that the same polynomial is capable of describing both ferroelectric and non-ferroelectric phases, to characterize the phase transition of $BaTiO_3$ [21].

Following [17], the Ginzburg-Landau theory is equivalent to a mean field theory, where the thermodynamic quantity - here, a dipole - is considered in the mean field of all the others. Close to the phase transition temperature, the free energy F can be expanded in a power series with powers of the order parameter P up to the sixth order:

$$F(P, T) = \frac{1}{2}g_2P^2 + \frac{1}{4}g_4P^4 + \frac{1}{6}g_6P^6 - P \cdot E. \quad (1.4)$$

No odd-power terms appear, as the polynomial has to be symmetrical against polarization reversal. The coefficients g_2 , g_4 , and g_6 are in general temperature-dependent, but simple examples of first- and second-order ferroelectric phase transitions are described with g_4 and g_6 independent of temperature [22]. Around the Curie-Weiss temperature T_0 , g_2 can be approximated by $g_2 = C^{-1}(T - T_0)$.

The thermodynamically stable states are obtained from the minima of the free energy (with $E = 0$) via,

$$\frac{\partial F}{\partial P} = P(g_2 + g_4 P^2 + g_6 P^4) = 0, \quad (1.5)$$

$$\frac{\partial^2 F}{\partial^2 P} = \chi^{-1} = g_2 + 3g_4 P^2 + 5g_6 P^4 > 0. \quad (1.6)$$

Equations (1.5, 1.6) are solved by $P = 0$ at $g_2 > 0$. This is the paraelectric (PE) phase. Other solutions exist for $\pm P_S \neq 0$. These are the ferroelectric (FE) solutions.

Paraelectric phase

In the paraelectric phase, $T > T_0$, the susceptibility is found to follow a Curie-Weiss law with a critical exponent $\gamma = 1$:

$$\chi(T) = \frac{C}{T - T_0} \propto (T - T_0)^{-\gamma}; \quad \gamma = 1. \quad (1.7)$$

First-order phase transition

Most perovskites, including $PbZr_xTi_{1-x}O_3$ ($x < 0.28$) [23] and $BaTiO_3$ undergo a first-order phase transition. This type of phase transition is characterized by the appearance of metastable phases, as the new phase has to nucleate out of the old phase. Sudden changes in the crystal structure and volume are further characteristics of first-order phase transitions.

Consider the free energy (eqn. (1.4)) for $g_4 < 0$ and $g_6 > 0$. In this case, the thermodynamically stable states are given by

$$P = 0, \quad (1.8)$$

or

$$P_S^2 = \frac{|g_4| + \sqrt{g_4^2 - 4C^{-1}(T - T_C)g_6}}{2g_6}. \quad (1.9)$$

Figure 1.4 (a) shows the free energy as a function of polarization for a first order phase transition. Here, the Curie-Weiss temperature T_0 is not equal to the phase transition temperature T_C . The following temperature regimes can be distinguished:

$T \gg T_C$: stable paraelectric phase ($P = 0$)

$T > T_C$: stable PE phase ($P = 0$), metastable FE phase ($\pm P_S \neq 0$)

$T = T_C$: coexistence of paraelectric and ferroelectric phase

$T_0 < T < T_C$: stable FE phase and metastable PE phase

$T < T_0$: stable ferroelectric phase

Somewhere during the cooling through the regime where the paraelectric phase coexists with the metastable ferroelectric phase ($T_0 < T < T_C$), the system undergoes a transition with a discontinuity in the spontaneous polarization. In other words, the spontaneous polarization jumps from zero to a finite value corresponding with the first-order phase transition.

In addition, using the known thermodynamical relations, one will get at $T = T_C$ discontinuous changes in susceptibility χ and entropy S .

Second-order phase transition

Second-order phase transitions are characterized by a continuous change in crystal structure and volume. The first known ferroelectric material, Rochelle salt, $NaKC_4H_4O_6 \cdot 4H_2O$ [24], as well as $PbZr_xTi_{1-x}O_3$ ($x > 0.28$) [23], undergo second-order phase transitions.

Here, it is sufficient to consider the polynomial expansion of the free energy (eqn. (1.4)) up to the fourth order and to take $g_4 > 0$. From these assumptions the following solutions are obtained:

$$P = 0, \quad (1.10)$$

or

$$P_S^2 = - \frac{(T - T_C)}{g_4 C}. \quad (1.11)$$

Phase transition temperature T_C and Curie-Weiss temperature T_0 are identical for a second-order phase transition. The critical exponent for the order parameter is 1/2:

$$P_S \propto (T - T_C)^\beta; \quad \beta = 1/2. \quad (1.12)$$

Figure 1.4 (b) schematically displays the free energy close to the second-order phase transition as a function of the spontaneous polarization. At the phase transition temperature, the stable minimum is at $P = 0$. Decreasing the temperature will shift this minimum continuously to finite values of the polarization.

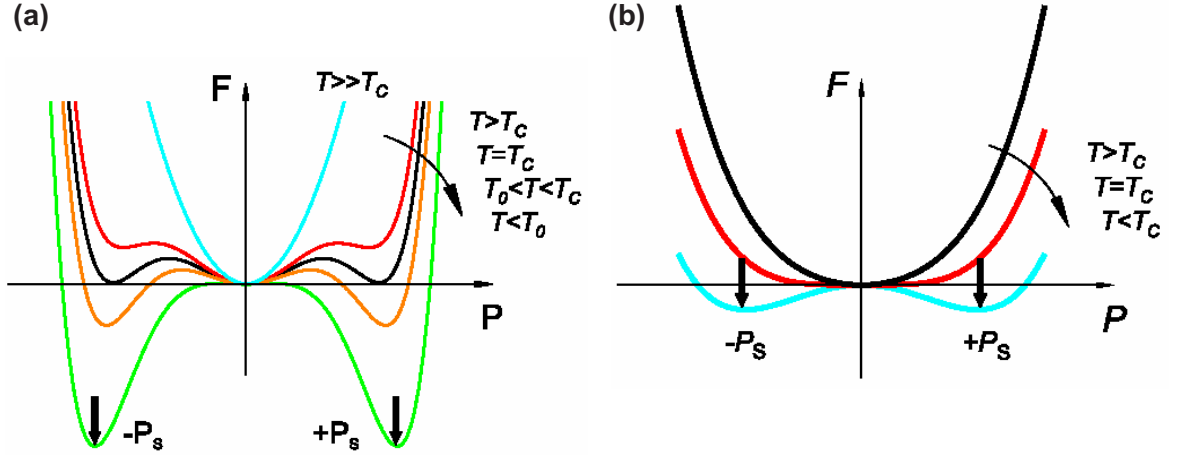


Figure 1.4: Schematic presentation of the free energy as a function of polarization for ferroelectrics with (a) first order and (b) second order phase transition. [17]

In summary, a second-order phase transition is characterized by a continuous change in polarization, inverse susceptibility, and entropy. Only the specific heat jumps at the phase transition [17].

Coercive field

This Section is about the coercive field of a ferroelectric thin film. The coercive field corresponds to the electric field necessary to reverse the polarization from one direction to the opposite direction. In polydomain samples the electric field that brings the mean polarization of a prepolarized sample down to zero is referred to as coercive field. In the first paragraph, the Ginzburg-Landau theory is used to calculate the coercive field for a free-standing film assuming that the domains all reorient simultaneously and independently. The second paragraph describes the switching kinetics in a real thin film and explains the disagreement between the coercive field obtained from Landau-Ginzburg theory and the experimentally observed coercive field in a ferroelectric thin film. Finally, the third paragraph deals with the frequency dependence of the coercive field.

Coercive field calculated from Ginzburg-Landau theory

Consider a polynomial expansion of the free energy (eqn. (1.4)) up to the fourth order [25] with the approximation for g_2 given on page 6:

$$F(P, T) = \frac{1}{2C}(T - T_C)P^2 + \frac{1}{4}g_4P^4 - P \cdot E. \quad (1.13)$$

The conditions of thermodynamic equilibrium, which corresponds to the minimization of the free energy, are given by

$$\frac{\partial F}{\partial P} = \frac{T - T_C}{C} P + g_4P^3 - E = 0, \quad (1.14)$$

$$\frac{\partial^2 F}{\partial P^2} = \frac{T - T_C}{C} + 3g_4P^2 > 0. \quad (1.15)$$

Equations (1.14, 1.15) are the necessary and sufficient conditions for a minimum of $F(P)$.

From eqn. (1.14) a 3rd order polynomial function is obtained:

$$E(P) = \frac{T - T_C}{C} P + g_4P^3. \quad (1.16)$$

The inversion of this function, excluding the parts that are not accessible for the system, gives the polarization hysteresis function $P(E)$ (Fig. 1.5). The magnitude of the coercive field E_c can be calculated from the extrema of eqn. (1.16). The conditions

$$\frac{\partial E}{\partial P} = \frac{T - T_C}{C} + 3g_4P^2 = 0, \quad (1.17)$$

$$\frac{\partial^2 E}{\partial P^2} = 6g_4P \neq 0 \Rightarrow P \neq 0 \quad (g_4 \neq 0, \text{ see p. 7}), \quad (1.18)$$

yield for $T = 0 \text{ K}$

$$P_{cr\pm} = \pm \sqrt{\frac{T_C}{3g_4C}}. \quad (1.19)$$

$P_{cr\pm}$ corresponds to the polarization for the reversal fields at $T = 0 \text{ K}$. Replacing P by P_{cr} in eqn. (1.16) yields the coercive field ($\vec{E} \uparrow \downarrow \vec{P}$):

$$\begin{aligned}
 |E_c| &= \left| -\frac{T_C}{C} P_{cr} + g_4 P_{cr}^2 P_{cr} \right| \\
 &= \frac{2 T_C}{3 C} P_{cr}.
 \end{aligned}
 \tag{1.20}$$

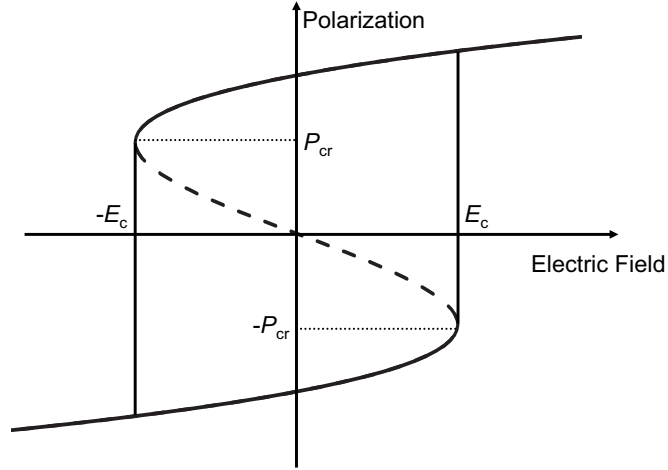


Figure 1.5: (Solid line) Ferroelectric hysteresis calculated from Ginzburg-Landau theory, (dashed line) part not accessible for the system.

Using typical parameters for $PbZr_{0.5}Ti_{0.5}O_3$ taken from Ref. [23]², the coercive field at 0 K for this material is

$$|E_c| \approx 0.65 \text{ MV/cm.} \tag{1.21}$$

It should be noted that the Landau-Ginzburg mean-field theory is based on thermodynamic equilibrium and does not address dynamics. As a result, the detailed mechanism of polarization reversal in ferroelectrics is not described by this approach.

Switching kinetics

In the previous paragraphs, the coercive field for the polarization reversal has been calculated using the Landau-Ginzburg theory for a free-standing film. The experimentally observed coercive field, however, is usually much smaller

²using $C = \epsilon_0 C'$

(about one order of magnitude in thin films and two orders of magnitude in bulk single crystals) - a result of dynamic processes not covered by the static Landau-Ginzburg theory.

In most cases, it is energetically favorable to switch the polarization of a domain not simultaneously, but by moving the domain walls.

Following [26], the switching process commonly proceeds as shown in Fig. 1.6. Consider a thin film with two stable polarization states visualized in Fig. 1.6 by the colors *grey* and *cyan*. I assume that the film is initially in the *grey*-colored polarization state. Primarily inhomogeneous nucleation occurs at the surface of the ferroelectric film (Fig. 1.6 (a)). This process involves fluctuations, in other words, *cyan-colored* domains nucleate, grow in size, shrink, disappear, and new nucleation occurs. These nucleation fluctuations continue until the nucleus reaches a critical size. The polarization switching then develops quickly in a needle-like geometry, growing parallel to the applied electric field (Fig. 1.6 (b)). Next, the domains spread out sideways (Fig. 1.6 (c)) switching the film to the *cyan-colored* domain (Fig. 1.6 (d)). These processes may also occur simultaneously.

According to [26], in oxide perovskite materials the nucleation time is about 1 ns and the time for a domain to propagate from the anode to the cathode is also approximately 1 ns. This can be estimated by assuming a propagation velocity of the speed of sound inside the material [26]. Unlike magnetic domain walls, ferroelectric domain walls do not seem to move supersonically. The sideways growth time is usually the slowest, typically a few ns to a μ s. For ferroelectrics other than oxide perovskites the relative values of nucleation time, forward growth time, and sideways growth time differ. For example, in tryglycine sulfate nucleation time and sideways growth time are about the same [26].

The polarization reversal is a complex phenomenon, and there does not seem to be an universal mechanism which describes polarization switching in all ferroelectrics. Thin films show more than 10 times higher coercive fields than single crystals. In addition, the experimentally observed coercive field E_c in thin films usually depends strongly upon film thickness. There is an ongoing discussion about the reasons for these phenomena, and various theoretical models have been proposed [27, 28, 29, 30, 31, 32]. Nevertheless, in most cases the coercive field increases for shrinking film thickness [33, 34, 35, 36].

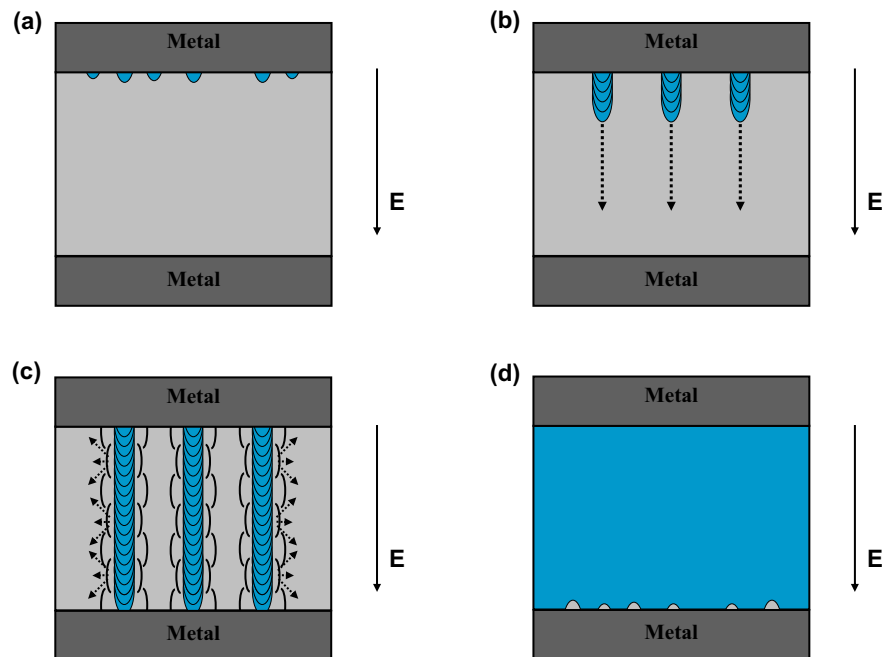


Figure 1.6: *Schematic of switching in a ferroelectric film. (a) Inhomogeneous nucleation at the surface. (b) Needle-like growth of domains. (c) Sideways growth of domains. (d) Polarization reversal completed.*

Frequency dependence of the coercive field

The coercive field does not only exhibit a strong thickness dependence, but it is also frequency dependent. This is especially important for the application of ferroelectrics in memory devices, as these devices have to operate at several hundred MHz.

As shown in the previous paragraph, polarization switching in ferroelectrics includes domain wall motion. This motion of domain walls through a ferroelectric involves a certain resistance, or viscosity, which generally increases with increasing frequency. Therefore, the coercive field of ferroelectrics increases with frequency [26].

The traditional approach to describe the switching kinetics in ferroelectrics is the Kolmogorov-Avrami model [37, 38]. The basic idea of this model is that ferroelectric domains, which have been initiated from independent nucleation centers, unrestrictedly grow under the action of the applied electric field. Ishibashi and Orihara predicted that the fractional area A of the cell that is switched with time depends on the applied electric field E and fre-

quency f [39]. Assuming that the domain wall velocity is a function only of the applied field E at the instant t and that the nucleation occurs at predetermined positions and at predetermined fields, the switched area is given by

$$A(E, f) = 1 - \exp(-f^D \cdot E^k), \quad (1.22)$$

where D is the domain dimension and k is approximately equal to 6.

Assuming $D = 3$ for $Pb(Zr, Ti)O_3$ [26], a power law is found for the frequency dependence of the coercive field:

$$E_c(f) = f^{1/2}. \quad (1.23)$$

Correlation volume of ferroelectrics

In a simple picture, ferroelectricity can be seen as a collective phenomenon, associated with the alignment of localized dipoles within a correlation volume, producing a spontaneous polarization [40].

Consider a single dipole in vacuum. Any moment applied to it will rotate the dipole. Therefore, no stable polarization can be based on a free dipole. A number of dipoles, however, will align parallel to the polarization due to the highly anisotropic character of the inter-cell dipole-dipole interaction. It is long-range parallel to the polarization axis and short-range perpendicular to the polarization axis. The volume filled up by the number of dipoles, necessary to achieve a stable polarization, is called the correlation volume. In Fig. 1.7 the correlation volume is schematically shown.

Please note that there is a short-range repulsion for the parallel alignment of two adjacent dipoles perpendicular to the polarization axis and energetically favorable, long-range Coulomb forces for the parallel alignment of two adjacent dipoles parallel to the polarization axis. Owing to the mentioned anisotropy, the energy gain associated with the parallel alignment of the dipoles is larger than the loss in energy associated with the parallel alignment of adjacent dipoles perpendicular to the polarization axis [41]. According to Lines and Glass [22], typical values for the correlation volume for many ferroelectrics are given by $L_c \sim 10 - 50$ nm and $L_a \sim 1 - 2$ nm.

The reduction of the thickness of the ferroelectric thin film below L_C will thus reduce the stability of the ferroelectric phase. In other words, the phase

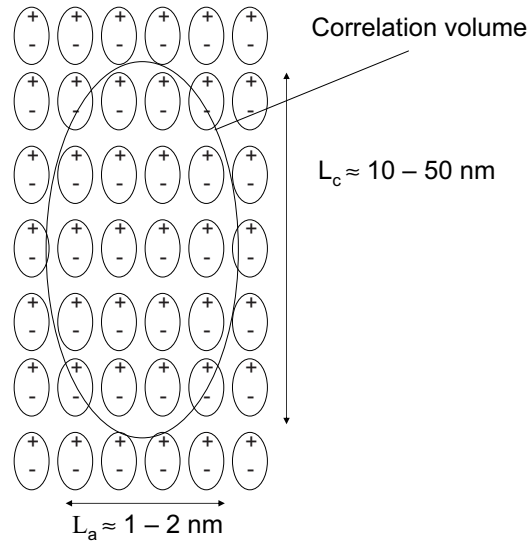


Figure 1.7: Correlation volume as a result of the highly anisotropic character of the inter-cell dipole-dipole interaction. [22]

transition temperature T_C will be lowered and at some point reach 0 K. Ferroelectricity will cease to exist.

A change in fundamental ferroelectric characteristics, such as P_r , E_c , T_C as a function of the sample size commonly is called size effect. Size effects are not only present in ferroelectrics. They have been discussed for other collective phenomena, e.g. superconductivity [42], superfluidity [43], and magnetism [44], as well.

The size of the correlation volume is not only a characteristic feature of the specific ferroelectric material, but, especially in epitaxial thin films, it depends on boundary conditions as well. The electrode material and the substrate lattice parameters may significantly alter the size of the correlation volume. Our interest in studying possible new effects in ferroelectric films as thin as a few nm requires an understanding of the influence of electrical and mechanical boundary conditions on size effects. The knowledge about the relation between boundary conditions and the ferroelectric properties is essential to find the conditions that stabilize the *ferroelectric* phase.

1.3 Electrical boundary conditions

The fundamental relation between electric displacement \vec{D} , field \vec{E} , and polarization \vec{P} is given by

$$\vec{D} = \varepsilon_0 \vec{E} + \vec{P}. \quad (1.24)$$

Here, the polarization arises from both the spontaneous parallel alignment of dipoles \vec{P}_S described in Chapter 1.2 and the polarizability of ferroelectrics in the presence of an electric field $\vec{P}_E = \chi \vec{E}$.

A homogeneous, spontaneous polarization along the z -axis $\vec{P}_S = (0, 0, P_S)$ of a ferroelectric film causes a depolarizing field $\vec{E}_D = -4\pi N \vec{P}_S$ oriented oppositely to \vec{P}_S (where N is equal to one for an infinite plate geometry). The electrostatic energy associated with this field may be minimized by three mechanisms: First, by domain formation with oppositely oriented polarization direction; second, by free-charges from the electrodes (external compensation); and third, by electrical conduction in the ferroelectric film (internal compensation).

Here, one of the main differences between ferroelectric and magnetic domains becomes evident. The possibility to screen the polarization charges by external or internal compensation arises from the existence of an electric monopole, whereas, the absence of a magnetic monopole does not allow a screening in magnetic domains.

Size effects due to 180° domain formation

Consider a ferroelectric film *in vacuum*. The ferroelectric film is idealized as a *perfect insulator* (i.e. no free charges inside the film), which could compensate the depolarizing field (see Fig. 1.8 (a)). In the absence of an external electric field the spontaneous polarization can develop along at least two directions. In order to reduce the electrostatic energy associated with the depolarizing field, different regions of the ferroelectric - called domains - will polarize in each of these directions (see Fig. 1.8 (b)). The width of the formed domains depends on the spontaneous polarization as $l \propto 1/P_S^4$ [4]. Mitsui and Furuichi [45] found for Rochelle salt that the domain width varies quadratically with crystal thickness, $l \propto d^2$. This dependence is due to the fact that the formation of a domain wall costs energy. Hence, the formation of domain walls will continue only till a balance is reached between the energy gained from the reduction of the electrostatic depolarizing field en-

ergy and the energy necessary to create the domain walls. In this case the long-range depolarizing field inside the film becomes negligible, whereas near the film surfaces on a length-scale comparable to the domain width a highly fluctuating depolarizing field is still present [46].

Size effects due to incomplete screening of the depolarizing field

External compensation

Large depolarizing fields can be avoided not only by the formation of domains, but also by the accumulation of compensating charges at the surfaces perpendicular to the polarization. Consider a ferroelectric film sandwiched between two metallic *electrodes* in a *short-circuit condition*. As it was the case for the ferroelectric film in vacuum, a homogeneous spontaneous polarization along the z-axis of the idealized *insulating* film gives rise to a depolarizing field oriented oppositely to its origin, the spontaneous polarization. Other than in the vacuum case, the metallic electrodes contain *free charges*, which can compensate for the polarization charges. In this case, the width of the domains is given by $l \propto 1/(P_S + \sigma)$ where σ is the surface charge density [4]. A monodomain sample is obtained for a complete compensation $\sigma = -P_S$ of the polarization.

It is known, however, that short circuited electrodes do not provide an exact cancellation of the depolarizing field. A complete compensation of the polarization charges cannot be achieved due to the separation of the free charges in the electrodes and the bounded charges in the ferroelectric (see Fig. 1.8 (c)). The compensation of the polarization depends on the screening length of the electrode. The Thomas-Fermi screening length in a metal is approximately $0.5 - 1 \text{ \AA}$, whereas the Debye-length in a semiconductor is larger by approximately three orders of magnitude [47].

Batra and Silverman showed that the incomplete compensation of the polarization charges changes the stability of the ferroelectric phase [2, 48, 49, 50, 51, 52, 3]. The depolarizing field that results from an incomplete compensation of the polarization charges becomes significant when the thickness of the ferroelectric film is reduced. It results then in a depression of the spontaneous polarization and transition temperature. The use of semiconducting electrodes can even change the nature of the phase transition from second to first-order [49].

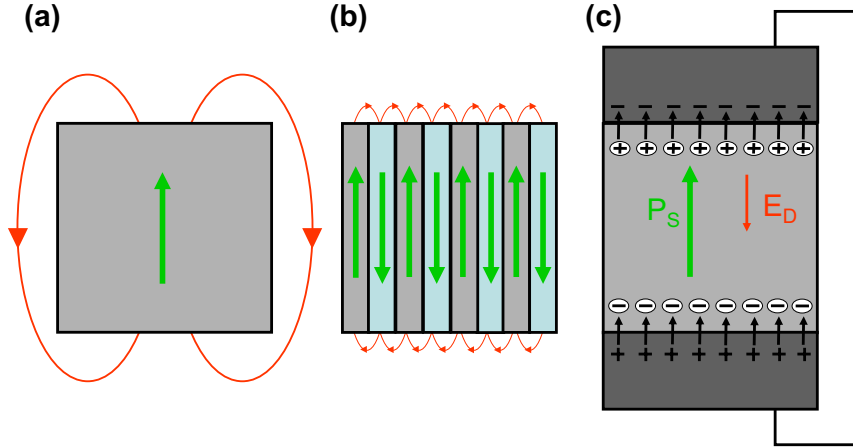


Figure 1.8: (a) Depolarizing field associated with spontaneous polarization (vacuum). (b) Formation of domains to reduce depolarizing field (vacuum). (c) Free-charges in metallic electrodes partially compensate the polarization charges.

For example, the critical thickness for single-domain ferroelectric tryglycine sulphate (TGS), assumed to be perfectly insulating, has been predicted to be 400 nm in between semiconducting electrodes and around 4 nm for metallic electrodes [2]. In another work, ferroelectricity in TGS between metallic electrodes is predicted to disappear at a thickness of $1 \mu\text{m}$ [53].

If *no single-domain* assumption is made, then the film will divide into domains to reduce the electrostatic energy associated with the residual depolarizing field resulting from the incomplete charge compensation.

Internal compensation

I. I. Ivanchik considered a *single-domain* ferroelectric layer with *semiconducting* properties placed in *vacuum* [54]. In the presence of a spontaneous polarization, charges will flow from the interior of the ferroelectric layer to its surface. This will screen the polarization charges. The diffusion current, however, will lead to an electric field inside the ferroelectric, oppositely oriented to the spontaneous polarization. This electric field for thick films tends exponentially to zero. For thin films, however, it will not vanish and a critical thickness can be calculated at which the electric field reaches the coercive field. Ivanchik calculated for BaTiO_3 a critical thickness of 20 nm. At this thickness the ferroelectric phase becomes unstable and the spontaneous polarization is reversed after a relaxation time of about 1 minute by the internal electric field.

Batra *et al.* studied the case of internal compensation of the polarization either by free carriers in space charge layers, or by charges trapped in surface states of the ferroelectric. They found that space charge regions occur at the surface of a ferroelectric [49, 3]. The reason for this incomplete compensation of polarization is the lack of states at the Fermi level for an only *slightly conducting* ferroelectric film.

In conclusion, it is unlikely to achieve a monodomain state for thin films if the injection of charge from external electrodes is excluded.

Size effects due to surface effects

Even if the surface charge is fully compensated at the metallic electrodes, a finite size effect can be present. Differences in the remanent polarization and coercive field for thin films compared to bulk material³ are often theoretically accounted for by introducing *subsurface layers*, whose electric properties differ from those of the bulk material.

Ions in a subsurface layer have a different number of nearest neighbors from those in the bulk, therefore, the local polarization is expected to vary in the vicinity of a surface. A depolarizing field arises from bound charges inside the ferroelectric. This depolarizing field is different from the one discussed by Batra *et al.*, which was the result of an incomplete compensation of polarization. Here, the depolarizing field is due to spatial variations of the polarization in the film.

Surface effects are described by an inhomogeneous Landau-Devonshire theory, which includes a spatial variation of the polarization in the vicinity of the surface [55]. In the approach proposed by Kretschmer and Binder [4, 56], the free energy is given by $F_{Film} = F_{bulk} + F_{surface}$. They introduce the *extrapolation length* λ , which measures the strength of coupling in the subsurface layers. The local polarization near the surface is expected to change over a distance comparable to the bulk correlation length ξ of polarization fluctuations. Please note that the correlation length ξ is not identical with the parameters of the correlation volume L_A and L_C introduced in Chapter 1.2. Usually λ is considered to be positive for ferroelectric thin films, which corresponds to a polarization suppression in subsurface layers. Scott [57] indicates

³I refer to bulk material as a sample for which the bulk properties are dominant over the surface properties.

that λ is also probably large compared with ξ . Sometimes λ is also assumed to be negative. In Figure 1.9 the variation of the local polarization in sub-surface layers is shown for a positive extrapolation length (blue curve) and a negative extrapolation length (red curve).

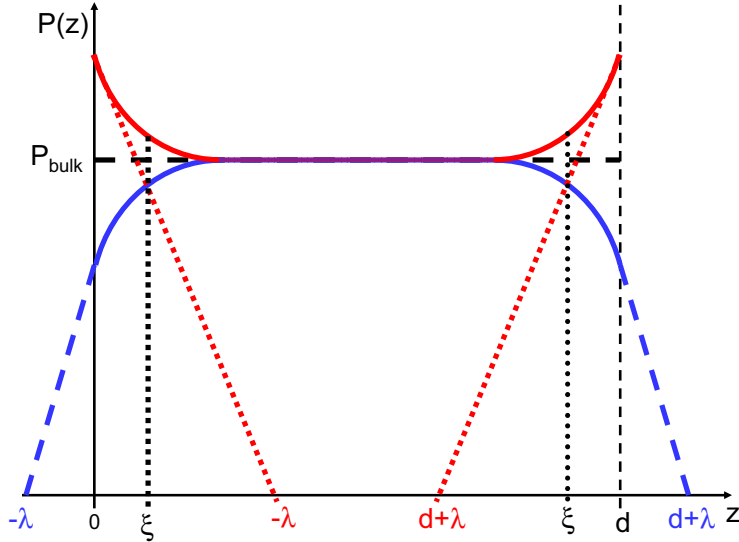


Figure 1.9: Variation of the local polarization $P(z)$ across a film of thickness d for positive extrapolation length λ (blue) and negative extrapolation length λ (red). [4]

Among others, Kretschmer [4] and Binder [56], Baudry and Tournier [55], Tilley and Zeks [58, 59], and Zhong *et al.* [60], have studied the influence of the model parameters λ and ξ on ferroelectric properties (e.g. shift of phase transition temperature) including and excluding depolarizing fields. A numerical evaluation of the critical sizes using an anisotropic, 3-dimensional, Landau-Ginzburg-Devonshire model excluding depolarizing fields, was done by Li *et al.* [61]. The critical thickness of $PbTiO_3$ and $PbZr_{0.5}Ti_{0.5}O_3$ at 0 K was calculated to be 4 nm and 8 nm, respectively.

1.4 Mechanical boundary conditions

All theoretical models and predictions that have been discussed so far have been made for free standing films. In this Chapter mechanical boundary conditions will be considered as well. This is necessary, because this thesis will be focused on epitaxial thin films, which are grown on much thicker substrates.

Extrinsic size effects of mechanical origin

The interaction of the film with the substrate can generate significant mechanical stresses in the film. *Growth stresses* may appear during the film deposition in the paraelectric phase. These stresses strongly depend on parameters of the deposition process [62]. Energetic deposition techniques, such as rf sputtering (see p. 59) or pulsed laser deposition (see p. 56), favor compressive growth stresses, whereas tensile growth stresses result from rapid low energy growth techniques, such as molecular oxide chemical vapor deposition or thermal evaporation (see p. 57) [63]. It has been shown that during the growth (usually in the paraelectric state) of thicker films, substantial stress relaxation is favored by the generation of arrays of misfit dislocations at the film/substrate interface [63], whereas thinner films grow in their coherent pseudomorphic cubic phase retaining their epitaxial strain [64].

During cooling from the growth temperature, *thermal stresses* may arise in the film due to differences between the mean coefficients of thermal expansion of substrate and film.

The paraelectric-ferroelectric phase transition, producing dimensional changes, introduces additional stresses leading to the formation of domains (elastic stress relaxation) and sometimes to additional formation of misfit dislocations [63].

Strain induced by the substrate may lead to lattice parameters in epitaxial thin films that differ considerably from those in bulk material. A misfit-strain S_m independent of the film polarization state is introduced into the theory to describe substrate effects on the spontaneous polarization. For perovskite films grown on cubic substrates, this strain may be defined as $S_m = (b - a_0)/b$, where b is the substrate lattice parameter and a_0 is the equivalent cubic cell constant of a free standing film [65]. This definition of S_m is only valid for fully strained films. Above a critical film thickness, misfit dislocations are introduced into the film and a substrate effective lattice parameter b^* instead of the actual lattice constant b has to be used [63]:

$$S_m = \frac{b^* - a_0}{b^*}. \quad (1.25)$$

Note that the strain is always given with respect to the paraelectric state. The polarization is coupled to the lattice strain due to electrostriction (see page 4). Therefore, according to thermodynamic calculations by Pertsev *et al.*, the magnitude and orientation of the spontaneous polarization \vec{P}_S

strongly depend on the value of S_m [5, 66]. A ferroelectric thin film, such as $BaTiO_3$ or $Pb(Zr, Ti)O_3$, grown on a *tensile* substrate $S_m > 0$ tends to form a ferroelectric phase with an in-plane polarization direction, whereas its growth on a *compressive* substrate $S_m < 0$ will stabilize the ferroelectric phase with an out-of-plane orientation and enhance the spontaneous polarization in this direction. Remarkably, in agreement with experimental results [8] the spontaneous polarization $P_S(S_m < 0)$ can be larger than the bulk polarization. Higher values of P_S can be obtained by increasing the magnitude of compressive strain in the film. This, however, will decrease the critical thickness at which misfit dislocations are introduced.

In conclusion of this Section, the size effect of mechanical origin is attributed to the thickness dependence of the film in-plane lattice strain S_m . For a given thickness of the ferroelectric thin film, the highest compressive strain, which is achievable without leading to misfit dislocations, will best stabilize the ferroelectric against the paraelectric phase.

Intrinsic size effects in strained epitaxial films

As discussed in Chapter 1.3 on page 19, Kretschmer and Binder added a surface term to the Landau expansion of the total free energy (eqn. (1.4)) and introduced the extrapolation length λ into the thermodynamic theory in order to describe surface effects. The expansion of the free energy, proposed by Kretschmer and Binder in the notation of Tilley and Zeks [59], for a film of thickness d is given by

$$\frac{F}{A} = \int_0^d \left[\frac{1}{2}BP^2 + \frac{1}{4}CP^4 + \frac{1}{2}E \left(\frac{dP}{dz} \right)^2 \right] dz + \frac{1}{2\lambda}E(P_-^2 + P_+^2).$$

Here, A is the surface area of the film. $P_- = P(0)$, $P_+ = P(d)$ and λ is the extrapolation length. The last term is the added surface term. Later, the free energy was expanded to powers of the order parameter P of up to the sixth [67] in order to describe ferroelectric materials that undergo a first-order phase transition (see Chapter 1.2)

$$\frac{F}{A} = \int_0^d \left[\frac{1}{2}BP^2 + \frac{1}{4}CP^4 + \frac{1}{6}DP^6 + \frac{1}{2}E \left(\frac{dP}{dz} \right)^2 \right] dz + \frac{1}{2\lambda}E(P_-^2 + P_+^2). \quad (1.26)$$

As mentioned above, Pertsev *et al.* studied the influence of substrate effects on the ferroelectric phase state using a thermodynamic theory. The two-dimensional clamping and straining of a ferroelectric film by a dissimilar thick substrate was found to affect considerably its phase state, shifting the temperature of the ferroelectric transition and changing its order [5, 66].

Zemilgotov *et al.* developed a phenomenological theory, which describes intrinsic surface effects on the polarization properties of films grown epitaxially on much thicker substrates [6]. This theory considers both surface effects discussed on page 19 *and* substrate effects discussed on page 22. Zemilgotov *et al.* considered epitaxial thin films of perovskite ferroelectrics grown in a high-temperature paraelectric state on a thick (001)-oriented compressive ($S_m < 0$) cubic substrate and sandwiched between extended identical electrodes. Films with a positive extrapolation length, corresponding to a polarization reduction in subsurface layers, were studied. Assuming that the polarization changes only along the film thickness direction and ignoring the depolarizing field, the Helmholtz free energy per unit area (eqn. (1.26)) modifies to

$$\frac{F}{A} = \int_0^d \tilde{F}(z) dz + \frac{1}{2\lambda} g_{11} (P_-^2 + P_+^2), \quad (1.27)$$

$$\tilde{F}(z) = \frac{S_m^2}{s_{11} + s_{12}} + a_3^*(S_m)P^2 + a_{33}^*P^4 + a_{111}P^6 + \frac{1}{2}g_{11} \left(\frac{dP}{dz} \right)^2, \quad (1.28)$$

$$a_3^* = a_1 - S_m \frac{2Q_{12}}{s_{11} + s_{12}}, \quad a_{33}^* = a_{11} + \frac{Q_{12}^2}{s_{11} + s_{12}}. \quad (1.29)$$

Here, a_1 , a_{11} and a_{111} are the dielectric stiffness and higher-order stiffness coefficients at constant stress; Q_{ij} are the electrostrictive constants; s_{ij} are the elastic compliances at constant polarization; λ is the extrapolation length; z is the out-of-plane direction; P is the out-of-plane polarization and P_- ; and P_+ are the polarization values on the film surfaces, i.e. at $z = 0$ and $z = d$, respectively. The dielectric stiffness constant a_1 is assumed to be a linear function of temperature near the Curie-Weiss temperature (Curie-Weiss-law: $a_1 = (T - T_0)/2\varepsilon_0 C$). All other coefficients are assumed to be independent of temperature. Using this thermodynamic approach it is possible to calculate the mean polarization \bar{P} as a function of the film thickness d , temperature T , and misfit-strain S_m in the epitaxially grown heterostructure.

The intrinsic size effect on the polarization in strained films was shown to be governed by the normalized film thickness d/ξ^* and the ratio λ/ξ^* . Here, $\xi^* = \sqrt{g_{11}/|a_3^*|}$ is the modified correlation length, which differs from the bulk correlation length $\xi = \sqrt{g_{11}/|a_1|}$ of a mechanically free bulk crystal. The correlation length $\xi_0^*(S_m = 0) = \xi(T = 0)$ was found to be about 1 nm for $PbTiO_3$ and 5 nm for $BaTiO_3$ [6].

The variation of the film mean polarization \bar{P} , with temperature T shown in Fig. 1.10 (a) for $PbTiO_3$ and in Fig. 1.10 (b) for $BaTiO_3$, results mainly from the temperature dependence of the dielectric stiffness a_1 . The surface effect hinders the development of spontaneous polarization during the film cooling. This intrinsic size effect is considerable only for ultrathin films and manifests itself in a decrease of the ferroelectric transition temperature T_C , as well as in a reduction of the mean polarization $\bar{P}(T)$ relative to the thick film polarization.

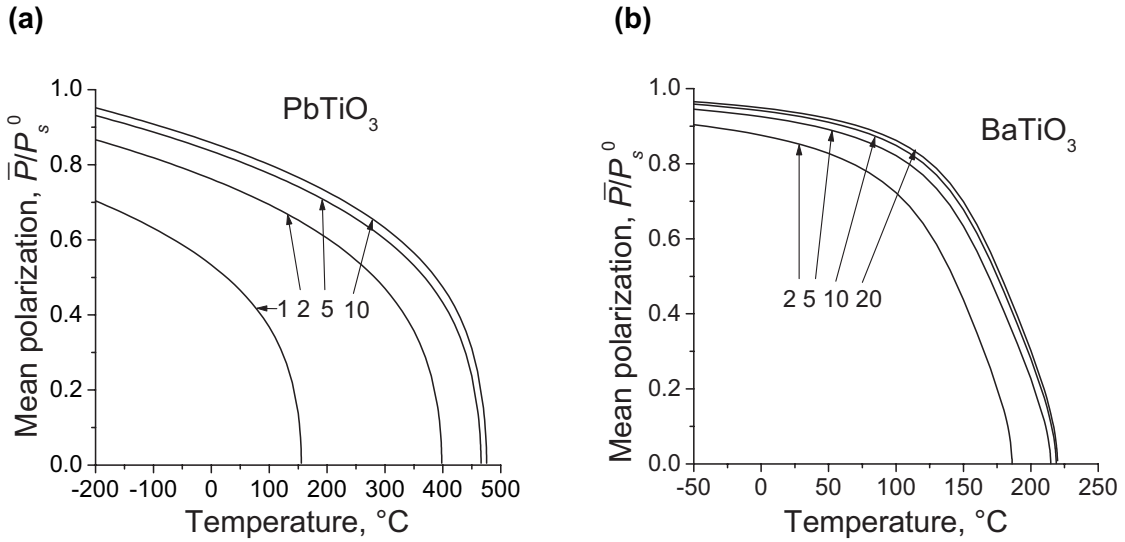


Figure 1.10: Normalized mean polarization $\bar{P}(T)/P_{bulk}^{T=0}$ of epitaxial (a) $PbTiO_3$ grown at $S_m = 0$ and (b) $BaTiO_3$ grown at $S_m = -4.6 \times 10^{-3}$ as a function of the temperature T . Numbers indicate the normalized film thickness d/ξ_0^* . $\xi_0^*(S_m = 0)$ coincides with the bulk correlation length $\xi_0(T = 0)$. [6]

The transition temperature for ultrathin epitaxial films is governed by the competition of substrate and surface effects on T_C (see Fig. 1.11 (a) for $PbTiO_3$ thin films). On the one hand, the transition temperature T_C shifts to higher values at negative misfit strains provided by a compressive substrate, on the other hand, the negative surface effect ($\lambda > 0$) tends to reduce T_C . Note that for thicker films surface effects can be neglected. A significant suppression of the transition temperature is expected to occur only at small misfit strains and a thickness of about $2\xi_0$ and below.

Finally, the mean polarization \bar{P} has been calculated at room temperature as a function of the misfit-strain S_m (see Fig. 1.11 (b) for $BaTiO_3$ thin films).

At large, compressive strain, substrate effects override surface effects and the mean polarization \bar{P} is considerably increased for thicker films ($d \gg \xi_0$) and ultrathin films ($d \sim \xi_0$), as well. According to the non-linear thermodynamic theory used by Zembilgotov and coworkers, the out-of-plane polarization of an epitaxial thin film may exceed the bulk spontaneous polarization. This effect is achieved for epitaxial films when they are grown on a sufficiently compressive substrate creating a large negative misfit in the epitaxial system and when they are sufficiently thin to avoid strain relaxation via generation of misfit dislocations.

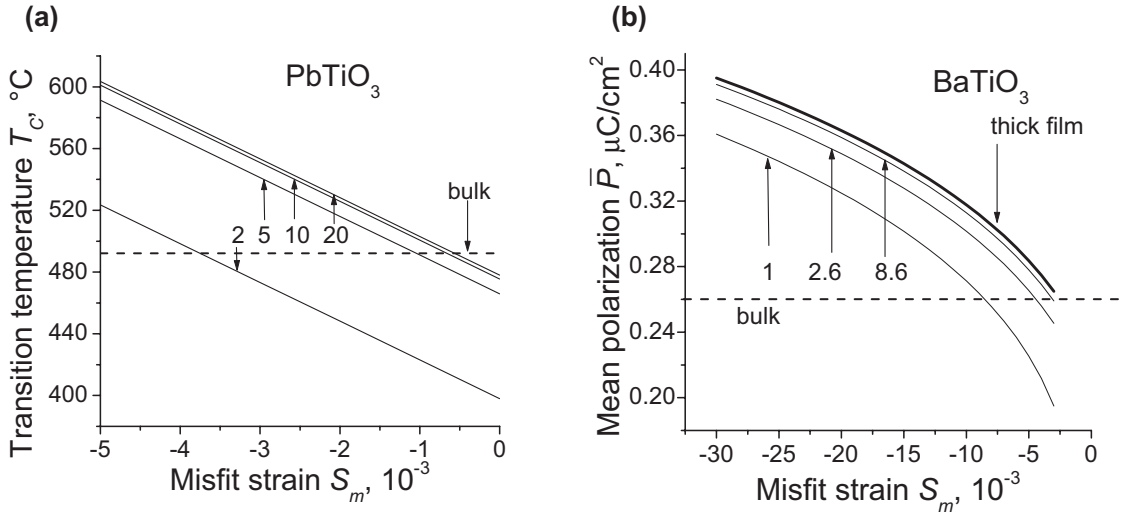


Figure 1.11: (a) Ferroelectric transition temperature T_C calculated as a function of misfit-strain S_m for $PbTiO_3$ films of several thicknesses. (b) Mean polarization \bar{P} calculated as a function of misfit-strain S_m for $BaTiO_3$ films of several thicknesses. Numbers indicate the normalized film thickness d/ξ_0 for respective curves. The correlation length $\xi_0^*(S_m = 0) = \xi(T = 0)$ was found to be about 1 nm for $PbTiO_3$ and about 5 nm for $BaTiO_3$. [6]

Zembilgotov *et al.* pointed out that their mean-field phenomenological approach is probably not valid for film thicknesses of about 1 nm and below. Nevertheless, they believe that films with a thickness of about 4 nm and above can be successfully described in the continuum approximation. Bearing this in mind, their mean-field approach predicts that intrinsic surface effects on ferroelectricity become weaker in epitaxial films grown on strongly compressive substrates, and an only 2 nm thick $PbTiO_3$ film under a sufficiently large compressive strain is ferroelectric at room temperature.

Recently, a further expansion of the total free energy has been suggested [68], accounting for the electric field inside the ferroelectric, the energy associated to the formation of domain walls in polydomain films, and spatial inhomogeneities of the polarization inside the film:

$$F_{film} = F_{bulk} + F_{surface} + F_{strain} + F_{electric\ field} + F_{domain\ wall} + F_{gradient}. \quad (1.30)$$

The existence of ferroelectricity in ultrathin films is further theoretically supported by ab-initio calculations [69, 70]. Using an effective Hamiltonian, Ghosez and Rabe predicted a stable ferroelectric phase in a free-standing $PbTiO_3$ film as thin as a few unit cells [7, 69].

The predicted minimum thickness for ferroelectricity has decreased over time significantly. Early works from Batra and Silverman predicted a minimum thickness of 400 nm. Nowadays, theoretical studies predict ferroelectricity in ultrathin films with only a few monolayers. This substantial change of the predictions over time is mainly due to a better understanding of the influence of electrical and mechanical boundary conditions. On the other hand, not only the predictions are more accurate nowadays. Especially in the last 5 years a lot of experimental work has been done and the outcome of the improved deposition and analytical techniques has been quite considerable. Ten years ago the thickness dependence of the remanent polarization was usually shown on a micrometer-scale [36]. Nowadays this dependence is plotted on a nanometer scale. Yanase *et al.* showed nicely shaped P - E curves for 12 nm thick $BaTiO_3$ films [8]. Based on their AFM-investigations, Tybell *et al.* reported on the existence of ferroelectricity in 4 nm thick $PbTiO_3$ [9]. Recently, Streiffer *et al.* found 180° stripe domains in 3 monolayers of $PbTiO_3$ [11, 10] by *in-situ* grazing-incidence x-ray scattering and followed the existence of ferroelectricity in this only 1.2 nm thick film.

In conclusion, under suitable boundary conditions ferroelectricity is likely to survive in films as thin as a few nm. The pursuit for the ferroelectric minimum in thickness has reached a thickness range where electron tunneling through these films may be expected.

Chapter 2

Quantum-mechanical tunneling

Electron tunneling through a thin insulating layer or vacuum in between two electrodes has been studied for 80 years. The observation of the tunneling effect supported the wave - particle dualism and, therefore, played a significant role in the development of quantum mechanics during the twenties [71, 72].

In this Chapter the tunneling through a metal-insulator-metal contact will be described as a quantum-mechanical effect. It will be shown that for a sufficiently thin insulating barrier, a current flow through this barrier is possible as a result of an overlap of the wave functions of the electrons in both metals. Elastic and inelastic tunneling will be introduced and the temperature and voltage dependencies of these conduction mechanisms will be discussed.

2.1 Tunneling effect

Consider two metals, M_1 and M_2 , separated by a thin insulating barrier with thickness d . In a simple model the barrier can be described by a one-dimensional, symmetric square potential of height V_0 and width d . This model only holds for a system for which the barrier heights Φ_1 and Φ_2 at both metal-insulator interfaces are the same. For tunnel junctions with different electrodes, however, different barrier heights have to be assumed resulting, in a simplified model, in a trapezoidal potential barrier [73]. In Fig. 2.1, a tunnel junction is shown schematically, consisting of a thin insulating layer with thickness d in between two metal layers, M_1 and M_2 . At 0 K the electrons, which exist in M_1 and M_2 in pairs in discrete energy levels, fill up the well to the Fermi levels E_{F1} and E_{F2} , respectively. The work functions of the metals W_1 and W_2 represent the minimum energy required to free electrons from the

interior of the respective metals at 0 K. Φ_1 and Φ_2 are the barrier heights at the metal-insulator interfaces. A trapezoidal potential barrier, with energy gap E_g and affinity χ of the electrons, is used to describe the barrier. In this simplified model, space charges in the barrier and image forces [74] are neglected. When electrons are described by wave functions, an electron in M_1 will have a finite probability of being found in M_2 . Applying a positive voltage V at the metal electrode M_2 will shift the Fermi level of this electrode by an amount of eV vertically downwards. This results in a net current of electrons tunneling from M_1 to M_2 .

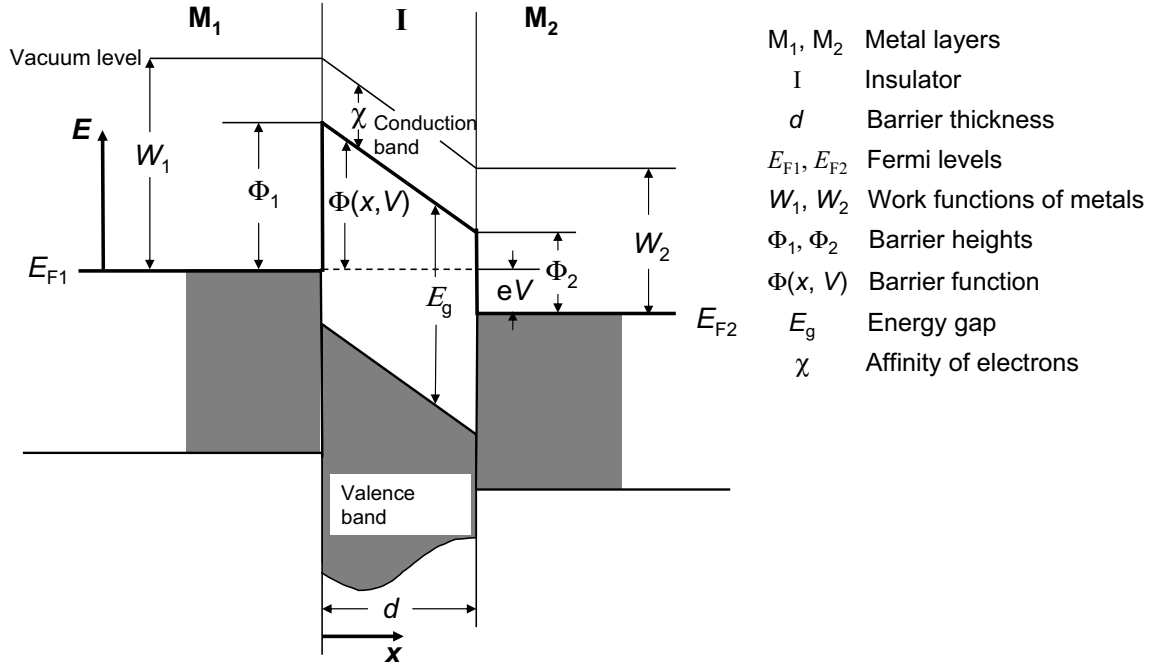


Figure 2.1: Band model for a metal-insulator-metal tunnel junction. [74]

The one-way tunnel current is proportional to an integral over all energies of the product of the number of electrons in one metal by the number of unoccupied states in the other metal at the corresponding energy times the probability for an electron at that energy to tunnel through the barrier. The net current is given by the difference in the opposed one-way currents. With the assumption that the tunneling probability is independent of E and that it is equal for the opposed one-way currents, the net tunnel current is given by [75]

$$I(V) = \text{const} \times \int \rho_2(E - eV) \rho_1(E) [f(E - eV) - f(E)] |M(E)|^2 dE. \quad (2.1)$$

Here, ρ_1 and ρ_2 are the densities-of-states functions for M_1 and M_2 , respectively. $f(E)$ is the Fermi distribution function and $M(E)$ is the transfer matrix element for the electrons of energy E from one side of the barrier to the other one. In the WKB approximation [76], which implies that the band structure of the metal-insulator-metal system varies only slowly compared to the electron wavelength, the tunneling probability is given by [77]

$$|M(E)|^2 = \exp \left(-2 \int_0^d [-k_x^2]^{1/2} dx \right), \quad (2.2)$$

where x and k_x are the coordinate and the electron wave number, respectively, normal to the film plane. The parabolic energy-momentum relation may be written as

$$\frac{p_x^2}{2m^*} = \frac{\hbar^2 k_x^2}{2m^*} = E_x - \Phi(x, V), \quad (2.3)$$

where $\Phi(x, V)$ is the barrier function and E_x is the energy of electrons in the barrier with the effective mass m^* . For $E_x > \Phi(x)$, the electron wave number is real, meaning that the electron wave function is periodic ($\Psi \sim e^{\pm i k_x x}$). On the other hand, for the electrons tunneling through the barrier ($E_x < \Phi(x)$), the electron wave number is imaginary and the electron wave function decays exponentially ($\Psi \sim e^{\pm k_x x}$) inside the barrier.

Using eqn. (2.3) the tunneling probability modifies to

$$|M(E)|^2 = c \cdot \exp \left(-\frac{4\pi}{h} \int_0^d \sqrt{2m^* (\Phi(x, V) - E_x)} dx \right). \quad (2.4)$$

In order to simplify the calculations, Simmons [78] replaced the barrier $\Phi(x)$ by an average barrier $\bar{\Phi} = (\Phi_1 + \Phi_2)/2$. However, by applying this approximation of an average barrier height, all information about barrier asymmetry is lost. Therefore, Brinkman introduced the parameter $\Delta\Phi = \Phi_2 - \Phi_1$ to account for an asymmetrical barrier [79]. He pointed out that even using the same metal material for top and bottom electrodes, different growth conditions at the metal/insulator and insulator/metal interfaces could lead to an asymmetry in the barrier. According to Brinkman, the tunnel current density for $\Phi \gg eV$, $d > 10 \text{ \AA}$, $\Delta\Phi/\bar{\Phi} < 1$ is given approximately by

$$\frac{I(V)}{A} \cong 3.16 \cdot 10^{10} \frac{\sqrt{\Phi}}{d} \exp(-1.025 d \sqrt{\Phi}) \left[V - 0.0213 \frac{d \cdot \Delta\Phi}{\Phi^{3/2}} V^2 + 0.0109 \frac{d^2}{\Phi} V^3 \right]. \quad (2.5)$$

Here, the current density is given in A/cm^2 , the barrier height in eV and the barrier thickness in Å.

2.2 Elastic and inelastic electron tunneling

The theories that will be introduced in this Chapter were developed to describe the different electron tunneling conduction mechanisms through amorphous barriers, e.g. amorphous silicon. Amorphous silicon is characterized by a large number of localized states in its forbidden band. The existence of those localized states, characteristic of non-crystalline materials, is crucial for the electron transport in amorphous materials. It is believed that the presence of a relatively high density of local defects in perovskite materials may allow the use of those theories for these crystalline grown materials as well [80, 81]. Local defects with an attractive potential act as localized states. Only the existence, not the origin of these localized states near the Fermi surface, is important for electron tunneling. In fact, Mott's $T^{-1/4}$ law (see p. 34) has been successfully used to identify variable range hopping as the dominant conduction mechanism in crystalline $SrTiO_3$ at temperatures above 130 K [80]. Direct tunneling and tunneling via N localized states have been found to fit experimental data for $SrTiO_3$ tunnel junctions [82, 83] and for $SrTiO_3$ bicrystal junctions [84], although doubts about the applicability of those theories were pointed out by the author himself.

Direct tunneling

The incident electron wave function decays inside the barrier exponentially over a distance known as the localization length α^{-1} . For a barrier thickness d , not much thicker than the localization length, direct tunneling from one electrode to the other is observed (see Fig. 2.2). It is known that the localization length for an amorphous silicon barrier is $\alpha^{-1} \approx 7$ Å. For epitaxial $SrTiO_3$, the localization length was found to be ≈ 4 Å [82, 83].

For small voltages the direct tunneling conductance is simply [85]:

$$G_0^{dir} = \hat{G}_0^{dir} \cdot \exp(-2\alpha d). \quad (2.6)$$

There is only a weak temperature dependence of the direct tunneling conductance [86] due to thermal broadening of the Fermi surface at finite temperatures [87]. However, as the barrier thickness increases transport via localized states (elastic and inelastic) becomes dominant.

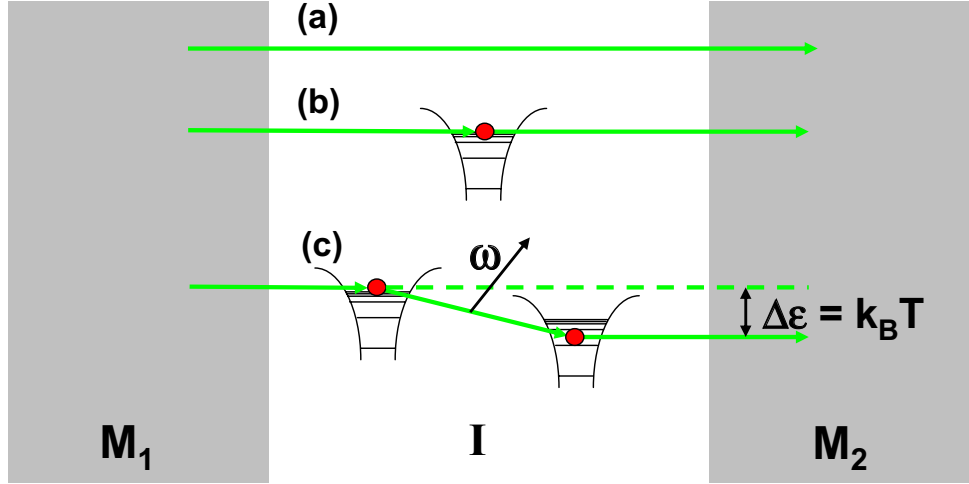


Figure 2.2: Sketch showing (a) direct tunneling, (b) resonant tunneling and (c) tunneling via two localized states

Resonant tunneling

An elastic electron transport via a localized state is referred to as resonant tunneling. Unlike direct tunneling, where electrons from one electrode are transferred to the other as a result of an overlap of the electron wave functions in both electrodes, here the barrier thickness is much thicker than the localization length and the transfer is composed by two single tunnel events. An electron tunnels from the left electrode to a localized state, then from this localized state to the right electrode (see Fig. 2.2). It has been shown that only localized states, situated at $(d + \alpha^{-1})/2$ and within an energy width $E_F \pm \frac{\Gamma}{2}$, are likely to contribute to the resonant tunneling conductance [85]. Here, Γ is referred to as the intrinsic width of the states. The total resonant tunneling conductance is given by the sum over the contributions from each resonant channel within the junction area A . In a simplified notation, the resonant tunneling conductance is given by

$$G_1^{res} = \hat{G}_1^{res} \cdot \exp(-\alpha d). \quad (2.7)$$

It can be easily seen from equations (2.6, 2.7) that for a sufficiently large barrier thickness d the resonant tunneling conductance becomes dominant over the direct tunneling conductance $G_1 > G_0$.

There are also theoretical studies [88, 89] claiming that resonant tunneling through two or more localized states should exist and predominate in the limit of very thick barriers at extremely low temperatures. The larger contribution to the conductance by phonon-assisted, inelastic hopping processes described in the following Section, however, prevent them from being experimentally observed.

Resonant tunneling is usually temperature-independent. As for direct tunneling, there is only a weak quadratic temperature dependence resulting from a smearing of the Fermi energy at finite temperatures. Glazman and Shekter [90], however, showed that an electron-phonon interaction will lead to an elastic and inelastic resonant tunneling part. The inelastic resonant effects will introduce a weak temperature-dependent correction to the resonant tunneling conduction.

It is generally believed that inelastic effects, resulting from electrons interacting with lattice phonons and phonon-assisted electron hopping destroy the phase coherence, which is essential to the resonance, and thereby reduce their relative significance.

Inelastic hopping via two or more localized states

In their phenomenological theory, Stone and Lee [91] proposed that variable range hopping (p. 34) is the main inelastic conduction mechanism that competes with resonant tunneling. They obtained their results treating the inelastic processes from a scattering point of view. No microscopic model of electron phonon interaction was assumed.

The dynamics of the tunneling process was first treated quantum mechanically by Glazman and Matveev [92]. They investigated in detail the process of inelastic tunneling through two localized states. Each of these is assumed to couple elastically only to the nearer electrode, whereas the coupling between them is assumed to be inelastic, via interaction (emission or absorption) with phonons (Fig. 2.2).

Electron-phonon interaction causes hopping between two localized states. This is especially important for the states with an energy separation of the

order of $k_B T$, since when $k_B T \gg \Gamma$ the elastic coupling between those states is negligible.

In the low bias-voltage limit, $eV \ll k_B T$, the studies by Glazman and Matveev predicted

$$G_2^{hop} \propto T^{(4/3)} \cdot \exp\left(\frac{-2\alpha d}{3}\right). \quad (2.8)$$

Three different factors result in this specific power law. First, a first-order expansion made in the small parameter $eV/k_B T$ contributes T^{-1} . Second, the integration over a linear phonon dispersion (appropriate for low-energy acoustic phonons) combined with the typical energy scale to which the phonons have to couple in order to give rise to the hopping, together contribute $T^{1/3}$. And finally, a T^2 contribution is obtained from the requirements that the first localized state is within $\sim k_B T$ of the Fermi level, so that electrons are available to tunnel onto it, and that the second state is within $\sim k_B T$ of the first, so that phonons are available to couple to them [85].

In the high bias-voltage and low temperature limit $eV \gg k_B T$, a similar power law is obtained

$$G_2^{hop} \propto V^{(4/3)} \cdot \exp\left(\frac{-2\alpha d}{3}\right). \quad (2.9)$$

The conduction, due to inelastic hopping along optimal chains, is exponentially larger than that of the resonant tunneling in the barrier thickness. This more than compensates for the small probability of realizing such configurations.

As the temperature is further increased and as the barriers become thicker, the energy window for hopping increases, and hopping chains with larger numbers of localized states optimally located, though even rarer, may dominate the conduction process.

The equations (2.8, 2.9) for hopping via two localized states can be generalized to give the average hopping conductance of the chains consisting of N localized states.

Low bias-voltage limit: $eV \ll k_B T$,

$$G_N^{hop} \propto T^{N-[2/(N+1)]} \cdot \exp\left(\frac{-2\alpha d}{N+1}\right). \quad (2.10)$$

High bias-voltage and low temperature limit: $eV \gg k_B T$,

$$G_N^{hop} \propto V^{N-[2/(N+1)]} \cdot \exp\left(\frac{-2\alpha d}{N+1}\right). \quad (2.11)$$

Variable range hopping

In the bulk limit, $d \gg l_{VRH}$, variable range hopping is the dominant conductance mechanism. Mott realized that the typical length of a hop, the variable hopping length l_{VRH} , had to be short enough so as to have a finite overlap of the electron wave functions on the two localized states involved. On the other hand, it had to be long enough to find a state with a comparable Fermi energy [93]. Mott predicted that the length of a hop increases with decreasing temperature as $T^{-1/4}$. The conductance, which is proportional to the probability of such a hop, is thus, given by

$$G^{VRH} = \hat{G}_0^{VRH} \cdot \exp\left(-\left(\frac{\tilde{T}}{T}\right)^{1/4}\right), \quad (2.12)$$

where \tilde{T} is a characteristic temperature.

Shklovskii proposed an analogous current-field relation for hopping in the limit of high fields [94]. He predicted that at sufficiently low temperatures ($eV \gg k_B T$) the current-field characteristic should be given by

$$J^{VRH} = \hat{j}_0^{VRH} \cdot \exp\left(-\left(\frac{\tilde{E}}{E}\right)^{1/4}\right), \quad (2.13)$$

where the current density $J(E)$ is assumed to be homogeneous and \tilde{E} is a characteristic field.

In summary, the total conductance at any temperature is the sum of the contribution of elastic and inelastic processes:

$$G_\Sigma(T) = G_0^{dir} + G_1^{res} + \sum_{N=2} G_N^{hop}(T) + G^{VRH}(T). \quad (2.14)$$

Chapter 3

Concept of a Ferroelectric Tunnel Junction

Technological and theoretical progress in the last few years allows the deposition of epitaxial ferroelectric films as thin as a few monolayers. Encouraged by this development, we present the concept of a ferroelectric tunnel junction (FTJ), with a thin ferroelectric barrier allowing electron tunneling. An FTJ is shown schematically in Fig. 3.1. It consists of two conducting electrodes separated by an ultrathin ferroelectric layer. Unlike superconducting or magnetic tunnel junctions, the term ferroelectric is not associated with a property of the electrode, but with a property of the barrier itself. Prior to the work presented in this thesis, there has been no experimental work on the combination of ferro- or piezoelectricity and quantum-mechanical tunneling phenomena. Only shortly before completing this thesis, we learned about a patent from Philips Corp. [95] and a publication from IBM [96] that deal with this topic. However, neither of them has published any experimental results or theoretical calculations.

In the following, I will present our ideas and theoretical studies on a possible interaction between piezoelectricity or ferroelectricity, on the one hand, and quantum-mechanical tunneling through the ultrathin ferroelectric barrier of an FTJ, on the other hand, and, if such an interaction can be assumed, how exactly this develops. First, a piezoelectric, but not necessarily ferroelectric, barrier material will be considered. Afterwards tunnel junctions with a ferroelectric barrier will be studied. However, before going into detail, some preliminary ideas developed in many stimulating discussions with various talented people are shown in Fig. 3.2. It should be noted that all of the drawings shown were made before any measurements on ultrathin films were performed. No further comment on these drawings will be made. Nev-

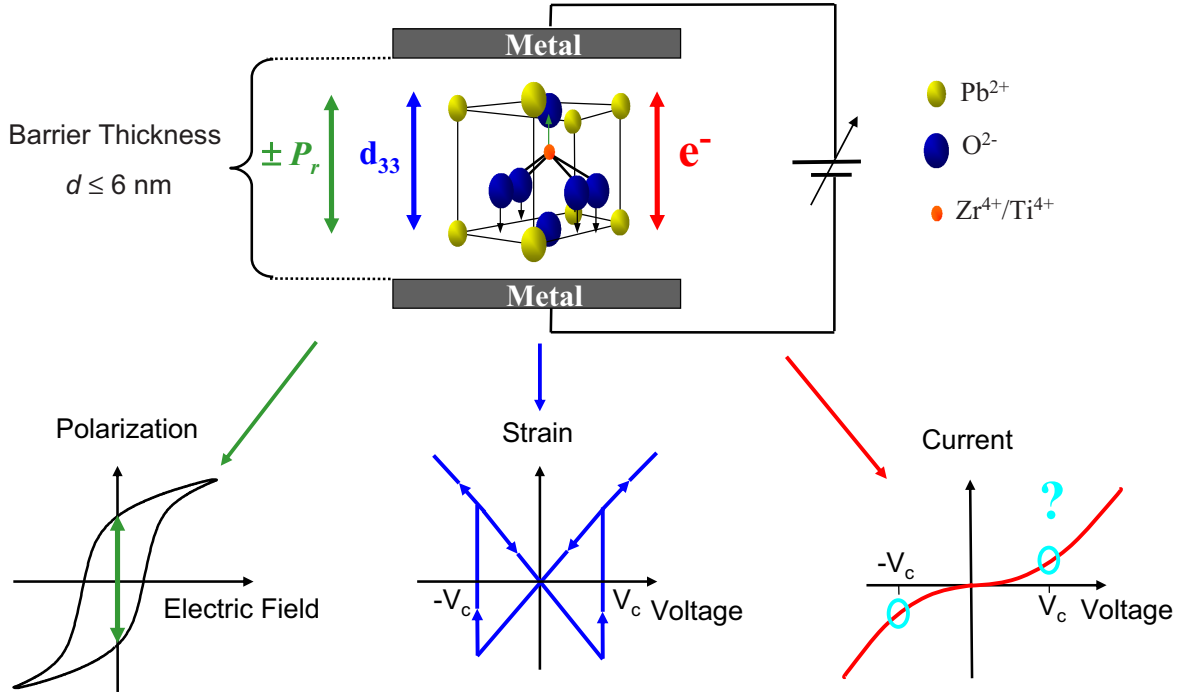


Figure 3.1: *Concept of a ferroelectric tunnel junction. Two electrodes separated by an ultrathin ferroelectric layer. Combination of macroscopic phenomena (i.e. polarization and strain) and quantum-mechanical tunneling.*

ertheless, the reader is strongly encouraged to return to this page and have a look at Fig. 3.2 after reading this thesis.

3.1 Piezoelectricity and tunneling

As discussed in Chap. 1.1, piezoelectric materials show a linear relationship between the applied electric field (or voltage) and the induced strain in the film. This is referred to as the *converse piezoelectric effect*. For example, a voltage V applied along the z -axis of a piezoelectric film induces a lattice strain S_{33} in the film according to

$$S_{33} = \frac{d - d_0}{d_0} = \frac{d_{33}V}{d_0}. \quad (3.1)$$

Here, d is the thickness of a barrier material, d_0 is the thickness of the bar-

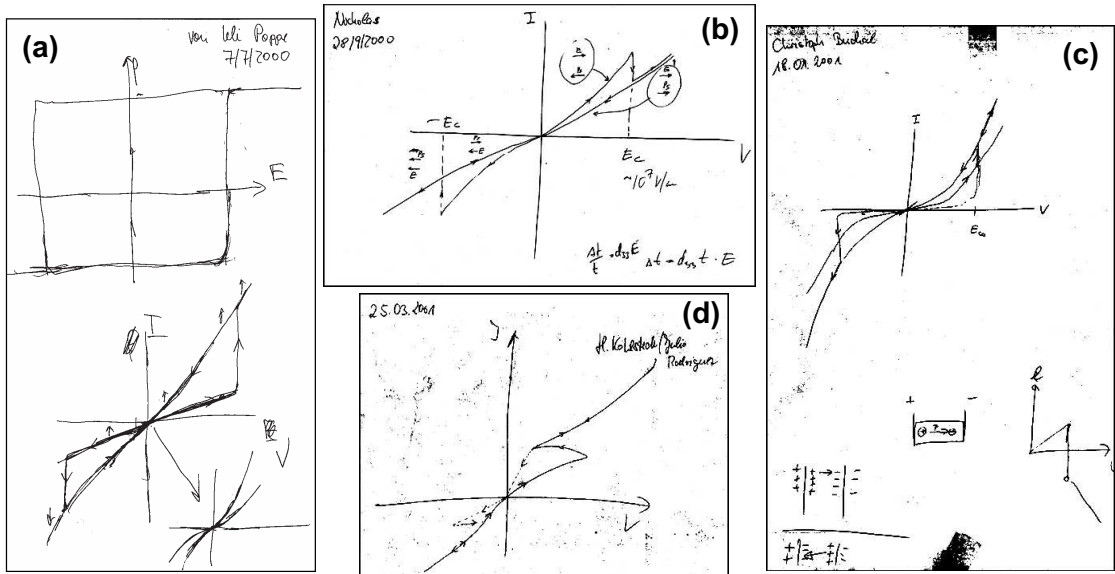


Figure 3.2: Results of discussions about the interplay of ferro- or piezoelectricity and quantum-mechanical tunneling with (a) U. Poppe, (b) N. A. Pertsev, (c) Ch. Buchal, and (d) H. Kohlstedt.

rier in the absence of an applied field and d_{33} is the longitudinal component of the piezoelectric third-rank tensor d_{ijk} in matrix notation (see Fig. 1.1 (a)).

In the following, various effects of lattice strain on the barrier properties, identified in collaboration with N. A. Pertsev, will be discussed. There are mainly three effects that arise from a change of strain in a piezoelectric film: first, the barrier thickness changes; second, the effective mass of electrons in the barrier changes due to a change of the lattice parameters; and third, the conduction and the valence band edges shift.

Change in barrier thickness

The most obvious consequence of the converse piezoelectric effect (i.e. the linear voltage dependence of the strain in the material) is the contraction or expansion of a piezoelectric material when a voltage is applied to it. The strain-free thickness of the piezoelectric material increases by the piezoelectric coefficient d_{33} times the applied voltage V . Consider a piezoelectric film with a strain-free thickness in the z -direction equal to d_0 . If a voltage is applied along the z -axis, the thickness d is given by

$$d = d_0 + d_{33}V. \quad (3.2)$$

Note that a voltage- or field-induced change in the thickness of the piezoelectric barrier implies an increase or decrease of the distance between the electrodes of a tunnel junction. This is particularly important due to the exponential dependence of conductance on the barrier thickness, which is a specific feature of tunneling.

Change of effective mass

Strain increases or decreases the thickness of the piezoelectric barrier. The change in the barrier thickness involves a change in the lattice parameters of the barrier, as the number of atoms inside the barrier does not change. Using the *Tight-Binding* method [97] proposed by Bloch, which is appropriate if electrons are "tightly bound" to the nuclei of the atoms or, in other words, when the distance between neighboring atoms, a , is large in comparison to the size of the atoms, the following relation between the effective mass m^* and the energy width of the conduction band ΔE_C (eqn. (5.20) in Ref. [47]) is obtained:

$$m^* = \frac{2 \hbar}{a^2 \cdot \Delta E_C}. \quad (3.3)$$

Using the exponential dependence of the energy width of the conduction band on the distance between neighboring atoms [47],

$$\Delta E_C \sim \exp\left(-\frac{a}{r_\alpha}\right), \quad (3.4)$$

where $r_\alpha \ll a$ is a positive constant, gives

$$m^* \sim \exp\left(\frac{a}{r_\alpha}\right). \quad (3.5)$$

Considering the strain-induced change of the lattice parameters, $a = a_0 + a_0 S_{33}$ (see eqn. (3.1)), the partial derivative of the effective mass with respect to the strain is given by

$$\begin{aligned} \frac{\partial m^*}{\partial S_{33}} &\sim \exp\left(\frac{a_0}{r_\alpha}\right) \cdot \frac{a_0}{r_\alpha}, \\ &\sim \exp\left(\frac{a_0}{r_\alpha}\right) > 0. \end{aligned} \quad (3.6)$$

Consequently, the effective mass of electrons inside a piezoelectric film can be written as

$$\begin{aligned}
m^* &= m_0^* + \frac{\partial m^*}{\partial S_{33}} S_{33}, \\
&= m_0^* + \frac{\partial m^*}{\partial S_{33}} \frac{d_{33}V}{d_0},
\end{aligned} \tag{3.7}$$

where the derivative of the effective mass with respect to the strain is positive, $\frac{\partial m^*}{\partial S_{33}} > 0$.

Shift of the conduction and valence band edges

The strain induces changes in the band structure of the barrier [98, 99, 100, 101]. Due to strain, both the conduction band and the valence band states are modified, leading to shifts of the corresponding band edges relative to their values for unstrained material. For simplicity, only the shift of the conduction band edge, E_C^0 , will be discussed here in the one-band model in WKB approximation. In the one-band model, only the conduction (or valence) band is considered, while the energy gap is virtually infinitely large. This implies for a metal-insulator-metal structure, that the barrier height must be sufficiently small in relation to the width of the band gap [77]. The electron wave number k near the bottom of the conduction band is given by [77]

$$\begin{aligned}
k^2 &= k_z^2 + k_\perp^2, \\
&= \frac{2m_\parallel^* E_z}{\hbar^2} + \frac{2m_\perp^* E_\perp}{\hbar^2}, \\
&= \frac{2m^*}{\hbar^2} \cdot (E - E_C).
\end{aligned} \tag{3.8}$$

The bottom of the conduction band may be written as

$$E_C = E_C^0 + \Delta\theta(z, V). \tag{3.9}$$

Here, E_C^0 is the bottom of the conduction band at $V = 0$ volts, and $\Delta\theta$ is the shift of the bottom of the conduction band as a function of the coordinate z and the applied voltage. The coupling of the conduction band edge to strain is described by the conduction band deformation potential κ . The bottom edge of the conduction band is shifted under a strain S_{33} (longitudinal component of strain, see Fig. 1.1, p. 4) by the conduction band deformation potential κ_{33} times strain S_{33} . In addition, and assuming a homogeneous electric field inside the barrier, if a positive voltage V is applied

at the metal electrode M_2 , the Fermi level E_{F2} is moved downwards by an amount of eV , and the conduction band E_C^0 is consequently shifted by $-\frac{eV}{d} z$. This gives

$$\begin{aligned} E_C(z, V) &= E_C^0 + \kappa_{33} S_{33} - \frac{eV}{d} z, \\ &= E_C^0 + \kappa_{33} \frac{d_{33}V}{d_0} - \frac{eV}{d_0 + d_{33}V} z. \end{aligned} \quad (3.10)$$

To our knowledge, the deformation potential κ is not known for any ferroelectric material. However, κ turns out to be negative for most of the materials in the literature [100]. Also, and most importantly, the deformation potential for the piezoelectric material *GaN* is negative [102]. Thus, it is likely that the conduction band deformation potential for ferroelectrics with oxide perovskite structure is negative as well.

Influence on tunneling probability

For simplicity, we consider only direct tunneling through the piezoelectric barrier of the FTJ. The tunneling probability (eqn. 2.4) for electrons in the conduction band of the electrode, assuming that the effective mass is constant in the z -direction, is given by

$$|M(E)|^2 = c \cdot \exp \left(-\frac{4\pi}{h} \cdot \sqrt{2m^*} \int_0^d \sqrt{(E_C(z, V) - E)} dz \right). \quad (3.11)$$

$E_C(z, V)$ is the energy of electrons near the bottom of the conduction band of the barrier with the effective mass m^* .

Replacing the barrier thickness d , the conduction band bottom E_C , and the effective mass m^* by the strain-dependent terms yields

$$\begin{aligned} |M(E)|^2 &= c \cdot \exp \left(-\frac{4\pi}{h} \sqrt{2 m_0^*} \left(1 + \frac{\partial m^*}{\partial S_{33}} \frac{d_{33}V}{d_0} \right) \right. \\ &\quad \times \left. \int_0^{d_0 + d_{33}V} \sqrt{E_C^0 - \frac{eV}{d_0 + d_{33}V} z + \kappa_{33} \frac{d_{33}V}{d_0} - E} dz \right). \end{aligned} \quad (3.12)$$

The tunneling probability for a piezoelectric barrier material is obtained by integration and a Taylor expansion around $V = 0$ for the effective mass term as

$$|M(E)|^2 = c \cdot \exp \left(-\frac{8\pi\sqrt{2} m_0^*}{3h} \frac{d_0 + d_{33}V}{eV} \left(1 + \frac{1}{2m_0^*} \frac{\partial m^*}{\partial S_{33}} \frac{d_{33}V}{d_0} \right) \right) \quad (3.13)$$

$$\times \left[\left(E_C^0 + \kappa_{33} d_{33} \frac{V}{d_0} - E \right)^{3/2} - \left(E_C^0 + \kappa_{33} d_{33} \frac{V}{d_0} - eV - E \right)^{3/2} \right].$$

Here, the terms accounting for the strain-induced change of the barrier thickness, the effective mass of the electrons and the shift of the conduction band are printed in red, green and blue, respectively. From this equation we can extract the change of the tunneling probability, and thus predict the change of the tunneling conductance for the application of a voltage inducing either a tensile strain $S_{33} > 0$ or a compressive strain $S_{33} < 0$:

- Tensile strain $S_{33} > 0$:
 - Distance between electrodes increases for tensile strain
 \Rightarrow Tunneling conductance decreases ↘
 - Change of the effective mass due to increased lattice parameters
 \Rightarrow Tunneling conductance decreases ↘
 - Shift of the conduction band assuming a negative deformation potential
 \Rightarrow Tunneling conductance increases ↗
- Compressive strain $S_{33} < 0$:
 - Distance between electrodes decreases for compressive strain
 \Rightarrow Tunneling conductance increases ↗
 - Change of the effective mass due to decreased lattice parameters
 \Rightarrow Tunneling conductance increases ↗
 - Shift of the conduction band assuming a negative deformation potential
 \Rightarrow Tunneling conductance decreases ↘

Here, the colors of the arrows correspond to the color code used above. Assuming that the deformation potential is negative (see p. 40), there is no unambiguous behavior of the tunneling conductance for tensile or compressive strain. Indeed, we cannot predict an increasing or a decreasing tunneling conductance for a given voltage-induced strain. Nevertheless, unless the three effects discussed above compensate each other, a strain-induced change of the tunneling conductance, and thus, a strain-induced change of the tunnel current is expected for a piezoelectric barrier.

3.2 Ferroelectricity and tunneling

Fig. 3.3 (upper part) shows the strain produced in a ferroelectric material by the application of a voltage. This converse piezoelectric effect for a ferroelectric material differs from that for a piezoelectric, but not ferroelectric material, only by the existence of two linear curves (one for each polarization state) and the jump from negative to positive strain at the coercive voltages $\pm V_c$. The free energy as a function of the polarization is plotted in the lower part of Fig. 3.3. The blue balls in plots (a)-(e) indicate the specific free energies $F_P = F(P)$ at the corresponding strain-field positions. The free energy functional possesses three extrema. Two of them are stable (i.e. the minima indicated by the blue ball in (b) and (e)). They correspond to the stable polarization states of the ferroelectric thin film at $V = 0$ volts and $P = \pm P_r \neq 0$. The third extremum of the free energy F_P is unstable. This extremum corresponds to the voltages $V = \pm V_c$ and coincides with a jump in the strain from a negative to a positive value (e.g. (c)).

No clear behavior has been obtained in our theoretical treatments of the tunneling conductance for a given voltage-induced strain in a piezoelectric material. Both the strain effects on the barrier thickness and the effective mass of electrons inside the barrier result in qualitatively similar changes of the tunneling conductance, whereas the effect on the position of the conduction band results in the opposite impact on the tunneling conductance. At present, no numerical calculations including all three effects discussed above are possible, due to a lack of knowledge of the deformation potential and the exact strain dependence of the effective mass of electrons. It is, however, possible to simulate the effect of a strain-induced change of the barrier thickness on the tunnel current through a ferroelectric tunnel junction. This will enable us to get a feeling as to what extent the expected influence of the converse piezoelectric effect on the barrier thickness may alter the I - V characteristic of an FTJ.

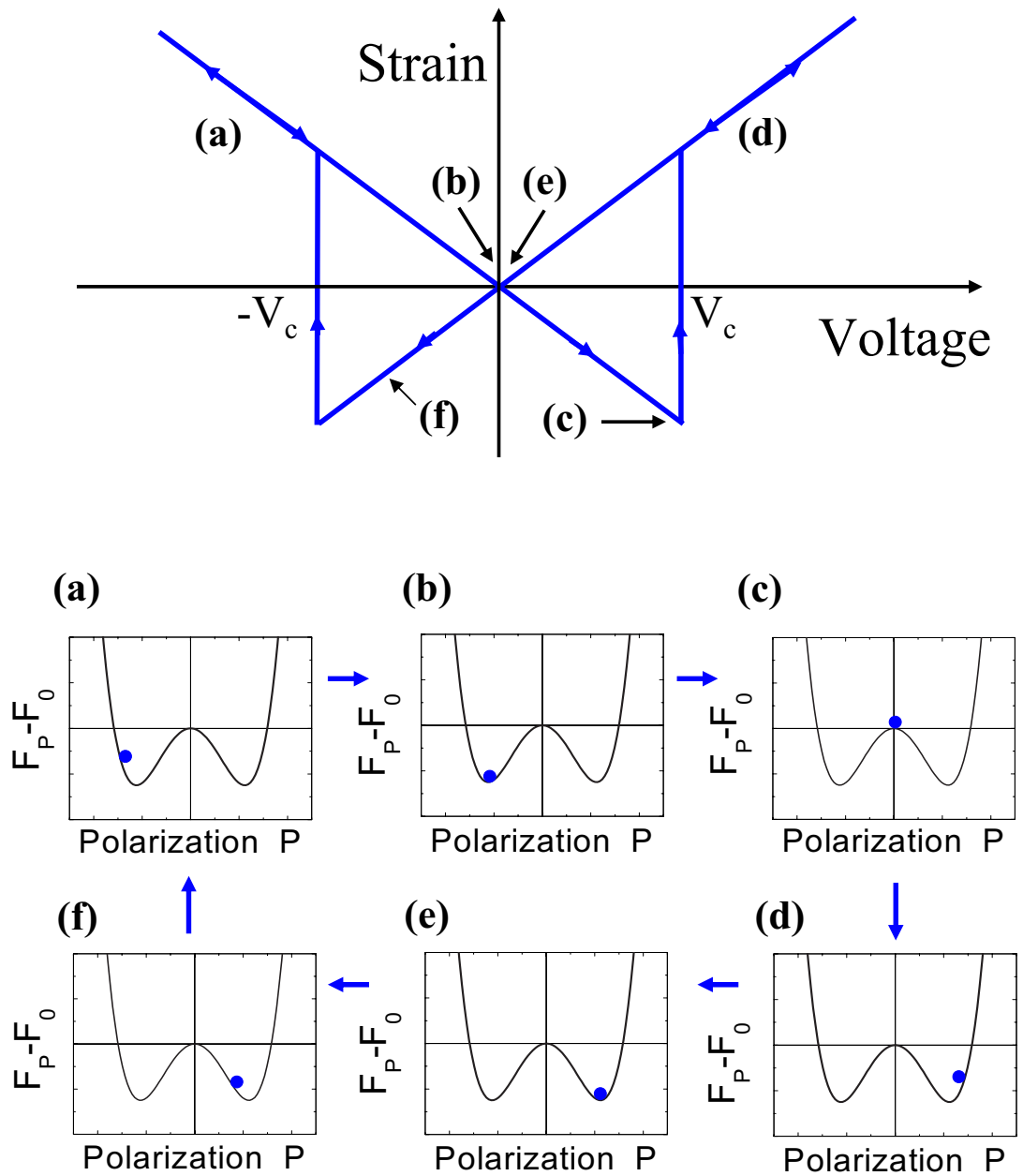


Figure 3.3: *Upper part: Illustration of the strain-field relation of a ferroelectric material. Lower part: Corresponding free energy plotted as a function of the polarization. Blue ball indicates free energy at specific strain-field positions marked (a)-(e).*

Modified Brinkman model accounting for a strain-induced change of the barrier thickness

Fig. 3.4 (a) illustrates the voltage dependence of the barrier thickness d of an FTJ. The blue and red curves indicate the curves for the two stable polarization states. We consider only direct tunneling through the ferroelectric barrier and modify the Brinkman model (eqn. (2.5)) to account for the voltage dependence of the barrier thickness (eqn. (3.2)):

$$\begin{aligned} \frac{I(V)}{A} &= 3.16 \cdot 10^{10} \frac{\sqrt{\bar{\Phi}}}{d_0 + d_{33}V} \exp \left(-1.025 (d_0 + d_{33}V) \sqrt{\bar{\Phi}} \right) \quad (3.14) \\ &\times \left[V - 0.0213 \frac{(d_0 + d_{33}V) \cdot \Delta\Phi}{\bar{\Phi}^{3/2}} V^2 + 0.0109 \frac{(d_0 + d_{33}V)^2}{\bar{\Phi}} V^3 \right]. \end{aligned}$$

Using this modified Brinkman model, the I - V characteristic (Fig. 3.4 (b)) and corresponding dynamic conductance dI/dV (Fig. 3.4 (c)) for an FTJ has been calculated. The parameters chosen for the simulation are $d_0 = 3$ nm, $d_{33} = \pm 200$ pm/V (typical of $PbZr_{0.52}Ti_{0.48}O_3$ thin films used in this work), $V_c = 0.1$ V, $\bar{\Phi} = 0.5$ eV and $\Delta\Phi = 0.1$ eV.

Three striking features can be observed in Fig. 3.4 (b) and (c). The first characteristic feature is represented by the jumps at $\pm V_c$, which coincide with the jumps in the barrier thickness shown in Fig. 3.4 (a). Both jumps reduce the current flowing through the ferroelectric barrier. This can be easily understood as the thickness of the barrier suddenly increases at both coercive voltages, leading to a reduced tunneling probability.

The second characteristic feature is the behavior of the red and the blue curves around $V = 0$ volts. Going through the origin, the blue and the red curves change the relative resistance with respect to each other. For example, when the voltage is switched from negative values to positive values, the blue curve changes from a higher resistance state to a lower resistance state with respect to the red curve. The reason for this phenomenon is simple. At $V = 0$ volts, the voltage-induced strain changes the sign (see Fig. 3.3 (upper part)). This implies that the thickness of the ferroelectric barrier changes from being larger than d_0 to being smaller than d_0 and vice versa for the red curve. For example, if a positive voltage ($0 < V < V_c$) is applied, then the thickness of the barrier increases for the polarization state corresponding to the red curve, and it shrinks for the polarization state corresponding to the blue curve.

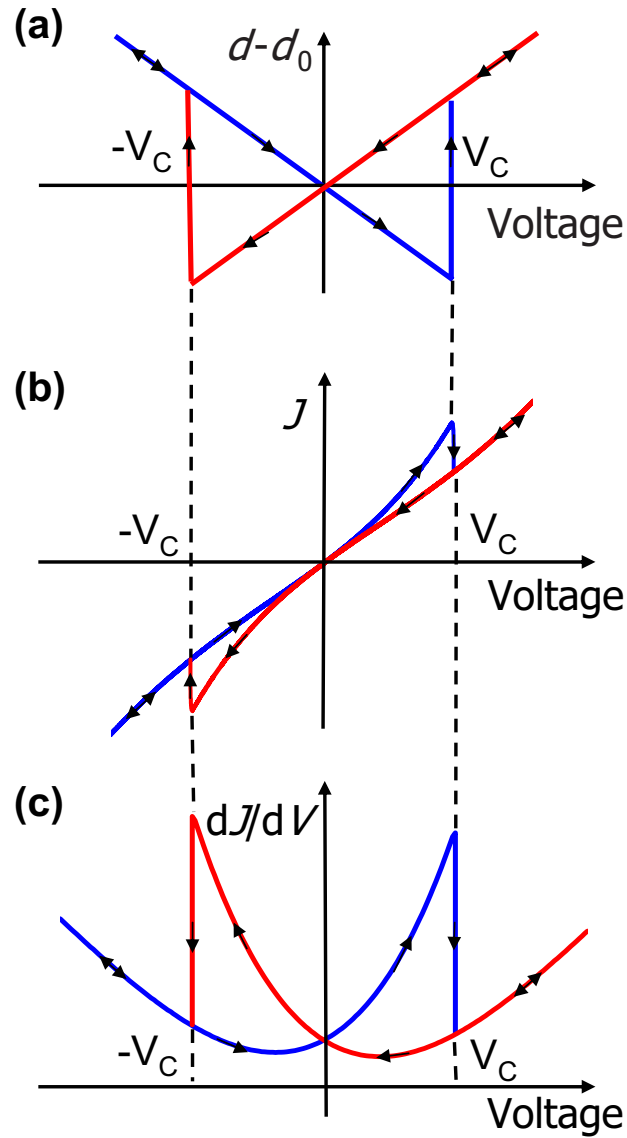


Figure 3.4: (a) Consequence of the converse piezoelectric effect for a ferroelectric material: Voltage-induced change of the thickness d of a ferroelectric material. (b) Application of Brinkman model to tunnel junctions with ferroelectric barriers (i.e. FTJ). (c) Dynamic conductance for current characteristic shown in (b). See text for details.

The third striking feature is a shift of the minimum of the dynamic conductance from $V = 0$ volts to positive and negative voltages for the red and blue curves, respectively. This feature does not have a simple physical explanation. Roughly speaking, it is a result of the superposition of the quadratic

relation of the dynamic conductance (in a strain-free material) for direct tunneling with the linear change of the barrier thickness.

Microscopic interface effect of the polarization switching on tunneling

The polarization reversal involves a shift of ions inside the ferroelectric barrier with respect to each other. This modification of the internal atomic structure changes the sign of the barrier function slope. This is deduced from the work of Karrer, Stutzmann and coworkers [103, 104], as well as of Rizzi and Lüth [105], on the piezoelectric GaN .

In the wurtzite structure of GaN , atoms of opposite electronegativity lie above each other along the symmetry axis and the charge displacement gives rise to a dipole along the same axis. The group III-nitride GaN was grown by molecular beam epitaxy, either with Ga -face or N -face at the Pt/GaN interface. It turns out that the (Schottky) barrier height differs for the Ga - and N -face. It is 1.1 eV for the Ga -face with the polarization directed away from the interface and 0.9 eV for the N -face with the polarization directed towards the interface. The growth of the piezoelectric GaN with Ga - and N -faces can be regarded as a model for the polarization reversal in a ferroelectric material with, other than that, the same properties as GaN . Consider a GaN film sandwiched between Pt electrodes with a Ga -face at one interface and a N -face at the other interface. In a simplified model, different barrier heights at the interfaces result in a trapezoidal potential barrier. The barrier function $\Phi(z)$ describing this system is a linear function in z , assuming a growth of the heterostructure along the z -axis. The growth of the same heterostructure with switched faces means reversing the polarization. At the same time, the sign of the slope of the barrier function is changed.

Fig. 3.5 displays the application of the Brinkman model (eqn. (2.5)) to a tunnel junction with fixed barrier thickness $d = 2$ nm, average barrier height $\bar{\Phi} = 0.5$ eV, and barrier asymmetry $\Delta\Phi_{red} = 0.5$ eV (red curve) and $\Delta\Phi_{blue} = -0.5$ eV (blue curve). These values for $\bar{\Phi}$ and $\Delta\Phi$ transform into the barrier heights $\Phi_{1,red} = 0.25$ eV, $\Phi_{2,red} = 0.75$ eV and $\Phi_{1,blue} = 0.75$ eV, $\Phi_{2,blue} = 0.25$ eV for the red curve and the blue curve, respectively. Thus, the simulation shown corresponds to a reflection of the barrier function $\Phi(z)$ at the center of the barrier (i.e. $d = d_0/2$). A voltage-induced change of the barrier thickness and further expected effects discussed above are neglected.

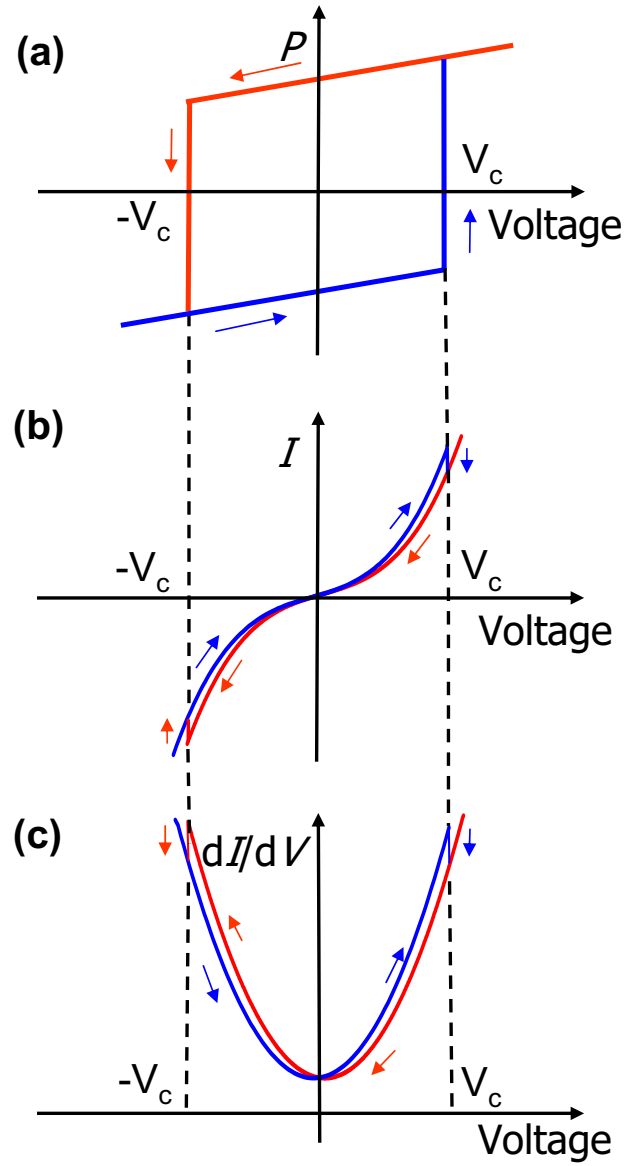


Figure 3.5: (a) Ferroelectric hysteresis loop, (b) current I and (c) corresponding dynamic conductance dI/dV as a function of the applied voltage. Fit parameters: $d = 2 \text{ nm}$, $\bar{\Phi} = 0.5 \text{ eV}$, $\Delta\Phi_{red} = 0.5 \text{ eV}$, $\Delta\Phi_{blue} = -0.5 \text{ eV}$.

Surprisingly, the I - V curve and the dynamic conductance dI/dV plotted in Fig. 3.5 show the same characteristic features as those observed and discussed in Fig. 3.4, where the curves were calculated for a strain-induced change of the barrier thickness. Despite the similarities, both effects are in-

dependent of each other. By changing the sign of $\Delta\Phi$, only the quadratic term in the voltage in the Brinkman equation (eqn. 2.5) is changed. For a positive $\Delta\Phi$, the current-voltage curve is shifted downwards by a quadratic term in voltage and vice versa for a negative $\Delta\Phi$. As a result, the current for the red curve $I_{\Delta\Phi>0}$ with respect to the current for the blue curve $I_{\Delta\Phi<0}$ is reduced for positive voltages and it is enhanced for negative voltages. The shift in voltage observed for the dynamic conductance is a simple mathematical consequence. The quadratic term in voltage that is changed in the Brinkman equation becomes linear for its derivative. Hence, a change of the sign of $\Delta\Phi$ results in a shift of the dynamic conductance along the voltage axis.

As a conclusion to this Chapter, we have presented the concept of a ferroelectric tunnel junction and called this novel device an FTJ. Theoretical calculations were presented to determine the influence of the converse piezoelectric effect on the direct tunnel current of a tunnel junction with a piezoelectric or ferroelectric barrier. Three effects have been identified leading to a strain-induced change of the tunnel current. It is expected that the thickness of the barrier changes, the effective mass changes, and that the positions of the conduction and valence band edges shift when a voltage is applied to an FTJ producing a strain in the barrier material. Unfortunately, only two of these effects, namely the change of the barrier thickness and the change of the effective mass, have the same consequence (i.e. the tunneling conductance decreases for tensile strain), whereas an increase of the tunneling conductance is expected for tensile strain, arising from a change of the position of the conduction band edge. Thus, we cannot unambiguously predict the consequence of the converse piezoelectric effect on the tunnel current. Nevertheless, we have calculated the I - V characteristic and the dynamic conductance for a tunnel junction accounting for two different effects. First, a voltage-induced change of the barrier thickness was modelled by modifying the Brinkman theory. Second, the microscopic interface effect was considered, resulting from the switching of the polarization and leading to a change of the atomic structure. Using typical parameters for $PbZr_{0.52}Ti_{0.48}O_3$, a ferroelectric material studied in this work, in both cases clearly different curves were obtained for two oppositely directed polarization states. Particularly, these simulations show that the mentioned effects on the tunnel current are large and should be observable in experimental direct tunneling curves as well.

Chapter 4

Heteroepitaxy of oxide perovskites

Perovskite is named for a Russian mineralogist, Count Lev Aleksevich von Perovski. The mineral was discovered and named by Gustav Rose in 1839 from samples found in the Ural Mountains.

Functional oxide perovskites are receiving more and more attention due to their unique dielectric, pyroelectric, piezoelectric, ferroelectric, magnetic and superconducting properties.

This Chapter deals with the perovskite materials used within this work and with the deposition methods employed for their growth.

4.1 Material systems

The heterostructures that have been primarily studied in this PhD thesis are Pt (or $SrRuO_3$) / $PbZr_{0.52}Ti_{0.48}O_3$ / $SrRuO_3$ and Pt (or $SrRuO_3$) / $(Ba, Sr)TiO_3$ / $SrRuO_3$, both grown on $SrTiO_3$ (100) substrates. In this Chapter a brief description of the materials used, excluding Pt ¹, will be given. The main emphasis will be on the properties which led to the specific material being chosen for use in this work. In addition, some properties will be mentioned which, in the author's opinion, are interesting. The following Sections, however, should not be regarded as comprehensive lists of the properties of these materials.

¹ Pt served as the top electrode and was either sputtered or e-beam-evaporated by Th. Schneller, RWTH Aachen, or H. Haselier, Forschungszentrum Jülich, respectively.

Pb(Zr, Ti)O₃

In the past years, ferroelectric $PbZr_xTi_{1-x}O_3$ solid solutions have been investigated for applications such as non-volatile memory devices [106], pyroelectric detectors [107], as well as electromechanical actuators, optical applications, and infrared detectors [108]. Epitaxial thin films have been grown by rf-sputtering [109], pulsed laser deposition [110], metal organic chemical vapor deposition [34, 111], and molecular beam epitaxy [112].

Haun and coworkers have extensively studied the physical and structural properties of $PbZr_xTi_{1-x}O_3$ solid solutions and have obtained important results using a Landau-Ginzburg phenomenological theory [23, 113]. Fig. 4.1 (a) depicts the phase diagram and Fig. 4.1 (b) the lattice constants as a function of the composition of $PbZr_xTi_{1-x}O_3$.

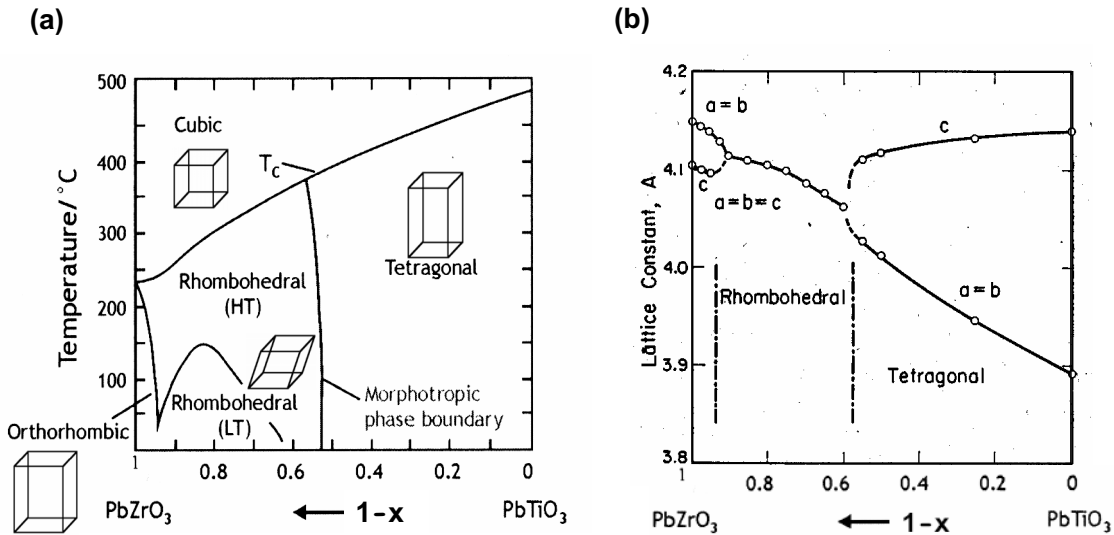


Figure 4.1: (a) Phase diagram as a function of the composition and temperature and (b) lattice parameters as a function of the composition of $PbZr_xTi_{1-x}O_3$. [114]

According to [23], the paraelectric-ferroelectric transformation of $PbZr_xTi_{1-x}O_3$ is a first-order phase transition for $x < 0.28$ and a second-order phase transition for $x > 0.28$. In thin films, however, the second-order type phase transition is extended to at least $x \geq 0.1$ due to two-dimensional clamping of the film on a thick substrate [5], irrespective of the misfit strain [115].

$PbZr_xTi_{1-x}O_3$ has various stable phases depending on temperature and composition. A morphotropic phase boundary separating the tetragonal from the rhombohedral phase is situated around $x = 0.48$. Recently, an intermediate monoclinic phase close to the morphotropic phase boundary has been discovered [116]. The existence of this phase for *single crystals* has been confirmed subsequently by simulations based on first-principle calculations [117], as well as thermodynamic calculations involving an expansion of the free energy up to the eighth order [118]. For *thin films*, Pertsev and coworkers have developed phase diagrams for several $PbZr_xTi_{1-x}O_3$ compositions taking into account the misfit strain in thin films [115]. These phase diagrams reveal the existence of a *monoclinic gap* in thin films for all studied compositions ($x = 0.4 - 0.9$) in a certain misfit strain range. In Fig. 4.2 (a) the phase diagram taken from [115] is shown for $PbZr_{0.5}Ti_{0.5}O_3$, and in Fig. 4.2 (b) the misfit strain dependence of the polarization components P_x , P_y , and P_z at room temperature is calculated for $PbZr_{0.6}Ti_{0.4}O_3$.

Of course, the spontaneous polarization P_S does not only depend on the misfit strain, but also on the Zr/Ti ratio. Pure $PbTiO_3$ exhibits the high-

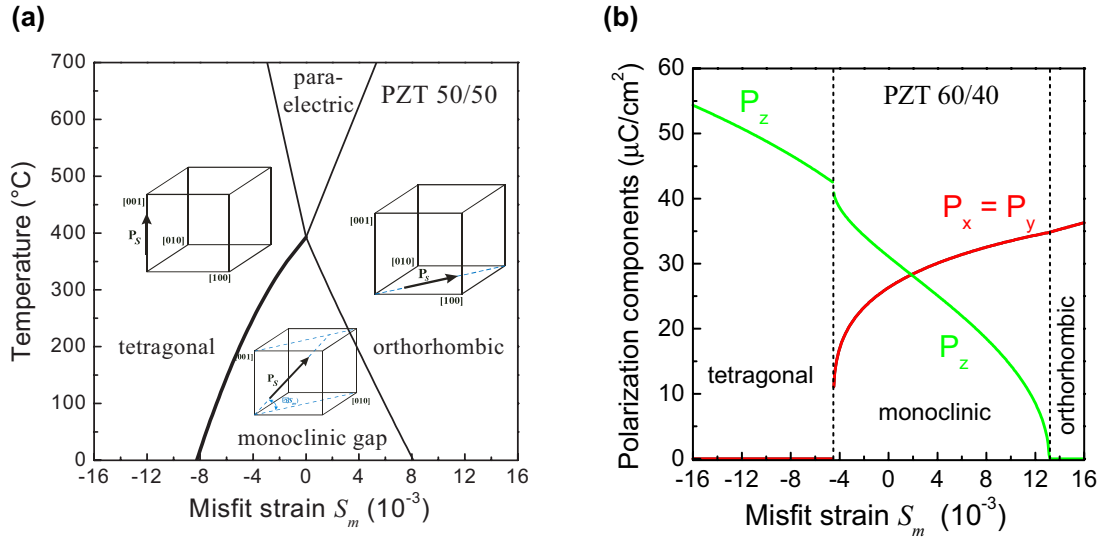


Figure 4.2: (a) Phase diagram of (00l)-oriented single domain $PbZr_{0.5}Ti_{0.5}O_3$ films epitaxially grown on dissimilar cubic substrates. First- and second-order phase transitions are shown by thick and thin lines, respectively. The quadruple point at $S_m = 0$ corresponds to the Curie-Weiss temperature of stress-free bulk material. (b) Misfit strain dependence of the polarization components P_x , P_y , and P_z in single domain $PbZr_{0.6}Ti_{0.4}O_3$ at room temperature. [115]

est spontaneous polarization of $81 \mu\text{C}/\text{cm}^2$. P_S decreases with increasing Zr -content. For $PbZr_{0.52}Ti_{0.48}O_3$, a value of $49 \mu\text{C}/\text{cm}^2$ has been determined [23]. $PbZr_xTi_{1-x}O_3$ close to the morphotropic phase boundary exhibits the strongest piezoelectric effect [14]. In fact, $PbZr_{0.52}Ti_{0.48}O_3$ was chosen for this work as a ferroelectric film because this composition combines a large spontaneous polarization with the strongest piezoelectric effect.

$Pb(Zr, Ti)O_3$ has a composition-dependent band gap of about 3 eV, in contrast to $E_g \approx 9$ eV for conventional dielectrics, such as SiO_2 [22]. Therefore, a significant electronic conduction can be present in this material. Bulk $Pb(Zr, Ti)O_3$ is often considered to be p -type conductive due to holes generated by the presence of lattice vacancies [119, 120], but there are also references in the literature according to which it is mixed or n -type conductive [26]. In comparison to other semiconductors, such as Si ($E_g = 1.12$ eV, $m^* \approx 10^{-1} m_0$) and $GaAs$ ($E_g = 1.42$ eV, $m^* = 6.6 \cdot 10^{-2} m_0$) [121, 97], the band gap of $Pb(Zr, Ti)O_3$ is very high and the electronic effective mass is low ($m^* \approx 10^{-3} m_0$) [122]. Assuming a perfectly ionic and trap-free ferroelectric material, one can calculate the barrier height from the difference between the metal work function and the electron affinity of the ferroelectric. Experimental values, however, are usually smaller, thus the barrier height is often calculated from a different relationship given in [123]. Experimental values for the barrier height of $Pt/Pb(Zr, Ti)O_3$ and $SrRuO_3/Pb(Zr, Ti)O_3$ are 0.6 eV [122] and approximately 0.35 eV [123], respectively.

(Ba, Sr)TiO₃

High-permittivity (high-k) materials have been investigated for many years. One of the most promising materials for future, high-density dynamic random access memories (DRAM) is $(Ba, Sr)TiO_3$ because of its high dielectric constant [124]. Epitaxial thin films have been grown by rf-sputtering [125, 126], pulsed laser deposition [127], metal organic chemical vapor deposition [128], and molecular beam epitaxy [129, 130, 131, 132, 133].

As illustrated in Fig. 4.3, the ferroelectric transition of $(Ba, Sr)TiO_3$ single crystals can be shifted in temperature by adjusting the Ba to Sr ratio. $BaTiO_3$ is a ferroelectric material with a Curie temperature of 120 °C, while $SrTiO_3$ is a paraelectric with no confirmed ferroelectric phase transition (see p. 55). At room temperature, the solid solution system is in a ferroelectric phase when the Ba content is in the range from 0.7 to 1.0, and in a paraelectric phase for a lower Ba content. Bulk $BaTiO_3$ undergoes a first-order paraelectric to ferroelectric phase transition. However, as it was the case

for $Pb(Zr, Ti)O_3$, the ferroelectric transformation of $BaTiO_3$ in an epitaxial layer may become a second-order phase transition due to two-dimensional clamping of the film on a thick substrate [5].

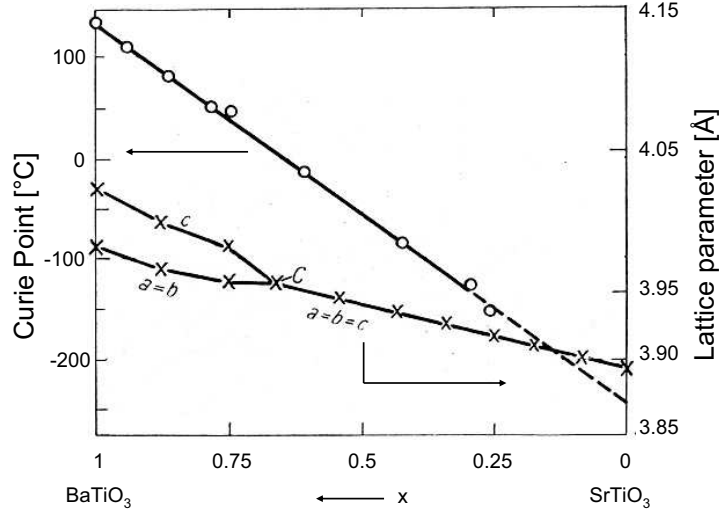


Figure 4.3: Ferroelectric phase transition temperature and lattice parameters as a function of the Ba-component in $(Ba, Sr)TiO_3$. Crosses and open circles show experimentally determined values. [134]

Also, the permittivity ϵ_r can be tuned by varying the composition of $(Ba, Sr)TiO_3$. At room temperature, it reaches its maximum of about 12,000 for $Ba_{0.7}Sr_{0.3}TiO_3$ single crystals. In thin films, however, the measured values for the permittivity are reduced to $\epsilon_r = 250 - 1000$ [135].

Despite the lower spontaneous polarization in $BaTiO_3$ single crystals of only $26 \mu C/cm^2$ and the weaker piezoelectric effect, $BaTiO_3$ was used in this work as a ferroelectric material. Its advantages compared to $PbZr_{0.52}Ti_{0.48}O_3$ are the smaller lattice mismatch (see Fig. 4.3), allowing for a thicker misfit-dislocation-free ferroelectric film and the chemical similarity to $SrTiO_3$. Since $SrTiO_3$ has already been successfully used as a barrier in manganite tunnel junctions [80, 136], it is likely that $BaTiO_3$ is a good choice for a ferroelectric tunnel barrier. In addition, $BaTiO_3$ does not contain any volatile elements, such as Pb in $Pb(Zr, Ti)O_3$ and, thus, the stoichiometry is more easily controlled.

According to Hartmann and coworkers [123], the barrier height of $SrRuO_3/(Ba, Sr)TiO_3$ is similar to that of $SrRuO_3/Pb(Zr, Ti)O_3$ of approximately 0.35 eV.

SrRuO₃

$SrRuO_3$ has been studied extensively and has become a widely used epitaxial electrode for perovskite ferroelectric materials. Single crystalline $SrRuO_3$ is a pseudo-cubic perovskite and a metallic conductor with a paramagnetic to ferromagnetic phase transition at 160 K [137]. Its work function is smaller than that of Pt of 5.3 eV [26]. It is 5.0 eV if $SrRuO_3$ is fully oxidized, and it is reduced to 4.6 eV in the case of oxygen deficiency [123]. Most reports on bulk materials indicate that its crystal structure is orthorhombic with lattice parameters of $a = 5.55 \text{ \AA}$, $b = 5.56 \text{ \AA}$, and $c = 7.84 \text{ \AA}$ [138, 139]. Three different phases have been found between 10 K and 1273 K [140, 141, 142]. Epitaxial thin films have been grown by sputtering [143], pulsed laser deposition [144, 145, 146], metal organic chemical vapor deposition [147], and molecular beam epitaxy [148, 149] on $SrTiO_3$ and $LaAlO_3$ substrates.

$SrRuO_3$ is an excellent electrode for the growth of a variety of ferroelectric materials, including $Pb(Zr, Ti)O_3$ and $BaTiO_3$. In addition to its perovskite crystal structure and pseudo-cubic lattice constant of 3.93 \AA [150], which provide excellent structural compatibility with these ferroelectrics, $SrRuO_3$ has been shown to significantly reduce fatigue in these materials [151] - an important advantage over metal electrodes [152].

SrTiO₃ (100) substrate

The choice of the substrate material is of great importance for the epitaxial growth of heterostructures. On the one hand, the growth of high-quality epitaxial materials requires substrates with structural and chemical compatibility to avoid structural defects, including dislocations, cracking, or even a complete loss of epitaxy, as well as interfacial reaction layers or interdiffusion of unwanted elements into the film. On the other hand, I have extensively discussed the influence of mechanical boundary conditions on the ferroelectric properties of thin films (Chap. 1.4). Strain induced by the much thicker substrate may alter the single crystal lattice parameters, shift the temperature of the paraelectric to ferroelectric phase transition, and even change the order of this phase transition in epitaxial thin films.

In view of the above mentioned considerations, (100)-oriented $SrTiO_3$ was chosen as substrate material. It represents an insulating and compressive substrate for the $SrRuO_3$ bottom electrode and the $Pb(Zr,Ti)O_3$ and $(Ba,Sr)TiO_3$ ferroelectric thin films. It thus allows for an epitaxial high-crystalline growth of these thin films and stabilizes the ferroelectric phase in the out-of-plane direction.

$SrTiO_3$ is a quantum paraelectric material that exhibits an increase in the dielectric constant as it is cooled [153]. It shows a structural phase transition to a tetragonal phase at 105 K [154]. Ferroelectricity in slightly off-stoichiometric $SrTi_xO_{3-\delta}$ has been demonstrated [155, 156, 157]. However, in pure $SrTiO_3$ crystals, the ferroelectric transition is not observed. Therefore, this compound is regarded as an incipient ferroelectric. It is expected, however, that the situation may change dramatically in $SrTiO_3$ epitaxial thin films. $SrTiO_3$ thin films grown on a sufficiently compressive or tensile substrate have been predicted to exhibit ferroelectricity at room temperature in the out-of-plane or in-plane direction, respectively [154].

4.2 Deposition techniques

Although significant time was spent to set up a high-pressure sputtering system and learning the complex growth techniques of molecular beam epitaxy, the description of these techniques will be brief. Additional information can be found in Refs. [158, 159].

A large variety of thin film deposition methods have been developed in the last decades. The choice of the best method is difficult and depends on the specific material to be grown on a specific substrate and the purpose of the deposited film. The deposition techniques can be divided into physical vapor deposition and chemical vapor deposition. Physical methods are characterized by a particle source and generally a free flight to the substrate. For chemical methods, so-called precursor molecules fill the reactor vessel as a vapor, dissociate at the hot substrate surface and release the atoms to be deposited [159].

One of the main differences between the different physical vapor deposition techniques is the mean free path of the atoms or molecules. This is the distance that a particle travels, on the average, before experiencing a collision. Assuming that gas atoms may be considered as non interacting with a Maxwell velocity distribution the mean free path $\bar{\lambda}$ of the atoms or molecules is obtained:

$$\bar{\lambda} = \frac{1}{\sqrt{2\pi}Nd^2} \quad (4.1)$$

where d is the molecular diameter and N the concentration of the gas [159]. Substituting N by the law of the ideal gas $N = p/k_B T$ yields

$$\bar{\lambda} = \frac{k_B T}{\sqrt{2\pi}pd^2}. \quad (4.2)$$

For instance, the mean free path at a typical growth temperature of 600°C in oxygen ($d = 370$ pm) is given by

$$\bar{\lambda} = \frac{1.98 \cdot 10^{-2}}{p [\text{mbar}]} \text{ cm}. \quad (4.3)$$

In the following Sections, the physical vapor deposition techniques used in this work will be described. High-pressure sputtered $SrRuO_3$ and $PbZr_{0.52}Ti_{0.48}O_3$ thin films, as well as $SrRuO_3$ and $BaTiO_3$ thin films by molecular beam epitaxy, were grown by the author himself, whereas pulsed laser deposited $BaTiO_3$ thin films were provided by J. Schubert and his group at ISG, Forschungszentrum Jülich.

Pulsed laser deposition

Pulsed laser deposition (PLD) is a physical vapor deposition technique allowing the growth of high-quality films with high growth rates (a typical growth rate is 1 nm/s). A sketch of the PLD-system is shown in Fig. 4.4 (a). A pulsed laser beam from an excimer laser² is focused onto a rotating target in a gas pressure environment of about 10^{-3} mbar. A plasma (Fig. 4.4 (b)) containing energetic neutral atoms, ions and molecules is formed as a result of the high energy density of $2-5 \text{ J/cm}^2$ at the target surface and reaches the substrate surface with a broad energy distribution of 0.1 eV to > 10 eV [159].

PLD has been used successfully to grow numerous perovskites exhibiting superconducting [160, 161] or ferroelectric properties [162]. For example, 1 μm thick $BaTiO_3$ films have been prepared by PLD for electro-optical applications [127]. These films grown on MgO substrates have been used for waveguides with low optical losses.

²for instance, KrF excimer laser with a wavelength of 248 nm and a repetition rate of 10 Hz

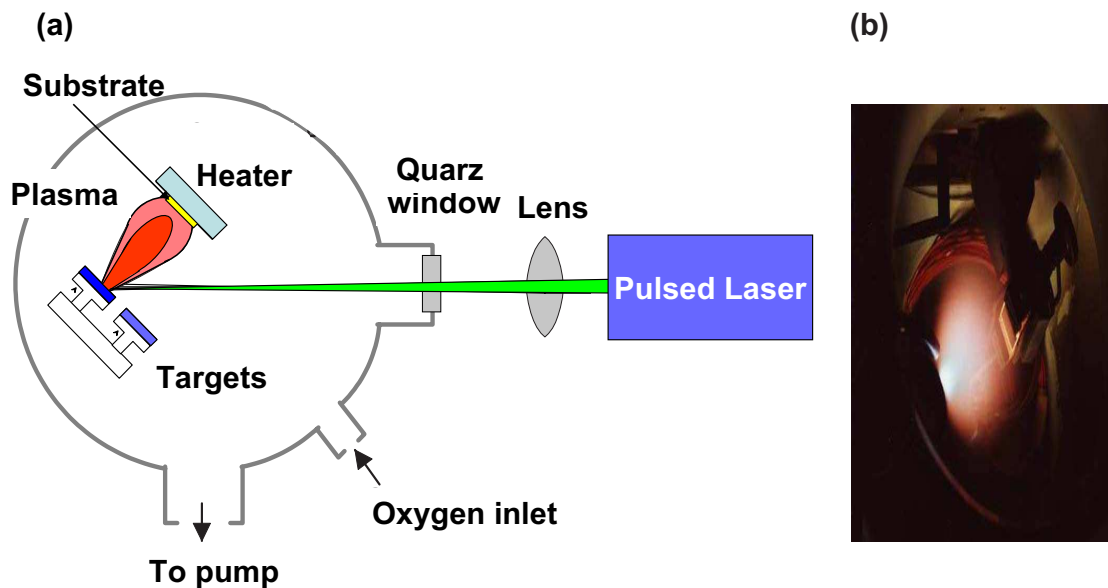


Figure 4.4: (a) Sketch of a PLD system. (b) Picture of a PLD plasma plume.

Molecular beam epitaxy

Molecular beam epitaxy (MBE) is a physical vapor deposition technique with demonstrated versatility and flexibility used to grow numerous complex compounds. The MBE technique relies on the thermal evaporation of elements from individual sources in a high vacuum environment ($10^{-6} - 10^{-9}$ mbar). A schematic view and a picture of the MBE system itself is shown in Fig. 4.5 (a) and (b), respectively.

MBE is used successfully for the growth of III-V compound semiconductors, such as *GaAs* and *InP*. The controlled synthesis of III-V materials is complicated due to the strongly different vapor pressure of the constituents. The separate control of the individual atomic species makes MBE an attractive choice to explore the growth of compounds [163].

Oxide MBE is relatively new. It was initially used for the growth of layered perovskite superconductors [164] after the discovery of high temperature superconductivity in oxides [165].

Its unique layering capabilities, able of depositing monolayers of several different elements in rapid succession, are superior to other thin film deposition techniques [167]. In addition, unlike single source sputtering and laser ablation, MBE does not require the fabrication of the desired compound.

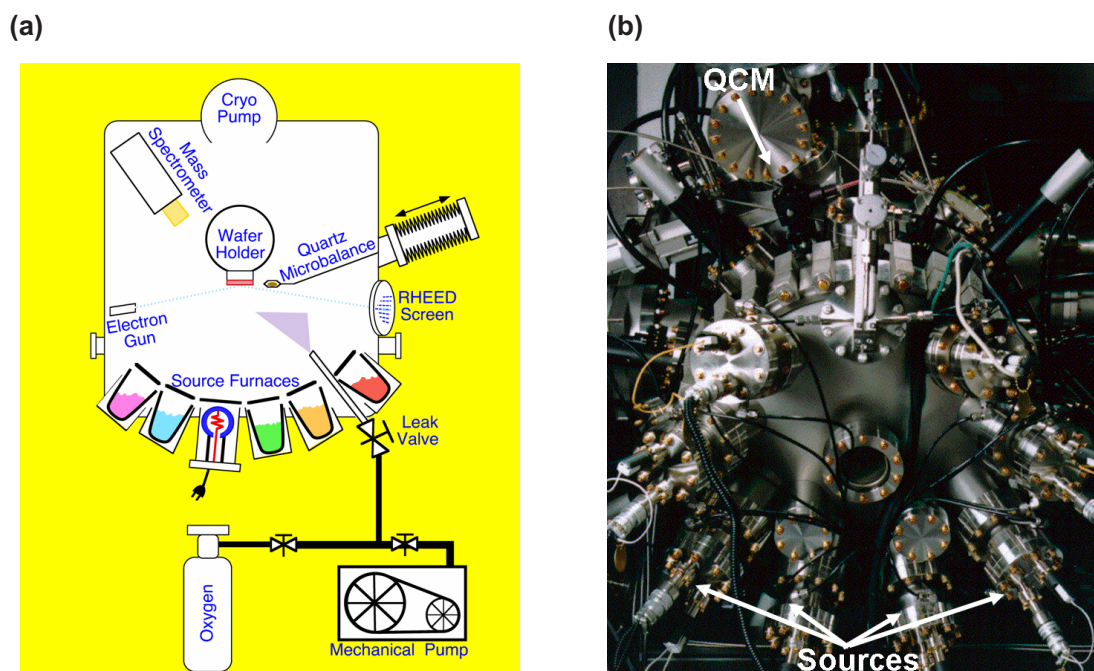


Figure 4.5: (a) Sketch of a MBE system [166]. (b) Picture of the Oxide-MBE system at The Pennsylvania State University.

Thus, the growth of many metastable compounds and structures that cannot be realized by bulk synthesis techniques can be achieved in a MBE system. The use of *in-situ* diagnostic tools, such as RHEED (see p. 64) and the UHV environment make MBE extremely attractive for interface and growth science.

Sputtering

Plasma sputtering is a physical vapor deposition technique known for 150 years, when W. R. Grove first observed the sputtering of surface atoms. Different sputtering techniques, such as dc- and rf-sputtering with or without a magnetron arrangement have been used to grow a variety of materials.

Fig. 4.6 (a) illustrates the principle of **dc-sputtering**. A potential of several 100 volts is applied between the target (cathode) and the heater (anode) accelerating positively charged ions towards the target. These accelerated particles sputter off the deposits, which finally arrive at the substrate. The discharge is maintained as the accelerated electrons continuously collide with the sputter gas ionizing new ions.

For insulating targets, such as ferroelectric targets, dc-sputtering is not suitable. Insulating targets have to be **rf-sputtered**. A frequency of typically 13.6 MHz is capacitively coupled to the target. A symmetrical arrangement of cathode and anode would result in similar sputtering and resputtering rates and no growth would be obtained. Therefore, non-symmetric conditions are introduced by the coupling of the rf and by the geometrical design of the target and the grounded heater and vacuum chamber.

In this work, high-pressure sputtering was used. The **high-pressure sputtering technique** of oxide materials was developed by U. Poppe [168] and served initially for the growth of oxide superconductors. A planar on-axis arrangement of target and substrate is used (Fig. 4.6 (b)). The high sputtering pressure of 2.5-3.5 mbar ($\bar{\lambda} = 6 \cdot 10^{-3}$ cm at 600°C), in comparison to 10^{-2} mbar ($\bar{\lambda} = 2$ cm at 600 °) used for conventional sputtering, leads to multiple scattering of the negatively charged oxygen ions accelerated towards the substrate. As a result of the thermalization of the charged ions, the resputtering of the deposited films, caused by negatively charged ions, is negligible. This technique yields excellent thin films due to the low kinetic energy of the deposits.

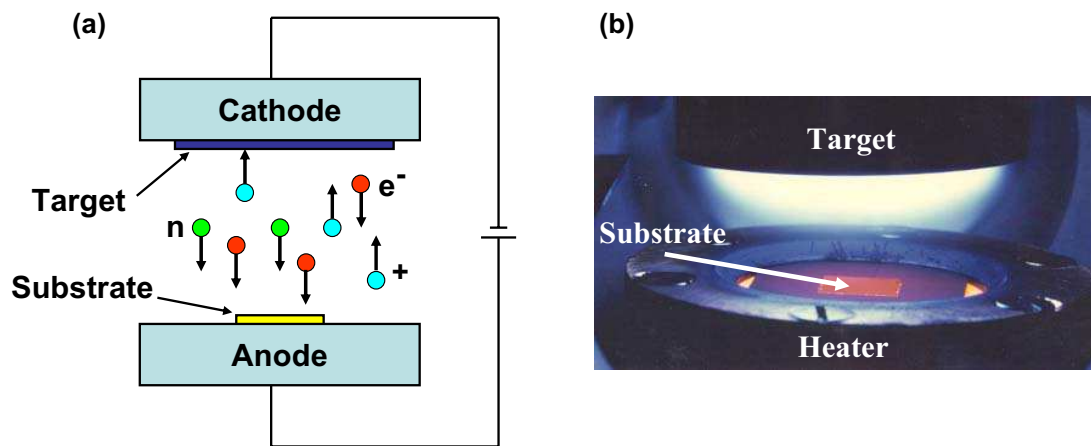


Figure 4.6: (a) Schematics of a DC-sputter system. Electrons (red), positive charged plasma ions (cyan) and neutral deposits (green) are shown. (b) Picture of a high-pressure sputtering system.

A disadvantage of the high-pressure sputtering technique might be the low deposition rate of some few nm per hour. To enhance the deposition rate, the

low ionization degree of less than 1 % of the atoms of a plasma is improved by use of magnetic fields forcing the electron onto helical paths close to the cathode, resulting in a much higher ionization probability. This so-called **magnetron sputtering** can be used for high-pressure sputtering [169], as well as for regular sputtering [170].

Chapter 5

Characterization techniques

The substantial progress in studying the ferroelectric limit has been achieved not only due to the advance in the understanding of boundary conditions, on the one hand, and improvements in the deposition techniques, on the other hand, but to a large extent on the capability of sophisticated analysis and characterization methods, too.

This Chapter provides a brief overview and description of the primary characterization tools used in this thesis. More information can be found in Refs. [171, 172, 173].

5.1 Structural characterization

Diffraction techniques are generally used to analyze the structural properties of crystals, powders and thin films. Different incident exciting probes, such as photons, electrons, or neutrons having different energies, are used to study the samples. This is partly due to the fact that in order to resolve the structural characteristics of a sample, the wavelength of the probing beam has to be in the same order of magnitude as the length scale of the structures under investigation. It is also partly due to the need of a strong interaction between probe and sample. For instance, magnetic properties are best investigated by neutrons, because of the strong interaction of magnetic fields with the magnetic moment of a neutron. The information is extracted from a change in energy, momentum, polarization or spin.

In this Chapter the most frequently used structural characterization techniques are presented.

X-ray diffraction

X-ray diffraction and reflectivity measurements provide information on the crystal structure, layer thickness (details can be found in Ref. [172]), surface roughness or, in case of a multilayer, the multilayer period and interface quality.

Within this work, studies of the crystallographic structure were performed by x-ray diffraction (XRD) measurements using a Philips *X'pert MRD* four-circle diffractometer with a copper x-ray tube (characteristic wavelength $\text{Cu-K}\alpha_1$, $\lambda = 0.15406 \text{ nm}$). For some few experiments a Picker four-circle diffractometer was used. Fig. 5.1 shows a schematic of the four-circle geometry. The detector (angle 2θ) and the sample (angle θ or ω) can be rotated independently in the axis perpendicular to the scattering plane, which is defined by the incident and diffracted beam. This enables probing of the crystalline planes in a film parallel to the substrate surface. The ϕ and ψ circles allow probing of reflections and planes that are not parallel to the surface of the substrate.

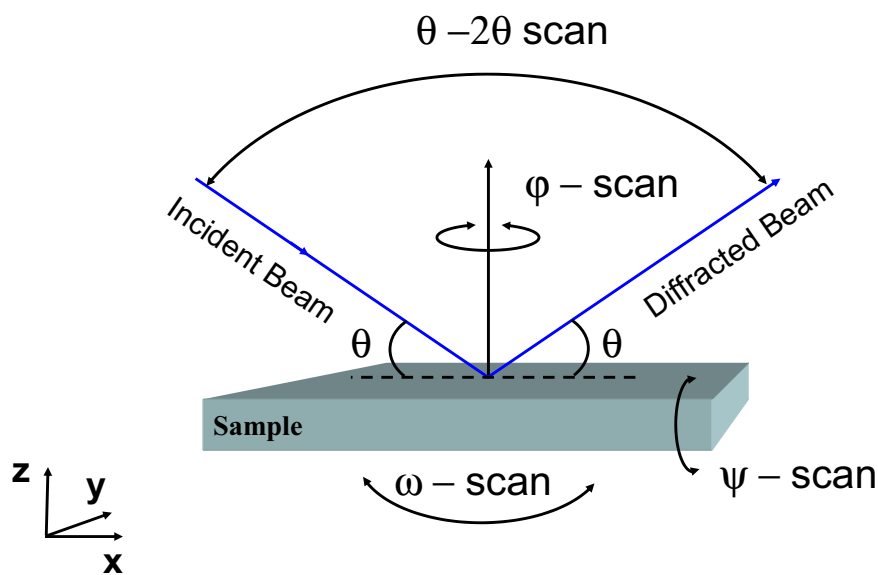


Figure 5.1: *Simplified illustration of the four-circle x-ray diffractometry.*

A x-ray beam¹ that impinge on the sample surface under the angle of

¹photons emitted by the anode of the x-ray tube with an energy characteristic for the anode material

incidence θ is elastically scattered by electrons. For a periodic structure, the constructive interference of the scattered probe results in sharp diffraction peaks at diffraction angles 2θ determined by the Bragg-condition [97]

$$2d \cdot \sin \theta = n\lambda \quad (n = 1, 2, 3, \dots) \quad (5.1)$$

where d is the distance between the atomic layer in a crystal and λ is the wavelength of the incident x-ray beam (Fig. 5.2). The out-of-plane lattice parameter (distance between the lattice planes parallel to the surface plane) can be determined by a θ - 2θ scan. If size effects are neglected, the full width at half maximum in 2θ (FWHM in 2θ) can be used as a measure of the spread in the distance between the lattice planes parallel to the surface plane.

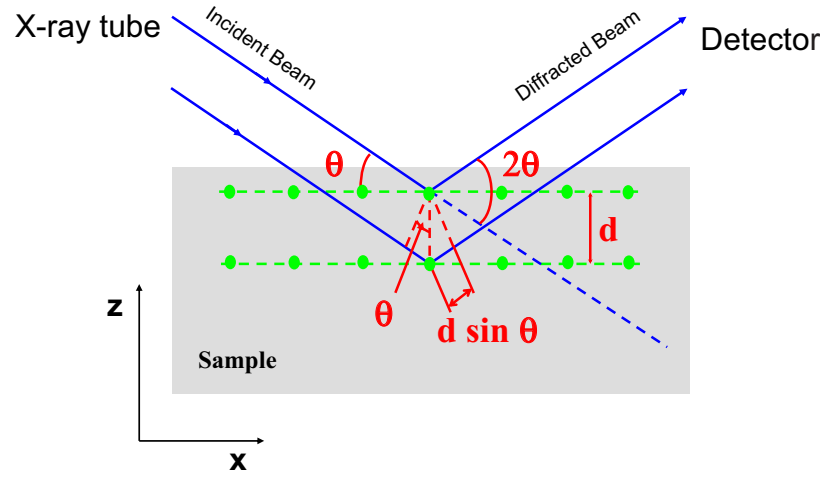


Figure 5.2: X-ray diffractometry in symmetrical reflection geometry.

The lattice parameters a , b and c of the unit cell and the Miller indices (hkl) can be determined from differently oriented grains using

$$\frac{1}{d_{hkl}^2} = \frac{h^2}{a^2} + \frac{k^2}{b^2} + \frac{l^2}{c^2}. \quad (5.2)$$

A direct determination of the in-plane lattice parameter in a $00l$ oriented thin film can only be performed in transmission geometry or in grazing angle geometry. The former geometry involves the thinning of the thick substrate, whereas the latter geometry requires the use of a synchrotron x-ray source because of the low intensity of the diffracted beam. Therefore, we chose to calculate the in-plane lattice length using the out-of-plane lattice parameter

and the (202) reflection² (measured at $\psi \approx 45^\circ$) of the corresponding thin film from the below written formula (obtained from eqn. (5.2) for a tetragonal system $a = b \neq c$)

$$a^2 = \frac{d_{hkl}^2(h^2 + k^2) \cdot c^2}{c^2 - d_{hkl}^2 l^2}. \quad (5.3)$$

The mosaic spread is a measure of the crystalline quality of a single-crystalline film. It usually involves the measurement of the variation in intensity of a simple Bragg reflection as the sample is rotated (ω and ϕ angle) and tilted (ψ angle). For a $00l$ oriented thin film the so-called rocking curve, or ω scan of a Bragg reflection, is performed to determine the spread and tilt of the film with respect to the substrate surface normal (Fig. 5.3 (a)). Here, the angles of sample and detector are first tuned to a Bragg-reflection angle. Next, the rocking curve is measured by rotating the angle θ , while the detector remains at a fixed position. For a single crystal, the intensity of the reflected beam approaches zero, when θ does not satisfy the Bragg-condition, but when the sample is composed by atomic layers that are not perfectly aligned to each other, a finite intensity is measured for $\theta \neq 2\theta/2$. Hence, the FWHM in ω provides a measure of the spread in the orientation of the atomic layers parallel to the substrate plane.

The thin film orientation in the substrate plane is investigated, recording ϕ scans of the substrate and thin film ($h0h$) reflections. An illustration of the spread of the atomic layer in the substrate plane is shown in Fig. 5.3 (b).

Reflective high energy electron diffraction

Reflective high energy electron diffraction (RHEED) is a real time, *in-situ* analysis technique [174, 175] for use in high-vacuum. This surface-sensitive, diffraction technique is characterized by its nonintrusive nature during crystal growth and its surface sensitivity. Typical RHEED geometry involves a beam of high energy (5-40 keV) electrons striking the surface of the sample at a low angle of incidence (1-3°) and diffracting toward a phosphorous detector screen. The diffracted electrons are detected as a diffraction pattern on a phosphor screen and are recorded by a CCD camera attached to the screen. Given the shallow angle of incidence and the energy of the impinging beam, the penetration depth of the electrons is low and RHEED is extremely surface

²In principle, every reflection containing an out-of-plane and in-plane contribution is suitable, however the sensitivity for the in-plane contribution increases for larger angles of ψ .

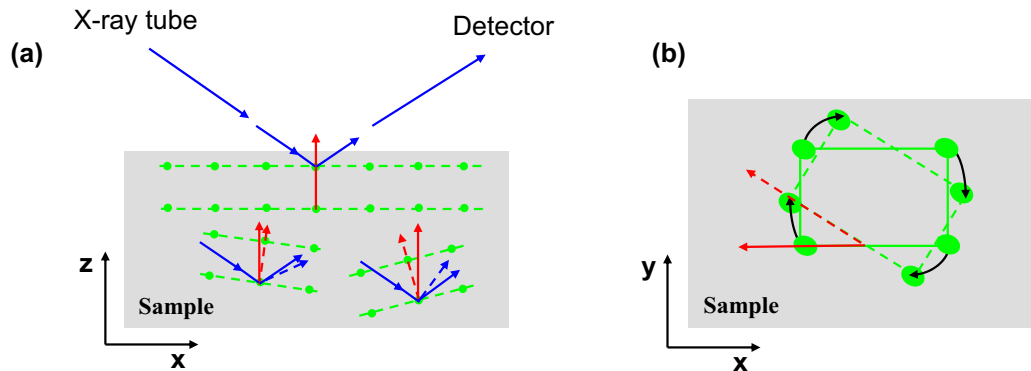


Figure 5.3: Illustration of the mosaic spread measured (a) by a rocking curve (ω scan) and (b) by a ϕ scan. In (a) the solid-line red arrow indicates the sample normal, whereas the dashed-line red arrows indicate the plane normal for the respective plane. In (b) the red arrows indicate the orientation of a plane that is for the actual angle ϕ in the scattering plane (solid line) and that is for an angle ϕ different from the actual one in the scattering plane (dashed line).

sensitive providing information on the top few monolayers of the deposited film. In addition, the small angle of incidence allows the monitoring of highly insulating oxide materials without the common charging problems associated with normal incidence electron probe techniques, such as low energy electron diffraction (LEED). Extensive information on the characteristics of the film surface can be obtained from a RHEED image, including its crystallinity, roughness, in-plane lattice constant, and phase purity. In addition, analysis of the RHEED intensity oscillations during growth can be used for composition and flux control. [167]

The radius of the Ewald sphere [97] is given by $r = \lambda^{-1}$ with λ being the wavelength of the probe beam. The wave length of x-rays is large compared to the wave length of the high energy electron beam used in RHEED. Thus, the Ewald sphere for x-rays is bent, whereas the Ewald sphere of the electron beam is almost flat. As a result, the Ewald sphere correspond to a given two-dimensional plane of the reciprocal lattice of the crystal. All points belonging to this plane will therefore appear in the electron diffraction [174, 163].

Kikuchi lines [176] appear on a diffraction pattern when the diffracting crystal is not too thin and when it is not so imperfect that the black and white lines are too blurred to be seen [171]. They are formed by electrons that have been diffusely scattered with some loss of energy [177]. Some of

these diffusely scattered electrons find themselves going in exactly the right directions to reflect from some planes in the crystal.

Rutherford backscattering spectrometry

Rutherford backscattering spectrometry (RBS) is a technique for determining stoichiometry, layer thickness, interface quality and crystalline perfection of a thin film.

In RBS, the sample is placed in front of a collimated beam of monoenergetic, low mass ions. For instance, within this work, the experiments were performed with 1.4 MeV He^+ ions. A small fraction of the ions that impinge on the sample are scattered back elastically by the nuclei of the atoms and are collected by a detector. The detector determines the energy of the backscattered ions, resulting in a energy spectrum - the so-called RBS spectrum.

In the *random* configuration (Fig. 5.4, left side) the sample is rotated to avoid the channeling of the He^+ beam. The energy transferred from a He^+ ion to the sample atom depends on the kinetic energy of incident ion and mass of the stationary sample atom. Energy loss, due to inelastic scattering by the electronic structure of the sample atoms, occurs for He^+ ions that penetrate deeper inside the sample. The energy of the ions collected in the detector, thus, provides information about the mass of sample atoms and the thickness of layers. In addition, information about the interface sharpness between two layers is obtained from the abruptness of the low energy edge of the energy interval for the respective sample atoms. Stoichiometry and layer thickness are obtained from the comparison of the so-called *random spectrum* (Fig. 5.4 (a)) with a simulation provided by the program RUMP [178].

The *channeling spectrum* is recorded without rotating the sample during the measurement (Fig. 5.4 (b)). Here, the sample is aligned to a low index crystal direction, allowing the beam to be guided by the atomic rows leading to a reduction of the probability of being backscattered. Defects inside the film will lead to scattering out of the *channeling* direction and a fraction of these ions will be backscattered and collected by the detector. A measure of the crystalline perfection of the sample is, therefore, the minimum yield χ_{min} . This is the minimum in the intensity ratio of *channeling* and *random spectra*.

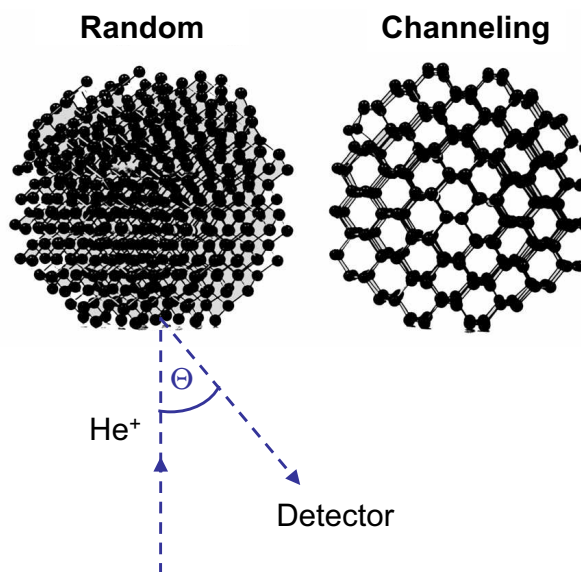


Figure 5.4: *Illustration of Rutherford backscattering spectrometry. Random (left side) and channeling (right side) experiments. [179]*

Atomic force microscopy

Scanning probe microscopy (SPM) is a fast developing technique that allows the surface analysis of thin films and single crystals with atomic resolution. A fine tip scans the surface of the sample. The interaction between surface and tip depends on the physical properties of the surface being investigated. A large family of SPM-related techniques have been developed to study various interactions between tip and surface arising from different physical properties. An overview can be found in Ref. [180].

The scanning probe technique used in this work is the atomic force microscopy (AFM)³ illustrated in Fig. 5.5. Here, a sharp tip positioned at a small distance from the sample scans the sample relative to the probing tip. The deflection of the cantilever as a function of lateral position is measured by means of a reflected laser beam striking a 4-quadrant photodiode, and it is subsequently visualized in a 3-dimensional surface image. Different scanning modes are used depending on sample properties and requested information. In the non-contact mode (distance between tip and sample surface greater than 1 nm), the tip-sample surface interactions involve van der Waals, electrostatic, magnetic or capillary forces. In the contact mode, ionic repulsion forces are dominant.

³AFM investigations presented in this work were performed by K. Szot, Forschungszen-

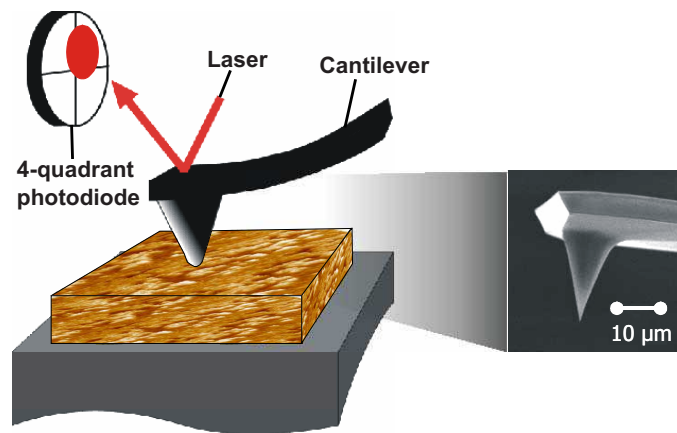


Figure 5.5: Schematic of the principle of atomic force microscopy [181].

High-resolution transmission electron microscopy

Transmission electron microscopy (TEM) and high-resolution TEM (HRTEM) yield extensive information on a variety of sample properties, such as morphology, structure at and near interfaces, density of defects inside the sample and lattice parameters. The samples have to be specially prepared for the measurements, which means that TEM is a destructive analyzing technique⁴.

5.2 Electrical characterization

In this Chapter the primarily used electrical characterization techniques are described.

Ferroelectric hysteresis measurement

The setup to measure ferroelectric hysteresis loops consisted of an aixACCT TF Analyzer 2000 with high-speed module and an oscilloscope Tektronix TDS220. The oscilloscope is used to increase the sampling rate and bandwidth necessary to perform measurements at high frequencies [182]. The aixACCT analyzer measures the hysteresis in the virtual ground mode. The frequency and voltage range provided by this commercially purchased system is 1 Hz - 250 kHz and 0 V - 13 V (23 V for frequency below 100 kHz).

trum Jülich.

⁴TEM and HRTEM measurements shown in this work were carried out by C. Jia, Forschungszentrum Jülich and W. Tian, University of Michigan.

The new software (Vers. 1.43) allows for an individually edited waveform. The typical waveform and excitation signal, however, used to measure a hysteresis is shown in Fig. 5.6 (a). The first pre-polarization pulse (black) establishes a defined negative relaxed polarization state P_{rel-} . This first pulse is followed by three bipolar pulses with a relaxation time t_D of 1 sec between the pulses. The current response, corresponding to the second and fourth pulse, is recorded and integrated to obtain the green and blue polarization loops shown in Fig. 5.6 (b). The second pulse (green) starts in P_{rel-} and cycles a complete hysteresis loop (green loop). The hysteresis loop of this second pulse ends in the negative remanent polarization state P_{r-} . The third pulse (black) establishes a positive relaxed polarization state P_{rel+} . Subsequently, the fourth pulse (blue) starts in the negative relaxed polarization state P_{rel+} and ends in the positive polarization state P_{r+} . Finally, the closed hysteresis loop plotted in red in Fig. 5.6 (b) is calculated from the second half of the second pulse and the second half of the fourth pulse.

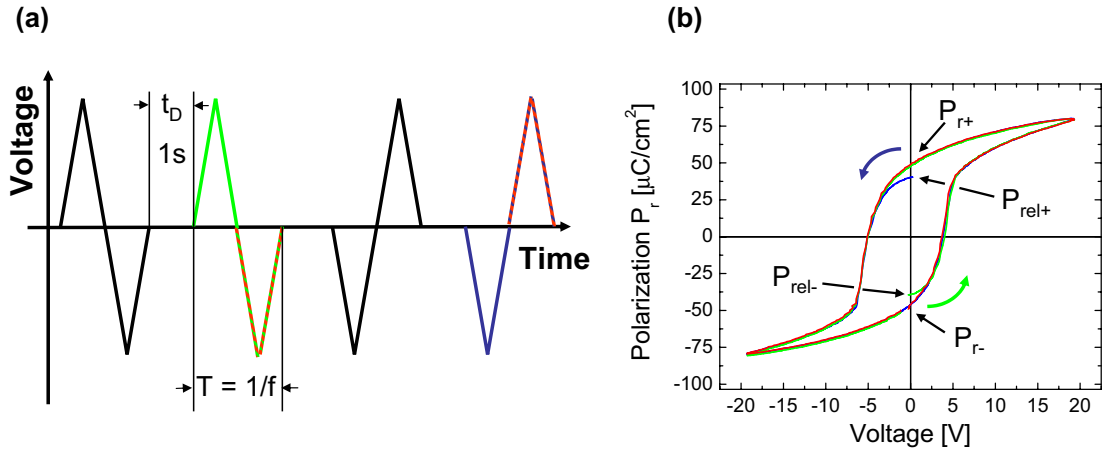


Figure 5.6: (a) Excitation signal for hysteresis measurement. (b) Typical hysteresis measurement graph indicating the starting point of pulse 2 (green) and pulse 4 (blue).

Ferroelectric fatigue measurement

One of the failure mechanisms of non-volatile ferroelectric memory devices is the loss in the remanent polarization as a function of cycles. This failure mechanism is called *fatigue*.

The same measurement setup is used as for the measurement of hysteresis loops. After measuring an initial hysteresis loop, the sample is cycled. This

cycling involves permanent polarization reversals with a frequency and voltage amplitude to be selected prior to measurement. The fatigue treatment is interrupted regularly for hysteresis measurements. Usually the remanent (or relaxed) polarization of the in between recorded hysteresis measurements is plotted as a function of the logarithm of the total number of fatigue cycles.

Current-voltage characteristic

I - V curves have been measured in a four-point arrangement to eliminate lead resistances. The fabrication process of the junctions will be described in Chapter 8. Most measurements shown here, have been recorded using a battery-powered current source. The voltage dependence of the dynamic conductance dI/dV was either simultaneously measured with a lock-in amplifier, or it was calculated from the I - V characteristic. Measurements in a temperature range from 4.2 K to 300 K have been performed in a continuous flow cryostat.

Part II

Experimental results

Chapter 6

Structural properties

All films grown by PLD, MBE and high-pressure sputtering were routinely characterized by XRD. RBS experiments have been carried out for most PLD and high-pressure sputtered thin films and for many MBE-grown films. AFM measurements were used to optimize the smoothness of the film surface. A few samples were investigated by HRTEM. The RHEED tool was only available in the MBE chamber.

6.1 Pulsed-laser-deposited $(Ba, Sr)TiO_3$ thin films

$BaTiO_3$ (BTO) and $Ba_{0.5}Sr_{0.5}TiO_3$ (BST) thin films were grown by PLD on $SrRuO_3/SrTiO_3$ substrates. The optimized growth temperature was 800°C and the oxygen growth pressure $2 \cdot 10^{-3}$ mbar for both, BTO and BST thin films. Details of the 100 nm thick high-pressure sputtered $SrRuO_3$ thin films are presented in Chap. 6.3.

XRD investigations were carried out and all films grown under optimized growth conditions were found to be single-crystalline having the c -axis oriented in the out-of-plane direction. $BaTiO_3$ and $Ba_{0.5}Sr_{0.5}TiO_3$ thin films have exact parallel orientations with the $SrTiO_3$ substrate ($[010]BTO/BST \parallel [010]SRO \parallel [010]STO$). $BaTiO_3$ shows an out-of-plane lattice parameter expansion for thinner films. The out-of-plane lattice parameter increases from 4.08 Å to 4.20 Å for thin films with a $BaTiO_3$ film thickness between 200 nm and 6 nm. The in-plane lattice parameter of 3.90 Å for the 6 nm thick film reveals that at least up to this thickness $BaTiO_3$ grows fully strained on the strained $SrRuO_3$ layer and the $SrTiO_3$ substrate. In contrast to $BaTiO_3$, the c -axis length of $Ba_{0.5}Sr_{0.5}TiO_3$ thin films is 4.01 Å for all investigated film thicknesses ranging from 25 nm to

200 nm. No data is available concerning the a -axis length of BST. Finally, the full width at half maximum (FWHM) in ω is small (BTO: 0.3° , BST: 0.1°) confirming the good quality of the PLD-grown thin films.

Fig. 6.1 shows **RBS** spectra and channeling measurements performed on (a) a 60 nm thick $BaTiO_3$ film and (b) a 56 nm thick $Ba_{0.5}Sr_{0.5}TiO_3$ film, both of them grown on $SrRuO_3/SrTiO_3$ substrates. The results are similar for all film thicknesses studied. A comparison with a simulation provided by RUMP [178] results in a Ba/Ti ratio of 1. The minimum yield value of 3% measured at the Ba-signal reveals the good crystalline quality of these films. RBS investigations on $Ba_{0.5}Sr_{0.5}TiO_3$ films confirm a stoichiometric growth and an excellent crystalline quality based on a minimum yield value of 0.4% measured at the Ba -signal.

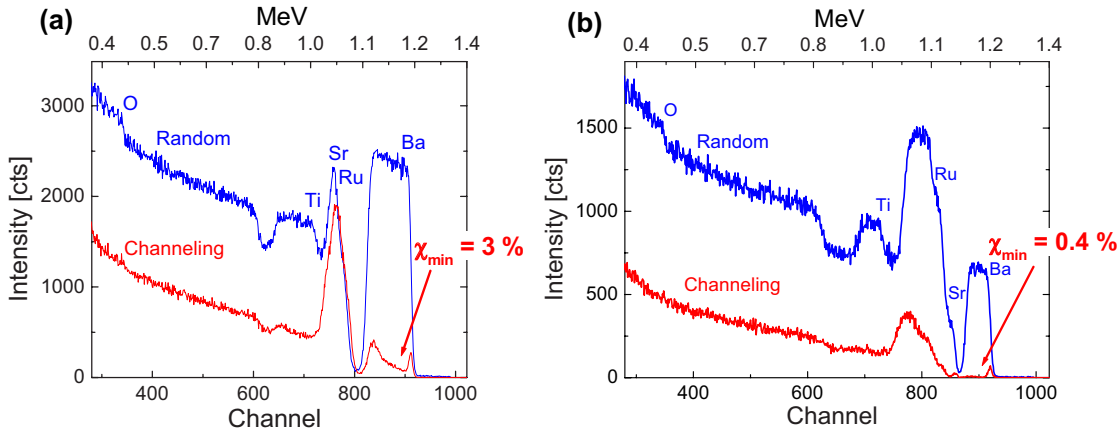


Figure 6.1: Rutherford backscattering spectrometry of (a) a 60 nm thick $BaTiO_3$ film and (b) a 56 nm thick $Ba_{0.5}Sr_{0.5}TiO_3$ film, both of them grown on $SrRuO_3/SrTiO_3(100)$ substrates.

AFM measurements were performed on an area of $1 \times 1 \mu m^2$ to investigate the surface roughness (see Fig. 6.2). The measured root mean square (rms) roughness of 3 Å on both a 60 nm thick $BaTiO_3$ and a $Ba_{0.5}Sr_{0.5}TiO_3$ thin film of similar thickness is only slightly larger than the surface roughness of the commercially purchased $SrTiO_3(100)$ substrates.

HRTEMs of a 10 nm thick $BaTiO_3$ film sandwiched between $SrRuO_3$ thin films reveal a Ruddlesden-Popper type planar fault at the lower interface. Figure 6.3 (a) shows a low magnification image of the film system viewed along the $[110]$ direction of $BaTiO_3$. At the lower interface, as in-

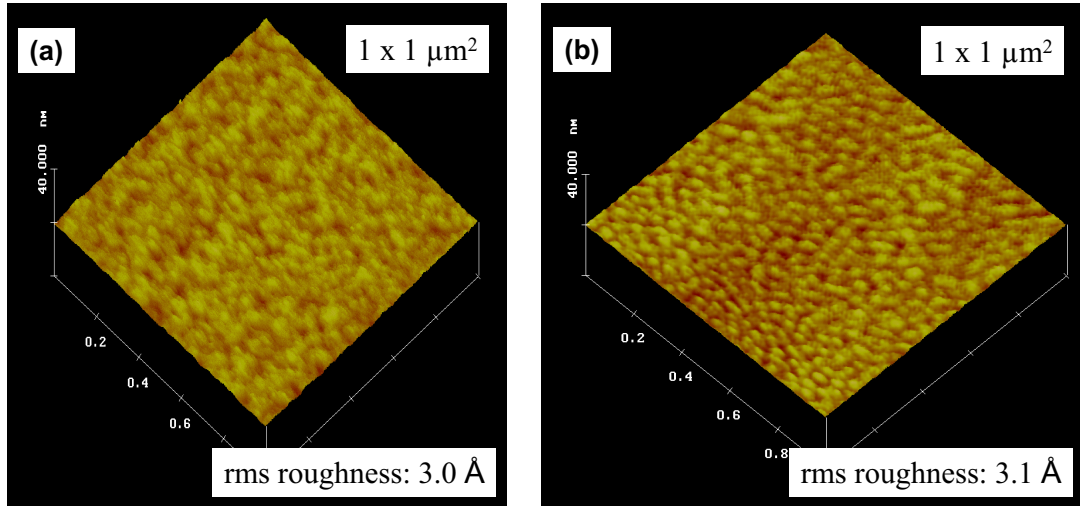


Figure 6.2: Atomic force microscopy of (a) a 60 nm thick $BaTiO_3$ film and (b) a 56 nm thick $Ba_{0.5}Sr_{0.5}TiO_3$ film, both of them grown on $SrRuO_3/SrTiO_3(100)$ substrates.

indicated by a horizontal arrow, a bright fringe occurs. Figure 6.3 (b) shows a cross-sectional $[110]$ high-resolution image of the interfacial defect. The defect can be recognized by a local lattice expansion. A double row of dots of about equal contrast is found corresponding to SrO columns, meeting each other as denoted by a pair of black arrows. The Ruddlesden-Popper fault occurs on the side of small spacing, i.e. in the $SrRuO_3$ layer. We attribute the formation of the Ruddlesden-Popper fault to the growth conditions of the $BaTiO_3$ layer. Both $SrRuO_3$ layer were high-pressure sputtered and no stacking fault whatsoever was observed for similar heterostructures with $Pb(Zr, Ti)O_3$ intermediate layer. It is thus likely that decomposition takes place during the exposure to the higher-temperature and lower oxygen pressure conditions in the PLD chamber. Indeed, RHEED observations (see Chap. 6.2, p. 77) indicate that RuO_2 easily evaporates from the $SrRuO_3$ surface and surface-near region. Based on this knowledge, a SrO double layer is possible. A more detailed analysis is given in [183].

As indicated by a thick arrow in Fig. 6.3 (a), occasionally interface steps occur. These in turn give rise to the formation of nanotwins or other defects in the $BaTiO_3$ layer. Residual epitaxial strain was detected in all three film layers by electron diffraction analysis. The strain in the $BaTiO_3$ device layer is found to be particularly strong. The lattice parameters obtained by

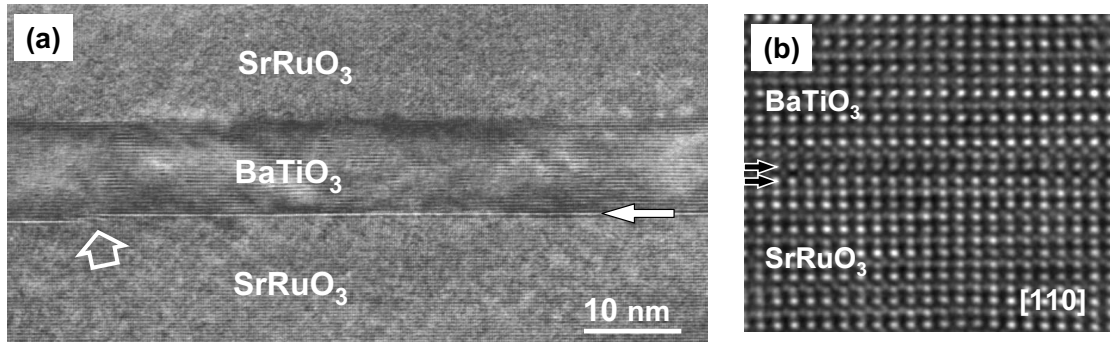


Figure 6.3: High-resolution TEM of a 10 nm thick $BaTiO_3$ film sandwiched between $SrRuO_3$ thin films grown on a $SrTiO_3(100)$ substrate. [183]

HRTEM are consistent with the data obtained by XRD. While no misfit dislocations were found in the lower interface area, dislocations were observed in the upper part of the $BaTiO_3$ layer giving rise to a partial relaxation of the $BaTiO_3$ thin film.

A strain-induced shift of the paraelectric to ferroelectric phase transition temperature resulting from a two-dimensional clamping of the substrate will be demonstrated using pulsed-laser-ablated BST thin films in Chap. 7.2, p. 106. The thickness dependence of ferroelectric properties for PLD-grown BTO films will be studied in Chap. 7.3, p. 108. In addition, the electrical characterization of ultrathin BTO films with a film thickness of 6 nm will be discussed in Chapter 8.

6.2 Molecular beam epitaxy of $SrRuO_3$ and $BaTiO_3$ thin films

Single crystalline $SrRuO_3$ and $BaTiO_3$ thin films were grown by MBE on $SrTiO_3(100)$ substrates. All $SrRuO_3$ thin films were grown 100 nm thick. The thickness of $BaTiO_3$ thin films varied between 2 nm and 100 nm. The $SrTiO_3$ substrates were etched prior to deposition based on the procedure developed by Masashi Kawasaki [184] and modified by Ivan Bozovic [185]. The etch procedure yields smooth TiO_2 -terminated $SrTiO_3$ surfaces. In addition, $SrRuO_3$ thin films were grown on lattice-matched $DyScO_3$.

The growth of $SrRuO_3$ was particularly challenging. Due to the high evaporation temperature of Ruthenium, e-beam evaporation was used. The

ruthenium flux demonstrated significant drift during deposition. Nevertheless, a successful growth of $SrRuO_3$ was possible because Ru or RuO_2 evaporates easily from the sample surface [186, 187, 188]. By growing $SrRuO_3$ using a layer-by-layer technique with a slight Ru -excess flux, a stoichiometric growth was achieved. Specific features in the RHEED pattern were used to identify large Ru -excess. The Ru -flux could be adjusted during the deposition by modifying the opening time of the Ru shutter, the e-beam current and by manually adjusting the e-beam spot (see Fig. 6.4).

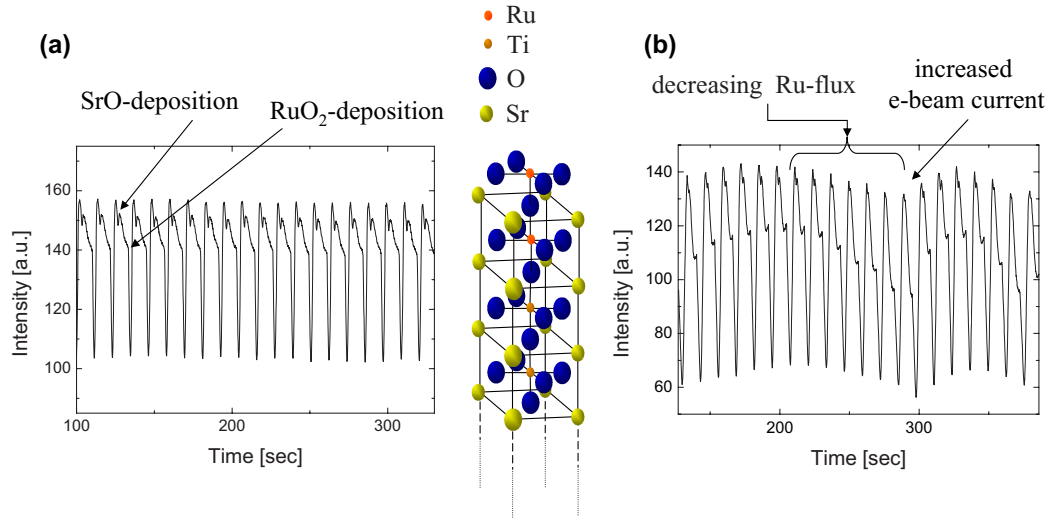


Figure 6.4: RHEED oscillations monitoring the specular spot of the $[100]$ azimuth. (a) Stable Ru -flux, (b) unstable Ru -flux. The sketch in the center schematically shows the $SrRuO_3/SrTiO_3$ heterostructure.

MBE-grown $SrRuO_3$ on $SrTiO_3$ substrates

$SrRuO_3$ thin films grown fully strained on $SrTiO_3$ (100) substrates adopt their a -axis lattice parameter of 3.895 \AA . If in first approximation a constant cell volume is assumed, a c -axis length of 3.95 \AA is expected. A significantly larger c -axis resulting in a larger cell volume is indicative of non-stoichiometry or the introduction of defects. The **XRD** measurements show that the expected out-of-plane lattice parameter is reached only for the highest investigated growth pressure of $5 \times 10^{-6} \text{ torr}^1$ in an $O_2/(10\%)O_3$ mixture.

¹All growth pressures used for the growth by MBE are given in torr, as this was the pressure unit used at PennState University. Nevertheless, the author is aware of the fact that torr is not a SI unit. To calculate the growth pressure in mbar the following relation is useful: $1000 \text{ mbar} = 760 \text{ torr}$.

The growth pressure and growth temperature were limited due to limitations of the heater that was used, and the threat of oxidizing the sources inside the chamber. An annealing of the samples after growth did not show any improvement, i.e. a smaller c -axis length. As can be seen from Fig. 6.5 (a), at a given growth pressure the c -axis lattice parameter gets closer to the desired value when ozone (10 %) is added to oxygen (solid blue line). A lower growth temperature also decreases the c -axis length, however, at the same time the full width at half maximum (FWHM) in ω increases (red lines). At a given growth temperature the c -axis length decreases for higher growth pressures, but at the same time again the FWHM in ω increases (see Fig. 6.5 (b)).

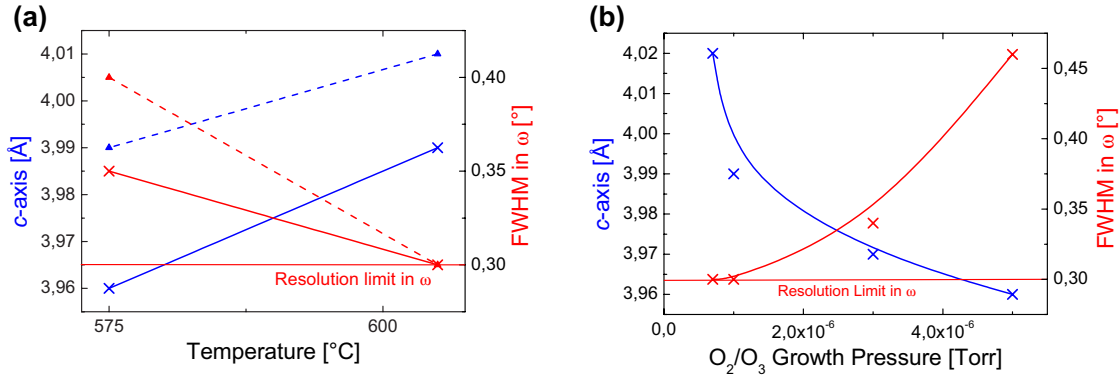


Figure 6.5: Results from XRD measurements on MBE-grown $SrRuO_3$ thin films. In (a) the temperature dependence for the growth in pure O_2 (dashed line) and in an O_2/O_3 mixture (solid line) at a growth pressure of 1×10^{-6} torr is shown. In (b) the O_2/O_3 mixture growth pressure dependence of the c -axis length and the FWHM in ω at 605 °C. Note that these XRD measurements were performed with a Picker four-circle diffractometer with a resolution limit in ω of 0.3° .

These results demonstrate the need for growth in an O_2/O_3 mixture at a growth pressure and temperature above the range investigated here in order to grow fully strained (and defect-free) $SrRuO_3$ thin films on $SrTiO_3$ (100) substrates with an out-of-plane lattice parameter of 3.95 Å and a low FWHM in ω .

The **RHEED** patterns shown in Fig. 6.6 confirm the increasing crystalline quality of the MBE-grown $SrRuO_3$ thin films for higher growth pressures. All pictures were taken after the growth of 100 nm thick films. The O_2/O_3 mixture growth pressure increases from the left to the right starting at 7×10^{-7} torr and ending at 5×10^{-6} torr. All thin films were grown at 605 °C.

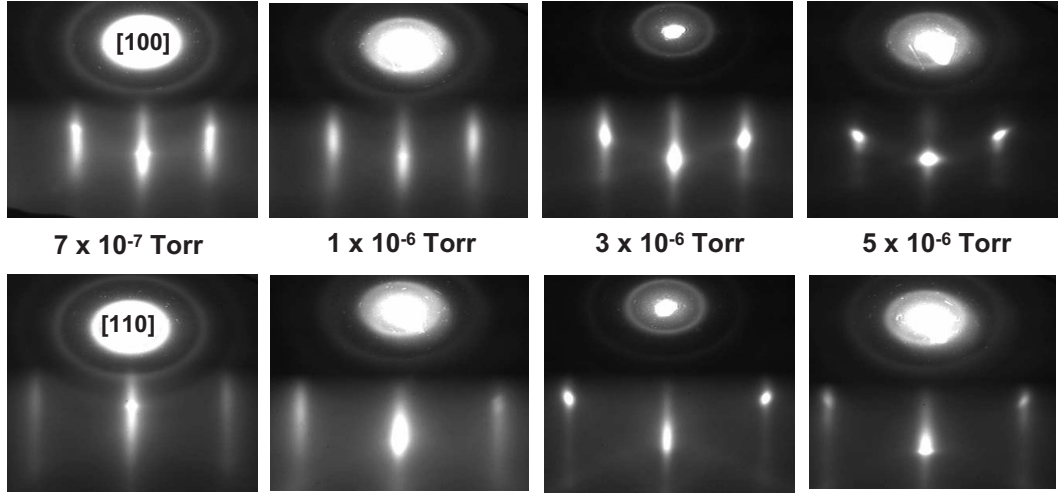


Figure 6.6: RHEED patterns of 100 nm thick $SrRuO_3$ films grown by MBE at $605^\circ C$ in an O_2/O_3 mixture. The upper and lower patterns show the $[100]$ and $[110]$ azimuth patterns, respectively.

RBS channeling experiments are consistent with XRD and RHEED results. The minimum yield χ_{min} decreases from 13% at growth pressures of 7×10^{-7} torr to 2.5% at 5×10^{-6} torr (Fig. 6.7).

AFM measurements demonstrate that $SrRuO_3$ thin films grown at stable Ru -flux have smooth surfaces. Fig. 6.8 shows a 3-dimensional illustration of the surface of a 100 nm thick $SrRuO_3$ film. The root mean square roughness is only 2.4 Å on an area of $5 \times 5 \mu m^2$ in size.

The metallic behavior of the temperature dependence of the resistivity is shown in Fig. 6.9 for various growth pressures. The resistivity decreases for higher O_2/O_3 pressures. The best value of $450 \mu C/cm^2$ at room temperature is obtained for the highest growth pressure of 5×10^{-6} torr. A kink in the $\rho(T)$ -curve is observable at the ferromagnetic-to-paramagnetic phase transition. The phase transition occurs at about 142 K for the film grown at 5×10^{-6} torr. This smaller value compared to bulk (see Chap. 4.1) could be due to a Ru -deficiency [187].

MBE-grown $SrRuO_3$ on lattice-matched $DyScO_3$

$DyScO_3$ is a novel substrate made by IKZ (Institut für Kristallzüchtung, Berlin). We report on the first results on $SrRuO_3$ thin films grown on

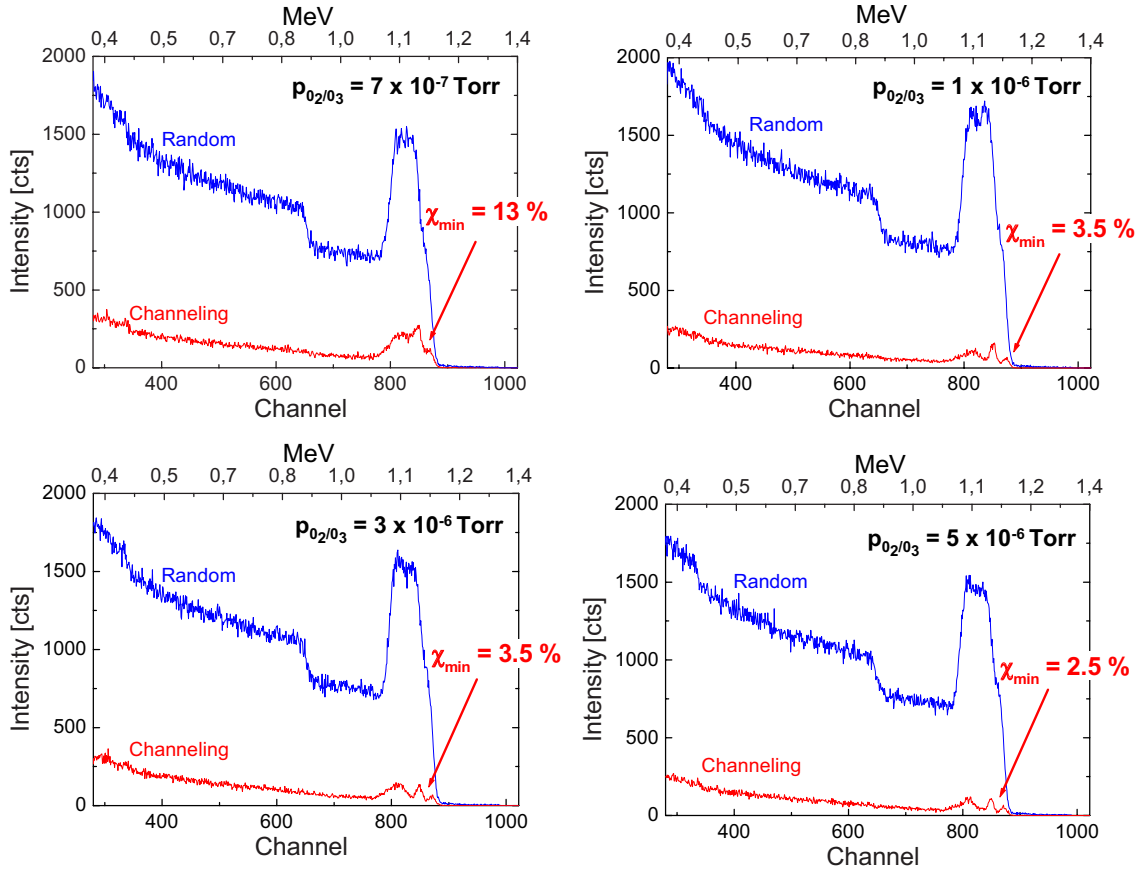


Figure 6.7: RBS random and channeling experiments of 100 nm thick $SrRuO_3$ films grown by MBE at several growth pressures at 605°C in an O_2/O_3 mixture.

$DyScO_3$ substrates. $SrRuO_3$ thin films were grown at 605°C and 3×10^{-6} torr in an O_2/O_3 mixture.

$SrRuO_3$ grown on $DyScO_3$ substrate is an almost perfectly lattice-matched heterostructure. Their pseudo-cubic lattice constants are 3.93 Å and 3.94 Å, respectively. $DyScO_3$ does not undergo a phase transition between 1000°C and room temperature and was found to have a similar thermal expansion to other oxide perovskites (e.g. $BaTiO_3$, $SrRuO_3$ or $SrTiO_3$), with an average thermal expansion of 8.4 ppm/°C [189]. The idea is to grow $BaTiO_3$ thin films on $SrRuO_3/DyScO_3$. The smaller lattice mismatch of this heterostructure compared to $BaTiO_3$ thin films grown on $SrRuO_3/SrTiO_3$ substrates should introduce less misfit-strain in the $BaTiO_3$ thin films. The critical film thickness for strain-relief via introduction of misfit dislocations

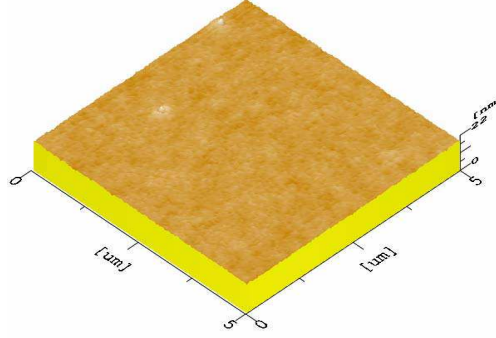


Figure 6.8: 3-dimensional AFM illustration of a 100 nm thick $SrRuO_3$ film grown by MBE. The root mean square roughness is 1.8 Å and 2.4 Å on areas $1 \times 1 \mu m^2$ and $5 \times 5 \mu m^2$ in size, respectively.

will be shifted to thicker films. As a result, the growth of thicker, fully strained and dislocation-free $BaTiO_3$ thin films should be achievable.

XRD measurements confirm the excellent lattice match between $SrRuO_3$ and $DyScO_3$. Fig. 6.10 (a) shows a theta-2theta scan. No peak separation for $SrRuO_3$ and $DyScO_3$ was observed for the pseudo-cubic [150] (001), (002) and (003) reflexes. A magnification of the pseudo-cubic (004) reflexes is shown in Fig. 6.10 (b). Here, four peaks are visible corresponding to the $K\alpha_1$ and $K\alpha_2$ reflexes of $SrRuO_3$ and $DyScO_3$. These reflexes correspond to out-of-plane lattice parameters of 3.937 Å and 3.945 Å. The higher inten-

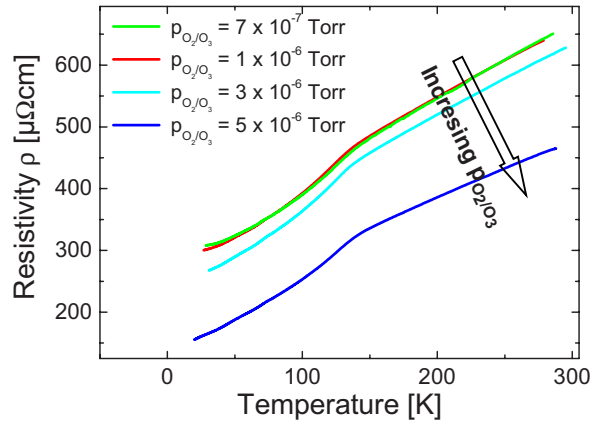


Figure 6.9: Growth pressure dependence of the resistivity for 100 nm thick $SrRuO_3$ films grown by MBE at 605°C for several growth pressures in an O_2/O_3 mixture.

sity suggests the former length to correspond to the much thicker $DyScO_3$ substrate and the latter to the MBE-grown $SrRuO_3$ thin film. The FWHM in ω (Fig. 6.10 (c)) for both materials is below 0.05° , which is the resolution limit of the x-ray diffractometer that was used.

Fig. 6.11 shows the **RHEED** patterns for various azimuths (in orthorhombic and pseudo-cubic notation) of the as-delivered $DyScO_3$ substrate.

The **RHEED** patterns of the $[100]$ azimuth (in pseudo-cubic notation) before, during and after growth are shown in Fig. 6.12. In addition, a picture of the pseudo-cubic $[110]$ azimuth taken after growth is included. The nice RHEED pattern after growth including Kikuchi lines indicate an excellent crystalline quality and a smooth surface.

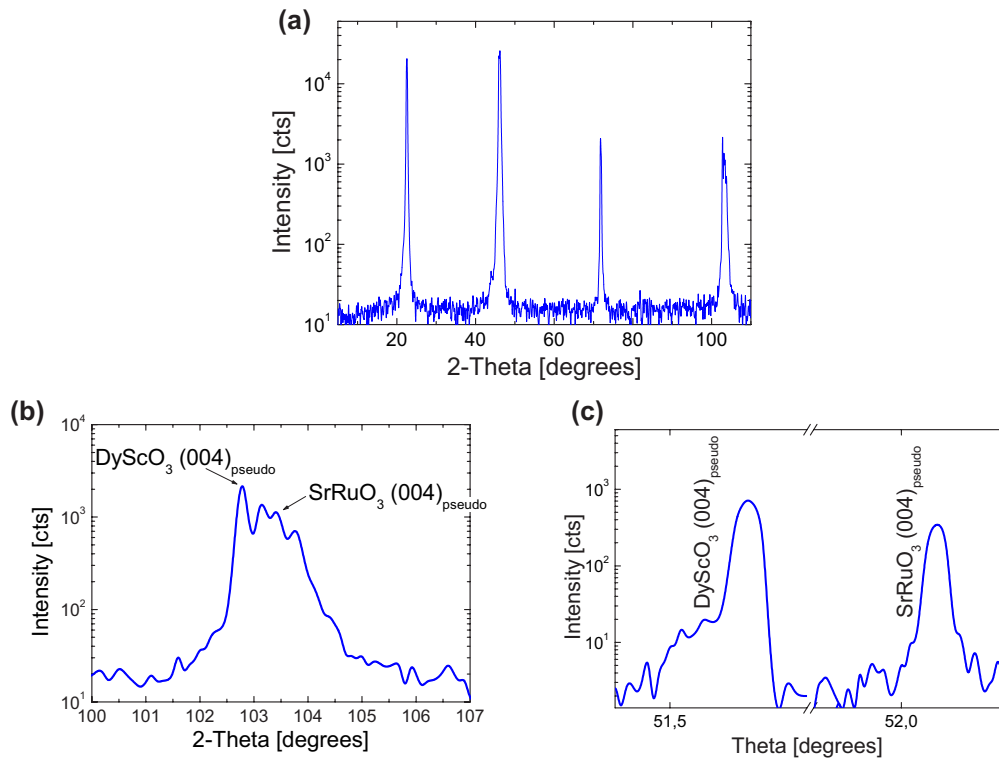


Figure 6.10: XRD measurements of a 100 nm thick $SrRuO_3$ film grown by MBE on a $DyScO_3$ substrate. (a) A theta-2theta scan, including (b) a magnification of the pseudo-cubic (004) peaks and (c) the rocking curves for the separated peaks shown in (b) are displayed.

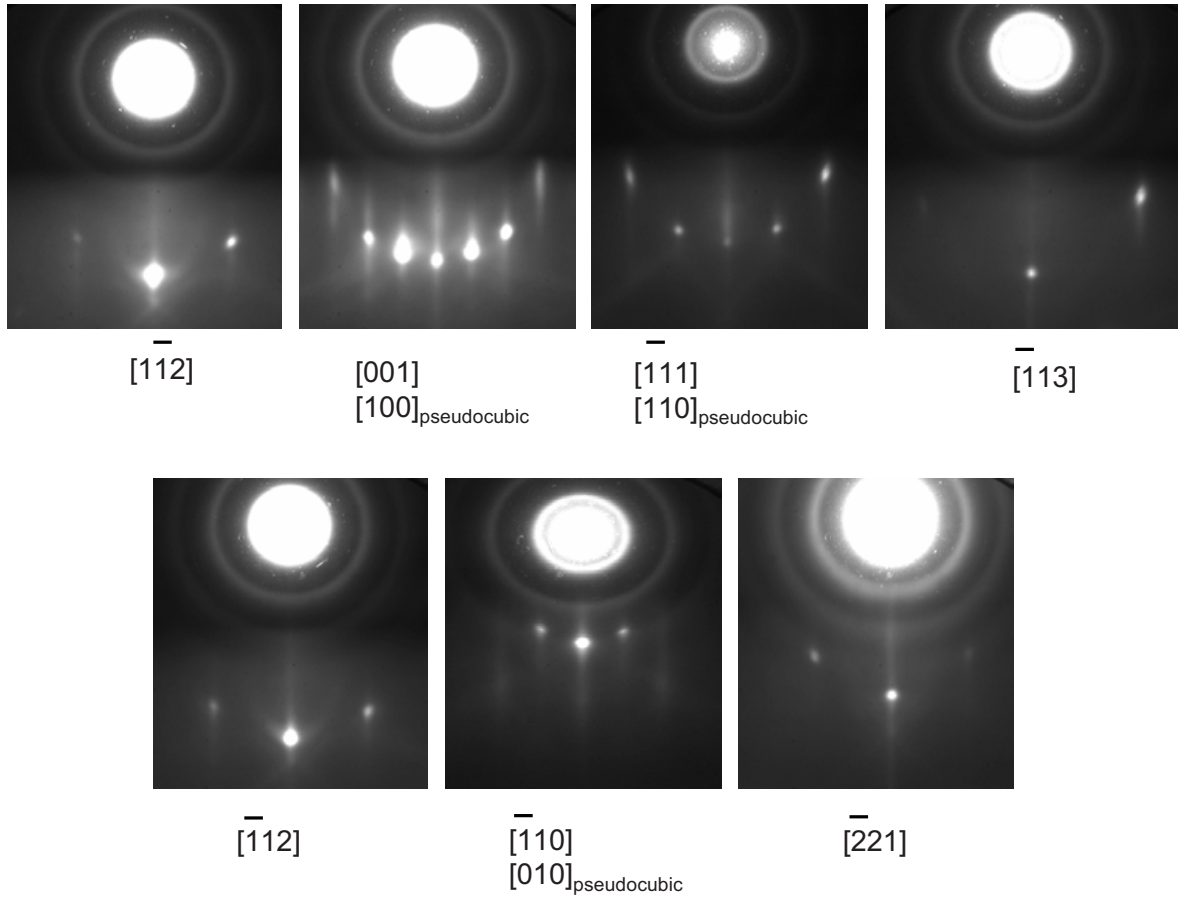


Figure 6.11: RHEED pattern for various azimuths of an as-delivered $DyScO_3$ substrate.

No conclusive results can be drawn from the **RBS** channeling experiments due to an overlap of the film signals with the Dy -signal from the substrate.

The 3-dimensional **AFM** illustration shown in Fig. 6.13 reveals some roughness. The root mean square roughness for this $1 \times 1 \mu m^2$ area is 3.7 \AA . This contradicts the smoothness indicated by the RHEED pattern after growth. Kikuchi lines, as visible in the RHEED-patterns after growth for both the $[100]$ and $[110]$ azimuth, are clearly indicative of a smooth surface. Therefore, we believe that the volatile Ru or RuO_2 was evaporated from the surface layers while cooling the sample or a chemical reaction occurred after removing the sample from the chamber and exposing it to air.

HRTEM investigations carried out by W. Tian, a member of the group

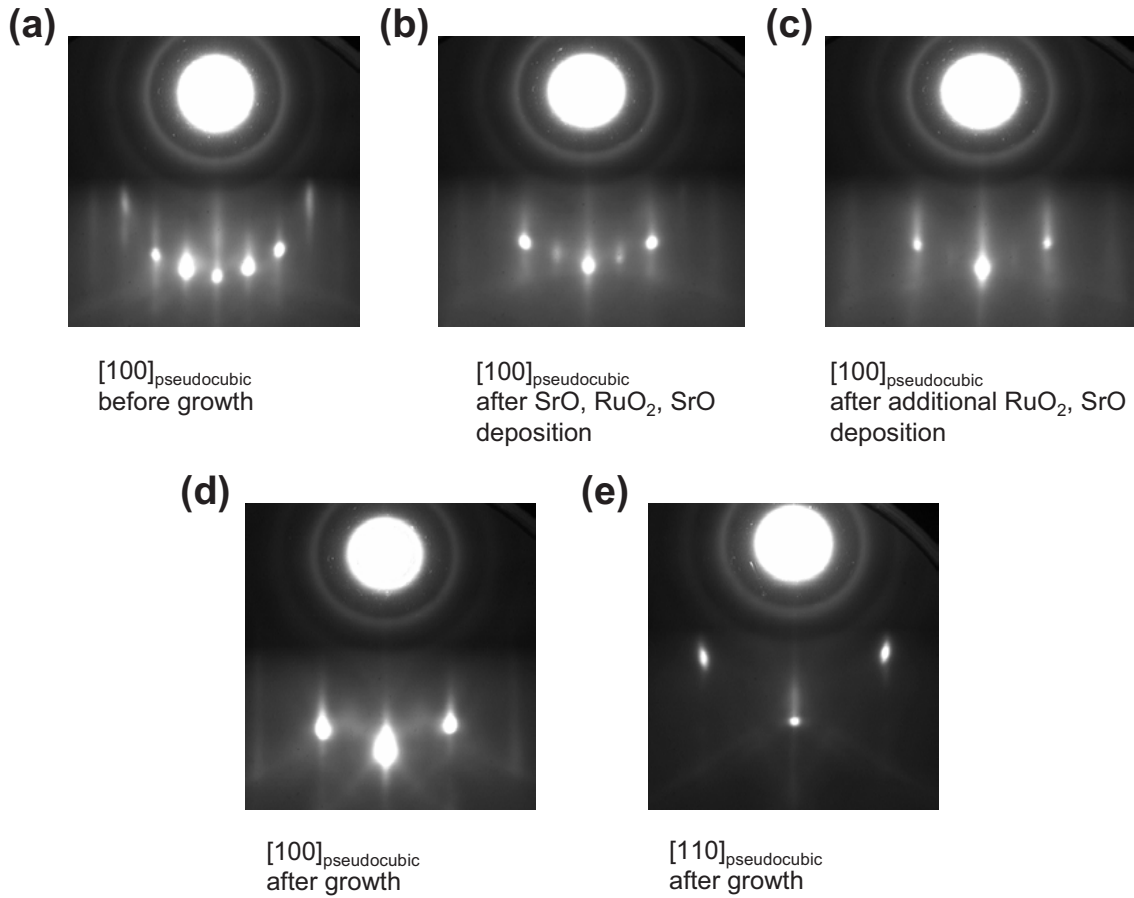


Figure 6.12: RHEED patterns before, during and after the growth of $SrRuO_3$ on a $DyScO_3$ substrate.

of X. Pan, University of Michigan, reveal a clean and atomically-abrupt interface (Fig. 6.14 (a)). No defects are observable in high-resolution TEM. Figures 6.14 (b) and (c) are $[111]$ zone axis selected-area electron diffraction (SAED) patterns taken from the film and substrate with the incident electron beam along the same direction. The epitaxial orientation relationship between the film and the underlying substrate was identified as $SrRuO_3 (1\bar{1}0)[111] \parallel DyScO_3 (1\bar{1}0)[111]$. A careful scan throughout the entire TEM specimen reveals that the film is untwined and single domain.

In summary, $SrRuO_3$ was successfully grown on a novel substrate material, $DyScO_3$, providing a perfect lattice match. Only a few substrates were available so that no optimization could be carried out. Nevertheless,

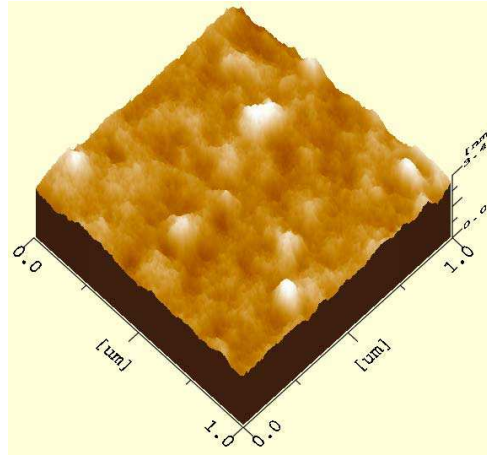


Figure 6.13: AFM picture of a $SrRuO_3$ film grown on $DyScO_3$ substrate. The rms roughness on this $1 \times 1 \mu m^2$ sized area is 3.7 \AA .

an excellent crystalline quality of $SrRuO_3$ thin films grown on $DyScO_3$ substrates was achieved according to XRD, RHEED and HRTEM investigations. HRTEM investigations reveal a twin-free and single domain growth. These first results make further investigations very promising with the aim of studying the effect of the smaller lattice mismatch on the critical thickness of e.g. $BaTiO_3$ films.

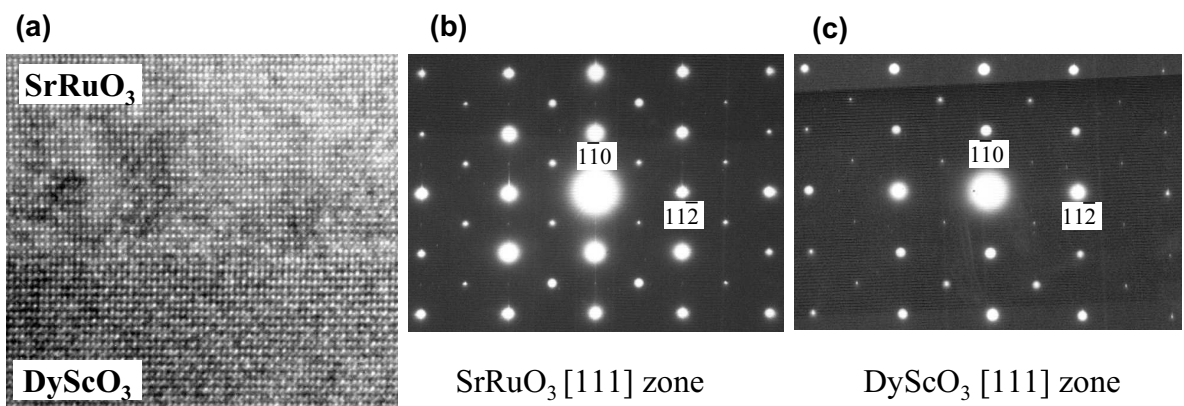


Figure 6.14: (a) HRTEM image of the $SrRuO_3/DyScO_3$ interface along the $[110]$ direction. $[111]$ zone axis selected-area electron diffraction (SAED) pattern taken from the (b) $SrRuO_3$ film and (c) $DyScO_3$ substrate.

Layer-by-layer and codeposition growth of $BaTiO_3$

$BaTiO_3$ thin films were grown on $SrTiO_3$ substrates using two different growth techniques, known as layer-by-layer and codeposition. The layer-by-layer growth technique was used for $SrRuO_3$ as well. Here, a sequence of monolayers (i.e. BaO , TiO_2 , BaO , ...) is deposited. For codeposition growth the fluxes of the different elements are adjusted to each other prior to deposition and the monolayers are obtained by reorientation of the atoms on the substrate stimulated by thermal and kinetic energies. The optimized growth conditions were 650°C and 5×10^{-6} torr O_2/O_3 for growth temperature and growth pressure, respectively.

In summary, no significant difference was observed between 60 nm thick $BaTiO_3$ films deposited either by the layer-by-layer or codeposition technique. $BaTiO_3$ thin films grown by layer-by-layer and codeposition show an excellent crystalline quality (channeling minimum yield $\chi_{min} = 1.3$ %) a slightly increased out-of-plane lattice parameter (4.08 Å) and a partially relaxed in-plane lattice parameter (3.96 Å). The $BaTiO_3$ layer grows on $SrTiO_3$ substrates without distortion ($BaTiO_3(220) \parallel SrTiO_3(220)$). For both growth techniques, the FWHM is 0.4° and 0.8° in ω and in ϕ , respectively.

MBE-grown $BaTiO_3$ on $SrRuO_3/SrTiO_3$ substrates

$BaTiO_3$ was grown *in-situ* by the layer-by-layer technique either on $SrRuO_3$ thin films or sandwiched between $SrRuO_3$ films. The thickness of the bottom and top $SrRuO_3$ thin films were always 100 nm and 25 nm, respectively. $BaTiO_3$ thin films were grown with thicknesses ranging from 2 nm to 100 nm.

The most striking result is the large difference in quality between fully *strained* and partially *relaxed* $BaTiO_3$ thin films. $BaTiO_3$ with a film thickness of up to about 25 nm grows fully *strained* on the $SrRuO_3/SrTiO_3$ substrate with an outstanding crystalline quality. At about 25 nm relaxation takes place, probably via the introduction of misfit dislocations, and the crystalline quality drops significantly. This can be clearly seen from XRD measurements, RHEED images and RBS channeling experiments.

XRD measurements are shown in Fig. 6.15 and 6.16. Strained $BaTiO_3$ films have an in-plane lattice parameter of 3.895 Å following the in-plane lattice parameter of the $SrTiO_3$ substrate and the *strained* $SrRuO_3$ layer. The out-of-plane lattice parameter is elongated (4.19 Å). The cell volume is

not changed compared to the bulk cell volume ($a = 3.98 \text{ \AA}$, $c = 4.025 \text{ \AA}$, $V_{cell} = 63.75 \text{ \AA}^3$) indicating that up to 25 nm film thickness of the $BaTiO_3$ layer no significant number of dislocations are introduced into the thin film.

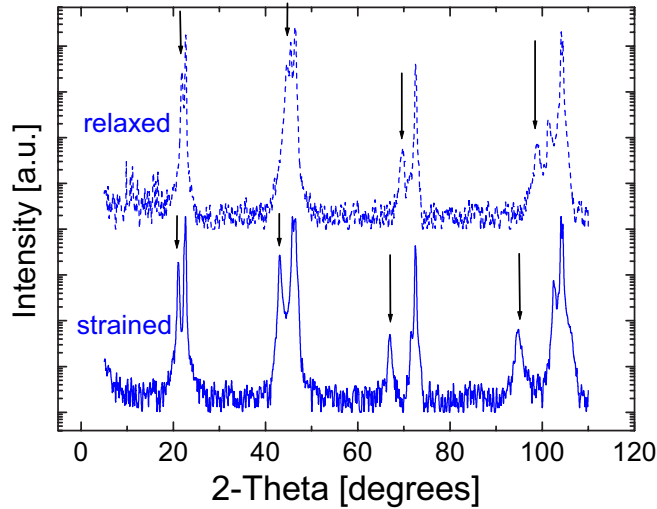


Figure 6.15: XRD theta-2theta scan of 60 nm thick relaxed (solid line) and 25 nm thick strained (dashed line) $BaTiO_3$ thin films grown *in-situ* on $SrRuO_3/SrTiO_3$ (100) substrates. Arrows indicate $BaTiO_3$ (001) reflexes.

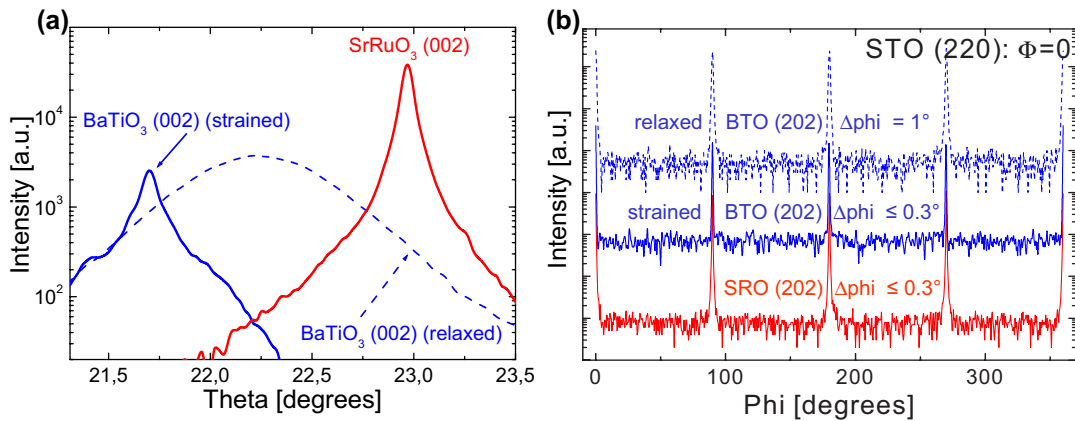


Figure 6.16: XRD (a) rocking curve and (b) phi-scan of 60 nm thick relaxed (solid blue line) and 25 nm thick strained (dashed blue line) $BaTiO_3$ films grown *in-situ* on 100 nm $SrRuO_3$ (red line) on $SrTiO_3$ (100) substrate.

At a thickness of about 25 nm, $BaTiO_3$ films grown *in-situ* on $SrRuO_3/SrTiO_3$ substrates relieve the stress. For a 60 nm thick film the in-plane lattice parameter increases to 3.98 Å and the out-of-plane lattice parameter decreases to 4.06 Å. These films probably relieve the stress by introducing dislocations and other defects. As a result, the cell volume and the mosaic spread increase considerably (Fig. 6.16). For a relaxed film the full width at half maximum in ω increases from 0.1° to 0.7° and in ϕ from the resolution limit of the XRD of 0.3° to 1°. Both *relaxed* as well as *strained* $BaTiO_3$ thin films have parallel orientations with the $SrRuO_3$ thin film and the $SrTiO_3$ substrate ([010]BTO || [010]SRO || [010]STO).

In Fig. 6.17 **RHEED** images for (a) a fully *strained* 25 nm thick film and (b) a *relaxed* 60 nm thick $BaTiO_3$ film are shown. The upper images correspond to the [100] azimuth and the lower images to the [110] azimuths. Fully *strained* films show nice RHEED images. Even Kikuchi lines can be observed for both azimuths. This is clear evidence for the brilliant crystalline quality and smoothness of *strained* films. On the contrary, *relaxed* thin films show stripes in the RHEED images and no Kikuchi lines are observable clearly indicating a significantly worsened crystalline quality.

RBS experiments confirm the results obtained by XRD and RHEED (see Fig. 6.18). Fully *strained* $BaTiO_3$ thin films have lower minimum yield χ_{min} values than *relaxed* films. The most striking feature, however, is the interface peak in the *Ba*-signal, which is clearly observable for the *relaxed* film, but not for the *strained* film. This proves the amazing $BaTiO_3/SrRuO_3$ interface quality of strained films.

HRTEM investigations shown in Fig. 6.19 demonstrate that ultrathin $BaTiO_3$ films grow homogeneously on $SrRuO_3/SrTiO_3$ (100) substrates. No defects are observable in the $BaTiO_3$ layer. The striking feature here is the tremendous sharpness of the interface. A similar HRTEM result was obtained for a 2 nm thick $BaTiO_3$ film.

In conclusion, *fully strained* $BaTiO_3$ films can be grown on $SrRuO_3/SrTiO_3$ (100) substrates up to a critical thickness of 25 nm. It is expected that *strained* $BaTiO_3$ thin films can be grown even thicker on $SrRuO_3/DyScO_3$ substrates. Fully *strained* $BaTiO_3$ thin films show an excellent crystalline quality, tremendously sharp interfaces with the bottom and top $SrRuO_3$ layers and a non-observable defect density in HRTEM. These structural properties were found and supported by XRD, RHEED, RBS and HRTEM investigations.

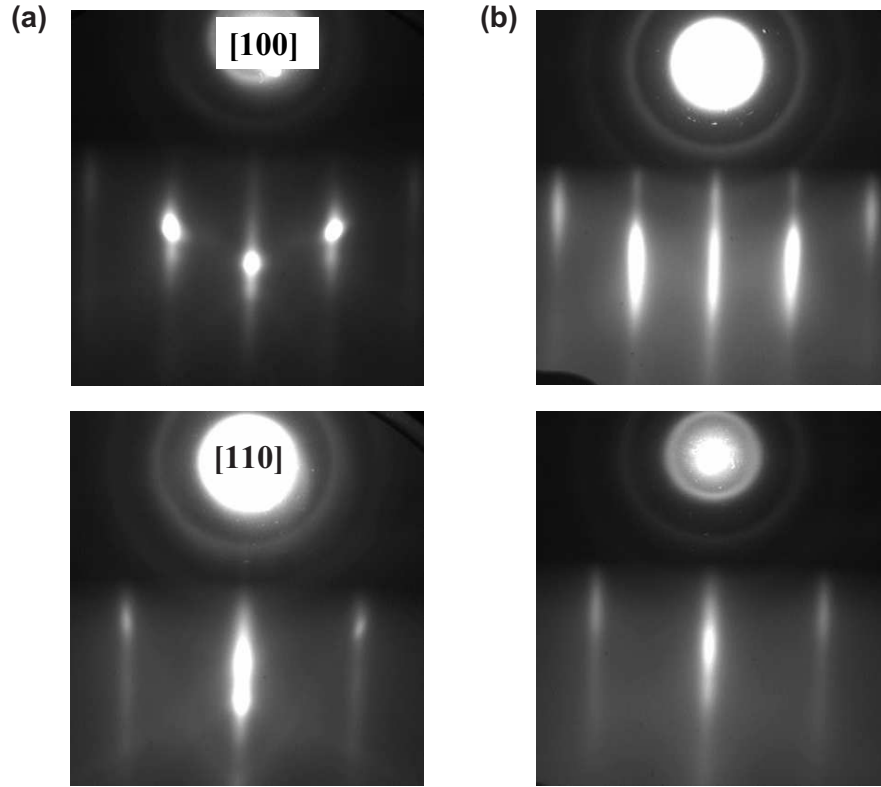


Figure 6.17: RHEED images of the $[100]$ azimuth (upper images) and the $[110]$ azimuth (lower images) of (a) a strained 25 nm thick $BaTiO_3$ and (b) a relaxed 60 nm thick $BaTiO_3$ film grown *in-situ* on $SrRuO_3/SrTiO_3$ (100) substrates.

Ferroelectric properties of MBE-grown $BaTiO_3$ films will be discussed in Chap. 7.2, p. 104.

6.3 High-pressure sputtered $SrRuO_3$ and $Pb(Zr,Ti)O_3$ thin films

We deposited $PbZr_{0.52}Ti_{0.48}O_3/SrRuO_3$ thin films on $SrTiO_3$ (100) substrates by high-pressure sputtering in pure oxygen atmosphere. A stoichiometric $SrRuO_3$ target was used to grow stoichiometric thin films, whereas a $PbZr_{0.52}Ti_{0.48}O_3$ target with a lead excess of 20% was necessary to compensate the loss of this volatile component and to fabricate stoichiometric $PbZr_{0.52}Ti_{0.48}O_3$ thin films. All $SrRuO_3$ thin films were grown 100 nm thick. The thickness of the $PbZr_{0.52}Ti_{0.48}O_3/SrRuO_3$ thin films varied be-

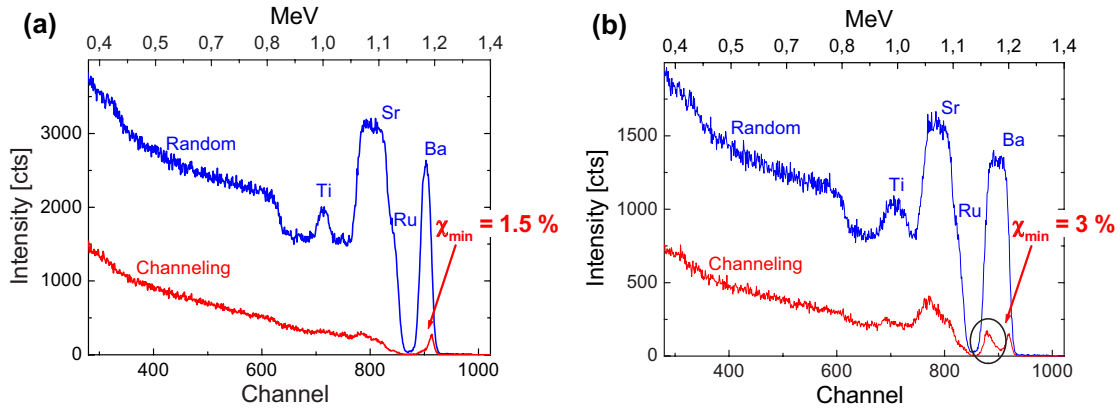


Figure 6.18: RBS experiments for (a) a strained 25 nm thick $BaTiO_3$ and (b) a relaxed 60 nm thick $BaTiO_3$ film grown *in-situ* on $SrRuO_3/SrTiO_3$ (100) substrates. The black circle shows the interface peak of the Ba-signal for the relaxed film.

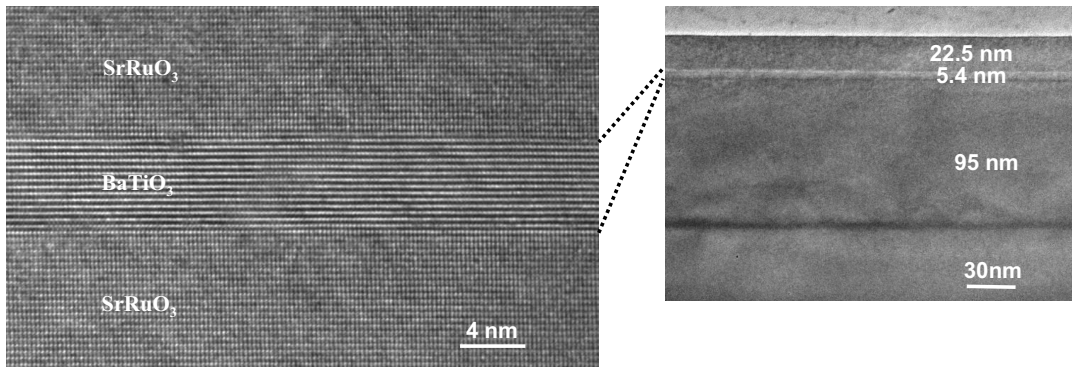


Figure 6.19: High-resolution TEM of a fully strained 5.4 nm thick $BaTiO_3$ film sandwiched between $SrRuO_3$ layers grown *in-situ*.

tween 2 nm and 250 nm. A deposition rate of 12 nm/h and 45 nm/h has been achieved for $PbZr_{0.52}Ti_{0.48}O_3$ and $SrRuO_3$, respectively. The deposition parameters, namely deposition temperature T_D , oxygen pressure p_{O_2} , target-substrate distance d_{TS} and the dc- and rf-power (p_{dc} and p_{rf}) for the $SrRuO_3$ and $PbZr_{0.52}Ti_{0.48}O_3$ deposition respectively, were investigated in a wide parameter range. All thin films were deposited *ex-situ* in order to characterize them individually².

²No difference in the crystalline quality was found between films deposited *in-situ* and *ex-situ*. This may in part be due to the high deposition pressure that cleans [190] the surface of carbon and hydrogen deposits or impurities before the following film is

The optimized growth conditions for sputtered $PbZr_{0.52}Ti_{0.48}O_3$ thin films were found to be $T_D = 650^\circ\text{C}$, $p_{O_2} = 3$ mbar, $d_{TS} = 21.5$ mm and $p_{rf} = 8.2$ W/cm². $SrRuO_3$ films were obtained with a high crystalline and electrical quality in a wide range of deposition parameters covering the set of deposition parameters for $PbZr_{0.52}Ti_{0.48}O_3$. Therefore the same sputter parameters as for $PbZr_{0.52}Ti_{0.48}O_3$ were chosen for $SrRuO_3$ being the applied dc-power density $p_{dc} = 6.4$ W/cm².

X-ray diffraction (XRD) (Fig. 6.20 (a)) indicates that both $PbZr_{0.52}Ti_{0.48}O_3$ and $SrRuO_3$ layers are single-crystalline and have their c -axis oriented in the out-of-plane direction. No significant secondary phase contribution, e.g. pyrochlore phase [191, 192, 109] in $PbZr_{0.52}Ti_{0.48}O_3$ films, was observed under optimized growth conditions. $PbZr_{0.52}Ti_{0.48}O_3$ and $SrRuO_3$ thin films both have exactly parallel orientations to each other and the $SrTiO_3$ substrate ($[010]PZT \parallel [010]SRO \parallel [010]STO$) (Fig. 6.20 (b)). Both the sputtered $PbZr_{0.52}Ti_{0.48}O_3$ and $SrRuO_3$ films possess a small mosaic spread ($PbZr_{0.52}Ti_{0.48}O_3$: FWHM in $\omega \leq 0.05^\circ$, FWHM in $\phi = 1^\circ$; $SrRuO_3$: FWHM in $\omega \leq 0.05^\circ$, FWHM in $\phi \leq 0.3^\circ$).

In comparison to the bulk parameters ($a, c = 3.93$ Å) the $SrRuO_3$ layer is compressively strained in the film plane and its in-plane lattice parameter follows that of the $SrTiO_3$ (100) substrate ($a = 3.895$ Å). Considering the lattice parameter of the substrate, the $SrRuO_3$ layer is forced to adopt a tetragonal structure with the elongated c -axis (3.96 Å) parallel to the film normal. $PbZr_{0.52}Ti_{0.48}O_3$ thin films grown on these $SrRuO_3/SrTiO_3$ substrates show a slight thickness dependence of their c -axis oriented along the out-of-plane direction and their a -axis length oriented along the in-plane direction (Fig. 6.21 (a))³. Even $PbZr_{0.52}Ti_{0.48}O_3$ thin films as thin as 8 nm are partially relaxed. The strain introduced by the $SrRuO_3/SrTiO_3$ substrate is progressively relieved for thicker films. The linear dependence of the misfit strain as a function of the inverse film thickness shown in Fig. 6.21 (b) is consistent with a strain relief via introduction of misfit dislocations [63] leading to an increased cell volume for thicker films (Fig. 6.21 (a)).

RBS experiments reveal the outstanding film quality of high-pressure sputtered $SrRuO_3$ thin films (Fig. 6.22 (a)). The interface peak in the chan-

deposited.

³Note that the in-plane lattice parameter is calculated from equation (5.3) using the (202) peak position of the corresponding thin film (Fig. 6.20 (c)).

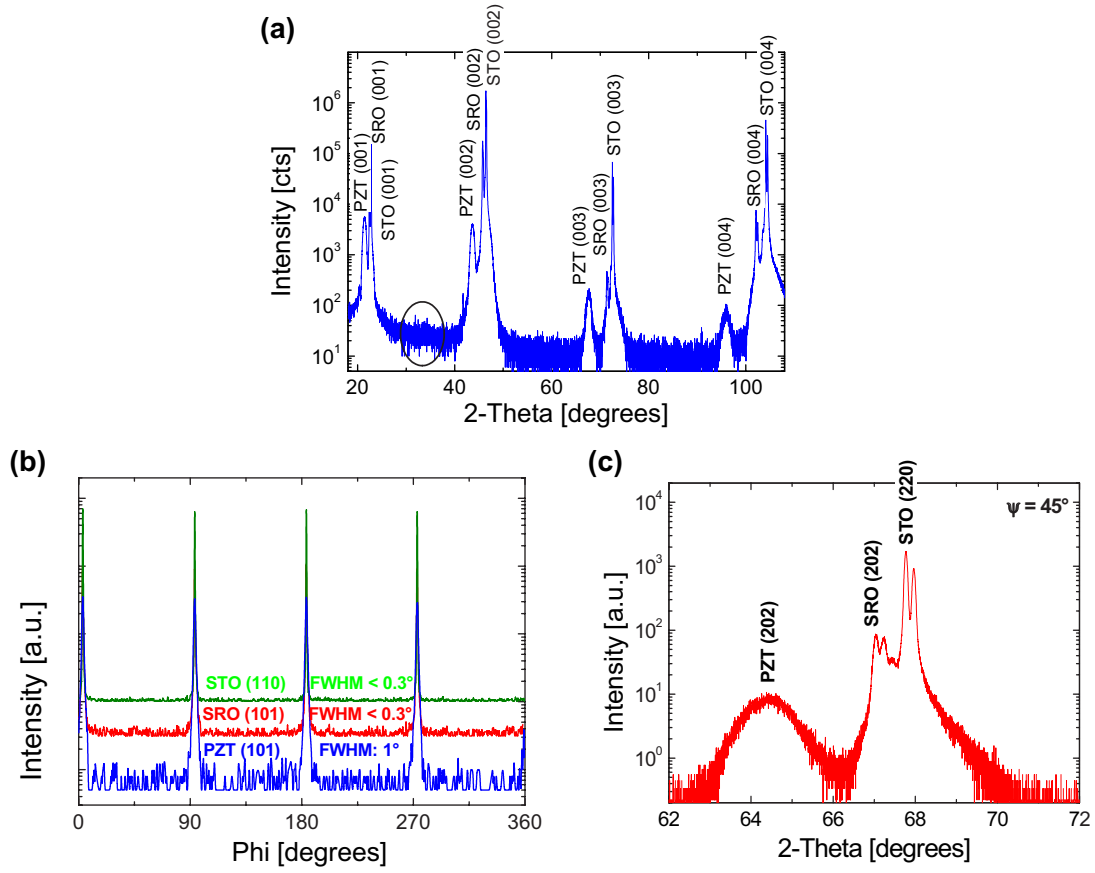


Figure 6.20: (a) *Theta-2theta* scan, (b) ϕ scan of (101)-reflexes of thin films and substrate, and (c) *theta-2theta* scan at $\psi \approx 45^\circ$ for high-pressure sputtered $PbZr_{0.52}Ti_{0.48}O_3/SrRuO_3$ thin films on a $SrTiO_3$ (100) substrate. The circle indicates the negligible pyrochlore phase intensity considering that the viewgraph is plotted on a logarithmic scale.

neling measurement is barely visible. A minimum yield χ_{min} of only 1° is obtained. An even lower value is probably prevented by the overlap of the *Ru* and *Sr* surface peaks.

Rutherford backscattering investigations verify the stoichiometric growth of $PbZr_{0.52}Ti_{0.48}O_3$ under the above mentioned optimized conditions. Although each deposition parameter has an influence on film quality and has to be considered when trying to grow the best achievable $PbZr_{0.52}Ti_{0.48}O_3$ films, film quality is mainly determined by the deposition temperature T_D . The stoichiometry, especially the *Pb*-content, is very sensitive to T_D . For example, increasing T_D by 10°C above the optimized deposition temperature

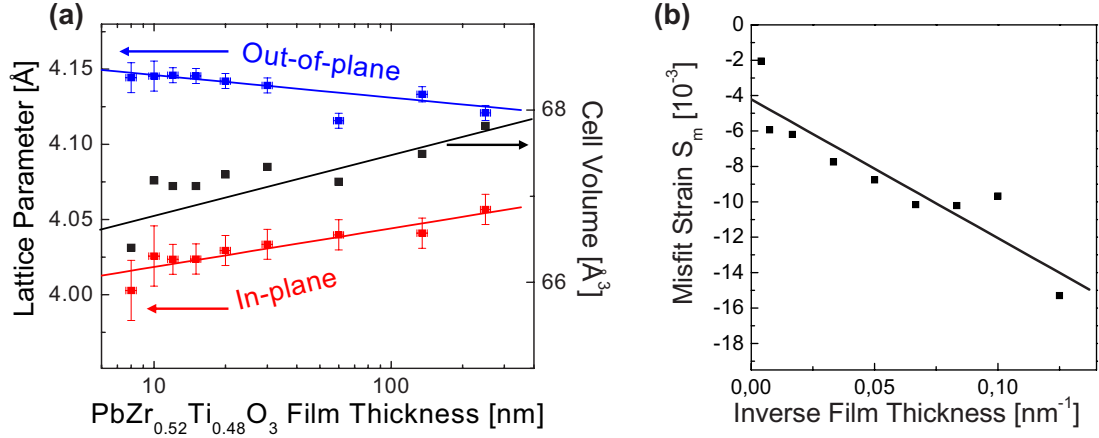


Figure 6.21: (a) Thickness dependence of the out-of-plane and in-plane lattice parameters of high-pressure sputtered $PbZr_{0.52}Ti_{0.48}O_3$ thin films on $SrRuO_3/SrTiO_3$ (100) substrates. The lines are only guides to the eyes and do not correspond to a physical model. (b) Misfit-strain as a function of the inverse film thickness.

leads to a 10% deficiency of the volatile lead. This results in a considerable deterioration of the $PbZr_{0.52}Ti_{0.48}O_3$ thin films as confirmed by XRD and RBS channeling investigations.

Fortunately, $SrRuO_3$ does not only have an outstanding quality itself, but it also significantly improves the crystalline quality of $PbZr_{0.52}Ti_{0.48}O_3$ thin films. Various $PbZr_{0.52}Ti_{0.48}O_3$ thin films with thicknesses between 10 nm and 100 nm were grown on $SrRuO_3/SrTiO_3$ and on $SrTiO_3$ substrates. The good quality of $PbZr_{0.52}Ti_{0.48}O_3$ achieved on $SrTiO_3$ substrates is significantly improved on $SrRuO_3/SrTiO_3$ substrates for all thicknesses. As example 60 nm thick $PbZr_{0.52}Ti_{0.48}O_3$ films are shown in Fig. 6.22 (b) and (c) for their growth on different substrates. The interface peak is greatly reduced for $PbZr_{0.52}Ti_{0.48}O_3$ grown on $SrRuO_3/SrTiO_3$. This can be easily taken from the Pb -signal in the channeling measurements (big arrow). The improvement of $PbZr_{0.52}Ti_{0.48}O_3$ thin film quality is not only limited to the interface region, but it is also true inside the film at a non-interface near region. In Ref. [193] we rule out the idea of a smaller lattice mismatch and favorable thermal expansion coefficients as a possible explanation for the observed improvement. A chemical interdiffusion across the interface during high-temperature film deposition, however, is possible. The formation of $SrPbO_3$ at the interface with a lattice parameter of 4.17 Å might help to relax the in-plane strain and improve the interface between $PbZr_{0.52}Ti_{0.48}O_3$ and

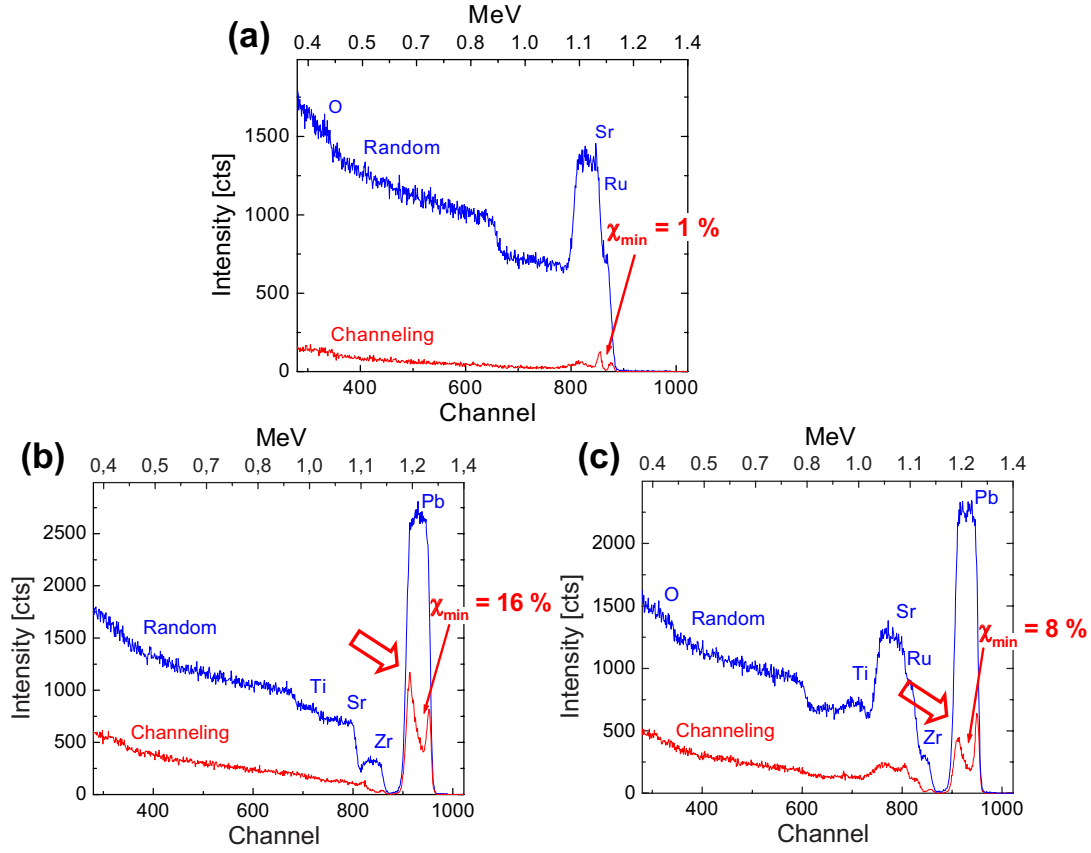


Figure 6.22: RBS random and channeling experiments for (a) 100 nm thick $SrRuO_3$ film on $SrTiO_3$, (b) 60 nm thick $PbZr_{0.52}Ti_{0.48}O_3$ film on $SrTiO_3$ and (c) 60 nm thick $PbZr_{0.52}Ti_{0.48}O_3$ film on $SrRuO_3/SrTiO_3$.

$SrRuO_3/SrTiO_3$. This idea is supported by energy-dispersive x-ray spectroscopy [194]. We believe, however, that the main reason for the improved interface as well as the enhanced crystalline quality of the $PbZr_{0.52}Ti_{0.48}O_3$ thin films is the defined SrO termination at the $SrRuO_3$ surface (see page 77). This may prevent the formation of grain boundaries, which can form at spots where different terminations are adjacent to each other [195].⁴

AFM measurements were performed to investigate the surface roughness. Flat surfaces with atomical steps were measured for 100 nm thick $SrRuO_3$ on $SrTiO_3$ samples (Fig. 6.23 (a)). The rms roughness of 1.6 Å is even

⁴Note that the $SrTiO_3$ (100) substrates were utilized as-delivered without any treatment prior to deposition. As a result, SrO and TiO_2 terminations are present on these substrates.

lower than the rms roughness measured on an as-delivered $SrTiO_3$ substrate (2.3 Å). This is particularly remarkable as the $SrRuO_3$ thin films were sputtered on $SrTiO_3$ substrates that had not been *HF*-etched prior to deposition to ensure a TiO_2 terminated surface.

Ultrathin $PbZr_{0.52}Ti_{0.48}O_3$ films deposited on these $SrRuO_3/SrTiO_3$ substrates display a smooth and very homogeneous surface (Fig. 6.23 (b)). The rms roughness on a $5 \times 5 \mu m^2$ area of a 6.5 nm thick film is only 2.5 Å. The roughness increases for thicker films (e.g. rms: 8.9 Å for 25 nm and rms: 10 Å for 100 nm thick $PbZr_{0.52}Ti_{0.48}O_3$).

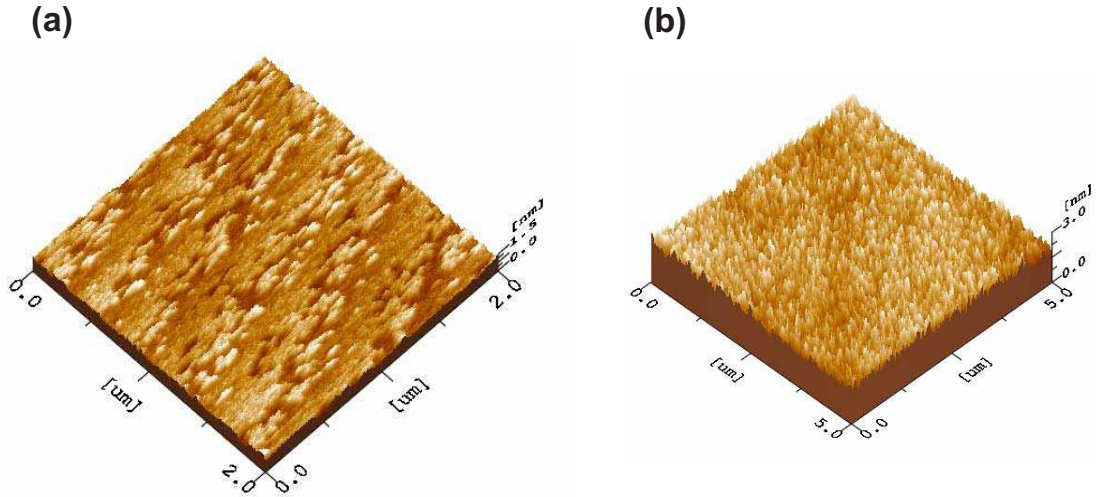


Figure 6.23: 3-dimensional AFM illustrations of (a) a 100 nm thick $SrRuO_3$ film on a $SrTiO_3$ substrate and (b) a 6.5 nm thick $PbZr_{0.52}Ti_{0.48}O_3$ film on a $SrRuO_3/SrTiO_3$ substrate.

HRTEM images were taken of 10 nm thin and 4 nm ultrathin $PbZr_{0.52}Ti_{0.48}O_3$ films. The latter is shown in Fig. 6.24. For both film thicknesses very homogeneous and atomically sharp interfaces without any observable defects in the $PbZr_{0.52}Ti_{0.48}O_3$ films were obtained [194, 196]. The lattice parameters obtained by HRTEM are consistent with the data for thicker films obtained by XRD.

Summarizing this Chapter, we grew fully strained $SrRuO_3$ thin films on $SrTiO_3$ (100) substrates. Film quality, surface smoothness and interface sharpness are brilliant. $SrRuO_3$ does not only serve as a conducting bottom layer, but it also significantly improves the crystalline quality of high-pressure

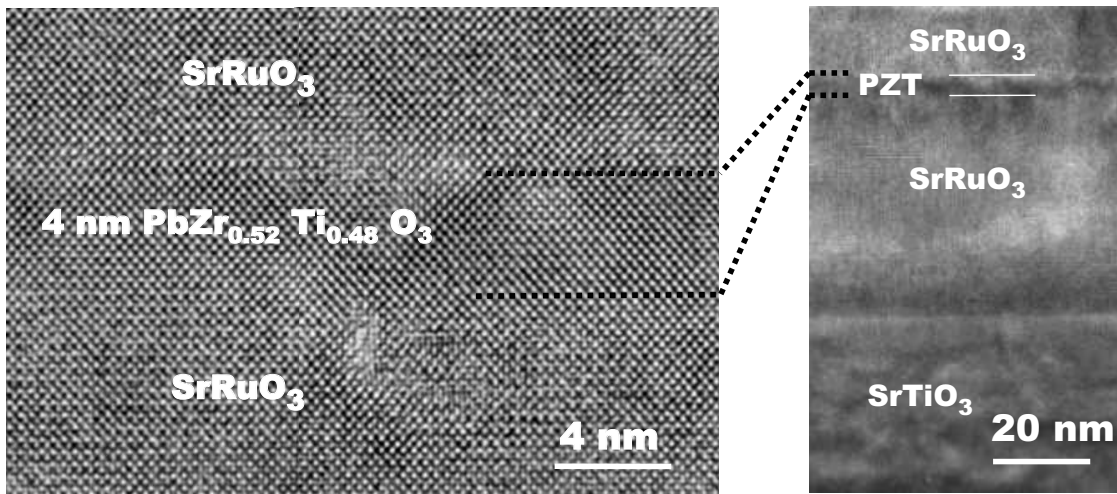


Figure 6.24: HRTEM image of a 4 nm thick $PbZr_{0.52}Ti_{0.48}O_3$ film sandwiched between $SrRuO_3$ layers.

sputtered $PbZr_{0.52}Ti_{0.48}O_3$ thin films. These films exhibit a high crystalline quality and ultrathin films are especially fascinating due to their smoothness and interface sharpness.

Extrinsic effects on ferroelectricity, such as the influence of the capacitor patterning method and the electrical boundary conditions will be demonstrated using high-pressure sputtered films in Chap. 7.1, p. 98 and p. 101. Ferroelectric properties and their thickness dependences for high-pressure sputtered $PbZr_{0.52}Ti_{0.48}O_3$ based capacitors with the thickness of the ferroelectric layer ranging from 8 nm to 250 nm will be discussed in Chap. 7.3. Finally, results for tunnel junctions with ultrathin $PbZr_{0.52}Ti_{0.48}O_3$ barriers (3 nm - 6 nm) and studies of the current mechanism through these devices will be presented in Chapter 8.

Chapter 7

Ferroelectric properties

In order to measure ferroelectric properties, top electrode/FE layer/bottom electrode heterostructures were patterned into capacitors with areas of $25 \times 25 \mu\text{m}^2$ to $200 \times 200 \mu\text{m}^2$. Three different methods, described below, were used in this work to prepare capacitors.

The **lift-off technique** is shown schematically in Fig. 7.1 (a). Photo resist is spun on top of the ferroelectric thin film and conventional photolithography defines the area of the capacitors. After sputtering *Pt* a lift-off process removes the photo resist together with the *Pt* in between the capacitors.

The second method is an **ion-beam etching (IBE) technique**. First, all three layers of the heterostructure are deposited on the (100)-oriented *SrTiO₃* substrate. Conventional photolithography and an *Ar*-etching step timed to stop in the ferroelectric layer or at the interface between bottom electrode and ferroelectric layer define the shape and the area of the capacitors (Fig. 7.1 (b)).

The third method is a **shadow mask technique**, which is shown schematically in Fig. 7.1 (c). Here, the top electrode is deposited through a shadow mask. The smallest areas obtained by this method and the specific shadow mask used here are about $1.5 \times 10^3 \mu\text{m}^2$. Size and shape of the capacitor area vary significantly from capacitor to capacitor. The areas of the capacitors have to be determined by optical techniques and software solutions [197]. The maximum error in the determination of area size is estimated to be about $\pm 10\%$.

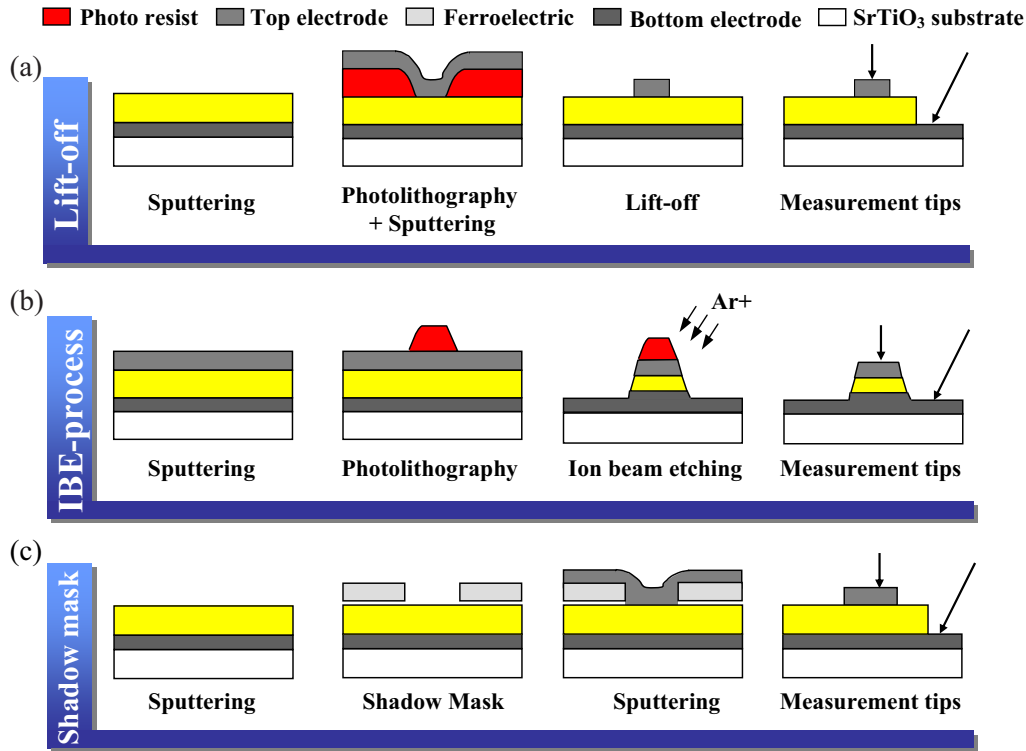


Figure 7.1: Illustration of the patterning of capacitors by (a) lift-off, (b) ion beam etching, and (c) shadow mask technique.

7.1 Influence of different patterning methods

$Pt/PbZr_{0.52}Ti_{0.48}O_3/SrRuO_3$ heterostructures with a ferroelectric film thickness between 23 nm and 165 nm were patterned into capacitors using either a *lift-off* process or an *ion-beam etching* technique, both described in the previous Section.

Fig. 7.2 shows the hysteresis curves and corresponding current responses for (a) *lift-off* patterned capacitors with film thicknesses of 89 nm, 61 nm and 23 nm, and (b) *ion-beam etched* capacitors with film thicknesses of 165 nm and 23 nm. The square shape of the P - E curve is softened for thinner films. Imprint¹ is observed for all loops. It is enhanced in capacitors processed by *lift-off* and it is progressively more pronounced for decreasing film thickness.

¹Imprint describes a shift of the P - E curve along the E -axis. An overview and a physical model describing this effect can be found in [198, 199].

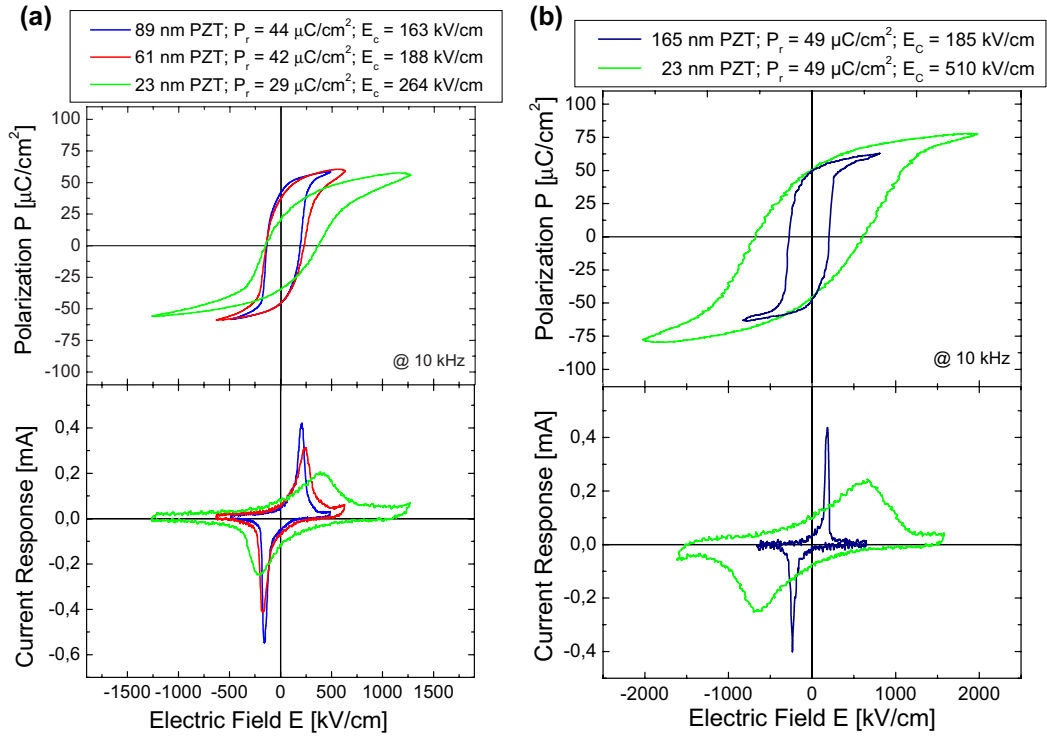


Figure 7.2: P - E curves and corresponding current responses for (a) lift-off and (b) ion beam etched capacitors measured at a hysteresis frequency of 10 kHz.

The reported values for the remanent polarization and the coercive field are calculated from:

$$P_r = \frac{1}{2} (P_{r+} + |P_{r-}|), \quad (7.1)$$

$$E_c = \frac{1}{2} (E_{c+} + |E_{c-}|). \quad (7.2)$$

For *lift-off processed* capacitors the remanent polarization decreases from $44 \mu\text{C}/\text{cm}^2$ to $29 \mu\text{C}/\text{cm}^2$ as the film thickness is reduced. Contrary to this behavior, no decrease in the remanent polarization is observed for *ion beam etched* capacitors. These capacitors show a remanent polarization of $49 \mu\text{C}/\text{cm}^2$. Remarkably, the remanent polarization obtained is equal to the predicted spontaneous polarization of a stress-free bulk $\text{PbZr}_{0.52}\text{Ti}_{0.48}\text{O}_3$ crystal [23]. We conclude that at a ferroelectric film thickness of 23 nm either no intrinsic size effect is present for *ion-beam etched* capacitors, or the intrinsic size effect is compensated by the strain effect resulting from the compressive substrate.

The size effect observed for *lift-off* processed films cannot be explained by extrinsic effects, such as film composition or quality, as the thin film deposition was identical for both patterning techniques. A possible explanation for the reduced remanent polarization could be a chemical decomposition of the ferroelectric layer at the surface, due to its exposure to solvents, photo resist, and developer during the *lift-off* process. This possibly leads to (sub-)surface layers in the ferroelectric film with suppressed ferroelectric properties.

The measured current responses shown in Fig. 7.2 (a) and (b) for *lift-off* and *ion-beam etched* capacitors, respectively, strongly indicate that the *lift-off* process damages the surface of the ferroelectric layer. Leakage currents increase for *lift-off* processed capacitors first for positive voltages at the top electrode (corresponding to positive electric fields in the current response). In contrast, for *ion beam etched* capacitors the leakage currents for positive voltages at the top electrode are considerably lower. Therefore, higher electric fields can be applied if necessary to saturate the P - E curve of capacitors with thinner $PbZr_{0.52}Ti_{0.48}O_3$ films. Here, leakage currents appear first for positive voltages at the bottom electrode (corresponding to negative electric fields in the current response). This observation suggests that leakage currents in ion-beam etched capacitors first originate from the $PbZr_{0.52}Ti_{0.48}O_3/SrRuO_3$ interface, whereas leakage currents for lift-off processed capacitors already increase with smaller applied electric fields originating from the $Pt/PbZr_{0.52}Ti_{0.48}O_3$ interface. As a consequence of leakage currents, it might not be possible to apply sufficiently large bias-voltages² in order to saturate the P - E curves.

We believe that the $PbZr_{0.52}Ti_{0.48}O_3$ surface treatment during the lift-off process results in a damaged surface layer leading to a reduced remanent polarization for thicker films. In addition, the typically observed increase of the coercive field for thinner films [200], and the non-saturation of the P - E curves due to increased leakage currents at higher voltages are responsible for the decreased remanent polarization for thinner films.

The second striking feature, which can be observed in Fig. 7.2 (a) and (b), is the increasing coercive field as the film thickness is decreased. This behavior is obtained irrespective of the patterning technique. However, the reported increase is considerably stronger in *ion-beam etched* capacitors.

²The application of a sufficiently large bias-voltage leads to the integration of high leakage currents (in addition to the displacement current). In this case, the P - E curve would not be the result of the integration of the displacement current.

We believe that a larger surface roughness arises from the surface treatment during the lift-off patterning, leading to the weaker increase of the coercive field obtained for *lift-off* processed capacitors in comparison to *ion-beam etched* capacitors. Surface roughness at the interface leads to an inhomogeneous field distribution at the $Pt/PbZr_{0.52}Ti_{0.48}O_3$ interface. In other words, the electric field at the interface is locally enhanced. As a result, the polarization reversal is likely to start at lower externally applied electric fields (cf. Fig. 1.6).

We conclude that etch degradation and residuals at the edges of the capacitors are less significant than the contact of the $PbZr_{0.52}Ti_{0.48}O_3$ surface with chemical solvents during *lift-off* processing. Nevertheless, in order to avoid any possible risk resulting from the contact of the ferroelectric surface with chemical solvents *and* from etch degradation and residuals, a shadow mask was used to fabricate the capacitors characterized in Chap. 7.3. Recently, our research group started using nano-stencil masks [201]. These specific shadow masks allow the fabrication of capacitors with *sub- μ m* areas without damaging the ferroelectric layer.

7.2 Influence of boundary conditions

In Chap. 1.3 and 1.4, the influence of boundary conditions on ferroelectricity has been extensively discussed from a theoretical point of view. In this Chapter it will be shown how boundary conditions may affect the specific experimental results.

Influence of electrical boundary conditions

The influence of the top electrode material on the ferroelectric properties of ferroelectric capacitors was studied. For this purpose $SrRuO_3/PbZr_{0.52}Ti_{0.48}O_3/SrRuO_3$ and $Pt/PbZr_{0.52}Ti_{0.48}O_3/SrRuO_3$ heterostructures were grown on $SrTiO_3$ (100) substrates. These heterostructures shown in the TEM images (Fig. 7.3) were processed into capacitors using ion beam etching (Fig. 7.1 (b)).

In Fig. 7.4 (a) the P - E loop for a 23 nm thick $PbZr_{0.52}Ti_{0.48}O_3$ film sandwiched between the $SrRuO_3$ top and bottom electrodes is shown. For comparison the P - E loop and current response for a similar capacitor with

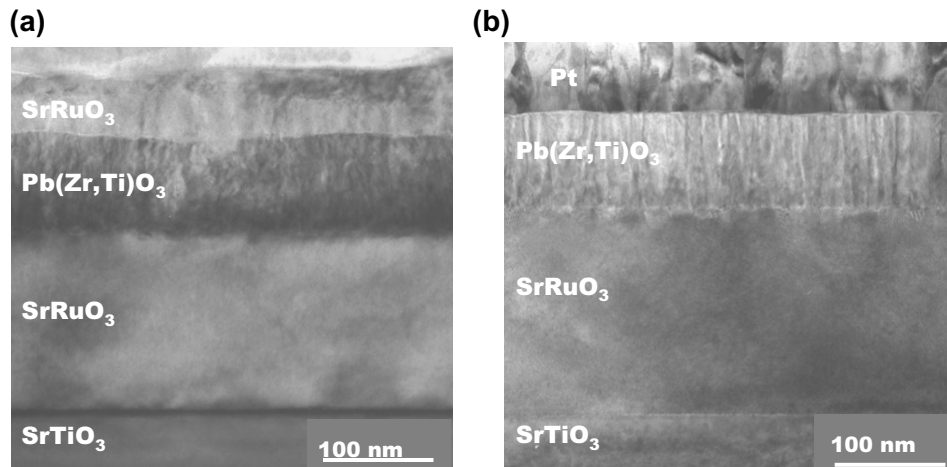


Figure 7.3: TEM images of (a) $SrRuO_3/PbZr_{0.52}Ti_{0.48}O_3/SrRuO_3$, and (b) $Pt/PbZr_{0.52}Ti_{0.48}O_3/SrRuO_3$ heterostructures.

Pt top electrode is displayed in Fig. 7.4 (b). Both capacitors, the one with $SrRuO_3$ top electrode and the one with Pt top electrode, were measured at a hysteresis frequency of 10 kHz. These P - E curves are typical of all investigated film thicknesses (12 nm - 60 nm) and all measured frequencies (1 kHz - 250 kHz).

The remanent polarization of capacitors with $SrRuO_3$ top electrodes does not reach the value of $49 \mu C/cm^2$. The coercive field for these heterostruc-

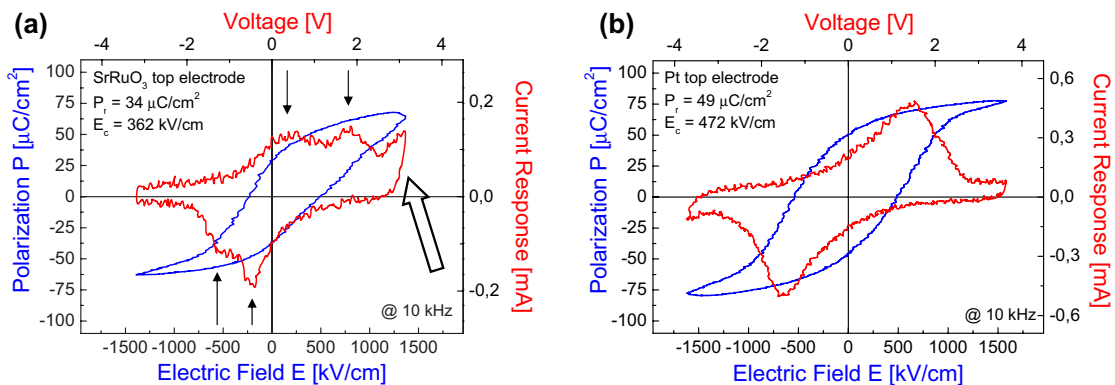


Figure 7.4: P - E curves and corresponding voltage dependences of the current response for (a) $SrRuO_3/PbZr_{0.52}Ti_{0.48}O_3/SrRuO_3$, and (b) $Pt/PbZr_{0.52}Ti_{0.48}O_3/SrRuO_3$ capacitors with a ferroelectric layer thickness of 23 nm.

tures is lower compared to capacitors having *Pt* top electrodes. These statements are especially true of thinner ferroelectric films.

The most striking feature, however, is the voltage dependence of the current response for $PbZr_{0.52}Ti_{0.48}O_3$ films with $SrRuO_3$ top electrode. High leakage currents for positive voltages at the top electrode are present (large arrow). No clear switching current is observed. Indeed, two maxima in the displacement current part of the current response are visible for each direction indicated by tiny arrows. It is difficult to speculate about the reasons for these two maxima. Maybe some regions inside the ferroelectric film are pinned at defects introduced during the sputtering of the top electrode. Another possible explanation is that 90° and 180° domains are present and have different coercive fields. Irrespective of the reason for the observed double peaks, what is obvious from Fig. 7.4 (a) is the fact that the P - E curve is not saturated. In other words, the polarization reversal is not complete.

The use of $SrRuO_3$ top electrodes, and generally the use of oxide electrodes, has been shown to reduce fatigue³ [151] in ferroelectric capacitors. On the other hand, we demonstrated that the use of $SrRuO_3$ top electrodes enhances leakage currents [199]. This can be attributed to a lower barrier height for $SrRuO_3/Pb(Zr,Ti)O_3$ compared to $Pt/Pb(Zr,Ti)O_3$ (see Chap. 4.1). Due to the increased leakage currents, and the increasing coercive field for decreasing film thickness, saturation of the P - E loop is challenging. As a result, the remanent polarization decreases for thinner films. This size effect, however, is not *intrinsic* to the ferroelectric film. The nature of this effect is clearly *extrinsic*. It is associated with the choice of the electrical boundary conditions.

We conclude that in addition to the thin film quality and the fabrication process of the capacitors, the choice of the electrode material is crucial as well. Hence, the influence of electrical boundary conditions on ferroelectricity has been successfully verified.

Influence of mechanical boundary conditions

In this Section I will try to experimentally verify two predictions discussed in Chap. 1.4 concerning the influence of compressive substrates. First, it will be investigated whether the elongated out-of-plane lattice parameter for

³Fatigue is one of the failure mechanisms of non-volatile ferroelectric memory devices; it describes the loss in the remanent polarization as a function of cycles. Various possible origins of fatigue are discussed in Refs. [202, 203, 204, 205, 206, 207, 208].

strained $BaTiO_3$ thin films reported in Chap. 6.2 does result in a higher remanent polarization. Afterwards, $Ba_{0.5}Sr_{0.5}TiO_3$ grown on a compressive substrate (see Chap. 6.1) with a bulk paraelectric to ferroelectric phase transition temperature of -60°C will be examined for ferroelectricity at room temperature.

Higher polarization due to increased tetragonality?

$SrRuO_3/BaTiO_3/SrRuO_3$ heterostructures were grown by MBE on $SrTiO_3$ (100) substrates with thicknesses ranging from 25 nm to 100 nm. Pt was sputtered on top to provide a better contact for the measurement tips. It turned out that $BaTiO_3$ films with MBE-grown $SrRuO_3$ electrodes has high leakage currents even after several annealing attempts. Relatively low growth pressures (due to limitations of the heater that was used, and the threat of oxidizing the sources inside the chamber), and the loss of RuO_2 during heating from 605°C ($SrRuO_3$ deposition temperature) to 650°C ($BaTiO_3$ deposition temperature) probably are the reasons for these leakage currents. In addition, we prepared the same heterostructures with MBE-grown $BaTiO_3$ and PLD-grown $SrRuO_3$. Here, the leakage currents were lower, but the capacitors still required an annealing step.

Unfortunately, no annealing experience was available. Therefore, annealing conditions optimized for MOCVD grown $BaTiO_3$, and $(Ba, Sr)TiO_3$ were first used [209, 210]. The first annealing results are shown in the upper part of Fig. 7.5. Here, $Pt/SrRuO_3/BaTiO_3/SrRuO_3$ stacks with a thickness of the ferroelectric layer of 100 nm, 60 nm, and 25 nm were annealed prior to Pt deposition for 20 minutes at 700°C in O_2 (type I annealing). P - E loops for all thicknesses of the ferroelectric layer are obtained. However, considerable leakage currents remained.

Afterwards, the samples were additionally annealed for 15 minutes at 700°C in *air* (type II annealing). The results are shown in the lower line of Fig. 7.5. The leakage currents are greatly reduced for all three thicknesses. The best results are obtained for 60 nm thick $BaTiO_3$. After the second annealing step the remanent polarization is closer to the bulk value of $26 \mu\text{C}/\text{cm}^2$, and the coercive field has increased. Surprisingly, the remanent polarization is reduced for the 100 nm, and 25 nm thick film. The higher remanent polarization after the first annealing cannot be solely attributed to the integration of leakage currents.

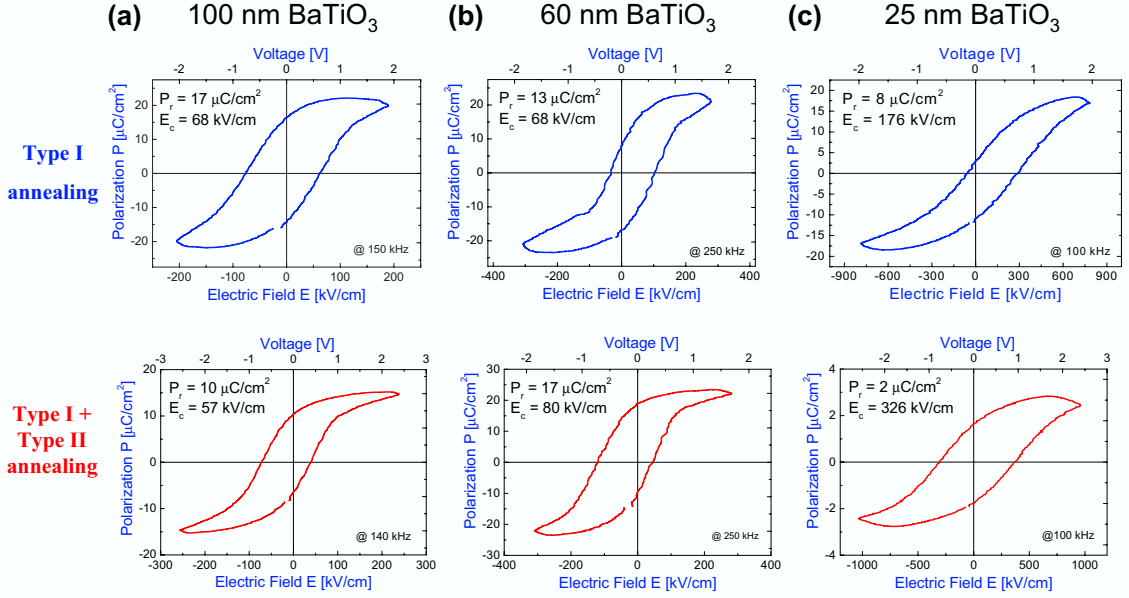


Figure 7.5: P - E curves for $Pt/SrRuO_3/BaTiO_3/SrRuO_3$ capacitors with a ferroelectric layer thickness of (a) 100 nm (b) 60 nm, and (c) 25 nm. The upper part shows P - E curves for capacitors that were annealed at 700°C in O_2 prior to Pt deposition and patterning (type I annealing). For the measurements in the lower part, the capacitors were additionally annealed at 700°C in *air* after the deposition of the complete stack and after ion-beam etching patterning (type II annealing).

Our conclusion from these and other annealing experiments carried out at different temperatures for some few minutes up to several hours, in *air*, in N_2 , and in O_2 is that of the conditions investigated, annealing in *air* for 20 minutes at 700°C is best for 60 nm thick films. Under these optimized annealing conditions the P - E loops are nicely shaped, have low leakage currents at a frequency of 30 kHz, and show high values for the remanent polarization (Fig. 7.6 (a)). As expected for oxide electrodes, no fatigue is observed up to at least 10^{11} cycles (Fig. 7.6 (b)).

In summary, the main challenge for MBE-grown $BaTiO_3$ thin films is the determination of an adequate annealing process. A large decrease in the leakage current can be achieved leading to nicely shaped and fatigue-free P - E curves with high values for the remanent polarization. However, different thicknesses of the ferroelectric layer require different annealing conditions. As a result, it is hardly possible to evaluate size effects in these samples. A higher remanent polarization due to the larger tetragonality for strained $BaTiO_3$ with thicknesses up to 25 nm could not be verified. A comprehen-

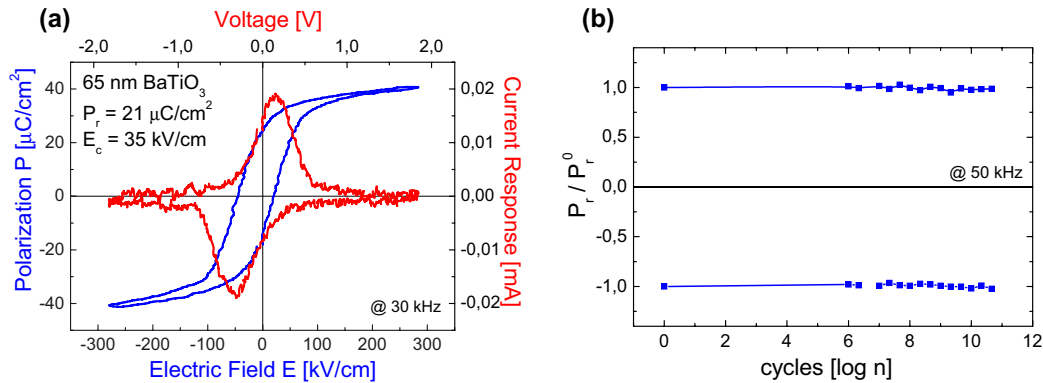


Figure 7.6: (a) P - E curve, and (b) fatigue measurements for a 65 nm thick $Pt/SrRuO_3/BaTiO_3/SrRuO_3$ capacitor annealed at $700^\circ C$ in air after deposition of the complete stack, and after ion-beam etching.

sive annealing study is necessary to obtain optimized annealing conditions for different thicknesses. A subsequent evaluation of the influence of the larger c/a ratio for strained $BaTiO_3$ will be very interesting.

Shift in phase transition temperature

$Pt/Ba_{0.5}Sr_{0.5}TiO_3/SrRuO_3$ heterostructures were grown on $SrTiO_3$ (100) substrates to study a predicted strain-induced enhancement of ferroelectricity. At room temperature a free-standing $Ba_{0.5}Sr_{0.5}TiO_3$ film is in the paraelectric state. The paraelectric-ferroelectric phase transition occurs at $-60^\circ C$ (see p. 53). Grown on a compressive substrate (e.g. $SrTiO_3$) a shift in the phase transition temperature may be expected (see Chap. 1.4).

Fig. 7.7 shows ferroelectric P - E curves for capacitors with a $Ba_{0.5}Sr_{0.5}TiO_3$ film thickness of 200 nm, 100 nm, and 60 nm. The P - E loops were measured at room temperature, verifying the predictions.

The phase transition temperature was shifted by at least $85^\circ C$. According to the theoretical results shown in Fig. 1.10 on page 24, and assuming that $BaTiO_3$ and $Ba_{0.5}Sr_{0.5}TiO_3$ behave similarly, all investigated film thicknesses should behave similarly to the bulk behavior, and should, thus, display similar P_r values. The experimental results do not support this prediction. However, it has to be noted that the results shown here are earlier results. Lift-off processing was used to pattern the capacitors without knowing the results obtained later and presented in Chap. 7.1. Hence, the observed decrease

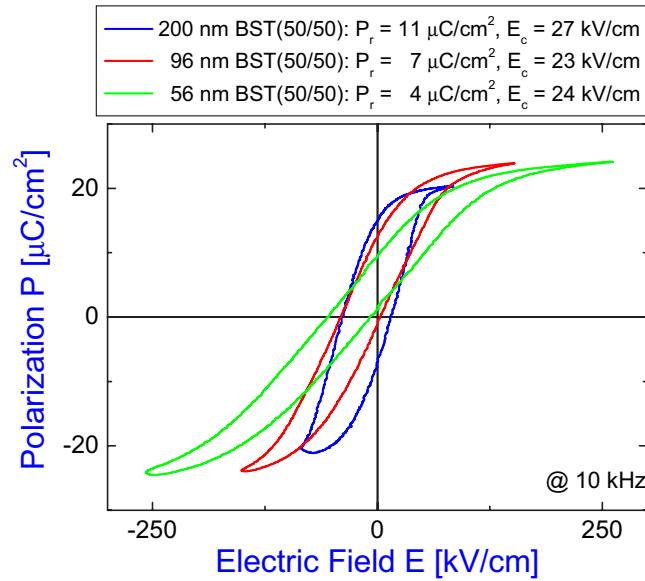


Figure 7.7: P - E curves for $Pt/Ba_{0.5}Sr_{0.5}TiO_3/SrRuO_3$ capacitors measured at room temperature.

in the remanent polarization can be attributed to the patterning method that was used, which was shown to be unsuitable especially for capacitors with thinner ferroelectric layers leading to poor ferroelectric properties.

In summary, we successfully verified a strain-induced shift of the paraelectric to ferroelectric phase transition temperature by at least 85°C . Thus, it has been experimentally shown that mechanical boundary conditions may be used to stabilize ferroelectricity in thin films.

7.3 Thickness dependence of ferroelectric properties

In Chap. 7.2 the influence of electrical and mechanical boundary conditions, as well as extrinsic effects (e. g. surface roughness or chemical decomposition by damaging surface treatments during the patterning of capacitors) on ferroelectricity were demonstrated experimentally. The ultimate goal is the stabilization of ferroelectricity in ultrathin films, a necessary requirement for investigating a possible interaction of ferroelectricity on electron tunneling in these films. Before I present our results for ultrathin films in Chapter 8,

I will first show the ferroelectric properties of ferroelectric capacitors with optimized boundary conditions and patterning schemes.

Size effects in PLD grown $BaTiO_3$ thin films

$SrRuO_3/BaTiO_3/SrRuO_3$ with various $BaTiO_3$ film thicknesses were grown by PLD (see Chap. 6.1) and high-pressure sputtering (see Chap. 6.3). These heterostructures were patterned into capacitors using an ion beam etching process shown schematically in Fig. 7.1 (b). In Chap. 7.2 lower leakage currents for $PbZr_{0.52}Ti_{0.48}O_3$ thin films with Pt top electrodes were found. In contrast, for $BaTiO_3$ thin films the use of $SrRuO_3$ top electrodes results in lower leakage currents⁴. Therefore, $SrRuO_3$ bottom and top electrodes⁵ were used.

Fig. 7.8 show P - E curves of $SrRuO_3/BaTiO_3/SrRuO_3$ capacitors with a $BaTiO_3$ film thickness of 100 nm, 25 nm, and 12 nm. The slope of the loops decreases for thinner films. The coercive field increases from approximately 150 kV/cm for a 100 nm thick film to 360 kV/cm for a 12 nm film.

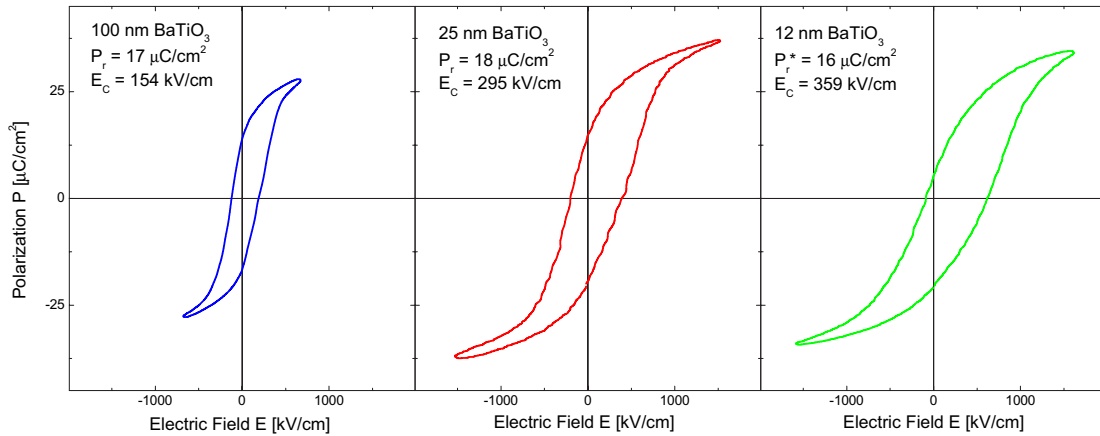


Figure 7.8: P - E curves for $SrRuO_3/BaTiO_3/SrRuO_3$ capacitors with a thickness of the ferroelectric layer of 100 nm, 25 nm, and 12 nm.

⁴No explanation has been found for this behavior.

⁵Although the same sputter conditions were used for both $SrRuO_3$ layers, substantial structural differences between bottom and top $SrRuO_3$ layer were observed [194].

For thinner films a shift of the P - E curve along the E -axis is observed. The strength of this so-called imprint depends on various aspects. For example, after heating the sample above T_C usually less imprint is observed. Sometimes imprint is reduced as a function of cycling number (Fig. 7.9 (b)). We therefore determine the remanent polarization from

$$P_r^* = \frac{1}{2} (P_{r+}(E^*) + |P_{r-}(E^*)|) \quad (7.3)$$

$$E_c = \frac{1}{2} (|E_{c-}| + E_{c+}) \quad (7.4)$$

$$E^* = E_{c-} + E_c$$

$$E_{c-} = \min\{E|P(E) = 0\}$$

$$E_{c+} = \max\{E|P(E) = 0\}.$$

Equation (7.3) gives the remanent polarization for the respective P - E curve, which is shifted along the E -axis to compensate the imprint effect. Using these expressions no thickness dependence of the remanent polarization P_r^* is observed in the thickness range studied. The remanent polarization varies between 16 and 18 $\mu\text{C}/\text{cm}^2$. This variation is within the uncertainty in the determination of the capacitor area.

The remanent polarization P_r determined at $E = 0$ (according to equation 7.1) does not change with respect to P_r^* for 100 nm, and 25 nm thick films, and it is reduced to 13 $\mu\text{C}/\text{cm}^2$ for 12 nm thick films. Hence, the apparent size effect obtained for the remanent polarization at zero external field may be attributed to imprint.

Finally, I would like to discuss the reduction of imprint by cycling. Fig. 7.9 (a) shows the normalized remanent polarization at $E = 0$ as a function of cycling number. The remanent polarization P_r increases with the number of cycles. This *negative fatigue* is due to two effects shown in Fig. 7.9 (b). First, imprint is reduced (indicated by the horizontal arrows), *and* second, additionally a real increase of the polarization takes place (indicated by the vertical arrows). The voltage dependence of the current response (Fig. 7.9 (c)) gives some clues about the origin of the observed fatigue. For positive voltages (and less for negative voltages), the displacement current consists of two well separated peaks. By cycling the P - E curve these two peaks approach each other. At negative voltages the two slightly separated peaks merge during the cycling to one peak. At positive voltages, the same can be expected if the cycling is continued. The existence of two peaks is

probably due to pinning in the ferroelectrics. Defects in the ferroelectric layer are known to act as pinning centers [18]. A higher electric field (activation energy) is necessary to switch the region close to a pinning center. As a result, two peaks are observed. Cycling is believed to depin these regions inside the film.⁶ Hence, size effects may result from pinning in the ferroelectric film.

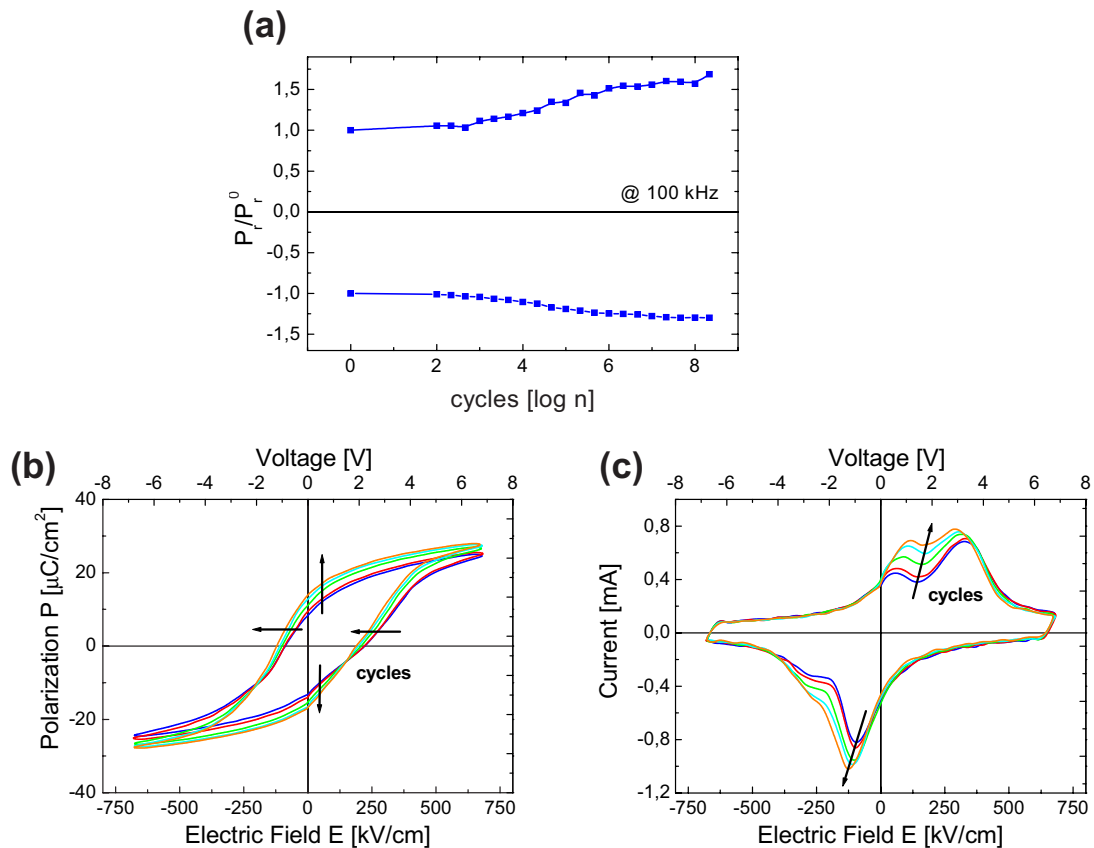


Figure 7.9: (a) Fatigue measurements of a 100 nm thick $BaTiO_3$ layer. (b) P - E curves and (c) current responses for increasing number of cycles.

Summarizing this Section, we grew $BaTiO_3$ thin films sandwiched between $SrRuO_3$ electrodes. A *negative fatigue* behavior occasionally observed may be due to depinning inside the ferroelectric film. For thinner films imprint is observed. Size effects, more precisely a decrease in the remanent polarization P_r , has been shown to result from imprint and pinning inside the ferroelectric film. The determination of the remanent polarization P_r^* of

⁶The exact depinning mechanism is still unknown.

I - V curves, which are shifted along the E -axis to compensate the imprint effect, should be performed according to eqn. (7.3,7.4). Using these equations and cycling the samples (if necessary), no decrease in the remanent polarization P_r^* is obtained for $BaTiO_3$ thin films ranging from 12 nm to 100 nm. However, an increase of the coercive field for thinner films is observed. This increase does not depend on imprint or pinning of the ferroelectric film.

Size effects in high-pressure sputtered $PbZr_{0.52}Ti_{0.48}O_3$ thin films

$PbZr_{0.52}Ti_{0.48}O_3$ with film thicknesses ranging from 6 nm to 250 nm were grown by high-pressure sputtering on $SrRuO_3/SrTiO_3$ substrates. Afterwards, Pt was evaporated through a shadow mask.

Fig. 7.10 (a) and (b) show the P - E curves and the corresponding current responses for 135 nm, and 10 nm thick $PbZr_{0.52}Ti_{0.48}O_3$ films. P - E curves of thick films ($t > 30$ nm) are nicely shaped and possess outstanding squareness. For decreasing film thickness the coercive field increases and the displacement current peaks arising from the polarization reversals are broadened.

Imprint, present also in thicker films, is especially observable in thinner films. As the film thickness decreases the curves are progressively shifted along the E -axis. The current response (and P - E curve) for the only 10 nm thick ferroelectric film best demonstrates the effect of imprint. After switching from the negative to the positive polarization state by applying a positive voltage, back-switching to negative polarization values takes place at zero volt. Imprint is the result of an internal field. This internal field is large enough to (partially) reverse the polarization in the absence of any applied external field. The origin of this internal field is currently being discussed in the literature [198, 199].

Leakage currents rise for thinner films. They are considered to be independent of the hysteresis frequency [211]. At the same time, the displacement current (current that arises from the displacement of the ions during the polarization reversal) does depend on the hysteresis frequency. The higher the hysteresis frequency the faster the ions are displaced, and the larger the displacement current ($I = \dot{Q}$) is which results from this displacement. For not too high leakage currents, the application of high frequencies results in a current response dominated by the displacement current. Unfortunately,

this method is not successful for higher leakage currents. Leakage currents through a capacitor are often described as a shunt resistance. In most cases, this does not describe the real situation. Leakage currents are usually non-linear. In fact, the maximum voltage holding $I_{displacement} \gg I_{leakage}$ is given by the specific leakage currents of a specific capacitor.

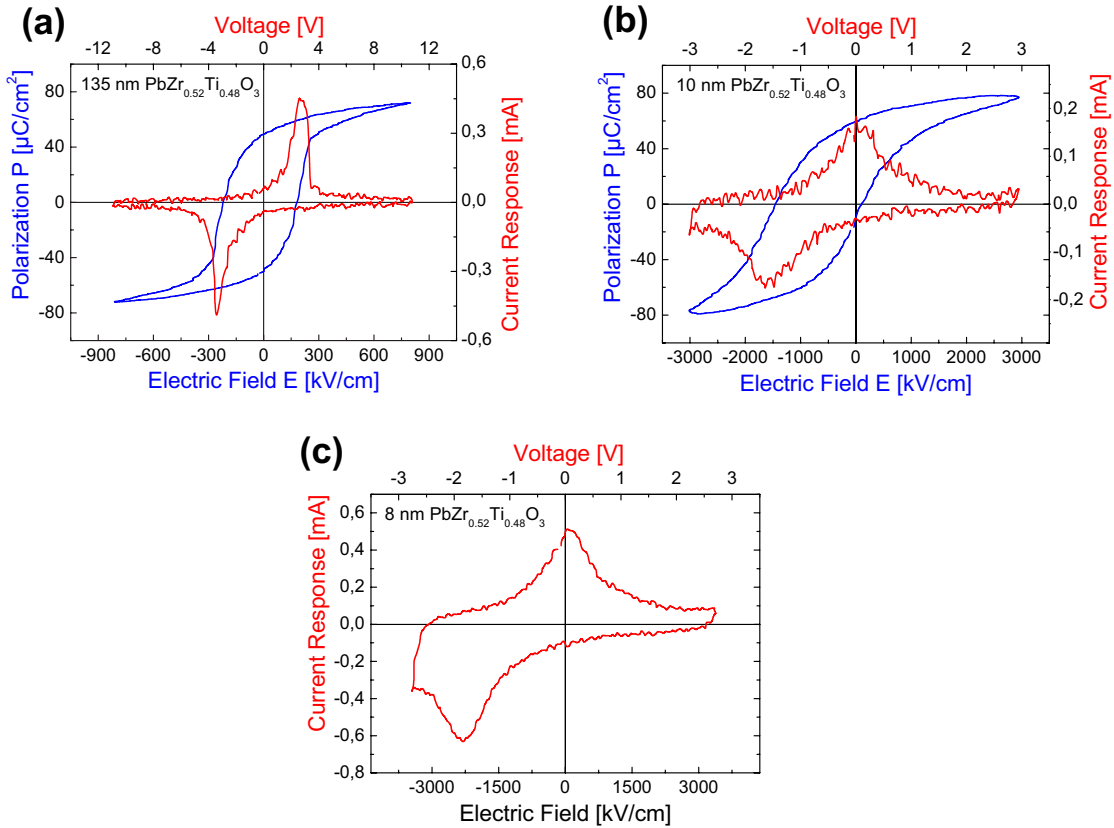


Figure 7.10: P - E curves and voltage dependences of the current response are shown for $\text{Pt}/\text{PbZr}_{0.52}\text{Ti}_{0.48}\text{O}_3/\text{SrRuO}_3$ capacitors with a ferroelectric film thickness of (a) 135 nm, and (b) 10 nm. Only the current response is shown in (c) for a 8 nm thick film.

Below 15 nm it is difficult to completely switch the polarization due to the rising leakage currents, the increasing coercive field and imprint. I will briefly explain this. First, as described above, there is a maximum voltage for which $I_{displacement} \gg I_{leakage}$ is still valid, and this voltage depends on the specific leakage currents for the specific capacitor. Second, the electric field necessary to reverse the polarization increases for thinner films. Therefore,

the corresponding voltage does not decrease as rapidly as expected. Finally, imprint causes a complete switching of the polarization in one direction at very low external applied voltages, but at the same time it takes a considerably higher voltage (coercive voltage + voltage to neutralize the internal field) to switch to the opposite polarization state.

Nevertheless, even an 8 nm thick $PbZr_{0.52}Ti_{0.48}O_3$ film is clearly ferroelectric. Figure 7.10 (c) shows the polarization reversals demonstrating ferroelectricity. Due to high leakage currents at negative voltages (corresponding to positive voltages at the bottom electrode), the P - E curve obtained from the integration of the current response is not shown.

For a 10 nm thick $PbZr_{0.52}Ti_{0.48}O_3$ film, ferroelectric polarization reversals in the current response have been observed up to the limit of the used heater of 300°C. Hence, the Curie temperature at this film thickness, under the specific boundary conditions, is still above 300°C. The thinnest film, in this work, for which ferroelectricity was unambiguously demonstrated by measuring the ferroelectric hysteresis loop has been 8 nm. In addition, piezoresponse force microscopy experiments performed by the group of L. M. Eng, Technische Universität Dresden, revealed ferroelectricity in 6 nm thick $PbZr_{0.52}Ti_{0.48}O_3$ films [212].

Thickness dependence of the remanent polarization

Especially for thinner films imprint is observable. Imprint is due to an effective internal field. In order to determine the remanent polarization at zero field, an external electric field has to be applied to compensate this internal field. Therefore, we defined a remanent polarization P_r^* , which determines the polarization at a field E^* . This calculated electric field compensates the shift in the P - E curve and is zero for vanishing imprint (see equation (7.3)).

Fig. 7.11 (a) shows the thickness dependence of the remanent polarization P_r^* . A nearly constant remanent polarization P_r^* is obtained from 10 nm to 250 nm film thickness. Remarkably, the remanent polarization obtained corresponds to the predicted spontaneous polarization of stress-free bulk material [113]. This might be a coincidence. In fact, the polarization is predicted to increase with decreasing film thickness due to the substrate effect (see Chap. 1.4). This is not observed in the experiments. A possible explanation is a compensation of the substrate effect by the surface effect.

For comparison, the thickness dependence of the remanent polarization at zero *external* field, P_r , is shown in Fig. 7.11 (b). Here, a decrease of the remanent polarization for thinner films is obtained below 15 nm. By comparing this thickness dependence with that for P_r^* , the size effect can be attributed to imprint.

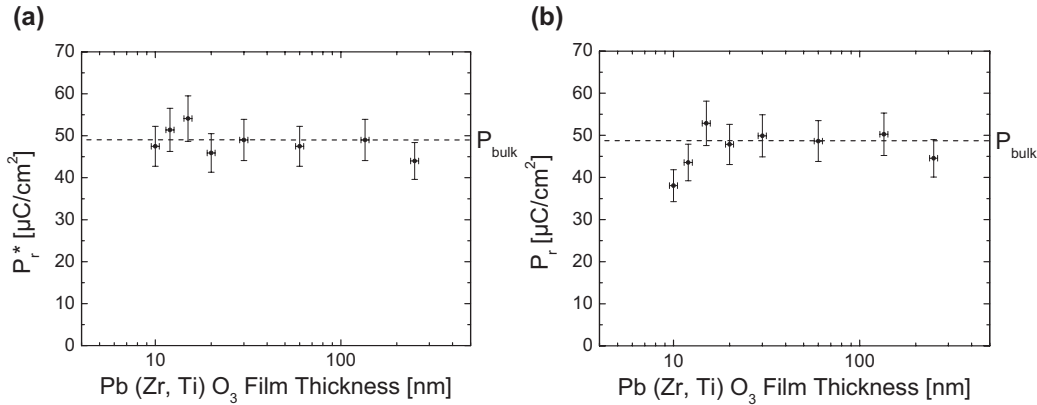


Figure 7.11: Thickness dependence of the remanent polarization (a) P_r^* (see text for details), and (b) P_r determined at $E_{ext} = 0$.

Thickness and frequency dependence of the coercive field

In Fig. 7.12 (a) the ferroelectric film thickness dependence of the coercive field and coercive voltage measured at a hysteresis frequency of 20 kHz is shown. Coercive field E_c and coercive voltage V_c are connected by a simple relation⁷: $E_c = \frac{V_c}{t}$, where t is the film thickness. The coercive field increases for thinner films. The coercive voltage decreases for thinner films and converges slightly below one volt. Note that the error bars for the coercive voltage account for the broadened displacement current peaks, whereas the error bars for the coercive field result from the uncertainties in the determination of the coercive voltage and the film thickness.

An increasing coercive field with decreasing film thickness has been reported by other groups [200], as well. Various explanations have been proposed for this size effect [29, 30, 31, 32]. In the following, I would like to explain our point of view. The thickness dependence of the coercive field may be due to a combination of three effects. First, the compressive strain

⁷A homogeneous field distribution is assumed.

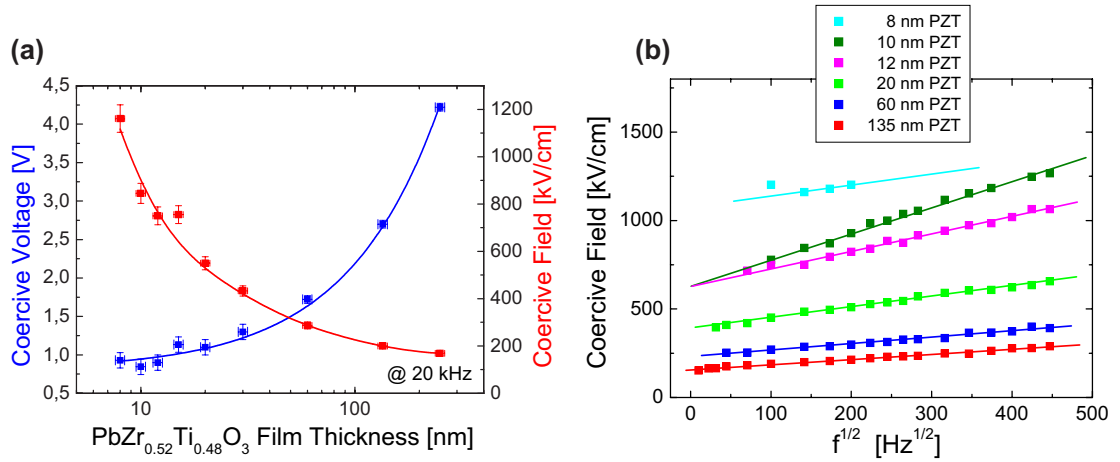


Figure 7.12: (a) Ferroelectric film thickness dependence of the coercive field and the coercive voltage measured at 20 kHz. (b) Coercive field as a function of the square root of the hysteresis frequency for various $\text{PbZr}_{0.52}\text{Ti}_{0.48}\text{O}_3$ film thicknesses. The solid lines are linear fits to the experimental results of the specific film thickness.

induced by the substrate may increase the coercive field considerably. Second, the presence of nucleation centers decreases for thinner films. And third, roughness for thicker films locally enhances the applied electric field leading to a lower coercive field for thicker films. I will briefly explain these effects.

It is well known that a thin film grown epitaxially on a dissimilar *compressive* substrate is strained leading to a stabilized out-of-plane polarization state [6]. This substrate effect is predicted because of the electrostrictive coupling between polarization and strain in ferroelectrics (see Chap. 1.4). Using the non-linear thermodynamic theory proposed by N. A. Pertsev [5], the coercive field of a ferroelectric thin film can be calculated as a function of temperature T and misfit strain S_m . According to this theory, the coercive field for our thinnest films is predicted to be 1.2 MV/cm at room temperature [213]. A strain-independent coercive field of only 0.65 MV/cm is estimated from the thermodynamic Ginzburg-Landau theory, not taking into account the substrate effect (Chap. 1.2, p. 10). This strong increase of the coercive field arises from an almost linear scaling of the coercive field with the cube of the polarization. However, it is at present an open question whether such a strong increase can be expected for the thin films studied here, because the polarization does not increase as strongly as predicted by theory.

Our second idea is based on the fact that the polarization reversal via creation and growth of nucleation centers is energetically favorable compared to the simultaneous switching of a single domain. Therefore, the density of nucleation centers determines the coercive field, and the coercive field increases with a decreasing nucleation center density. Defects in perovskites⁸ may act as pinning centers. Such pinning centers may act as nucleation centers, and thus decrease the electric field necessary to switch the polarization. Based on high-resolution TEM and TEM investigations, our thinner films show a smaller defect density compared to thicker films [216]. As a result, a higher coercive field may be due to the presence of less nucleation centers in thinner films.

Finally, the reduced coercive field can also be attributed to a larger surface roughness obtained for thicker films. AFM measurements show very smooth surfaces for thinner films, e.g. an rms roughness of only 2.5 Å is achieved for a 4 nm thick $PbZr_{0.52}Ti_{0.48}O_3$ film. In contrast, thicker films show a rougher surface. For example, an rms roughness of 9 Å is obtained for a 25 nm thick film. As it was discussed above, surface roughness is very likely to lead to a reduced coercive field due to locally enhanced electric fields, where nucleation of domains with reversed polarization may take place at reduced externally applied electric fields.

The thickness dependence of the coercive field in Fig. 7.12 (a) has been determined at a hysteresis frequency of 20 kHz. In Fig. 7.12 (b) the coercive field as a function of the square root of the hysteresis frequency is shown for various ferroelectric film thicknesses. The model of Ishibashi discussed in Chap. 1.2, p. 13, predicts a power law $E_c = f^{1/2}$. The experimental results perfectly fit this model, which is based on the Kolmogorov-Avrami model, for all investigated thicknesses and all applied hysteresis frequencies.

Current response of a 6 nm thick $PbZr_{0.52}Ti_{0.48}O_3$ film

It has been mentioned that capacitors with a $PbZr_{0.52}Ti_{0.48}O_3$ thickness ranging from 6 nm to 250 nm were prepared. So far, capacitors with film thicknesses down to 8 nm have been shown and discussed. In Fig. 7.13 (b) the current response for the 6 nm sample is shown. Numbers from 1 to 8 and arrows indicate the direction of scan. For comparison the already known current response for the 8 nm sample is shown in Fig. 7.13 (a). The current

⁸Perovskites are known for their large defect density of about $10^8 - 10^9 \text{ cm}^{-2}$ [214, 215].

response for the 6 nm thick $PbZr_{0.52}Ti_{0.48}O_3$ capacitor measured at a frequency of 1 kHz differs drastically from that measured for thicker samples. The current is increased by almost one order of magnitude⁹. As a result, the resistance of the capacitor and of the bottom electrode become comparable. Therefore, the applied external voltage differs from the voltage applied to the capacitor. For this reason, I do not show the scale for the voltage and the electric field axis. No displacement current peaks are observed. Instead, switching events in the $I-V$ curve are obtained for hysteresis frequencies up to 150 kHz. Chapter 8 will focus on this effect where the current transport through ultrathin films will be studied, and the origin of the switching events will be discussed in detail.

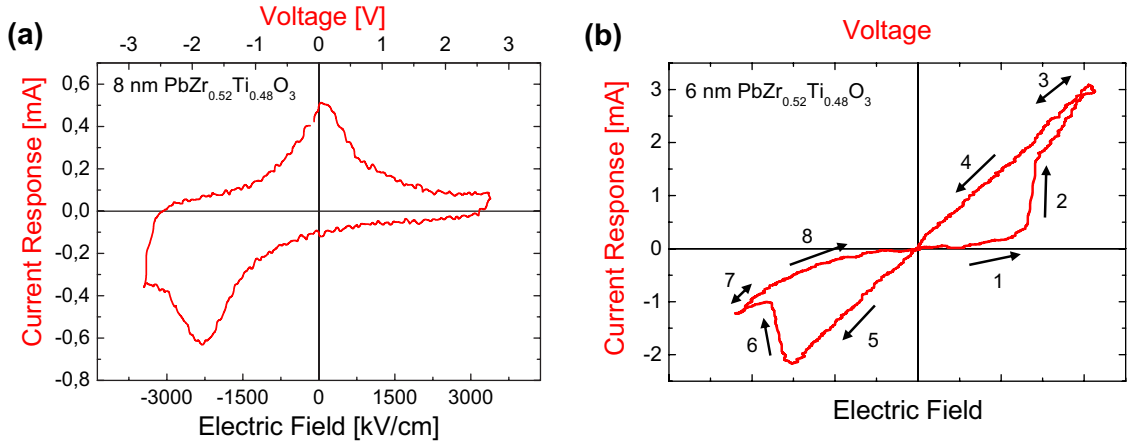


Figure 7.13: Current response of (a) a 8 nm, and (b) a 6 nm thick $PbZr_{0.52}Ti_{0.48}O_3$ film. In the latter case no values for voltage and field are shown because the applied voltage differs from the voltage applied to the capacitor in this voltage-driven measurement due to the comparable resistance of capacitor and bottom electrode.

Summarizing this Chapter, we grew $PbZr_{0.52}Ti_{0.48}O_3/SrRuO_3$ heterostructures by high-pressure sputtering. The ferroelectric film thickness varied from 6 nm to 250 nm. Pt was evaporated through a shadow mask and served as the top electrode defining at the same time the capacitor area size. Ferroelectricity was demonstrated for all film thicknesses from 8 nm upwards. In addition, piezoresponse experiments revealed ferroelectricity in 6 nm thick films. Imprint was present, leading to a shift of the $I-V$ curves along the voltage-axis. We defined equations which compensate the imprint effect and allow the determination of the remanent polarization, P_r^* , at zero field. A

⁹The capacitor areas of both capacitors are comparable.

nearly constant value for P_r^* was obtained for film thicknesses ranging from 10 nm to 250 nm. Remarkably, this remanent polarization corresponds to the spontaneous polarization of a stress-free bulk $PbZr_{0.52}Ti_{0.48}O_3$ crystal. The predicted strain-induced increase of the polarization is not observed. This is attributed to the compensation by the surface effect. Besides, the coercive field increases for decreasing film thickness. Various possible explanations have been given for this size effect. The hysteresis frequency-coercive field relation agrees with the model of Ishibashi discussed in Chap. 1.2. Switching events in the current response were observed for the 6 nm thick film at hysteresis frequencies up to 150 kHz. These switching events will be discussed in detail in the following Chapter.

Chapter 8

Current transport through ultrathin films

Compared to the fabrication of capacitors described in Chap. 7, a more complex process has been applied to pattern tunnel junctions. In total, three photo mask steps define tunnel junctions by conventional photolithography and ion beam etching [80, 136]. First $Pt/PbZr_{0.52}Ti_{0.48}O_3/SrRuO_3$ or $Pt/SrRuO_3/BaTiO_3/SrRuO_3$ heterostructures with a ferroelectric barrier thickness between 3 nm and 6 nm are *Ar*-etched to define the shape of the bottom electrode (Fig. 8.1 (a)). Rectangular junctions with areas between $4 \mu m^2$ and $200 \mu m^2$ are formed by the use of a second photo mask and ion milling step, timed to end at the top surface of the bottom electrode (Fig. 8.1 (b)). The surroundings of the mesas are insulated by a 200 nm thick SiO_2 layer deposited by rf-magnetron sputtering using a self-aligned process (Fig. 8.1 (c)). After lift-off, the third photo mask step determines the wiring layer, which provides an electrical contact to the top electrode of the tunnel junction (Fig. 8.1 (d)). In addition to 45 tunnel junctions, three $100 \times 100 \mu m^2$ crossovers without tunnel junctions serve as test structures to measure the insulation resistance of the SiO_2 film. The resistance of these structures always exceeded $10 M\Omega$. Therefore, possible parallel current paths through the insulating SiO_2 layer were neglected in the tunneling measurements. In Fig. 8.1 (e), the top view of a tunnel junction including the current-voltage lead in a four-point arrangement is shown schematically. This arrangement eliminates the lead resistances.

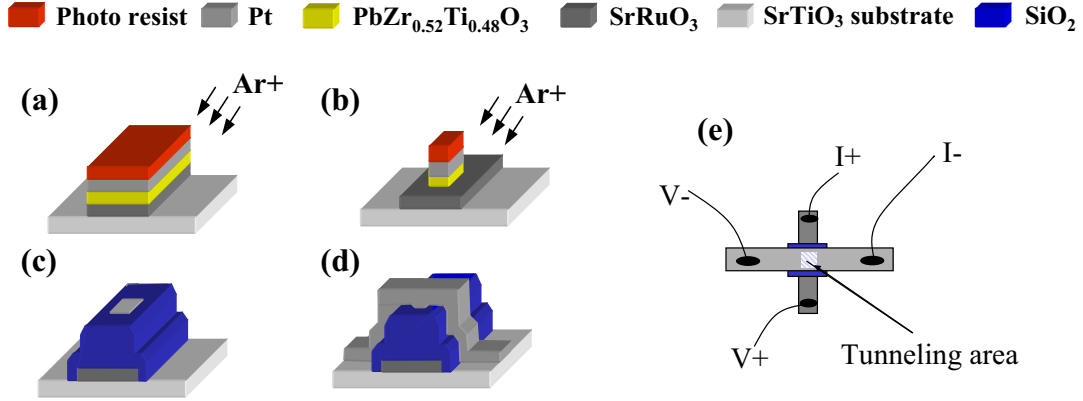


Figure 8.1: Patterning of tunnel junctions shown schematically for $Pt/PbZr_{0.52}Ti_{0.48}O_3/SrRuO_3$ heterostructures. An analogous process was used for $BaTiO_3$ -based heterostructures. See text for details.

8.1 Resistive switching effects in I - V curves

Junctions with ultrathin high-pressure sputtered $PbZr_{0.52}Ti_{0.48}O_3$ and pulsed laser ablated $BaTiO_3$ barriers ranging from 3 nm to 6 nm were fabricated. All measurements shown below were performed with a battery-powered current source, although in all graphs the current is plotted as a function of the voltage. This is done in order to be consistent with the standard I - V curves. All curves shown in this Chapter are reproducible. Qualitatively similar results are obtained for both materials studied in this work. Therefore, the figures presented here can be regarded as valid for both materials.

Fig. 8.2 (a) shows a typical I - V characteristic of a 6 nm thick $BaTiO_3$ film recorded at 260 K. A complete cycle lasted 10 minutes ($f \approx 1.7$ mHz). Numbers from 1 to 7 and arrows show the direction of scan. Simultaneously, the applied voltage dependence of the dynamic conductance dI/dV was measured with a lock-in amplifier Fig. 8.2 (b). The parabolic behavior of the dynamic conductance is indicative of electron tunneling through an insulator. One cycle is composed of the red and the green curve. In the following, I will refer to the red curve as the low-resistance curve and to the green curve as the high-resistance curve.

The I - V curve displays clear switching events at $V_{switching}^- = -0.56$ V and $V_{switching}^+ = 0.84$ V, and a crossover at the origin. The switching is highly reproducible even after several I - V cycles. The resistance ratio of the high-resistance (3.8 k Ω) and the low-resistance (0.9 k Ω) curve at the origin

is about 4. The asymmetry in the I - V curve for positive and negative bias-currents may be caused by different barrier heights of the top and bottom electrode-barrier interfaces.¹ Remember that an asymmetry (shift along the E -axis) was observed in thick-film capacitors as well (see Chapter 7.3).

Figure 8.2 (c) demonstrates the history effect. Prior to the measurement, a negative current pulse, corresponding to a negative electric voltage, was applied. The applied current is then increased from 0 mA to the maximum value, and decreased back to 0 mA (solid line). The direction of scan, performed in a quasi-static regime, is indicated by numbers and arrows. Initially the voltage increases along the high-resistance curve (1). At a defined value for the voltage a sudden decrease of the voltage from the high-resistance to the low-resistance curve takes place (2). As the current is further increased the I - V characteristic moves along the low-resistance curve (3). Then the current is reduced to 0 mA (4). This cycle is repeated, but this time without applying a negative current prior to the measurement. Only a slight hysteresis is obtained along the low-resistance curve (5). The first scan is not reproduced unless a sufficiently negative current is applied exceeding the critical voltage $V_{switching}^-$.

The critical voltage (and field) for the switching from the high-resistance to the low-resistance curve $V_{switching}^+$ (and $E_{switching}^+$), marked in Fig 8.2 (c) by an arrow and a cross, was determined for temperatures between 125 K and 300 K. In Fig. 8.2 (d) the temperature dependence of $V_{switching}^+$ (and $E_{switching}^+$) is shown. A slight increase of the critical field for decreasing temperature indicates a thermally-assisted switching.

With decreasing temperature the negative electric field increases, which is needed to switch to the high-resistance curve. At 100 K an electric field of approximately 2.5 MV/cm deteriorates the junction.² This happened to other tunnel junctions as well. Therefore, we never measured a whole I - V cycle at temperatures below 125 K. However, the low-resistance and the high-resistance curve could be measured separately down to 4.2 K by switching to the respective state at higher temperatures.

The dashed line in Fig. 8.3 (a) shows the I - V curve of a 4 nm thick $PbZr_{0.52}Ti_{0.48}O_3$ film for an applied bias-current corresponding to an electric

¹The bottom and top electrodes are both $SrRuO_3$. Nevertheless, different structural properties were found for them [183].

²Note that J. Desu reported on a breakdown field in $BaTiO_3$ of 4 MV/cm [62].

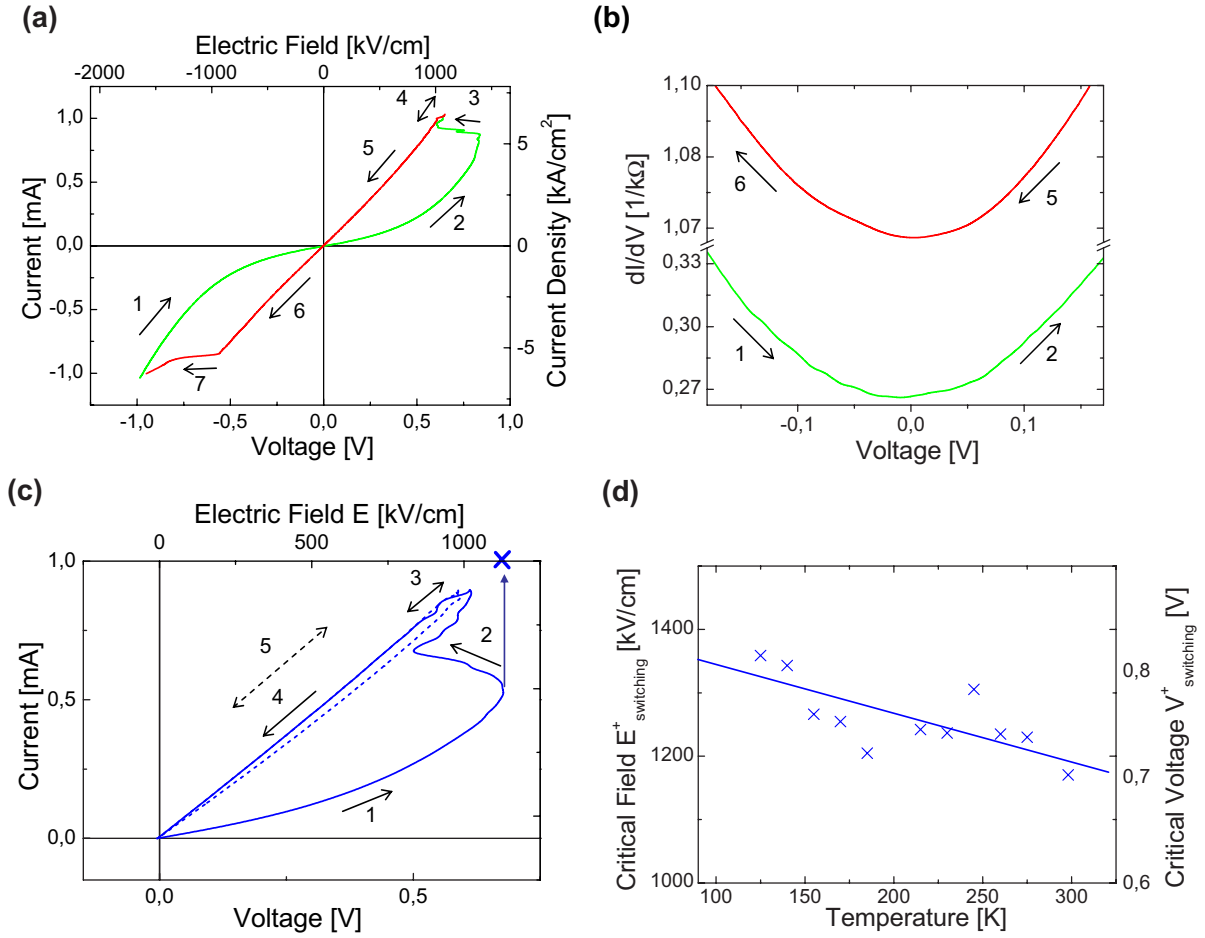


Figure 8.2: (a) I - V curve of a 6 nm thick $BaTiO_3$ film at 260 K. (b) Simultaneously measured dynamic conductance. (c) Demonstration of history effect (for details see text). (d) Temperature dependence of $E_{switching}^+$ (see (c) and text).

field that is insufficient to switch to the high-resistance curve. An increase of the maximum applied bias-current from 1.2 mA to 1.5 mA drastically changes the measured I - V characteristic (solid line). Figure 8.3 (b) shows the I - V curve of a 6 nm thick $PbZr_{0.52}Ti_{0.48}O_3$ film. The I - V curves for both barrier thicknesses are qualitatively similar. Both of them show a crossover at the origin, and switching events at critical fields. These critical fields are larger for tunnel junctions with thinner barriers. The asymmetric shape of the I - V curves in these junctions most likely arises from different work functions at the $Pt/PbZr_{0.52}Ti_{0.48}O_3$ and $PbZr_{0.52}Ti_{0.48}O_3/SrRuO_3$ interfaces. The resistance ratio of the low- and high-resistance curve at the origin are similar for both film thicknesses. The ratio is around 3 for the 4 nm thick

sample resulting from a resistance of $0.5 \text{ k}\Omega$ and $1.5 \text{ k}\Omega$ for the low-resistance and the high-resistance curve, respectively. For the 6 nm thick sample, the ratio is close to 4 with a resistance of $1.1 \text{ k}\Omega$ and $4.3 \text{ k}\Omega$ for the corresponding curves. The current density, and the $R \cdot A$ -product, however, differ by two orders of magnitude.

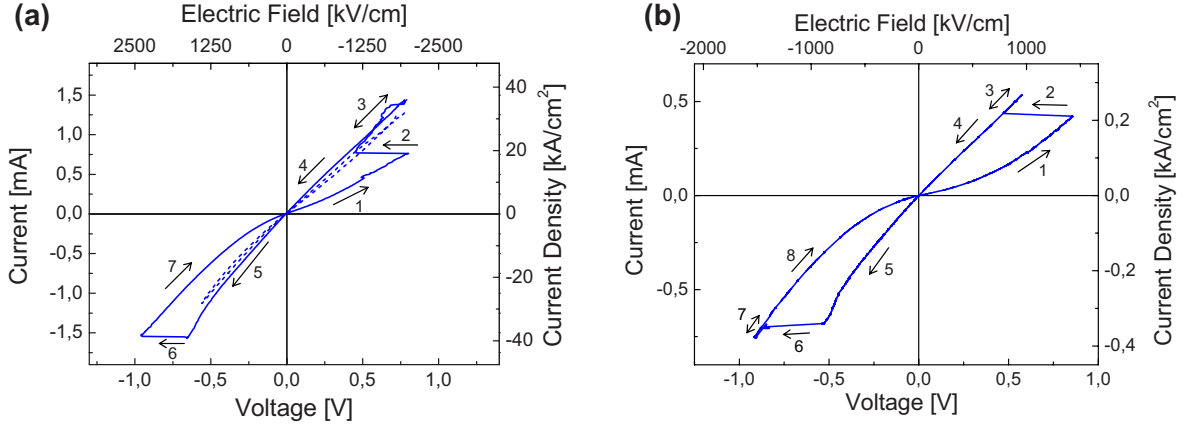


Figure 8.3: (a) I - V curve of a 4 nm thick $\text{PbZr}_{0.52}\text{Ti}_{0.48}\text{O}_3$ film. Dashed line: Electric field insufficient to switch to the high-resistance state. (b) I - V curve of a 6 nm thick $\text{PbZr}_{0.52}\text{Ti}_{0.48}\text{O}_3$ film.

The mean critical field $E_{switching}$ is determined from the mean switching voltage $V_{switching} = 1/2 (|V_{switching}^-| + V_{switching}^+)$ to account for the asymmetry in the I - V curves. The thickness dependence of the mean critical voltage and field of $\text{PbZr}_{0.52}\text{Ti}_{0.48}\text{O}_3$ tunnel junctions with a barrier thickness of 4 nm , 5 nm , and 6 nm is shown as a function of the barrier thickness in Figs. 8.4 (a) and (b). For a 3 nm thick $\text{PbZr}_{0.52}\text{Ti}_{0.48}\text{O}_3$ film the field, which has to be reached to achieve a full switching, is close to the breakdown field of approximately 3 MV/cm . Thus, no data for this sample is shown here. In order to check whether the reported switching effect may reflect the polarization reversal in the tunnel barrier the coercive voltage V_c and field E_c extracted from the polarization hysteresis loops of thicker $\text{PbZr}_{0.52}\text{Ti}_{0.48}\text{O}_3$ films (see Chap. 7.3, p. 114) is included in Figs. 8.4 (a) and (b).

The coercive voltage of the thinnest capacitors is nearly constant, and so is the critical voltage of the tunnel junctions. At the same time, both the coercive field and the critical field increase rapidly with decreasing film thickness. The extrapolation of the coercive voltage and coercive field does not fit the data for the resistive switching. However, owing to the frequency

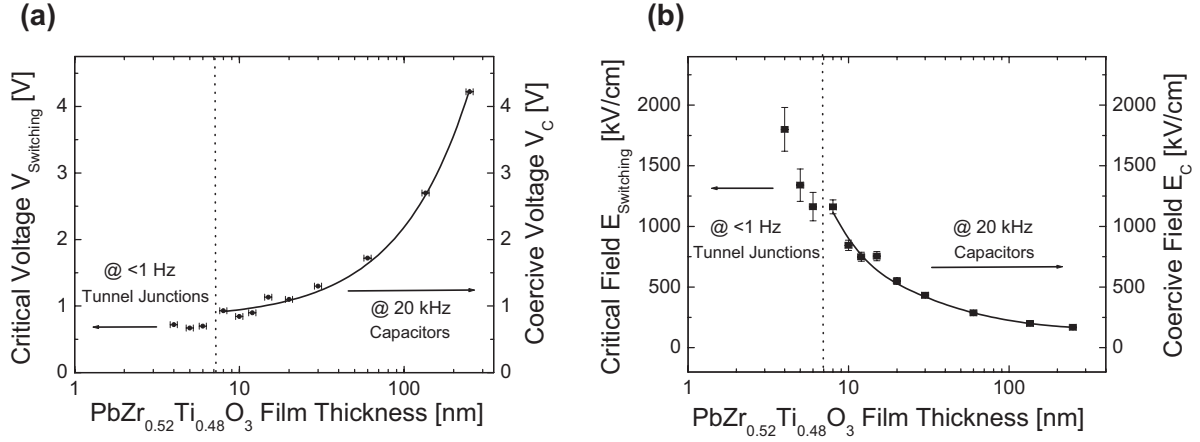


Figure 8.4: Thickness dependence of the (a) critical and coercive voltage, and (b) critical and coercive field.

dependence of the coercive field (Fig. 7.12 (b)) and a much lower frequency of the I - V measurements, the critical voltage and field of the resistive switching are indeed expected to be lower than the extrapolated coercive voltage and field.

The good agreement between the film thickness dependences of the coercive voltage and field, and the critical voltage and field indicates the same origin of both discussed phenomena. Thus, the resistive switching in ultrathin ferroelectric films is probably due to the polarization reversal in the barrier.

8.2 Current transport mechanisms

In this Chapter emphasis is given to the current transport through ultrathin films. The parabolic voltage dependence of the dynamic conductance shown in the previous Chapter is indicative of electron tunneling. In the following, the tunneling mechanisms present in our films will be studied.

Direct tunneling

I - V curves of $\text{SrRuO}_3/6 \text{ nm BaTiO}_3/\text{SrRuO}_3$ junctions were fitted by the Brinkman equation (eqn. (2.5)) in order to extract the apparent average barrier thickness d and its heights Φ_1 and Φ_2 . At 300 K, the barrier heights were determined as $\Phi_{1,low} = 0.8 \text{ eV}$ and $\Phi_{2,low} = 0.5 \text{ eV}$ for the low-resistance state and $\Phi_{1,high} = 0.5 \text{ eV}$ and $\Phi_{2,high} = 0.7 \text{ eV}$ for the high-resistance state. The

average barrier thickness for both states were found to be about $d = 1.4$ nm. The large discrepancy between the barrier thickness and the as-deposited film thickness may be due to a strong contribution of thermally-assisted inelastic transport processes (see Ref. [85]). In fact, magnetic tunnel junctions with $SrTiO_3$ barriers show a similar behavior caused by the presence of parallel defect-assisted conductance shunting out the direct, spin-dependent conduction process [217]. For decreasing temperature, the barrier thickness extracted by the application of the Brinkman-model increases as it is shown in Fig. 8.5 (b). At 4.2 K the Brinkman-fit yields an average barrier thickness of 5.8 nm and 5.6 nm for the low- and high-resistance state, respectively, in very good agreement with the as-deposited film thickness of 6 nm (Fig. 8.5 (a)). However, the extracted barrier heights are below 0.1 eV for both resistance states and for both interfaces. These barrier heights are too low (see Chap. 4.1).

A further possibility of discovering whether direct tunneling is the dominant current mechanism is given by the determination of the $R \cdot A$ -product. Using eqn. (2.5), the $R \cdot A$ -product in $k\Omega\mu m^2$ as a function of the barrier thickness d in \AA and the average barrier height $\bar{\Phi}$ in eV is obtained as

$$R \cdot A = 0.03 \cdot (d/\sqrt{\bar{\Phi}}) \cdot \exp(10.25 \cdot d \cdot \sqrt{\bar{\Phi}})/1000. \quad (8.1)$$

In Figure 8.6 $R \cdot A$ -curves for several average barrier heights calculated

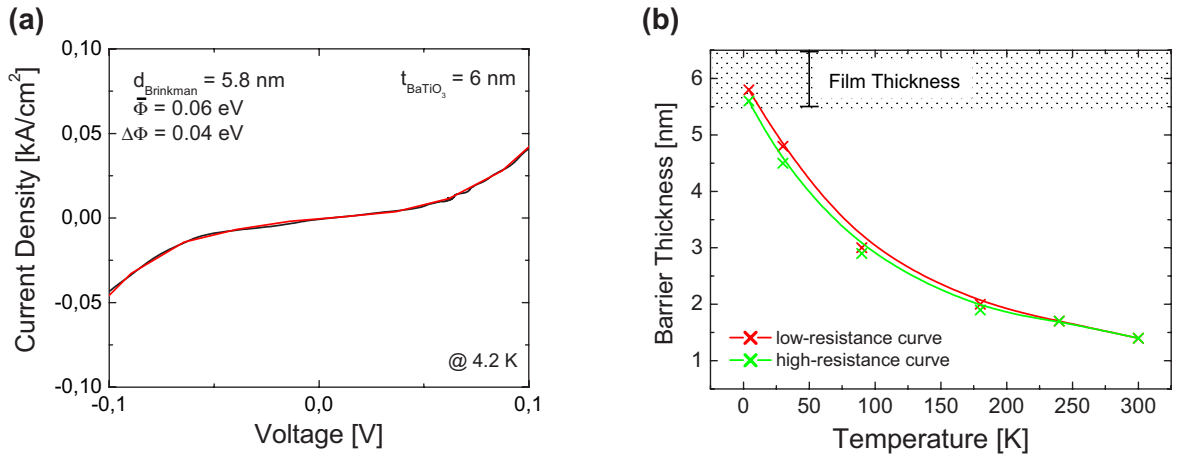


Figure 8.5: (a) Brinkman-fit of the low-resistance I - V curve for a 6 nm thick $BaTiO_3$ film measured at 4.2 K. (b) Temperature dependence of the barrier thickness extracted from Brinkman-fits at temperatures between 4.2 K and 300 K.

from eqn. (8.1) are plotted. The experimental values are included for $PbZr_{0.52}Ti_{0.48}O_3$ and $BaTiO_3$ tunnel junctions measured at 4.2 K. The as-deposited film thickness is set equal to the barrier thickness. In agreement with the results obtained by the application of the Brinkman model, the experimental values are close to the curve corresponding to an average barrier height $\bar{\Phi}$ of 0.05 eV. This is about one order of magnitude lower than expected [122].

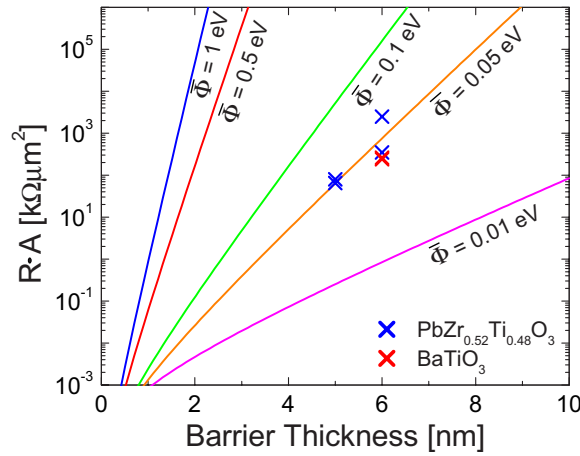


Figure 8.6: Simulated $R \cdot A$ -product as a function of barrier thickness d and average barrier height $\bar{\Phi}$. Experimental values for the $R \cdot A$ -product obtained at 4.2 K are included. The as-deposited film thickness is set equal to the barrier thickness.

The Brinkman model takes into account the direct tunneling only. In this case, electrons tunnel elastically through the barrier without interaction with the material inside it. In real junctions, however, additional current paths through the barrier may exist leading to fit parameters which do not reflect reality. In addition, at temperatures above 0 K, thermally-assisted transport mechanisms have to be taken into account. Besides, the presence of localized states in the barrier influences the conductance for film thicknesses much larger than the localization length.

In conclusion, the current transport through the ultrathin films studied here is not dominated by direct tunneling. More precisely, it is not dominated by direct tunneling at any temperature between 4.2 K and 300 K. Instead, strong contributions of phonon-assisted inelastic transport processes are believed to be present.

Inelastic tunneling

In the following, a detailed analysis of the current transport for a 6 nm thick $PbZr_{0.52}Ti_{0.48}O_3$ sample sandwiched between Pt and $SrRuO_3$ electrodes will be presented.

The I - V curve measured at 300 K (Fig. 8.3 (b)) has already been discussed. In Fig. 8.7 (a) I - V curves obtained at temperatures between 4.2 K and 300 K are shown in the voltage range between -0.08 V and +0.08 V. The I - V curves for the lowest and the highest temperature are plotted in red for the low-resistance and in green for the high-resistance state. The parabolic shape of the voltage dependence of the dynamic conductance, indicative of electron tunneling through an insulating barrier, is shown in Fig. 8.7 (b) for both resistance states at 4.2 K and 300 K. The asymmetry in the I - V curves that probably results from different barrier heights at the interfaces manifests itself in a shift of the minima in the dynamic conductance, whereas the shift of the minima with respect to each other might be due to different barrier heights for the high-resistance and the low-resistance state. The resistance at the origin increases for both resistance states with decreasing temperature (Fig. 8.7 (c)). The increase of the $R \cdot A$ -product for decreasing temperature is particularly strong for the high-resistance curve. Here, the $R \cdot A$ -product rises threefold between 300 K and 4.2 K (from $867 \text{ k}\Omega\mu\text{m}^2$ to $2492 \text{ k}\Omega\mu\text{m}^2$), whereas for the same temperature range, the $R \cdot A$ -product of the low-resistance curve only increases by half of its value at 300 K (from $229 \text{ k}\Omega\mu\text{m}^2$ to $341 \text{ k}\Omega\mu\text{m}^2$). As a result, the resistance ratio of the low- and high-resistance curve at the origin is about 3.8 at 300 K and 7.3 at 4.2 K.

What are the dominant tunneling mechanisms at temperatures between 4.2 K and 300 K? Direct tunneling has been ruled out already. Nevertheless, for completeness the application of the Brinkman model at 4.2 K is shown in Fig. 8.8 (a). The average barrier thickness extracted from these fits are 4.4 nm for the low-resistance curve and 5.2 nm for the high-resistance curve in reasonable agreement with the as-deposited film thickness of 6 nm. However, the barrier heights (~ 0.1 eV for both states and interfaces) are about 5 times smaller than expected. Above, we attributed the disagreement between the extracted and the expected barrier heights to a large contribution of phonon-assisted inelastic tunneling.

Hopping via a small number of localized states in the barrier is one example of inelastic tunneling. In order to check whether this mechanism can be identified as the dominant current transport mechanism, we fitted

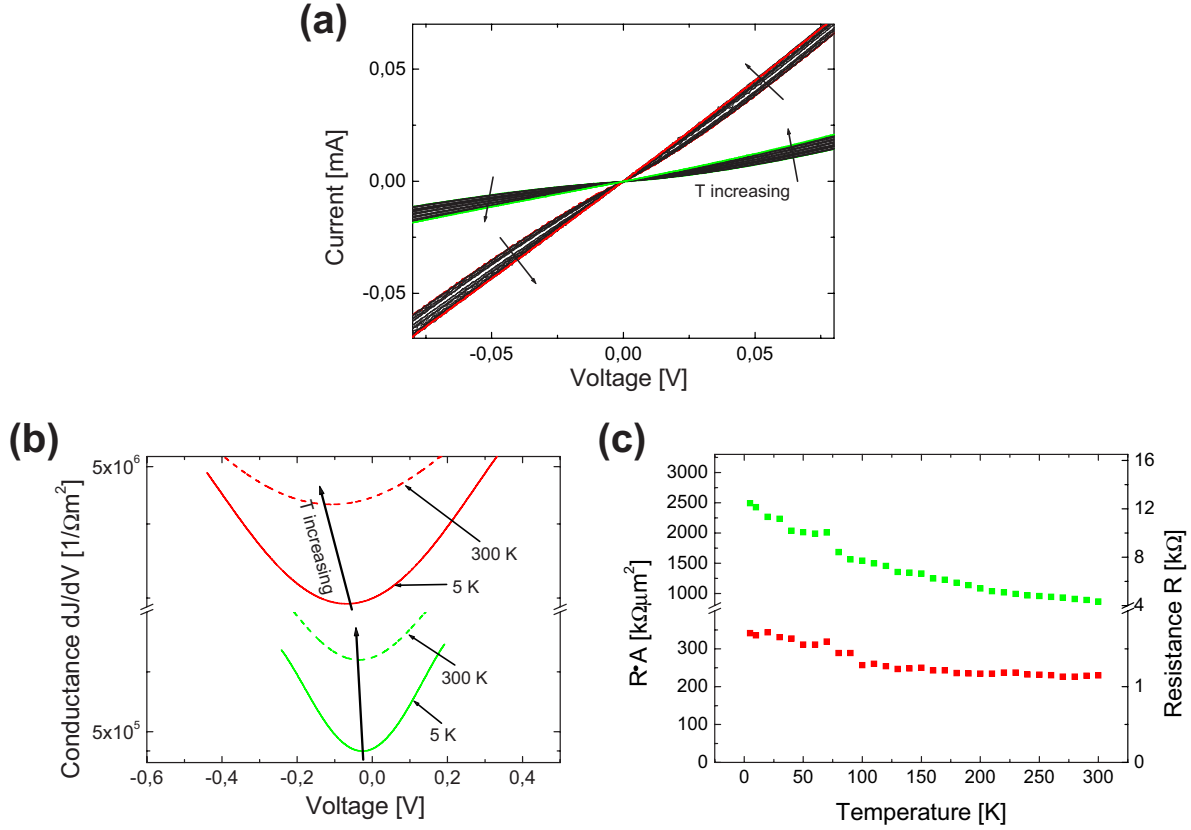


Figure 8.7: Temperature dependence of (a) I - V curve, (b) dynamic conductance, and (c) $R \cdot A$ -product for a tunnel junction with a 6 nm thick $\text{PbZr}_{0.52}\text{Ti}_{0.48}\text{O}_3$ barrier.

the data with the model of Matveev-Glazman in the low bias-voltage limit (eqn. (2.10)). Note that the low bias-voltage requirement $eV \ll k_B T$ is not fulfilled. To satisfy the requirement at 100 K, the conductance would have to be determined for voltages much smaller than $25/3$ mV. At a temperature of 4.2 K the low bias-voltage limit would only be reached for voltages much smaller than 0.4 mV. Although sufficient data points were measured to satisfy this requirement, the determination of the conductance in this regime is impossible, as the noise is too large. Nevertheless, a successful description of the tunneling transport mechanisms may be achieved if the conductance is determined in the ohmic regime of the measured I - V curve [85]. Therefore, we extracted the conductance from the data in the ohmic regime between ± 10 mV. In Fig. 8.8 (b) the temperature dependence of the conductance is shown including the corresponding fits for the low-resistance state (red) and the high-resistance state (green). The dashed lines show the fits for hopping

via two localized states to the form

$$G_2^{hop}(T) = \sigma_0 + \sigma_1 T^{4/3}, \quad (8.2)$$

and the solid lines correspond to fits for hopping via three localized states in the barrier:

$$G_3^{hop}(T) = \sigma_0 + \sigma_1 T^{4/3} + \sigma_2 T^{5/2}. \quad (8.3)$$

The low-resistance fit for hopping via two localized states is accurate for temperatures up to about 40 K. At about 40 K a crossover to $N = 3$ channel takes place. Above 40 K and up to 90 K hopping channels with three localized states are dominant. In the case of the high-resistance state, hopping via two localized states is found up to about 70 K followed by hopping via three localized states up to about 150 K.

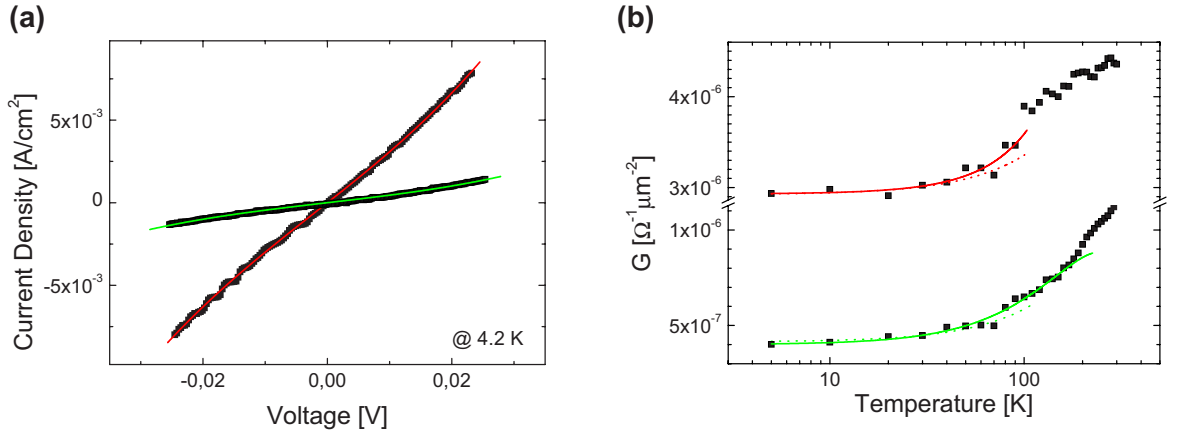


Figure 8.8: (a) Brinkman-fit (direct tunneling), and (b) fit for tunneling via two (dashed lines) or three (solid lines) localized states of the low-resistance (red) and high-resistance (green) state of a 6 nm thick $PbZr_{0.52}Ti_{0.48}O_3$ film.

According to the theoretical models discussed in Chapter 2, a crossover from hopping via N localized states to variable range hopping may be expected for thick barriers as the temperature is increased. In Fig. 8.9 (a) the conductance of the low-resistance and the high-resistance state is plotted on a logarithmic scale versus $T^{-1/4}$. The behavior of both resistance states closely follows the prediction of Mott's VRH theory (see page 34) in the temperature range between 100 K and room temperature, and 150 K and room temperature for the low-resistance and the high-resistance state, respectively. The green and red lines are fits to the form

$$G^{VRH} = \hat{G}_0^{VRH} \cdot \exp\left(-\left(\frac{\tilde{T}}{T}\right)^{1/4}\right). \quad (8.4)$$

Fig. 8.9 (b) is a logarithmic plot of the current density versus $E^{-1/4}$. The data is fitted to Shklovskii's model

$$J^{VRH} = \hat{J}_0^{VRH} \cdot \exp\left(-\left(\frac{\tilde{E}}{E}\right)^{1/4}\right). \quad (8.5)$$

The Shklovskii model (see page 34) precisely fits the data in the high bias-voltage regime ($eV \gg k_B T$) of both the low-resistance and the high-resistance curve.

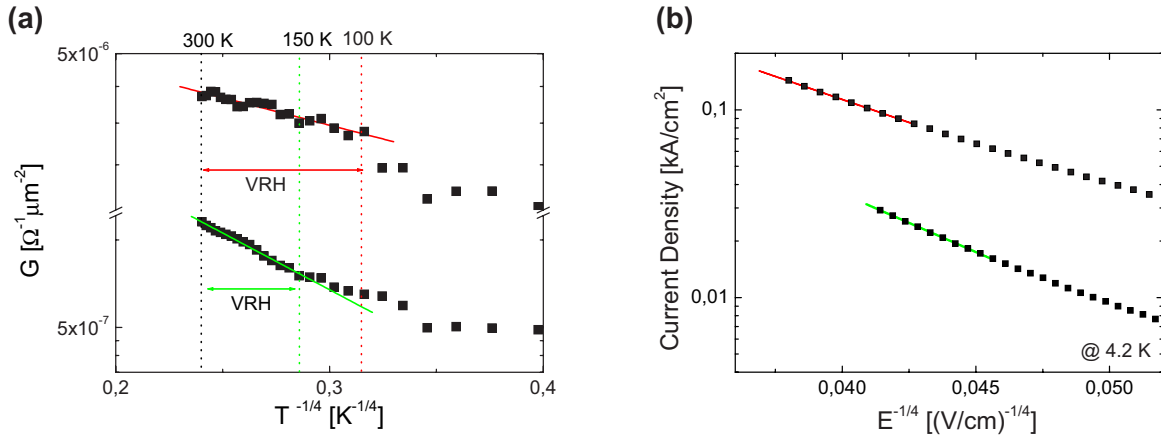


Figure 8.9: Application of (a) Mott's law, and (b) Shklovskii's model to the low-resistance (red) and high-resistance (green) state of a 6 nm thick $\text{PbZr}_{0.52}\text{Ti}_{0.48}\text{O}_3$ film.

In conclusion, the electron tunneling theories developed for amorphous materials have been applied to our single-crystalline thin films. Those theories are believed to be applicable to perovskite materials, due to their large defect density (see Chapter 2). We have demonstrated that the current transport through the studied $\text{PbZr}_{0.52}\text{Ti}_{0.48}\text{O}_3$ and BaTiO_3 barriers with film thicknesses between 4 nm and 6 nm is dominated by phonon-assisted inelastic tunneling processes for all temperatures between 4.2 K and 300 K. We have analyzed in detail the current transport mechanisms through a 6 nm thick $\text{PbZr}_{0.52}\text{Ti}_{0.48}\text{O}_3$ film. For the low-resistance curve, hopping via two

localized states has been identified as the dominant current mechanism between 4.2 K and about 40 K. From 40 K up to approximately 90 K hopping via three localized states and from about 100 K up to 300 K variable range hopping has been found to be dominant. For the high-resistance curve, the crossover from hopping via two localized states to hopping via three localized states takes place at about 70 K, and the crossover to variable range hopping occurs at 150 K. In addition, variable range hopping is the dominant current transport mechanism for both resistance states at high bias-voltages.

8.3 Similar switching effects reported by other groups

Switching processes in thin films have been reported for a variety of material systems. In the late 1960s such effects were already found in amorphous semiconductors [218, 219], $ZnSe - Ge$ heterostructures [220], as well as in several binary oxides, such as Nb_2O_5 [221], Ta_2O_5 [222], TiO_2 [223], and NiO [224, 225]. More recently, bistable states have been observed in porous Si [226], and conducting polymers [227, 228, 229]. In the following, the focus will be on switching events reported in complex perovskite materials.

Fig. 8.10 (a) shows the current-voltage characteristic of 300 nm thick $SrZrO_3$ films doped with 0.2% Cr , and sandwiched between $SrRuO_3$ bottom electrodes and Au top electrodes. Beck *et al.* from IBM Research, Switzerland, measured the $I-V$ curve using a voltage source [230]. A striking property of their capacitors is the observed multi-level switching illustrated in Fig. 8.10 (b). Different low-resistance states can be addressed by varying the length and amplitude of the applied voltage pulse. Beck *et al.* attribute the multi-level switching effect to impurities with different oxidation states (Cr^{3+} and Cr^{4+}) and vacancies forming a series of states at various levels within the energy gap.

In a more recently published letter, Rossel *et al.*, from the same group at IBM Research, Switzerland, presented the $I-V$ characteristic shown in Fig. 8.11 (a) [231]. This $I-V$ curve was recorded for a $Pt/SrZrO_3(0.2\%Cr)/SrRuO_3$ capacitor. The thickness of the $SrZrO_3$ was 35 nm. Surprisingly, the thickness of the electrodes was only 5 nm for the top electrode and 4 nm for the bottom electrode. The question arises of whether in particular the low conductivity of the $SrRuO_3$ electrode does not play an important role

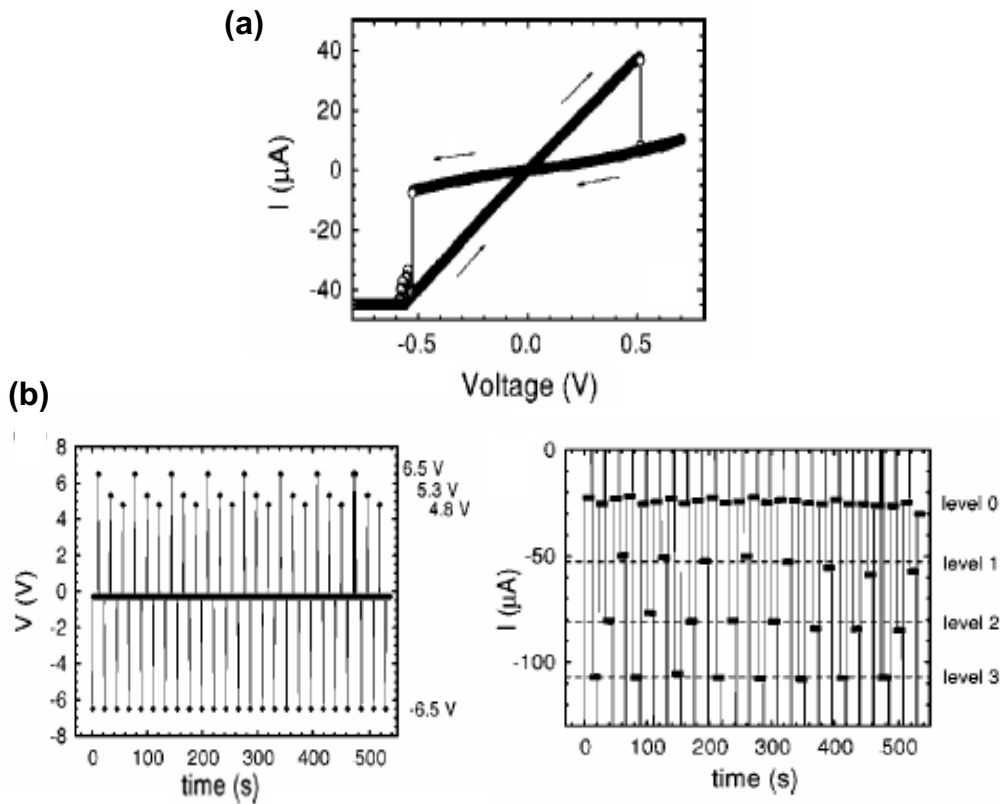


Figure 8.10: Beck et al.: (a) I - V curve of a 300 nm thick $SrZrO_3$ film doped with 0.2% Cr , and sandwiched between Au and $SrRuO_3$ electrodes. (b) Illustration of multi-level switching. [230]

in their measurements. By comparing transport measurements with a special scanning technique that visualizes conduction paths (Fig. 8.11 (b)), they showed that the main current flow is restricted around some, but not all, intrinsic defects in the Cr -doped $SrZrO_3$ film. Based on their studies, they concluded that the electrical switching in thin films correlates to a large extent to the properties of individual conducting paths that can be locally turned on and off or changed in intensity by varying the amplitude of the applied current. Rossel and coworkers claim that the Cr ions act as local traps within the insulator, and in addition to other intrinsic defects form a broad band of localized states. According to their model, electrons injected from the cathode tunnel to these localized states, if the applied voltage exceeds a certain threshold equivalent to the energy defining the top of the localized levels with respect to the Fermi level. The storage of negative charges near the top of the localized band in the insulator reduces the electrical field at the interface and consequently reduces the current flowing through the insu-

lator. Hence, a higher resistance state is reached by storing trapped charges, whereas the lower resistance state is reestablished by releasing them. The ratio of the two resistance states is given by the amount of charge stored in the system.

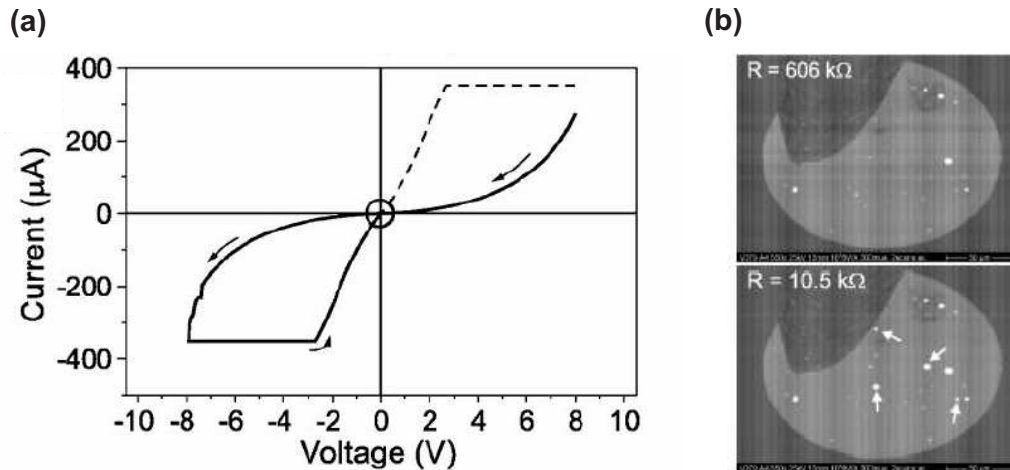


Figure 8.11: Rossel et al.: (a) I - V curve of a 35 nm thick $SrZrO_3$ film doped with 0.2% Cr sandwiched between Pt and $SrRuO_3$ electrodes. (b) Electron beam induced current (EBIC) images visualizing current paths through the $SrZrO_3$ film. [231]

The IBM group also studied Cr -doped $SrTiO_3$ single crystals with a thickness of 10 μm [232]. The observed I - V curve at room temperature is shown in Fig. 8.12 (a). The resistance decreases for increasing temperature and remains stable between 4.2 K and 10 K. As was reported for thin films, multi-level states can be addressed in single crystals as well (Fig. 8.12 (b)).

Y. Watanabe reported on hysteresis in diodelike I - V curves of metal/ Pb -based ferroelectrics/ n -type and p -type semiconductor heterostructures with a poor reproducibility at 4.2 K [233] and a good reproducibility at room temperature [234, 235, 236]. Figs. 8.13 (a) and (b) show the I - V characteristic for a maximum applied voltage of 1 volt and 2 volts, respectively. He discussed various possible origins of the observed hysteresis effect, e.g. Fowler-Nordheim-type tunneling [235] or electromigration at the interface, which could change the Schottky barrier height [233].

In summary, resistive switching effects have been found for a variety of material systems. A brief overview of some of the results published for

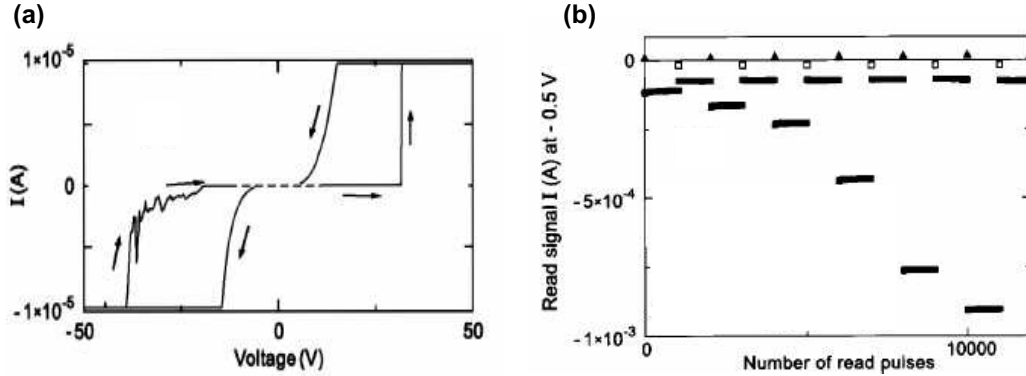


Figure 8.12: Watanabe and coworkers at IBM Zürich: (a) I - V curve recorded at 296 K on a $SrTiO_3 : Cr$ single crystal. (b) Multiple low-resistance states obtained at 4.5 K after write pulses (\blacktriangle) with different current amplitudes of 1.5, 2.2, 2.5, 2.7, 3.0, 3.5 mA and erase pulses (\square) with a fixed amplitude of -3.55 mA. Each pulse is followed by 1000 readouts at -0.5 V. [232]

perovskite materials has been given in this Chapter. Particularly the I - V characteristics obtained by the IBM group show some interesting similarities with the current-voltage curves reported in this PhD thesis. Nevertheless, we do believe that the current transport and the origin of the switching effects are different. We base our assumption on the following distinctions: First, the thickness of our films is smaller by at least one order of magnitude. Besides, the switching effects presented in Chap. 8.1 for 4 nm to 6 nm thick $PbZr_{0.52}Ti_{0.48}O_3$ and $BaTiO_3$ films were not observed for 12 nm thick barriers. I - V curves recorded for junctions with this thickness showed non-reproducible jumps or hysteresis in the I - V characteristic at much higher voltages, most likely due to a deterioration of the ferroelectric film. Second, we do not find multi-level resistance states in our junctions. And finally, the temperature dependence of the resistance, which decreases with decreasing temperature, differs from that measured for tunnel junctions with $PbZr_{0.52}Ti_{0.48}O_3$ or $BaTiO_3$ barriers, where the resistance increases with decreasing temperature.

8.4 Final remarks on resistive switching and current transport mechanisms

The thickness dependence of the coercive voltage (and coercive field) for thick-film capacitors can be extrapolated to ultrathin films. Taking into ac-

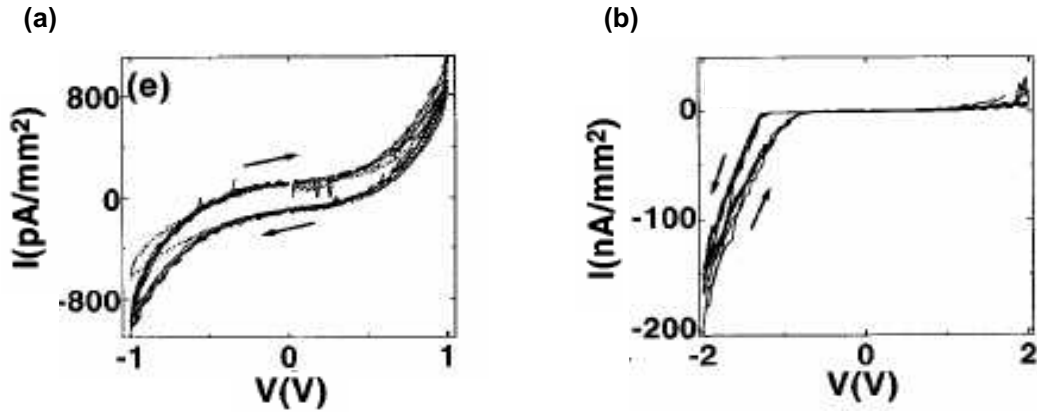


Figure 8.13: Watanabe et al.: I - V curves of metal/ $Pb_{0.9}La_{0.1}Zr_{0.7}Ti_{0.3}O_3/La_{1.99}Sr_{0.01}CuO_4$ heterostructures for a maximum applied voltage of (a) 1 volt and (b) 2 volts. [236]

count the frequency dependence of the coercive field (Fig. 7.12 (b)), a good agreement is obtained with the critical voltage (and critical field) of the resistive switching events. Based on this result, the observed resistive switching events are likely to originate from the ferroelectric polarization reversal in the tunnel barrier.

Resistive switching

In the following, our predictions will be compared with the experimental results. Theoretical calculations were presented in Chapter 3 to determine the influence of the converse piezoelectric effect (i.e. the voltage-induced strain in a piezoelectric or ferroelectric film) on direct electron tunneling in a ferroelectric tunnel junction. In addition, a microscopic interface effect was considered, which arises from the ionic movements in the barrier associated with the polarization reversal. Due to a lack of knowledge of some specific material properties (e.g. the deformation potential), no unambiguous prediction on the influence of the combination of all identified effects was possible. Nevertheless, the influence of two phenomena, i.e. a strain-induced change in the barrier thickness of an FTJ and the influence of the microscopic interface effect, was predicted.

Figure 8.14 shows the predicted I - V characteristics for (a) a strain-induced change of the barrier thickness, and (b) the microscopic interface effect. Details can be found in Chapter 3. Experimentally obtained I - V

curves for tunnel junctions with 6 nm thick $PbZr_{0.52}Ti_{0.48}O_3$ barriers are shown in Fig. 8.14 (c) for a voltage-driven measurement and in (d) for a current-driven measurement. In Fig. 8.14 (c) the voltage scale is not shown because the applied external voltage differs from the voltage applied to the ferroelectric film. For details refer to p. 117 and p. 123, respectively.

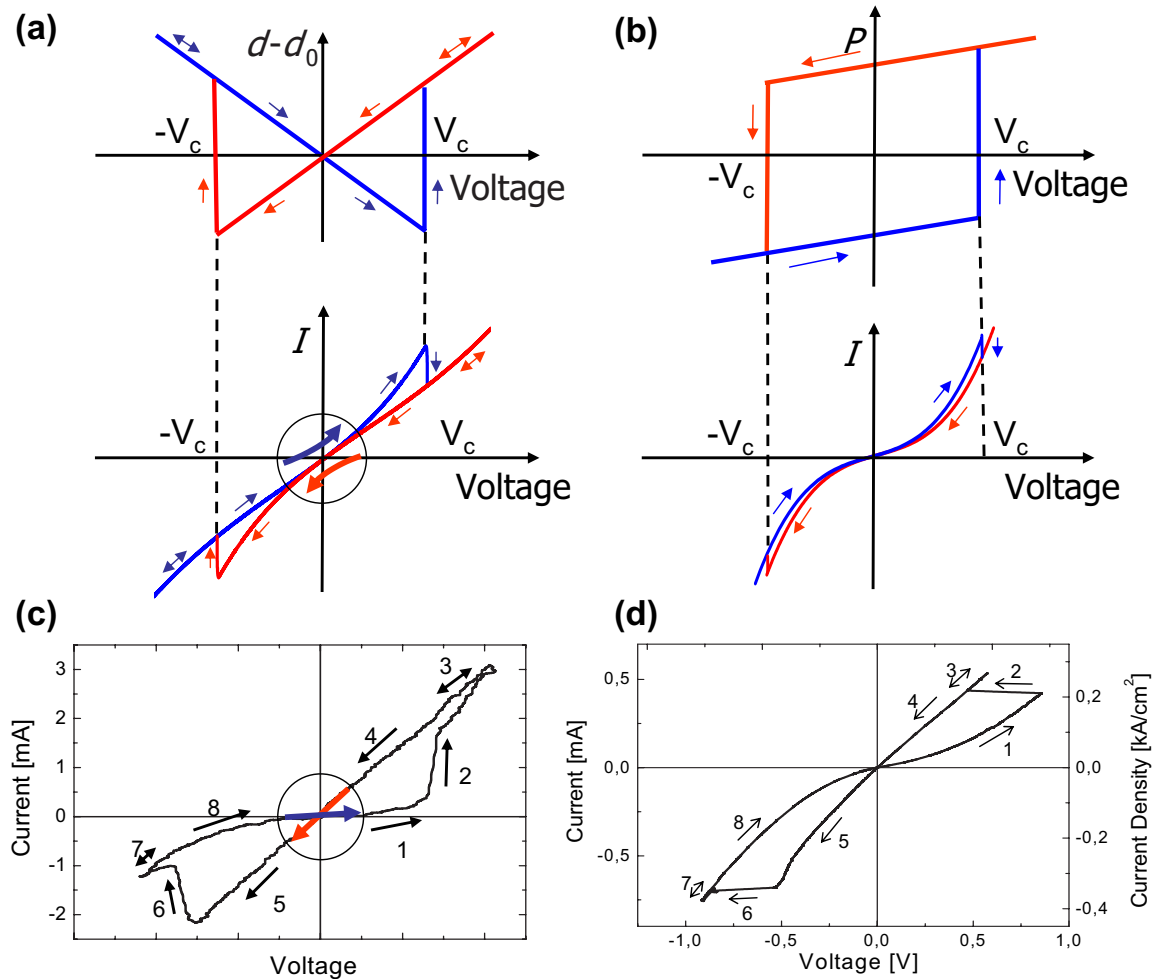


Figure 8.14: (a) Consequence of the converse piezoelectric effect for a ferroelectric barrier: Voltage-induced change of the barrier thickness. (b) Microscopic interface effect due to polarization reversal. (c) Voltage-driven measurement of a 6 nm thick $PbZr_{0.52}Ti_{0.48}O_3$ barrier. (d) Current-driven measurement of a 6 nm thick $PbZr_{0.52}Ti_{0.48}O_3$ barrier. See text for details.

An apparent distinction between the current-driven measurements and the predicted curves is the direction of the switching events. Measurements performed with a current source show sudden changes in voltage, because a

current source supplies a predetermined current. Hence, the voltage-driven and current-driven measurements are in agreement with the predictions with respect to the direction of the switching events.

The I - V curves for the strain-induced change of the barrier thickness and the microscopic interface effect both show a step-like reduction of the conductance at $\pm V_c$. However, such a reduction is not present in the experimental curves at $V_{switching}^+$.

The most striking difference between predicted and observed I - V curves is their behavior at the origin (marked by circles in Figs. 8.14 (a) and (c)). A crossover is observed in the experiments in disagreement with the predictions. Thus, the symmetry of the I - V characteristics is different. It should be noted that the predicted symmetry is a characteristic feature for all effects arising from the piezoelectric effect (e.g. strain-induced shift of the conductance and valence band edges).

In conclusion, some features are identical for the predicted and the experimentally observed I - V characteristics. However, the observed switching events in the I - V curves cannot be exclusively explained by either the converse piezoelectric effect, or by a change of the barrier heights of the metal-ferroelectric and the ferroelectric-metal interfaces. Especially the different symmetry of the predicted and the measured curves demonstrates that further research is necessary to unambiguously verify the nature of the observed resistive switching effects. At present, it is an open question whether the observed distinctions may be associated with further manifestations of ferroelectricity or caused by additional effects not related to ferroelectricity.

Current transport mechanisms

In order to simplify the theoretical study, an elastic current transport mechanism is desirable. In fact, direct electron tunneling was assumed for the theoretical treatment of ferroelectricity and electron tunneling presented in Chapter 3. The presence of inelastic transport processes may lead to additional, superimposed effects, which might be larger than those discussed for direct tunneling.

In our tunnel junctions with $PbZr_{0.52}Ti_{0.48}O_3$ and $BaTiO_3$ barriers, inelastic current transport mechanisms are dominant for all investigated barrier thicknesses and all temperatures between 4.2 K and room temperature. Di-

rect electron tunneling is probably achievable for a barrier thickness below two nm. Morán *et al.* studied the current transport for tunnel junctions with a $SrTiO_3$ barrier thickness ranging from 2 nm to 20 nm [82, 83]. They observed elastic tunneling, but only for a barrier thickness of nominally 2 nm. Even for slightly thicker $SrTiO_3$ barriers, tunneling and hopping via a small number of localized states dominated the transport behavior. $SrTiO_3$ is a perovskite titanate like the ferroelectric materials used in this work. It thus seems straightforward to grow films with thicknesses of 2 nm and less. However, the switching field for a 2 nm thick $PbZr_{0.52}Ti_{0.48}O_3$ barrier, assuming a switching voltage of 0.7 V, is as large as 3.5 MV/cm. Recalling that the breakdown field was already reached for 3 nm thick $PbZr_{0.52}Ti_{0.48}O_3$ films. The breakdown in $BaTiO_3$ films was observed for even smaller fields. For future studies the use of ferroelectric materials with lower coercive fields is suggested.

Summary

The concept of a ferroelectric tunnel junction has been presented. The device was termed FTJ and consists of a ferroelectric layer sandwiched between metal electrodes. The ferroelectric layer has to be thin enough to allow quantum-mechanical electron tunneling.

The aim of this work was the study of a possible interaction of ferroelectricity and the quantum-mechanical electron tunneling through the ferroelectric barrier. This involved both experimental and theoretical tasks.

From the experimental point of view, the main challenge was the growth of *ferroelectric* films as thin as a few nm. Size effects may decrease the manifestation of ferroelectricity. They may even completely suppress ferroelectricity in sufficiently thin films. Hence, the first step was the selection of the appropriate material system yielding favorable boundary conditions with the ultimate goal of stabilizing the ferroelectric phase.

In this thesis, we primarily studied the heterostructures of $Pt/PbZr_{0.52}Ti_{0.48}O_3/SrRuO_3$ and $SrRuO_3/BaTiO_3/SrRuO_3$, both grown on $SrTiO_3$ (100) substrates. Three different deposition techniques were used, namely high-pressure sputtering, molecular beam epitaxy, and pulsed laser deposition. For the characterization and optimization of the thin films, various analytical methods were utilized, among them XRD, RBS, AFM, HRTEM, and RHEED (for MBE-grown thin films).

Compressive strain is induced in the ferroelectric $PbZr_{0.52}Ti_{0.48}O_3$ and $(Ba, Sr)TiO_3$ thin films by the $SrTiO_3$ substrate due to its smaller in-plane lattice parameter. This substrate effect is an opponent of the surface effect, which tends to decrease the polarization in subsurface layers. On the other hand, it has to be taken into account that too much strain leads to strain relief via generation of misfit dislocations. First, very promising results were obtained on the novel substrate material, $DyScO_3$. This substrate provides a

perfect lattice match for the growth of $SrRuO_3$ thin films, which we used as a bottom electrode. In comparison with $SrTiO_3$, the in-plane lattice parameters of $DyScO_3$ are slightly larger. This reduces the compressive strain in oxide perovskite materials, such as $PbZr_{0.52}Ti_{0.48}O_3$ and $BaTiO_3$. Thus, its use as substrate material is expected to increase the critical film thickness for the introduction of strain-releasing defects. The conducting oxide perovskite $SrRuO_3$ was employed as the bottom electrode due to its good structural and chemical compatibility with $SrTiO_3$ and the ferroelectrics used. Remarkably, we were able to grow $SrRuO_3$ exhibiting an even smoother surface than the bare $SrTiO_3$ substrate. Needless to say, a smooth surface leading to a sharp interface between the electrode and the barrier is a strong requirement for the successful preparation of a tunnel junction with a barrier consisting of a few monolayers. The most frequently studied ferroelectric perovskite was employed in the composition $PbZr_{0.52}Ti_{0.48}O_3$ because it combines a large spontaneous polarization with the strongest piezoelectric effect. The second ferroelectric material studied within this work was $BaTiO_3$. Its main advantage compared to $PbZr_{0.52}Ti_{0.48}O_3$ is the smaller lattice mismatch with the $SrRuO_3/SrTiO_3$ heterostructure allowing for a thicker ferroelectric film without misfit dislocations. So far, only mechanical boundary conditions have been considered. However, electrical boundary conditions are important as well. For example, the use of $SrRuO_3$ as top electrode material for $PbZr_{0.52}Ti_{0.48}O_3$ -based capacitors resulted in an extrinsic size effect. We attributed this size effect to increased leakage currents due to a smaller barrier height at the $SrRuO_3/PbZr_{0.52}Ti_{0.48}O_3$ interface in comparison to the barrier height at the $Pt/PbZr_{0.52}Ti_{0.48}O_3$ interface. In contrast, the opposite observation for $BaTiO_3$ thin films, i.e. higher leakage currents in the case of Pt top electrodes, remains unexplained.

Once the growth techniques were well established, and the material systems were selected, the ferroelectric properties of thick-film capacitors of progressively shrinking film thickness could be studied. It was of particular interest to determine both the thickness dependence of the remanent polarization and the thickness dependence of the coercive field. The purpose of doing this can be stated as follows. First, the observation of a ferroelectric hysteresis loop with a non-zero remanent polarization demonstrates the presence of ferroelectricity in the film. Besides, $PbZr_{0.52}Ti_{0.48}O_3$ and strained $BaTiO_3$ films are predicted to undergo a second-order phase transition from the ferroelectric to the paraelectric phase. Thus a continuous change of the polarization may be expected. Therefore, its thickness dependence yields information about the stability of the ferroelectric phase. And second, typical analytical methods fail to detect ferroelectricity in ultrathin

films, although they might be ferroelectric. Instead, knowledge of the thickness dependence of the coercive field can be used to extrapolate the coercive field for an ultrathin ferroelectric film, which serves as barrier in a FTJ. We started by growing 250 nm thick $PbZr_{0.52}Ti_{0.48}O_3$ films and 100 nm thick $BaTiO_3$ films. A nearly constant remanent polarization was observed for both ferroelectric materials studied, i.e. for $PbZr_{0.52}Ti_{0.48}O_3$ films in a film thickness range between 250 nm and 10 nm and $BaTiO_3$ films with a thickness ranging from 100 nm to 12 nm. Remarkably, the value for the remanent polarization in $PbZr_{0.52}Ti_{0.48}O_3$ thin films was identical to the spontaneous polarization of a stress-free bulk single crystal for this composition. Based on this result, we concluded that either no intrinsic size effect is present for this thickness range, or the intrinsic size effect is compensated by the substrate effect. A further proof, showing that the ferroelectric phase in a 10 nm thick $PbZr_{0.52}Ti_{0.48}O_3$ film is still far from losing the stability, was the observation of ferroelectric polarization reversals at 300°C. In fact, ferroelectricity was demonstrated in 8 nm thick films, and piezoresponse force microscopy experiments revealed ferroelectricity even in 6 nm thick $PbZr_{0.52}Ti_{0.48}O_3$ films. This is already a thickness regime in which electron tunneling may be observed. Hence, the study of thick-film capacitors with the ultimate goal of ensuring ferroelectricity in ultrathin tunnel barriers was successful. The second important result was the determination of the coercive voltage, which was constant for the thinnest $PbZr_{0.52}Ti_{0.48}O_3$ thin films. At the same time, the coercive field was increasing for thinner films.

The optimization of thin-film growth conditions typically takes a long time and does not provide much entertainment. This is the best time to develop some theoretical ideas on what might be expected if we succeeded in measuring a tunneling current through a ferroelectric barrier.

From a fundamental point of view, direct electron tunneling is the only current transport mechanism present in a metal-insulator-metal structure at 0 K. Chapter 3 of this thesis deals with the term, which describes the tunneling probability for direct electron tunneling. In collaboration with N. A. Pertsev, we identified and predicted various interactions of the converse piezoelectric effect and the ferroelectric polarization reversal with direct electron tunneling. In the following, I will briefly summarize these effects.

The converse piezoelectric effect, i.e. the linear voltage dependence of the strain in a piezoelectric material, leads to three strain-induced effects, each of which alters the tunneling probability. First, a strain-induced change of the barrier thickness. Second, a strain-induced change of the effective mass of the

electrons in the barrier arising from a change of the lattice parameters. And third, a strain-induced shift of the valence and conduction band edges. Due to a lack of knowledge of some specific material properties, no unambiguous prediction on the influence of the combination of all three identified strain-induced effects was possible. In fact, it is likely that the first two effects mentioned and the latter effect partially compensate each other. Nevertheless, it seems very unlikely that they could compensate each other exactly. Irrespective of this uncertainty, a current-voltage characteristic was calculated taking into account a strain-induced change in the barrier thickness of a FTJ. Using typical values for $PbZr_{0.52}Ti_{0.48}O_3$, considerable effects were obtained. The features characterizing this strain-induced thickness variation were a sudden change of the tunneling current at the coercive field of the barrier material, and a shift of the minima in the dynamic conductance with respect to each other and with respect to the origin.

In addition to the converse piezoelectric effect, the idea was discussed that the microscopic manifestation of the polarization reversal, i.e. a change in the atomic structure, may change the barrier potential. Surprisingly, the I - V curve for the simulation of this effect is characterized by the same main features as obtained above for the strain-induced change of the barrier thickness. Despite these similarities, both effects are independent of each other.

After significant experimental improvements, we were able to grow thin films exhibiting ferroelectric properties at a film thickness, which can be regarded as an upper limit for electron tunneling. At the same time, we had speculated, what the I - V curves for a FTJ might look like. So, it was about time to start the fabrication of *ferroelectric tunnel junctions*.

Tunnel junctions with $PbZr_{0.52}Ti_{0.48}O_3$ and $BaTiO_3$ barriers were successfully prepared with a thickness of the barrier ranging from 4 nm to 6 nm. The I - V curves displayed clear switching events at well defined electric fields and a crossover at the origin. The switching was highly reproducible and was observed at frequencies ranging from 10^{-4} Hz to 10^6 Hz. At room temperature, the resistance ratio of the high-resistance and the low-resistance curves at the origin was typically around 4. This ratio was increased for lower temperatures, and it was around 8 at 4.2 K.

An extrapolation of the thickness dependence of the coercive voltage to ultrathin films revealed a good agreement between the resistive switching effects in tunnel junctions and the ferroelectric polarization reversal in thick-film capacitors. Based on this result, the resistive switching in ultrathin

ferroelectric films is likely to be the consequence of the polarization reversal in the barrier.

A comparison with the theoretical concepts stated above yielded identical features for the predicted and the experimentally observed I - V characteristics. However, other experimentally observed features, e.g. the direction of the switching events and the crossover at the origin, did not agree with the predictions. Hence, the observed switching events in the I - V curves cannot be exclusively explained by either the converse piezoelectric effect, or by a change of the barrier heights of the metal-ferroelectric and the ferroelectric-metal interfaces. At present, it is an open question, whether the observed distinctions may be associated with further manifestations of ferroelectricity or caused by additional, superimposed effects not related to ferroelectricity.

Finally, the current transport mechanisms through the FTJ barriers were studied. The current transport was found to be dominated by phonon-assisted inelastic tunneling processes for all temperatures between 4.2 K and 300 K. We analyzed a 6 nm thick $PbZr_{0.52}Ti_{0.48}O_3$ barrier in detail. For the low-resistance curve, hopping via two localized states was identified as the dominant current transport mechanism between 4.2 K and about 40 K. From 40 K up to approximately 90 K hopping via three localized states and from about 100 K up to 300 K variable range hopping was found to be dominant. For the high-resistance curve, the crossover from hopping via two localized states to hopping via three localized states took place at about 70 K, and the crossover to variable range hopping occurred at 150 K. In addition, variable range hopping was the dominant current mechanism for both resistance states at high bias-voltages.

Outlook

It would be highly desirable, if a current transport mechanism dominated solely by electron tunneling could be realized. This would simplify the investigation of the interaction of ferroelectricity and tunneling through a ferroelectric barrier. A barrier thickness between 4 nm and 6 nm is too thick to achieve pure direct electron tunneling. To that end, a barrier thickness not greater than 2 nm is required [82, 83]. Low-magnification TEM in combination with high-resolution TEM verified the homogeneous and, based on the resolution limit of this technique, defect-free growth of 2 nm thick $BaTiO_3$ films. However, the expected coercive voltage for this film thickness exceeds

the breakdown field. Therefore, for future studies the use of ferroelectric materials, such as *Zr*-rich $PbZr_xTi_{1-x}O_3$ with lower coercive fields [111] is suggested.

A different approach could be the fabrication of tunnel junctions with a $SrTiO_3$ barrier grown on a sufficiently compressive substrate. The advantages of this barrier material over the well-established ferroelectric materials, $Pb(Zr, Ti)O_3$ and $BaTiO_3$, are the following. First, direct electron tunneling through $SrTiO_3$ barriers has already been demonstrated for a film thickness of 2 nm. Second, the strain-induced paraelectric to ferroelectric phase transition temperature is expected to be well below room temperature providing a small coercive field in the ferroelectric phase (see eqn. (1.20)). And finally, a low phase transition temperature allows the measurement of I - V curves below T_C and above T_C . A resistive switching in the ferroelectric state and no switching effect in the paraelectric state could be taken as an unambiguous proof of a ferroelectric origin of the resistive switching.

Bibliography

INTRODUCTION

- [1] L. E. CROSS AND R. E. NEWNHAM, in *Ceramics and Civilization, Vol. III, High Technology Ceramics - Past, Present, and Future*, (ed. W. D. Kingery, American Ceramic Society, Columbus, OH), 1987
- [2] I. P. BATRA AND B. D. SILVERMAN, *Solid State Commun.* Vol. 11, 291, 1972
- [3] P. WURFEL AND I. P. BATRA, *Ferroelectrics* Vol. 12, 55, 1976
- [4] R. KRETSCHMER AND K. BINDER, *Phys. Rev.* Vol. B20 (3), 1065, 1979
- [5] N. A. PERTSEV, A. G. ZEMBILGOTOV, AND A. K. TAGANTSEV, *Phys. Rev. Lett.* Vol. 80, 1988, 1998
- [6] A. G. ZEMBILGOTOV, N. A. PERTSEV, H. KOHLSTEDT, AND R. WASER, *J. Appl. Phys.* Vol. 91 (4), 2247, 2002
- [7] J. JUNQUERA AND PH. GHOSEZ, *Nature* Vol. 422, 506, 2003
- [8] N. YANASE, K. ABE, N. FUKUSHIMA, AND T. KAWAKUBO, *Jpn. J. Appl. Phys.* Vol. 38, 5305, 1999
- [9] T. TYBELL, C. H. AHN, AND J.-M. TRISCONE, *Appl. Phys. Lett.* Vol. 75, 856, 1999
- [10] S. STREIFFER, J. A. EASTMAN, D. D. FONG, C. THOMPSON, A. MUNKHOLM, M. V. RAMANA MURTY, O. AUCIELLO, G. R. BAI, G. B. STEPHENSON, *Phys. Rev. Lett.* Vol. 89 (6), 067601, 2002
- [11] D. D. FONG, G. B. STEPHENSON, S. K. STREIFFER, J. A. EASTMAN, O. AUCIELLO, P. H. FUOSS, C. THOMPSON, submitted to *Nature*

- [12] M. JUILLÈRE, Phys. Lett. Vol. 54A, 225, 1975
- [13] B.D. JOSEPHSON, Phys. Lett. Vol. 1, 251, 1962

CHAPTER 1

- [14] B. JAFFE, W. R. COOK, AND H. JAFFE, *Piezoelectric Ceramics*, (Academic Press, London and New York), 1971
- [15] A. ROELOFS, PhD thesis, RWTH Aachen, Germany, unpublished
- [16] J. F. NYE, *Physical Properties of Crystals*, (Clarendon Press, Oxford), 1979
- [17] D. RICHTER AND S. TROLIER-MCKINSTRY, in *Nanoelectronics and Information Technology*, (R. Waser (ed.), Wiley-VCH, Weinheim), 2003
- [18] D. DAMJANOVIC, Rep. Prog. Phys. Vol. 61, 1267, 1998
- [19] L. LANDAU, Phys. Z. Sowjun. Vol. 11, 26, 1937
- [20] V. GINZBURG, Journal of Phys. Vol. X (2), 107, 1946
- [21] A. F. DEVONSHIRE, Phil. Mag. Vol. 40, 1040, 1949; A. F. DEVONSHIRE, Phil. Mag. Vol. 42, 1065, 1951
- [22] M. E. LINES AND A. M. GLASS, *Principles and Applications of Ferroelectrics and Related Materials*, (Oxford University Press, Oxford), 1979
- [23] M. J. HAUN, E. FURMAN, S. J. JANG, AND L. E. CROSS, Ferroelectrics Vol. 99, 63, 1989
- [24] X. SOLANS, C. GONZALEZ-SILGO, AND C. RUIZ-PÉREZ, J. Solid State Chem. Vol. 131 (2), 350, 1997
- [25] Thin films undergoing a *second-order* paraelectric to ferroelectric phase transition can be successfully described by a polynomial expansion of the free energy up to the fourth order (see page 8). Most perovskites experience a *first-order* phase transition. However, it has been shown for $PbTiO_3$ and $BaTiO_3$ [5] that a two-dimensional clamping of the film on a thick substrate may change the order of the phase transition from first-order in bulk to second-order in thin film.

- [26] J. F. SCOTT, *Ferroelectric memories*, (Springer-Verlag, Berlin Heidelberg), 2000
- [27] H. F. KAY AND J. W. DUNN, *Phil. Mag.* Vol. 7, 2027, 1962
- [28] A.V. BUNE, V.M. FRIDKIN, S. DUCHARME, L.M. BLINOV, S.P. PALTO, A.V. SOROKIN, S.G. YUDIN, A. ZLATKIN; *Nature* Vol. 391, 874, 1998
- [29] A. K. TAGANTSEV, *Ferroelectrics* Vol. 184, 79, 1996; A. K. TAGANTSEV, I. STOLICHNOV, N. SETTER, J. S. CROSS, AND M. TSUKADA, *Phys. Rev.* Vol. B66, 214109, 2002; A. K. TAGANTSEV, *Appl. Phys. Lett.* Vol. 74 (9), 1326, 1998
- [30] M. DAWBER, P. CHANDRA, P. B. LITTLEWOOD, AND J. F. SCOTT, *J. Phys.: Condens. Matter* Vol. 15, L393L398, 2003
- [31] P. CHANDRA, M. DAWBER, P. B. LITTLEWOOD, AND J. F. SCOTT, "Thickness-Dependence of the Coercive Field in Ferroelectrics", unpublished
- [32] N. I. LEBEDEV AND A. S. SIGOV, *Integr. Ferroelectrics* Vol. 4, 21, 1994
- [33] C. H. LIN, P. A. FRIDDLE, C. H. MA, A. DAGA, AND H. CHEN, *J. Appl. Phys.* Vol. 90 (3), 1509, 2001
- [34] H. FUJISAWA, S. NAKASHIMA, K. KAIBARA, M. SHIMIZU, AND H. NIU, *Jpn. J. Appl. Phys.* Vol. 38, 5392, 1999
- [35] S. HORII, S. YOKOHAMA, H. NAKAJIMA, AND S. HORITA, *Jpn. J. Appl. Phys.* Vol. 38, 5378, 1999
- [36] Y. SAKASHITA, H. SEGAWA, K. TOMINAGA, AND M. OKADA, *J. Appl. Phys.* Vol. 73 (11), 7857, 1993
- [37] A. N. KOLMOGOROV, *Bull. Acad. Sci. USSR* Vol. 3, 355, 1937
- [38] M. J. AVRAMI, *J. Chem. Phys.* Vol. 7, 1103, 1939; Vol. 8, 212, 1940; Vol. 9, 177, 1941
- [39] Y. ISHIBASHI AND H. ORIHARA, *Integ. Ferroelec.* Vol. 9, 57, 1995
- [40] T. M. TYBELL, PhD thesis, Université de Genève, Switzerland, 2000
- [41] S. H. WEMPLE, *Phys. Rev.* Vol. B2, 2679, 1970

- [42] P. G. GENNES, *Rev. Mod. Phys.* Vol. 36, 225, 1965
- [43] E. GUYON AND C. D. MITESCU, *Thin Solid Films* Vol. 12, 355, 1972
- [44] C. A. NEUGEBAUER, *Phys. Rev.* Vol. 116, 1441, 1959
- [45] T. MITSUI AND J. FURUICHI, *Phys. Rev.* Vol. 90, 193, 1953
- [46] N. A. PERTSEV, private communication
- [47] V. L. BONCH-BRUEVICH, S. G. KALASHNIKOV, *Halbleiterphysik*, (Deutscher Verlag der Wissenschaften: Berlin), 1982
- [48] P. WURFEL, I. P. BATRA, AND J. T. JACOBS, *Phys. Rev. Lett.* Vol. 30 (24), 1218, 1973
- [49] I. P. BATRA, P. WURFEL, AND B. D. SILVERMAN, *J. Vac. Sci. Technol.* Vol. 10 (5), 687, 1973
- [50] I. P. BATRA, P. WURFEL, AND B. D. SILVERMAN, *Phys. Rev.* Vol. B8 (7), 3257, 1973
- [51] I. P. BATRA, P. WURFEL, AND B. D. SILVERMAN, *Phys. Rev. Lett.* Vol. 30, 384, 1973
- [52] P. WURFEL AND I. P. BATRA, *Phys. Rev.* Vol. B8 (11), 5126, 1973
- [53] V. L. VINETSKII, M. A. ITSKOVSKII, AND L. S. KREMENCHUGSKII, *Sov. Phys. Sol. St.* Vol. 15, 2330, 1974
- [54] I. I. IVANCHIK, *Sov. Phys. Solid State* Vol. 3 (12), 2705, 1962
- [55] L. BAUDRY AND J. TOURNIER, *J. Appl. Phys.* Vol. 90 (3), 1442, 2001
- [56] K. BINDER, *Ferroelectrics* Vol. 35, 99, 1981
- [57] J. F. SCOTT, H. M. DUIKER, P. D. BEALE, B. POULIGNY, K. DIMMLER, M. PARRIS, D. BUTLER, AND S. EATON, *Physica* Vol. B150, 160, 1988
- [58] D. TILLEY, *Ferroelectrics* Vol. 134, 313, 1992
- [59] D. TILLEY AND B. ZEKS, *Solid State Commun.* Vol. 49, 823, 198
- [60] W. L. ZHONG, B. D. QU, P. L. ZHANG, AND Y. G. WANG, *Phys. Rev.* Vol. B50 (17), 12375, 1994

- [61] S. LI, J. A. EASTMAN, J. M. VETRONE, C. M. FOSTER, R. E. NEWNHAM, AND L. E. CROSS, *Jpn. J. Appl. Phys.* Vol. 36, 5169, 1997
- [62] S. B. DESU, *J. Electrochem. Soc.* Vol. 140 (10), 2981, 1993
- [63] J. S. SPECK AND W. POMPE, *J. Appl. Phys.* Vol. 76 (1), 466, 1994
- [64] B. S. KWAK, A. ERBIL, B. J. WILKENS, J. D. BUDAI, M. F. CHISHOLM, AND L. A. BOATNER, *Phys. Rev. Lett.* Vol. 68, 3733, 1992
- [65] H. KOHLSTEDT, N. A. PERTSEV, AND R. WASER, *Mat. Res. Soc. Symp. Proc.* Vol. 688, 161, 2002
- [66] N. A. PERTSEV, A. G. ZEMBILGOTOV, AND A. K. TAGANTSEV, *Ferroelectrics* Vol. 223, 79, 1999
- [67] J. S. ZHU, X. M. LU, P. LI, W. JIANG, AND Y. N. WANG, *Solid State Comm.* Vol. 101 (4), 263, 1997
- [68] O. AUCIELLO, Extension of the total free energy was suggested during the *International Symposium on Integrated Ferroelectrics (ISIF)* in Colorado Springs, CO, 2003
- [69] PH. GHOSEZ AND K.M. RABE, *Appl. Phys. Lett.* Vol. 76, 2767, 2000
- [70] B. MEYER AND D. VANDERBILT, *Phys. Rev.* Vol. B63, 205426, 2001

CHAPTER 2

- [71] J. FRENKEL, *Phys. Rev.* Vol. 36, 1604, 1930
- [72] E. L. WOLF, *Principles of tunneling spectroscopy*, Plenum Press, p. 183, 1990
- [73] D. V. GEPPERT, *J. Appl. Phys.* Vol. 34, 490, 1963
- [74] K. H. GUNDLACH, PhD thesis, Technische Universität Clausthal, 1970
- [75] S. SHAPIRO, P. H. SMITH, J. NICOL, J. L. MILES, P. F. STRONG, *IBM Journal* Vol. 34(1), 1962

- [76] F. SCHWABL, *Quantenmechanik*, 2nd ed. Springer, p. 183, 1990
- [77] K. H. GUNDLACH, J. Appl. Phys. Vol. 44 (11), 5005, 1973
- [78] J.G. SIMMONS, J. Appl. Phys. Vol. 35, 2655, 1964
- [79] W. F. BRINKMAN, R. C. DYNES, AND J. M. ROWELL, J. Appl. Phys. Vol. 41, 1915, 1970
- [80] J. Z. SUN, L. KRUSIN-ELBAUM, P.R. DUNCOMBE, A. GUPTA, AND R. B. LAIBOWITZ, Appl. Phys. Lett. Vol. 70(13), 1769, 1997
- [81] L. I. GLAZMAN, private communication
- [82] O. MORÁN CAMPAÑA, PhD thesis, Forschungszentrum Karlsruhe, Germany, 2002
- [83] O. MORÁN CAMPAÑA, to be submitted to J. Appl. Phys
- [84] C. HÖFENER, PhD thesis, Universität zu Köln, Germany, 2000
- [85] Y. XU, D. EPHRON, AND M. R. BEASLEY, Physical Rev. Vol. B52 (4), 1995
- [86] J. WINGBERMÜHLE, PhD thesis, Forschungszentrum Jülich, Germany, 2002
- [87] R. STRATTON, J. Phys. Chem. Solids Vol. 23, 1177, 1962
- [88] A. I. LARKIN AND K. A. MATVEEV, Sov. Phys. JETP Vol. 66, 580, 1987
- [89] Y. XU, PhD thesis, Stanford University, USA, 1992
- [90] L. I. GLAZMAN AND R. I. SHEKTER, Sov. Phys. JETP Vol. 67, 163, 1988
- [91] A. D. STONE AND P. A. LEE, Phys. Rev. Lett. Vol. 54, 1196, 1985
- [92] L. I. GLAZMAN AND K. A. MATVEEV, Sov. Phys. JETP Vol. 67, 1276, 1988
- [93] N. F. MOTT AND E. A. DAVIS, *Electronic Processes in Non-Crystalline Materials*, 2nd ed. (Oxford University Press, New York), 1979

- [94] B. I. SHKLOVSKII, *Sov. Phys. Semicond.* Vol. 6 (12), 1964, 1973

CHAPTER 3

- [95] R. WOLF, P. W. M. BLOM, AND M. P. C. KRIJN, *TUNNEL DIODE WITH SEVERAL PERMANENT SWITCHING STATES*, U. S. Patent, Patent Number 5,541,422, July 30th, 1996
- [96] L. ESAKI, R. B. LAIBOWITZ, AND P. J. STILES, IBM Technical Disclosure Bulletin Vol. 13 (8), 2161, 1971; L. L. CHANG AND L. ESAKI, IBM Technical Disclosure Bulletin Vol. 14 (4), 1250, 1971
- [97] CH. KITTEL, *Introduction to Solid State Physics, 7th Ed.*, (Wiley, New York), 1996
- [98] W. Q. CHEN AND S. K. HARK, *J. Appl. Phys.* Vol. 77 (11), 5747, 1995
- [99] T. B. BAHDER, *Phys. Rev.* Vol. B41 (17), 11992, 1990; *Phys. Rev.* Vol. B45 (4), 1629, 1992
- [100] C. G. VAN DE WALLE, *Phys. Rev.* Vol. B39 (3), 1871, 1989
- [101] P. WALTEREIT, A. E. ROMANOV, AND J. S. SPECK, *Appl. Phys. Lett.* Vol. 81 (25), 4757, 2002
- [102] S. GHOSH, P. WALTEREIT, O. BRANDT, H. T. GRAHN, AND K. H. PLOOG, *Phys. Rev.* Vol. B65, 075202, 2002; S.-H. PARK AND S.-L. CHUANG, *J. Appl. Phys.* Vol. 87 (1), 353, 2000
- [103] U. KARRER, O. AMBACHER, AND M. STUTZMANN, *Appl. Phys. Lett.* Vol. 77, 2012, 2000
- [104] M. STUTZMANN, O. AMBACHER, M. EICKHOFF, U. KARRER, A. LIMA PIMENTA, R. NEUBERGER, J. SCHALWIG, R. DIMITROV, P. J. SCHUCK, AND R. D. GROBER, *Phys. Stat. Sol.* Vol. 228 (2), 505, 2001
- [105] A. RIZZI AND H. LÜTH, *Appl. Phys.* Vol. A75, 69, 2002

CHAPTER 4

- [106] J. F. SCOTT AND C. A. PAZ DE ARAUJO, *Science* Vol. 246, 1400, 1989
- [107] D. L. POLLA, C. YE, AND T. TAMAGAWA, *Appl. Phys. Lett.* Vol. 59, 3539, 1991
- [108] G. H. HAERTLING, *J. Vac. Sci. Technol.* Vol. A9, 414, 1991
- [109] R. AIDAM AND R. SCHNEIDER, *Thin Solid Films* Vol. 384, 1, 2001
- [110] J. F. M. CILLESSEN, M. W. J. PRINS, AND R. M. WOLF, *J. Appl. Phys.* Vol. 81 (6), 2777, 1997
- [111] C. M. FOSTER, G.-R. BAI, R. CSENCISITS, J. VETRONE, R. JAMMY, L. A. WILLS, E. CARR, AND J. AMANO, *J. Appl. Phys.* Vol. 81 (5), 2349, 1997
- [112] C. D. THEIS, J. YEH, D. G. SCHLOM, M. E. HAWLEY, AND G. W. BROWN, *Thin Solid Films* Vol. 325, 107, 1998
- [113] M. J. HAUN, T. R. HALEMANE, R. E. NEWNHAM, AND L. E. CROSS, *Jpn. J. Appl. Phys.* Vol 24 (Supplement 24-2), 209, 1985
- [114] F. JONA AND G. SHIRANE, *Ferroelectric Crystals - International Series of Monographs on Solid State Physics Vol. 1* (R. Smoluchowski and N. Kurti (eds.), Pergamon Press, Oxford, London, New York, Paris), 1962
- [115] N. A. PERTSEV, V. G. KUKHAR, H. KOHLSTEDT, AND R. WASER, *Phys. Rev.* Vol. B67, 054107, 2003
- [116] B. NOHEDA, D. E. COX, G. SHIRANE, J. A. GONZALO, L. E. CROSS, AND S.-E. PARK, *Appl. Phys. Lett.* Vol. 74, 2059, 1999; B. NOHEDA, J. A. GONZALO, L. E. CROSS, R. GUO, S.-E. PARK, D. E. COX, AND G. SHIRANE, *Phys. Rev.* Vol. B61, 8687, 2000; B. NOHEDA, D. E. COX, G. SHIRANE, R. GUO, B. JONES, AND L. E. CROSS, *Phys. Rev.* Vol. B63, 014103-1, 2000
- [117] L. BELLAICHE, A. GARCIA, AND D. VANDERBILT, *Phys. Rev. Lett.* Vol. 84, 5427, 2000

- [118] D. VANDERBILT AND M. H. COHEN, Phys. Rev. Vol. B63, 094108, 2001
- [119] L. WU, T.-S. WU, C.-C. WEI, AND H.-C. LIU, J. Phys. Vol. C16, 2823, 1983
- [120] R. GERSON AND H. JAFFE, J. Phys. Chem. Solids Vol. 24, 979, 1963
- [121] D. K. SCHRODER, *Semiconductor Material and Device Characterization, 2nd Ed.*, (John Wiley & Sons, Inc., New York, Chichester, Weinheim, Brisbane, Singapore, Toronto), 1998
- [122] C. SUDHAMA, A. C. CAMPBELL, P. D. MANIAR, R. E. JONES, R. MOAZZAMI, C. J. MOGAB, AND J. C. LEE, J. Appl. Phys. Vol. 75 (2), 1014, 1994
- [123] A. J. HARTMANN, M. NEILSON, R. N. LAMB, K. WATANABE, AND J. F. SCOTT, Appl. Phys. Vol. A70, 239, 2000
- [124] A. I. KINGON, S. K. STREIFFER, C. BASCERI, AND S. R. SUMMERFELT, MRS Bulletin, p. 46, July 1996
- [125] K. ABE, N. YANASE, T. KAWAKUBO, Jpn. J. Appl. Phys. Vol. 40, 2367, 2001; K. ABE, N. YANASE, AND T. KAWAKUBO, Jpn. J. Appl. Phys. Vol. 39, 4059, 2000; N. YANASE, K. ABE, N. FUKUSHIMA, AND T. KAWAKUBO, Jpn. J. Appl. Phys. Vol. 38, 5305, 1999; K. ABE AND S. KOMATSU, J. Appl. Phys. Vol. 77 (12), 6461, 1995
- [126] J. C. SHIN, J. PARK, C. S. HWANG, AND H. J. KIM, J. Appl. Phys. Vol. 86 (1), 506, 1999
- [127] M. SIEGERT, J. G. LISONI, C. H. LEI, A. ECKAU, W. ZANDER, J. SCHUBERT, AND CH. BUCHAL, Mat. Res. Soc. Proc. Vol. 597, 145, 2000
- [128] F. FITSILIS, S. REGNERY, P. EHRHART, R. WASER, F. SCHIENLE, M. SCHUMACHER, H. JUERGENSEN, Integr. Ferroelec. Vol. 38, 211, 2001
- [129] R. A. MCKEE, F. J. WALKER, AND M. F. CHISHOLM, Science Vol. 293 (5529), 468, 2001; R. A. MCKEE, F. J. WALKER, E. D. SPECHT, G. E. JELLISON, JR., L. A. BOATNER, AND J. HARDING, Phys. Rev. Lett. Vol. 72 (17), 2741, 1994; R. A. MCKEE, F. J. WALKER, J. R. CONNER, AND E. D. SPECHT, Appl. Phys. Lett. Vol. 59 (7), 782, 1991

- [130] K. SHIMOYAMA, K. KUBO, M. IIDA, K. YAMABE, AND T. MAEDA, *J. Vac. Sci. Technol.* Vol. A19 (5), 2083, 2001
- [131] Y. YONEDA, T. OKABE, K. SAKAUE, H. TERAUCHI, H. KASATANI, AND K. DEGUCHI, *J. Appl. Phys.* Vol. 83 (5), 2458, 1998
- [132] H. SHIGETANI, K. KOBAYASHI, M. FUJIMOTO, W. SUGIMURA, Y. MATSUI, AND J. TANAKA, *J. Appl. Phys.* Vol. 81 (2), 693, 1997
- [133] T. TSURUMI, T. SUZUKI, M. YAMANE, AND M. DAIMON, *Jpn. J. Appl. Phys.* Vol. 33, 5192, 1994
- [134] GMELIN HANDBOOK OF INORGANIC AND ORGANOMETALLIC CHEMISTRY, Main: Titan, Vol. 41, (Springer Verlag, New York), 1951
- [135] F. FITSILIS, PhD thesis, Forschungszentrum Jülich, 2002
- [136] Y. LU, X. W. LI, G. Q. GONG, G. XIAO, A. GUPTA, P. LECOEUR, J. Z. SUN, Y. Y. WANG, AND V. P. DAVID, *Phys. Rev.* Vol. B54, 8357, 1996
- [137] A. CALLAGHAN, C. W. MOELLER, AND R. WARD, *Inorg. Chem.* Vol. 5, 1572, 1996
- [138] R. J. BOUCHARD AND J. L. GILLSON, *Mater. Res. Bull.* Vol. 7, 873, 1972
- [139] A. KANBAYASI, *J. Phys. Soc. Japan* Vol. 44, 89, 1978
- [140] J. C. JIANG AND X. Q. PAN, *Phil. Mag. Lett.* Vol. 80 (5), 271, 2000
- [141] J.-P. MARIA, H. L. MCKINSTRY, AND S. TROLIER-MCKINSTRY, *Appl. Phys. Lett.* Vol. 76 (23), 3382, 2000
- [142] B. C. CHAKOUMAKOS, S. E. NAGLER, S. T. MISTURE, AND H. M. CHRISTEN, *Physica* Vol. B241-243, 358, 1998
- [143] C. B. EOM, R. J. CAVA, R. M. FLEMING, J. M. PHILLIPS, R. B. VAN DOVER, J. H. MARSHALL, J. W. P. HSU, J. J. KRAJEWSKI, AND W. F. PECK, *Science* Vol. 258, 1766, 1992
- [144] X. D. WU, S. R. FOLTYN, R. C. DYE, Y. COULTER, AND R. E. MUENCHAUSEN, *Appl. Phys. Lett.* Vol. 62, 2434, 1993

- [145] Q. X. JIA, F. CHU, C. D. ADAMS, X. D. WU, M. HAWLEY, J. H. CHO, A. T. FINDIKOGLU, S. R. FOLTYN, J. L. SMITH, AND T. E. MITCHELL, *J. Mater. Res.* Vol. 11, 2263, 1996
- [146] M. HIRATANI, C. OKAZAKI, K. IMAGAWA, AND K. TAKAGI, *Jpn. J. Appl. Phys.* Vol. 35, 6212, 1996
- [147] H. FUNAKUBO, T. OIKAWA, N. HIGASHI, AND K. SAITO, *J. Cryst. Growth.* Vol. 229, 450, 2001
- [148] L. KLEIN, Y. KATS, A. F. MARSHALL, J. W. REINER, T. H. GEBALLE, M. R. BEASLEY, AND A. KAPITULNIK, *Phys. Rev. Lett.* Vol. 84 (26), 6090, 2000; L. KLEIN, A. F. MARSHALL, J. W. REINER, C. H. AHN, T. H. GEBALLE, M. R. BEASLEY, AND A. KAPITULNIK, *J. Magn. Magn. Mater.* Vol. 188, 319, 1998; C. H. AHN, R. H. HAMMOND, T. H. GEBALLE, M. R. BEASLEY, J.-M. TRISCONI, M. DECROUX, Ø. FISCHER, L. ANTOGNAZZA, AND K. CHAR, *Appl. Phys. Lett.* Vol. 70 (2), 206, 1996; L. KLEIN, J. S. DODGE, C. H. AHN, G. J. SNYDER, T. H. GEBALLE, M. R. BEASLEY, AND A. KAPITULNIK, *Phys. Rev. Lett.* Vol. 77 (13), 2774, 1996; L. KLEIN, J. S. DODGE, C. H. AHN, J. W. REINER, L. MIEVILLE, T. H. GEBALLE, M. R. BEASLEY, AND A. KAPITULNIK, *J. Phys.: Condens. Matter* Vol. 8, 10111, 1996; S. J. BENEROFE, C. H. AHN, M. M. WANG, K. E. KIHLMSTROM, K. B. DO, S. B. ARNASON, M. M. FEJER, T. H. GEBALLE, M. R. BEASLEY, AND R. H. HAMMOND, *J. Vac. Technol.* Vol. B12 (2), 1217, 1994
- [149] M. IZUMI, K. NAKAZAWA, Y. BANDO, Y. YONEDA, AND H. TERAUCHI, *J. Phys. Soc. Jap.* Vol. 66, 3893, 1997
- [150] Note that the pseudo-cubic (001) reflexes correspond to the orthorhombic (hh0) reflexes. The pseudo-cubic lattice constant was calculated using the following formula: $a_{pseudo} = ((a/\sqrt{2}) (b/2) (c/\sqrt{2}))^{1/3}$ where a , b and c are the orthorhombic unit cell lattice constants and a_{pseudo} is the pseudo-cubic lattice constant.
- [151] C. B. EOM, R. B. VAN DOVER, J. M. PHILLIPS, D. J. WERDER, J. H. MARSHALL, C. H. CHEN, R. J. CAVA, R. M. FLEMING, AND D. K. FORK, *Appl. Phys. Lett.* Vol. 63, 2570, 1993
- [152] O. AUCIELLO, C. M. FOSTER, AND R. RAMESH, *Annu. Rev. Mater. Sci.* Vol. 28, 501, 1998

- [153] E. TOSATTI AND R. MARTOŇÁK, *Solid State Comm.* Vol. 92, 167, 1994
- [154] N. A. PERTSEV, A. K. TAGANTSEV, AND N. SETTER, *Phys. Rev.* Vol. B61, R825, 2000; N. A. PERTSEV, A. K. TAGANTSEV, AND N. SETTER, *Phys. Rev.* Vol. B65, 219901, 2002
- [155] D. FUCHS, C. W. SCHNEIDER, R. SCHNEIDER AND H. RIETSCHEL, *J. Appl. Phys.* Vol. 85, 7362, 1999
- [156] D. FUCHS, M. ADAM, P. SCHWEISS, S. GERHOLD, S. SCHUPPLER, R. SCHNEIDER AND B. OBST, *J. Appl. Phys.* Vol. 88 (4), 1844, 2000
- [157] K. ASTAFIEV, V. O. SHERMAN, A. K. TAGANTSEV, N. SETTER, P. K. PETROV, T. KAYDANOVA, D. S. GINLEY, S. HOFFMANN-EILERT, U. BOETTGER, AND R. WASER, "Stress Induced Shift of Phase Transition Temperature in $SrTiO_3$ and $Ba_{0.6}Sr_{0.4}TiO_3$ Thin Films", Poster contribution at *International Symposium on Integrated Ferroelectrics (ISIF)* in Colorado Springs, CO, 2003
- [158] J. E. MAHAN, *Physical Vapor Deposition of Thin Films*, (John Wiley & Sons, Inc., New York, Chichester, Weinheim, Brisbane, Singapore, Toronto), 2000
- [159] P. EHRHART, in *Nanoelectronics and Information Technology*, (R. Waser (ed.), Wiley-VCH, Weinheim) , 2003
- [160] J.-K. HEINSOHN, R. DITTMANN, J. RODRÍGUEZ CONTRERAS, J. SCHERBEL, A. M. KLUSHIN, M. SIEGEL, C. L. JIA, S. GOLUBOV, AND M. YU. KUPRYANOV, *J. Appl. Phys.* Vol. 89 (7), 3852, 2001
- [161] J.-K. HEINSOHN, R. DITTMANN, J. RODRÍGUEZ CONTRERAS, E. GOLDOBIN, A. M. KLUSHIN, M. SIEGEL, D. HAGEDORN, R. PÖPEL, R. DOLATA, F.-IM. BUCHHOLZ, AND J. NIEMEYER, *J. Appl. Phys.* Vol. 90 (9), 4623, 2001
- [162] M. SUGA, M. HIRATANI, C. OKAZAKI, M. KOGUCHI, AND H. KAKIBAYASHI, *Integr. Ferroelec.* Vol. 18, 389, 1997
- [163] J. LETTIERI, PhD thesis, The Pennsylvania State University, 2002
- [164] D. G. SCHLOM, J. N. ECKSTEIN, E. S. HELLMAN, C. WEBB, F. TURNER, J. S. HARRIS, M. R. BEASLEY AND T. H. GEBALLE, in *Extended Abstracts, High-Temperature Superconductors II*, (D. W.

- Capone, W. H. Butler, B. Batlogg, and C. W. Chu (eds.), Materials Research Society, Pittsburgh), 1988
- [165] J. G. BEDNORZ AND K. A. MÜLLER, *Z. Phys.* Vol. B64, 189, 1986
- [166] D. G. SCHLOM, Courtesy of the Schlom group, The Pennsylvania State University
- [167] J. H. HAENI, PhD thesis, The Pennsylvania State University, 2002
- [168] U. POPPE, J. SCHUBERT, R. ARONS, W. EVERS, C.H. FREIBURG, W. REICHERT, K. SCHMIDT, W. SYBERTZ, AND K. URBAN, *Solid State Commun.* Vol. 66, 661, 1988
- [169] C. RINCÓN, G. ZAMBRANO, A. CARVAJAL, P. PRIETO, H. GALINDO, E. MARTÍNEZ, A. LOUSA, AND J. ESTEVE, *Surf. Coat. Technol.* Vol. 148, 277, 2001
- [170] C.-H. YANG, S.-S. PARK, AND S.-G. YOON, *Integ. Ferroelec.* Vol. 18, 377, 1997

CHAPTER 5

- [171] CH. BARRETT AND T. B. MASSALSKI, *Structure of Metals - Crystallographic Methods, Principles and Data, 3rd revised edition*, International Series on Materials Science and Technology, Vol. 35, 1987
- [172] B. D. CULLITY AND S. R. STOCK, *Elements of X-ray Diffraction*, (Prentice Hall, Upper Saddle River, New Jersey), 2001
- [173] O. H. SEECK, in *Nanoelectronics and Information Technology*, (R. Waser (ed.), Wiley-VCH, Weinheim) , 2003
- [174] W. BRAUN, *Applied RHEED*, (Springer, Berlin), 1999
- [175] J. E. MAHAN, K. M. GEIB, G. Y. ROBINSON, AND R. G. LONG, *J. Vac. Sci. Technol.* Vol. A8, 3692, 1990
- [176] S. KIKUCHI, *Japan. J. Phys.* Vol. 5, 83, 1928
- [177] W. HARTL AND H. RAETHER, *Z. Physik* Vol. 161, 238, 1961

- [178] RUMP - RUTHERFORD BACKSCATTERING DATA ANALYSIS PLOTTING AND SIMULATION PACKAGE, Computer Graphic Service, LTD., 9565 Japonica, El Paso, TX 79924, 1987-2002
- [179] S. MANTL, in *IFF-Ferienkurs: Festkörperforschung für die Informationstechnik*, (Forschungszentrum Jülich, Jülich), Vol. 21, p. 25.1-24, 1990
- [180] P. EBERT, K. SZOT AND A. ROELOFS, in *Nanoelectronics and Information Technology*, (R. Waser (ed.), Wiley-VCH, Weinheim) , 2003
- [181] MODIFIED FROM SKETCH DRAWN BY A. ROELOFS AND U. KALL, RWTH AACHEN, GERMANY
- [182] MANUAL - AIXACCT TF ANALYZER 2000

CHAPTER 6

- [183] C. L. JIA, J. RODRÍGUEZ CONTRERAS, J. SCHUBERT, M. LENTZEN, U. POPPE, H. KOHLSTEDT, K. URBAN, AND R. WASER, *J. Crystal Growth* Vol. 247, 381, 2003
- [184] M. KAWASAKI, K. TAKAHASHI, T. MAEDA, R. TSUCHIYA, M. SHINOHARA, O. ISHIYAMA, T. YONEZAWA, M. YOSHIMOTO, AND H. KOINUMA, *Science* Vol. 266, 1540, 1994
- [185] I. BOZOVIC, 1) Mix 10 M stock etching solution (8.89 M NH_4F + 1.11 M HF)-pH 4.2: 125 g pure NH_4F (anhydrous) + 17 ml concentrated HF (49.5%) solution + DI H_2O until final volume of mixture is 380 ml. 2) Add (drop-by-drop) enough stock etching solution to cover substrate surface completely. 3) Etch for 2.5 minutes (i.e., wait, no agitation involved) at room temperature. Optimal etch times were evaluated by AFM. They varied from 2-10 minutes, depending on the as-received $SrTiO_3$ substrate. 4) Drop substrate covered with etching solution into beaker of DI water. 5) Rinse in DI water for several minutes. 6) Rinse substrate in isopropanol. (Our procedure: Isopropanol and acetone treatment prior to etching, but not after etching.) 7) Remove substrate from beaker and blow dry with filtered N_2 (our procedure: spin dry to avoid damage from N_2 bombardement).

- [186] G. RIJNDERS, *The Initial Growth of Complex Oxides - Study and Manipulation*, (Printpartners Ipskamp, Enschede), p. 61-81, 2001
- [187] C. B. EOM, private communication
- [188] Various indications were obtained: (a) Specific features which appeared in the RHEED pattern clearly indicating *Ru*-excess disappeared after the growth over a short time. (b) Stopping the growth after *RuO*₂ deposition and restarting the growth after a short time with *SrO* deposition resulted in a disturbed time dependence of the RHEED intensity. Therefore, the growth if necessary was only stopped after *SrO* deposition.
- [189] M. D. BIEGALSKI, J. H. HAENI, S. TROLIER-MCKINSTRY, D. G. SCHLOM, C. D. BRANDLE, AND A. V. GRAITIS, unpublished
- [190] O. AUCIELLO, talk at the *Workshop on Science and Technology of Ferroelectric Materials*, Panamerican Advanced Study Institute (PASI) in Rosario, Argentina, 2002
- [191] C. V. R. VASANT KUMAR, R. PASCUAL, AND M. SAYER, *J. Appl. Phys.* Vol. 72 (2), 864, 1992
- [192] R. AIDAM, PhD thesis, Forschungszentrum Karlsruhe, Germany, 1999
- [193] J. RODRÍGUEZ CONTRERAS, H. KOHLSTEDT, J. SCHUBERT, U. POPPE, K. SZOT, CH. BUCHAL, AND R. WASER, submitted to *Thin Solid Films*
- [194] C.L. JIA, J. RODRÍGUEZ CONTRERAS, U. POPPE, H. KOHLSTEDT, R. WASER AND K. URBAN, *J. Appl. Phys.* Vol. 92, 101 (2002)
- [195] M. ZURBUCHEN, PhD thesis, The Pennsylvania State University, USA, 2002
- [196] J. RODRÍGUEZ CONTRERAS, J. SCHUBERT, U. POPPE, O. TRITHAVEESAK, K. SZOT, CH. BUCHAL, H. KOHLSTEDT, AND R. WASER, *Mat. Res. Soc. Symp. Proc.* Vol. 688, C8.10, 2002

CHAPTER 7

- [197] IMAGE TOOL FOR WINDOWS VERS. 3.00, University of Texas Health Science Center in San Antonio (UTHSCSA), May 2002
- [198] M. GROSSMANN, PhD thesis, RWTH Aachen, Germany, 2001
- [199] M. GROSSMANN, O. LOHSE, T. SCHNELLER, D. BOLTEN, U. BOETTGER, J. RODRÍGUEZ CONTRERAS, H. KOHLSTEDT, AND R. WASER, *Int. Ferroelectrics* Vol. 37 (1-4), 205, 2001
- [200] P. K. LARSEN, G. J. M. DORMANS, D. J. TAYLOR, AND P. J. VAN VELDHOVEN, *J. Appl. Phys.* Vol. 76, 2405, 1994; A. K. TAGANTSEV, CZ. PAWLACZYK, K. BROOKS, AND N. SETTER, *Int. Ferroelectrics* Vol. 4, 1, 1994; J. F. M. CILLESSEN, M. W. J. PRINS, AND R. W. WOLF, *J. Appl. Phys.* Vol. 81, 2777, 1997; S. DUCHARME, V. M. FRIDKIN, A. V. BUNE, S. P. PALTO, L. M. BLINOV, N. N. PETUKHOVA, AND S. G. YUDIN, *Phys. Rev. Lett.* Vol. 84, 175, 2000
- [201] J. BRUGGER, J. W. BERENSCHOT, S. KUIPER, W. NIJDAM, B. OTTER, AND M. ELWENSPOEK *Microelectron. Eng.* Vol. 53, 403, 2000; V. BUCHER, J. BRUGGER, D. KERN, G. M. KIM, M. SCHUBERT, AND W. NISCH, *Microelectron. Eng.* Vol. 6162, 971, 2002
- [202] A. Q. JIANG, J. F. SCOTT, M. DAWBER, AND C. WANG, *J. Appl. Phys.* Vol. 92 (11), 6756, 2002
- [203] X. F. DU AND I. W. CHEN, *Appl. Phys. Lett.* Vol. 72, 1923, 1998
- [204] E. L. COLLA, D. TAYLOR, A. TAGANTSEV, AND N. SETTER, *Appl. Phys. Lett.* Vol. 72, 2478, 1998
- [205] I. STOLICHNOV, A. TAGANTSEV, E. L. COLLA, AND N. SETTER, *Appl. Phys. Lett.* Vol. 73, 1361, 1998
- [206] A. M. BRATKOVSKY AND A. P. LEVANYUK, *Phys. Rev.* Vol. B63, 132103, 2001
- [207] A. M. BRATKOVSKY AND A. P. LEVANYUK, *Phys. Rev. Lett.* Vol. 84, 3177, 2000
- [208] M. DAWBER AND J. F. SCOTT, *Appl. Phys. Lett.* Vol. 76, 1060, 2000; Vol. 76, 3655, 2000

- [209] F. FITSILIS, private communication
- [210] R. LIEDTKE, private communication
- [211] M. GROSSMANN, private communication
- [212] C. LOPPACHER, F. SCHLAPHOF, L. M. ENG, J. RODRÍGUEZ CONTRERAS, H. KOHLSTEDT, AND R. WASER, unpublished
- [213] N. A. PERTSEV, private communication, Coercive field at room temperature for $PbZr_{0.5}Ti_{0.5}O_3$ thin films under a compressive strain $S_m = -16 \cdot 10^{-3}$
- [214] K. SZOT, W. SPEIER, R. CARIUS, U. ZASTROW, AND W. BAYER, Phys. Rev. Lett. Vol. 88, 075508, 2002
- [215] R. WANG, Y. ZHU, AND S. M. SHAPIRO, Phys. Rev. Lett. Vol. 80, 2370, 1998
- [216] J. RODRÍGUEZ CONTRERAS, H. KOHLSTEDT, C. JIA, AND J. WU, unpublished

CHAPTER 8

- [217] J. Z. SUN, Phil. Trans. R. Soc. Lond. A Vol. 356, 1693, 1998
- [218] J. F. DEWALD, A. D. PEARSON, W. R. NORTHOVER, AND W. F. PECK, J. Electrochem. Soc. Vol. 109, 243c, 1962
- [219] S. R. OVSHINSKY, Phys. Rev. Lett. Vol. 36, 1469, 1968
- [220] H. J. HOVEL AND J. J. URGELL, J. Appl. Phys. Vol. 42 (12), 5076, 1971
- [221] T. W. HICKMOTT AND W. R. HIATT, Solid-State Electron. Vol. 13 (7), 1033, 1970
- [222] K. L. CHOPRA, J. Appl. Phys. Vol. 36, 184, 1965
- [223] F. ARGALL, Solid State Electron. Vol. 11, 535, 1968
- [224] J. F. GIBBONS AND W. E. BEADLE, Solid State Electron. Vol. 7, 785, 1964

- [225] J. C. BRUYERE AND B. K. CHAKRAVERTY, *Appl. Phys. Lett.* Vol. 16 (1), 40, 1970
- [226] K. UENO AND N. KOSHIDA, *Appl. Phys. Lett.* Vol. 74, 93, 1999
- [227] H. J. GAO, K. SOHLBERG, Z. Q. XUE, H. Y. CHEN, S. M. HOU, L. P. MA, X. W. FANG, S. J. PANG, AND S. J. PENNYCOOK, *Phys. Rev. Lett.* Vol. 84, 1780, 2000
- [228] S. G. LIU, P. J. WU, Y. Q. LIU, AND D. B. ZHU, *Mol. Cryst. Liq. Cryst.* Vol. 275, 211, 1996
- [229] YU. G. KRIGER, N. F. YUDANOV, I. K. IGUMENOV, AND S. B. VASHCHENKO, *J. Struct. Chem.* Vol. 34 (6), 966, 1993
- [230] A. BECK, J. G. BEDNORZ, CH. GERBER, C. ROSSEL, AND D. WIDMER, *Appl. Phys. Lett.* Vol. 77 (1), 139, 2000
- [231] C. ROSSEL, G. I. MEIJER, AND D. WIDMER, *J. Appl. Phys.* Vol. 90 (6), 2892, 2001
- [232] Y. WATANABE, J. G. BEDNORZ, A. BIETSCH, CH. GERBER, D. WIDMER, A. BECK, AND S. J. WIND, *Appl. Phys. Lett.* Vol. 78 (23), 3738, 2001
- [233] Y. WATANABE, *Appl. Phys. Lett.* Vol. 66 (1), 28, 1995
- [234] M. OKANO, Y. WATANABE, *Appl. Phys. Lett.* Vol. 76 (2), 233, 2000
- [235] Y. WATANABE, *Phys. Rev.* Vol. B57 (10), 5563, 1998
- [236] Y. WATANABE, *Phys. Rev.* Vol. B59 (17), 11257, 1999

Erklärung

Ich versichere, daß ich die von mir vorgelegte Dissertation selbstständig angefertigt, die benutzten Quellen und Hilfsmittel vollständig angegeben und die Stellen der Arbeit - einschließlich Tabellen, Karten und Abbildungen -, die anderen Werken im Wortlaut oder dem Sinn nach entnommen sind, in jedem Einzelfall als Entlehnung kenntlich gemacht habe; daß diese Dissertation noch keiner anderen Fakultät oder Universität zur Prüfung vorgelegen hat; daß sie - abgesehen von unten angegebenen Teilpublikationen - noch nicht veröffentlicht worden ist sowie, daß ich eine solche Veröffentlichung vor Abschluß des Promotionsverfahrens nicht vornehmen werde. Die Bestimmungen dieser Promotionsordnung sind mir bekannt. Die von mir vorgelegte Dissertation ist von Prof. Dr. Ch. Buchal betreut worden.

Köln, 26. Mai 2003

Publikationen

- J. Rodríguez Contreras, H. Kohlstedt, U. Poppe, R. Waser, Ch. Buchal, N. A. Pertsev, *Resistive switching in metal-ferroelectric-metal junctions*, Appl. Phys. Lett. Vol. 83, 4595, 2003
- J. Rodríguez Contreras, H. Kohlstedt, U. Poppe, R. Waser, Ch. Buchal, *Surface treatment effects on the thickness dependence of the remanent polarization of $PbZr_{0.52}Ti_{0.48}O_3$ capacitors*, Appl. Phys. Lett. Vol. 83 (1), 126, 2003
- J. Rodríguez Contreras, J. Schubert, U. Poppe, O. Trithaveesak, K. Szot, Ch. Buchal, H. Kohlstedt, and R. Waser, *Structural and Ferroelectric Properties of Epitaxial $PbZr_{0.52}Ti_{0.48}O_3$ and $BaTiO_3$ Thin Films Prepared on $SrRuO_3/SrTiO_3(100)$ Substrates*, Mat. Res. Soc. Symp. Proc. Vol. 688, C8.10, 2002

- N. A. Pertsev, J. Rodríguez Contreras, V. G. Kukhar, H. Kohlstedt, and R. Waser, *Coercive field of ultrathin $PbZr_{0.52}Ti_{0.48}O_3$ films*, Appl. Phys. Lett. Vol. 83, 3356, 2003
- C.L. Jia, J. Rodríguez Contreras, U. Poppe, H. Kohlstedt, R. Waser and K. Urban, *Lattice strain and lattice expansion of the $SrRuO_3$ layers in $SrRuO_3/Pb(Zr,Ti)O_3/SrRuO_3$ multilayer thin films*, J. Appl. Phys. Vol. 92 (1), 101, 2002
- C.L. Jia, J. Rodríguez Contreras, J. Schubert, M. Lentzen, U. Poppe, H. Kohlstedt, K. Urban and R. Waser, *Engineering and characterization of interfacial defects in $SrRuO_3/BaTiO_3/SrRuO_3$ multilayer films*, J. Crystal Growth Vol. 247, 381, 2003
- M. Grossmann, O. Lohse, T. Schneller, D. Bolten, U. Boettger, J. Rodríguez Contreras, H. Kohlstedt, and R. Waser, *Imprint in ferroelectric $Pb(Zr,Ti)O_3$ thin films with thin $SrRuO_3$ layers at the electrodes*, Int. Ferroelectrics Vol. 37, 1-4, 535, 2001

Patente

H. Kohlstedt, J. Rodríguez Contreras, "Ferroelektrischer Tunnelkontakt", Deutsche Patent Nummer 10059357.7-33, Internationale Patent Nummer PCT/DE 01-04447

Konferenz-Vorträge

- International Symposium on Ferroelectrics (ISIF 2003), Colorado Springs, CO, USA: *Properties Of Ultrathin Epitaxial $BaTiO_3$ Films Grown By MBE*, J. Rodriguez Contreras, J. Schubert, K. Szot, C.L. Jia, H. Kohlstedt, R. Waser, Ch. Buchal, J. Haeni, M. Biegalski, D. G. Schlom
- Workshop on Oxide Electronics (WOE 9) 2002, St. Petersburg, FL, USA: *Structural and Ferroelectric Properties of MBE-Grown $BaTiO_3/SrRuO_3$ Thin Films*, J. Rodríguez Contreras, J. Schubert, K. Szot, C. Jia, J. Haeni, M. Biegalski, H. Kohlstedt, R. Waser, and D. G. Schlom
- Panamerican Advanced Studies Institute (PASI) workshop 2002, Science and Technology of Ferroelectric Materials, Rosario, Argentina: *Size Effects in Ferroelectrics*, J. Rodríguez Contreras, A. Gerber, J. Schubert, U. Poppe, K. Szot, C. Jia, J. Haeni, M. Biegalski, Ch. Buchal, H. Kohlstedt, R. Waser, and D. G. Schlom

- Workshop on Oxidic Surfaces 2002, Halle, Germany: *Influence of patterning method on ferroelectric properties of $PbZr_{0.52}Ti_{0.48}O_3$ capacitors*, J. Rodríguez Contreras, J. Schubert, U. Poppe, K. Szot, Ch. Buchal, H. Kohlstedt, R. Waser
- Materials Research Society (MRS) Fall Meeting 2001, Boston, MA, USA: *Experimental Approach to Investigate the Influence of Ferroelectricity on a Tunnel Current*, J. Rodríguez Contreras, J. Schubert, U. Poppe, K. Szot, C. L. Jia, O. Trithaveesak, Ch. Buchal, H. Kohlstedt, R. Waser
- Frühjahrstagung der Deutschen Physikalischen Gesellschaft (DPG) 2001, Hamburg: *Sputtered $PbZr_{0.52}Ti_{0.48}O_3/SrRuO_3$ films on $SrTiO_3$ substrates*, J. Rodríguez Contreras, U. Poppe, J. Schubert, K. Szot, C. Jia, H. Kohlstedt, R. Waser